Conformational Dynamics in the Regulation of MAP Kinase, ERK2

by

Yao Xiao

B.S., Fudan University, 2008

A thesis submitted to the

Faculty of the Graduate School of the

University of Colorado in partial fulfillment

of the requirement for the degree of

Doctor of Philosophy

Department of Chemistry and Biochemistry

2015

This thesis entitled:
Conformational Dynamics in the Regulation of MAP Kinase, ERK2
Written by Yao Xiao
has been approved for the Department of Chemistry and Biochemistry

_____
Dr. Natalie G. Ahn

_____
Dr. Arthur Pardi

Date_____

The final copy of this thesis has been examined by the signatories, and we find that both the content and the form meet acceptable presentation standards of scholarly work in the above mentioned discipline.

Xiao, Yao (Ph.D., Department of Chemistry and Biochemistry)

Conformational Dynamics in the Regulation of MAP Kinase, ERK2

Thesis directed by Professor Natalie G. Ahn

The MAP kinase, extracellular signal-regulated kinase 2 (ERK2), is a key regulator of cell signaling. Aberrant up-regulation of ERK2 has been correlated with various diseases. ERK2 can be activated by MAP kinase kinases through dual phosphorylation at the activation loop. It remains a challenging question how changes in conformational dynamics contribute to kinase activation. NMR relaxation dispersion experiments were used to monitor changes in Ile, Leu, and Val (ILV) methyl motions in microsecond-millisecond timescale upon activation of ERK2. A structure-based procedure was developed to assign $^{13}C^{1}H_3$-labeled methyls, by comparing NMR distance constraints with the X-ray structure. This procedure yielded 60% of the methyl assignments in inactive and active forms of ILV $^{13}C^{1}H_3$-methyl labeled ERK2. In inactive ERK2, localized conformational dynamics was observed among methyls. Upon activation, the dynamics of assigned methyls in ERK2 were altered throughout the kinase core, including many residues in the catalytic pocket. The majority of methyls in active ERK2 fit to a single conformational exchange process, suggesting global domain motions involving interconversion between two states. A mutant of ERK2, engineered to enhance flexibility at the hinge region linking the N- and C-terminal domains, induced two-state conformational exchange throughout the kinase core. A mono-phospho-mimetic form of this mutant showed 25% of the dual-phosphorylated ERK2 activity. Thus, activation of ERK2 leads to a dramatic shift in conformational exchange, from a “tense” (T) state to a “relaxed” (R) state, likely through release of constraints at the hinge. To understand the effects on the conformational dynamics of ERK2 during catalysis and upon inhibitor binding, complexes of ERK2 with various ligands were formed. The binding of nucleotides and/or peptide substrates showed no significant perturbation to the T/R conformational equilibrium, with small enhancement of the T state population in active ERK2. In addition, differential conformational stabilization effects, which were not previously reported for ERK2, were observed upon the binding of different tight-binding inhibitors of ERK2. This thesis reports that ERK2

activation enhances microsecond-millisecond interconversion between conformers underlying different enzyme intermediates, thus linking protein dynamics to the catalytic cycle. The perturbations of conformational equilibrium by inhibitors reflect a novel allosteric mechanism in ERK2.

Dedication

To the ascending spiral journey

and the enjoyable moments

Acknowledgements

I would like to start by thank my advisor, Dr. Natalie Ahn. Natalie has showed unbelievable patience and confidence on me since the first day that we met, and has been consistent with these. She has spent tremendous amount of time and energy to guide me on my project over these years, and also provided me lots of opportunities to see the scientific field by going to conferences, giving talks, and writing reviews. I would like to thank my co-advisor, Dr. Arthur Pardi. Art has been incredibly generous with his time, effort and strategies in training me to think logically and critically, and express accurately and simply. It is incredible how tolerant and persistent he has been while I was struggling. His training is "brain-washing" and provided me with the vision to think independently in the future. It's a cherish period of time doing my graduate work with these advisors who really cares about their students, and my expression of appreciation is limited by this paragraph.

My other committee members, Drs. Marcelo Sousa, Johannes Rudolph and Loren Hough have been paying close attention to my progresses and concerns, provided insightful suggestions and opportunities, during and out of the committee meeting. Marcelo and Johannes also served on my oral exam committee. During these years, Marcelo never hesitated to help me whenever I needed. Johannes was my awesome enzymology teacher during the core class, and has recently brought his huge creativity and collabrativity to the Ahn lab. Loren created opportunity for me to interact with invited professor. I definitely owe a huge thank for their generous help.

I am grateful of all the Ahn lab and Pardi lab members, for their expertise, understanding, friendship, and accompanying. In the Ahn lab, Tianjing Hu and Akiko Tanimoto helped me quickly settle down in the lab. Tianjing, who has been sitting next to me for at least 3 years, is a solid source of support and friendship. Akiko and I spent a short period of two months together, not only intensitively purifying proteins for this project, but also sharing all her knowledge and kindness. Dr. Thomas Lee

backed me up throughout these years, and has been giving me countless encouragements and suggestions. Dr. Kevin Sours, Dr. Scott Stuart, Dr. Mary Tarrant Connacher, and Jennifer Liddle constantly give me help and feedbacks with their own expertises.

Drs. Lisa Warner, Laura Johnson and Krisztina Varga offered me tremendous help when I started rotating in the Pardi group. Lisa not only shared her knowledge, but also advised me to work independently even she was (and is still) always there when I needed help. Laura is a wonderful tutor, explainer, listener and friend. Previous member of the Pardi group, Dr. Michael Latham, has been a constant source of support with his NMR expertise. Thinking about how much I learned from him, how much we collaborated and communicated, I already fogot that I've only met him for only a few times. I'm grateful to Sabrina Hunt, who has been organizing the NMR club, offering me help, discussion and feedbacks all the time.

I would like to express my gratitude for Drs. Richard Shoemaker and Geoffery Armstrong, who are responsible NMR managers and beyond that are wonderful NMR teachers for me. I am also hugely indebted to Dr. Jeremy Balsbaugh, who is now the director of MS facility. It was a great pleasure to work with these people, who helped me with huge patience and tolerance.

I also am highly grateful to my family and friends. My parents never hesitated to support me on pursuing higher education, even to places ~7k miles from home, wheras they would love my accompanying. Neither of them is in scientific majors, but they enjoyed (or I hope that they enjoyed) being listeners for me on my projects.

Thank you all. This thesis will not exist or will not be the same without the help from any of you.

Contents

Tables Table of Content

Figure Table of Contents

Chapter 1. Introduction

1.1. Mitogen-Activated Protein Kinase Signaling Pathway

The mitogen-activated protein (MAP) kinase signaling pathway (Figure 1.1) regulates many types of cellular functions.[1, 2] Typically, following extra-cellular stimuli (e.g. growth factors) binding to the cell membrane, receptor tyrosine kinases become activated through dimerization, leading to GTP loading and activation of Ras. This recruits Raf to the membrane, where it is phosphorylated by other protein kinases (suspected to be Src family kinases).[3, 4] The activation of Raf proteins is also associated with hetero-dimerization which forms a B-Raf:C-Raf complex[5] and mediated by the kinase suppressor of Ras (KSR), which is also known as one of the scaffolding proteins for Raf/MKK/ERK pathway.[6, 7] Alternatively, the activation of B-Raf could be a result of the stimulation of G-protein coupled receptor (GPCR) relevant signaling pathways,[8] some of which is likely mediated by G-protein β and γ subunits in a Ras-dependent manner,[9] whereas others require the participation of protein kinase C.[10] The activation of B-Raf by phosphorylation initiates the so-called "MAP kinase (MAPK) phosphorylation cascade", where B-Raf activates MAP kinase kinases 1 and 2 (MKK1/2) by dual phosphorylation on serine residues, and MKK activates extracellular signal-regulated kinases 1 and 2 (ERK1/2) by dual phosphorylation on threonine and tyrosine residues. Once ERK is activated, it either stays in cytoplasm and catalyzes the phosphorylation of cytoplasmic targets, or translocates into the nucleus and phosphorylates nuclear targets. Many transcription factors are known to be direct substrates for phosphorylation by ERK, such as Elk1, c-Fos and c-Myc, the regulation of which controls cell proliferation, differentiation and survival.

The aberrant regulation of the MAPK signaling pathway is observed in various diseases, such as cancer, heart disease and Alzheimer disease.[2, 11, 12] For example, the MAPK signaling pathway plays

a key role in metastatic melanoma, making it an important therapeutic target for this cancer. As many as 50% of melanoma patients have activating B-Raf mutations,[13] which has encouraged decades of research in the development of B-Raf and MKK inhibitors. However, metastatic melanoma patients treated with B-Raf and MKK inhibitors relapse after a median of 6-7 months.[14, 15] Combinatorial treatment using B-Raf and MKK inhibitors extend this "progression-free survival" period to a median of 10-12 months, but also result in patient relapse.[16] This transient "progression-free" period motivates the development of ERK1/2 inhibitors. It is found that ERK1/2 inhibitors are effective against cells with acquired resistance to the inhibitors of upstream kinases.[17, 18] Thus, a better understanding of the regulation of ERK2 is essential to the development of effective therapeutics to treat melanoma.

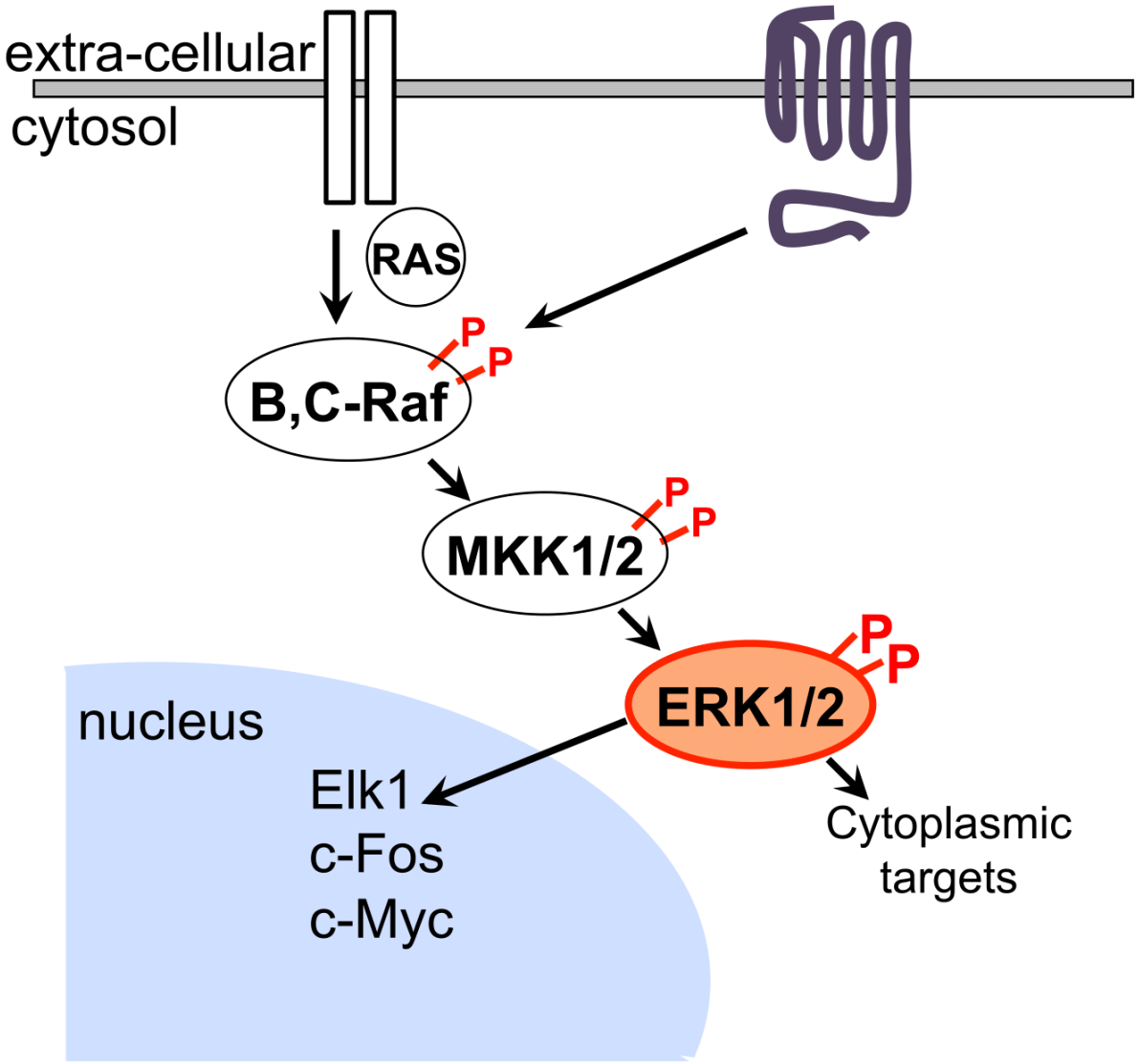

Figure 1.1. A simplified MAP kinase signaling pathway.
The receptor tyrosine kinase is shown as two trans-membrane subunits. G-protein-coupled-receptor (GPCR) is shown in purple with the 7-helical segment trans-membrane receptor. Either the stimulation of receptor tyrosine kinase and G-protein-coupled receptors could lead to activation of B-Raf and C-Raf, followed by the activation of the MAPK signaling pathway, mediated by the downstream kinases, MKK1/2 and MAP kinases, ERK1 and ERK2.

1.2. Structures of Protein Kinases

1.2.1. Structural Overview of Protein Kinases

The involvement of eukaryotic protein kinases in nearly all intracellular processes has prompted extensive structural studies on this important class of enzymes, beginning with the first X-ray structure of a protein kinase more than 20 years ago.[19, 20] Since then, more than 6000 kinase structures have been added to the Protein Data Bank (PDB) database, and have yielded deep insights into the mechanisms underlying kinase regulation. Eukaryotic protein kinases share a conserved catalytic domain comprised of N-terminal and C-terminal lobes connected by a hinge (Figure 1.2).[20-22] ATP binds the active site cleft between the lobes, forming critical contacts with residues and motifs that are conserved among kinases. These contacts include a conserved Lys residue and backbone amides in a Gly-rich motif (usually referred to as "Gly-loop" in protein kinases, and "P-loop" in other kinases, dehydrogenases and ATPases) in the N-terminal lobe that form hydrogen bonds to the ATP phosphoryl oxygens; backbone atoms in the hinge that form hydrogen bond with the adenine ring; and the Asp side chain in a conserved Asp-Phe-Gly (DFG) motif (or called DFG-loop) in the C-terminal lobe that coordinates Mg^{2+}. The activation loop and peptide recognition segment (P+1 loop) in the C-terminal lobe of the kinase form contacts with substrates, which confer sequence specificity and positioning of the substrate hydroxyl acceptor. A conserved Asp residue in the active site serves as the catalytic base for phosphoryl transfer from ATP to substrate.

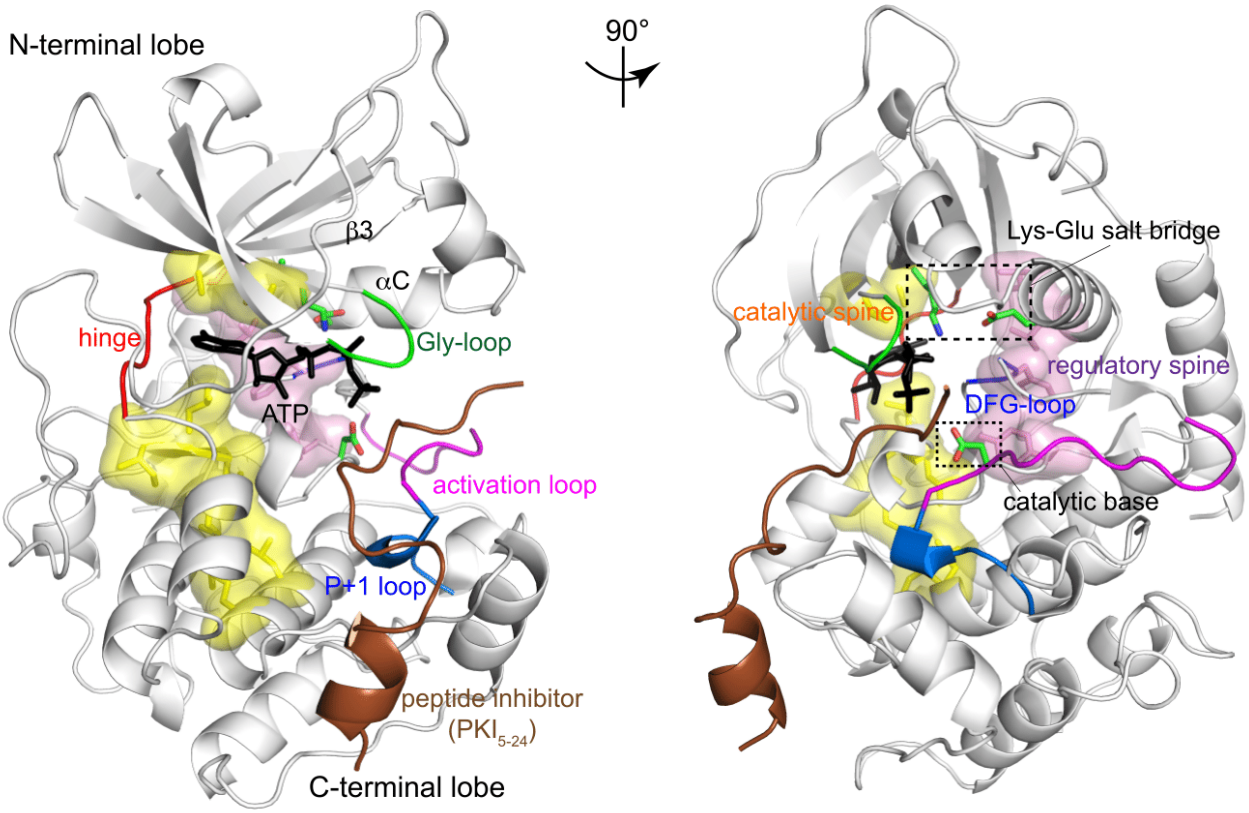

Figure 1.2. The architecture of protein kinases.
The X-ray structure of the protein kinase A (PKA) catalytic subunit bound to ATP (black), and peptide inhibitor, PKI_{5-24} (brown) (PDB:1ATP[23]). Elements conserved among protein kinases that are needed for catalytic function are labeled, including the Gly-loop, Lys-Glu salt bridge, DFG-motif (or DFG-loop), hinge, activation loop, P+1 loop, and catalytic base. Space filled segments indicate internal hydrophobic structural motifs, named regulatory (pink) and catalytic (yellow) "spines".

1.2.2. Common Structural Models for Protein Kinase Activation Don't Apply to ERK2

Key structural arrangements accompany kinase activation by covalent modifications or by interactions with regulatory subunits and domains.[24-26] The activation loop is a flexible segment that can rearrange substantially, and is often the location for regulatory phosphorylation.[21, 25] Phosphorylation at the activation loop allows ion pair interactions with an active site Arg residue to orient the catalytic base. The conserved N-terminal Lys, located in strand β3, interacts with a Glu residue in helix αC to form a Lys-Glu salt bridge, often coupled with lateral movement of helix αC (Figure 1.3).[27] The DFG motif in the N-terminus of the activation loop forms a productive conformation ("in"), in contrast to a flipped "out" conformation in the inactive kinase (Figure 1.3).

Catalytic activity requires the proper alignment of internal hydrophobic residues, which form structural motifs, termed regulatory and catalytic "spines", which stabilize the position of active site residues.[28] In particular, the assembled regulatory spine is often considered to be an indicator of an active kinase (Figure 1.3).[28] Together, these represent common locations for conformational changes that contribute to kinase activation.

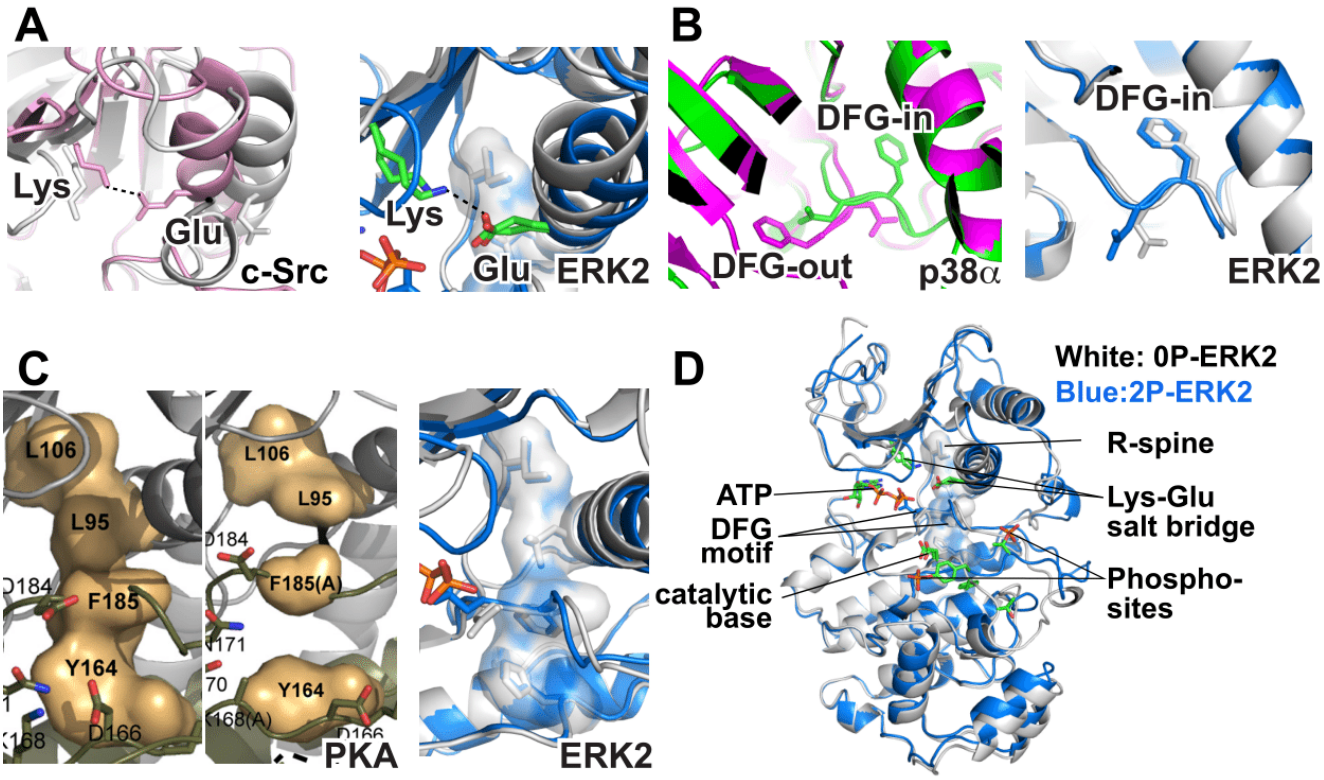

Figure 1.3. Common structural models of protein kinase activation/inactivation don't apply to ERK2. (A) Intact Lys-Glu salt bridge was observed in active c-Src (pink), whereas broken Lys-Glu salt bridge was observed in inactive c-Src (white). Both inactive (white) and active (blue) ERK2 showed intact Lys-Glu salt bridge. (B) Active p38α (green) showed DFG-in conformation, whereas DFG-out conformation is characteristic for inactive p38α (magenta). Both inactive (white) and active (blue) ERK2 showed DFG-in conformation. (C) Intact regulatory spine (R-spine) was found in active protein kinase A, whereas a broken regulatory spine was characteristic of inactive protein kinase A. Adapted from reference [29], following the copyright permission policy of Journal Biological Chemistry (no permission needed). Both inactive (white) and active (blue) ERK2 showed intact R-spine. (D) Structural overlay of inactive, 0P-ERK2 (white) and active, 2P-ERK2 (blue). ATP, Lys-Glu salt bridge, DFG-motif, catalytic base, R-spine, and phosphor-sites were represented with sticks.

The MAP kinase, extracellular regulated kinase-2 (ERK2), is activated by dual phosphorylation at Thr and Tyr residues in the activation loop,[30] increasing the rate of phosphoryl-transfer by 60,000-

fold.[31] X-ray structures of the active, phosphorylated kinase (2P-ERK2) and the inactive, unphosphorylated kinase (0P-ERK2) show that phosphorylation rearranges the activation loop to accommodate substrate binding, reorganizes active site residues, and exposes a pocket for substrate docking.[32-34] The crystal structures of both inactive and active ERK2 showed intact Lys-Glu salt bridge, "DFG-in" conformation and intact regulatory spine. Thus, these common structural models for protein kinase activation cannot be used to explain the activation of ERK2.

1.3. Probing Protein Dynamics using NMR Spectroscopy

The static views of proteins obtained by X-ray crystallography are greatly enhanced by complementary solution studies that probe conformational dynamics. Solution nuclear magnetic resonance (NMR) spectroscopy is a powerful approach to probe protein dynamics since it provides access to a wide range of time scales that are relevant for various types of protein motion.[35] NMR techniques detecting spin relaxation (e.g. T_1, T_2 and NOE) have been developed for accessing fast (ps-ns) timescale dynamics and probing motions such as single bond vibration, libration and side chain rotation.[35] Slower (μs-ms) protein motions occur during processes such as ligand binding, protein folding and allosteric regulation can be probed from the chemical shift difference between conformational states (e.g. Carr-Purcell-Meiboom-Gill experiments and line shape analysis).[35]

Protein kinases usually have rates of turnover (k_{cat}) in millisecond time scale. [31, 36] Thus, the catalysis or the regulation of a protein kinase is most likely to be contributed by slow (μs-ms) timescale dynamics that can be accessed by NMR. For example, the Carr-Purcell-Meiboom-Gill (CPMG) relaxation dispersion experiment is used to monitor dynamics on the μs-ms timescale.[35, 37] It measures exchange by analysis of transverse relaxation rates ($R_{2,eff}$) as a function of the interval between refocusing pulses. The transverse relaxation rate can be described from two components: the transverse relaxation rate independent of exchange ($R_{2,0}$) and the exchange contribution (R_{ex}). If the

system is undergoing conformational exchange, it will result in imperfect refocusing, thus increasing the relaxation rates and decreasing the intensity of the NMR signal. Increasing the pulse frequency (or decreasing the pulse interval) provides less of a chance for conformational exchange to occur between two pulses and leads to better refocusing and higher peak intensity. In contrast, the lack of conformational exchange on the μs-ms timescale will result in constant peak intensity with varied pulse frequencies. Thus, the changes in relaxation rates, reflected by changes in peak intensity, against various intervals between refocusing pulses yield a curvature containing information about conformational dynamics. An exchange reaction between two conformational states can be described as $A \rightleftharpoons B$, in which k_{AB} is the rate constant of the forward reaction, and k_{BA} is the rate constant of the reverse reaction. The exchange rate constant k_{ex} is the sum of k_{AB} and k_{BA}. Under optimal conditions, each methyl can be fit to a two-state model to extract the transverse relaxation rate independent of exchange ($R_{2,0}$), the rate constant for exchange (k_{ex}), the populations of the two states (p_A, p_B) and the chemical shift difference between the two states ($|\Delta\omega|$).[38]

Previous studies using CPMG relaxation dispersion experiment have revealed that the conformational transitions of enzymes (e.g. dihydrofolate reductase) could be rate limiting for certain stages of enzymatic reaction.[39] The dihydrofolate reductase (DHFR) catalyzes the hydride transfer reaction from NADPH and 7,8-dihydrofolate (DHF) to $NADP^+$ and 5,6,7,8-tetrahydrofolate (THF); then it rebinds NADPH to perform THF dissociation. The rate that the DHFR:NADPH:THF complex converted from a major conformational state to a minor state (12-18 s^{-1}) was comparable with the rate of THF dissociation (13 s^{-1}), and chemical shift differences between the two states suggested that the minor state was similar to the DHFR:NADPH complex.[39]

Another powerful technique to probe slow timescale dynamics is NMR line shape analysis, where nuclei that interconvert between multiple conformations can adopt varying line widths and

numbers of peaks, depending on the ratio of the difference in chemical shift ($|\Delta\omega|$) and rate constant for exchange between conformers (k_{ex}).[35] Assuming two-state exchange (e.g., $A \rightleftharpoons B$, where $k_{ex} = k_{AB} + k_{BA}$), slow interconversion ($k_{ex} << |\Delta\omega|$) leads to two resolved peaks, each representing a distinct state, whereas fast interconversion ($k_{ex} >> |\Delta\omega|$) yields only one peak having a chemical shift at the population-weighted average of the two states. When interconversion occurs in an intermediate time regime ($k_{ex} \approx |\Delta\omega|$), line broadening leads to reduction of peak height. Thus, changes in peak number or line shape can reflect changes in dynamics and provide information about exchange rate constants. One example is the change in conformational dynamics observed within the kinase domain upon activation of Eph receptor tyrosine kinase (RTK) EphB2.[40] In active states of EphB2, a similar set of amide resonances showed chemical shift perturbations from the autoinhibited state.[40] These amides in an active mutant of EphB2 showed two peaks in slow exchange, whose chemical shifts indicated a major autoinhibited state and a new, lower populated state.[40] This suggested a model in which the dynamics of the activated Eph receptor tyrosine kinase enables it to sample rare active conformers against a larger population of autoinhibited conformers.

1.4. NMR Spectroscopy for Large Proteins

Solution NMR spectroscopy is a powerful technique to study the dynamics of proteins in solution, but until early 2000s there have been only limited applications of NMR to studies of large proteins, such as protein kinases, since their relatively large size leads to fast relaxation of the NMR signals. NMR techniques that increase the signal-to-noise for larger proteins include transverse relaxation-optimized spectroscopy (TROSY) methods,[41-43] which select slow relaxation signals, and protein labeling methods[44, 45] such as perdeuteration, which reduces the effect of surrounding protons on relaxation.

The TROSY method observes only the sharpest component of the four-component multiplet, in a heteronuclear two-spin system that is coupled through a covalent bond such as the amide ^{1}H-^{15}N.[42, 43] It takes advantage of the different relaxation properties of these components, due to dipole-dipole coupling and the chemical shift anisotropy interference. This sharpest component could reach almost full cancellation of transverse relaxation effects within the ^{1}H-^{15}N spin system at high magnetic fields (e.g. 1GHz).[43] Whereas previous to the development of TROSY method, the four components of the multiplet are conventionally averaged into a single broader peak with lower height through decoupling schemes to avoid spectral complication. Thus, the signal loss in the TROSY method by sacrificing 3 out of 4 broader components actually leads to a significant enhancement in spectral resolution and sensitivity, allowing numerous NMR applications on large proteins.[46]

Accompanying the development of the NMR technology, the development of protein isotope-labeling schemes to reduce the transverse (T_2) relaxation by surrounding protons also greatly promoted NMR studies on large proteins. In the middle of 1990s, it was found that samples prepared in a partial or fully deuterated background showed significantly improved spectral resolution and sensitivity relative to protonated molecules.[47, 48] This was immediately followed by the ^{13}C methyl-labeling scheme on the side chains of selective residues such as Ala, Ile, Leu and Val in the late 1990s,[49-51] utilizing the favorable relaxation properties of methyls[52] as well as methyl-TROSY,[53] to yield more probes to detect protein structure and function.[45] Currently, more residues can be selectively ^{13}C methyl labeled, including Ala, Thr and Met.[45, 54, 55] These methods now allow glimpses into solution structures and the dynamics of protein kinases.

One challenge of utilizing the methyl probes is obtaining their resonance assignments. Standard protein assignment methods employ through-bond backbone experiments on uniformly ^{13}C/^{15}N-labeled proteins. A conventional way of obtaining methyl assignments is linking them to the previously

assigned backbone.[56] However, for larger proteins, this through-bond assignment procedure often breaks down due to rapid relaxation and spectral overlap. Another common way of obtaining assignments is mutagenesis, which is both time and sample consuming, as well as leading to high ambiguity of assignments.[57] Alternatively, a "divide-and-conquer" approach could be applied, where methyl assignments could be obtained in small subunits of proteins prior to being mapped onto the large protein complex.[58] However, this method will be difficult to apply if the protein has no discrete subunits.

1.5. Overview

This thesis reports conformational perturbations of methyls on Ile, Leu and Val (ILV) side chains of the MAP kinase, ERK2, upon activation and ligand binding, monitored using NMR relaxation experiments and line shape analysis. Although Ghose and co-workers published part (~50%) of the backbone assignments of ERK2 in 2011,[59] no backbone assignments of ERK2 were published prior to the onset of this thesis project. Thus, *de novo* assignments were made to the ILV methyls of ERK2 as the first step towards the NMR analysis of the structure, dynamics and interactions.

In Chapter 2, a novel, structure-based approach to obtain ILV methyl assignments of active and inactive ERK2 is described. This approach overcomes the requirement of conventional backbone assignments, using a comparison of inter-methyl distance constraints provided by NOE and X-ray structure. A hierarchical clustering approach is used, which sorts the NOE constraints into clusters, and a larger NOE cluster that is more likely to be unique is mapped onto the structure before a smaller one. This approach yielded 60% of the ILV methyl assignments for active and inactive ERK2.

Chapter 3 reports that phosphorylation of ERK2 induced global dynamics that is consistent with a two-state exchange process in μs-ms time scale using CPMG relaxation dispersion experiments and line shape analysis. The data support that inactive ERK2 is constrained into one conformation

(e.g., A), whereas the active ERK2 forms two conformations that exchange on a millisecond timescale (e.g., A ⇌ B). Insight into the nature of the constraint in inactive ERK2 was provided by a mutant that modified hinge residues to increase flexibility ($M^{106}E^{107}$/GG). This mutant showed the global conformational exchange, even in absence of phosphorylation. Thus, the dominant conformation in inactive ERK2 is believed to be a "tight" (T) state, whereas the new conformation in active ERK2 is believed to be a "relaxed" (R) state.

Chapter 4 reports conformational perturbations on ERK2 upon ligand binding, towards its catalytically relevant forms or inhibited forms. The catalytically relevant forms of ERK2 don't shift to 100% R conformation; instead, they show no significant perturbations on the T ⇌ R equilibrium, with small enhancement to the T population. The ligand binding studies show that the T ⇌ R equilibrium between the two states in 2P-ERK2 can be differentially shifted upon the binding of various inhibitors, revealing a new mechanism for conformation selection.

Chapter 2. Structure-Based Assignment of Ile, Leu and Val Methyl Groups in the Active and Inactive Forms of the MAP Kinase ERK2

2.1. Introduction

2.1.1. Previous Methyl Assignments from Backbone Information or Mutagenesis

Side-chain methyl groups represent valuable probes for nuclear magnetic resonance (NMR) studies, where the rapid rotation of the methyl group combined with transverse relaxation-optimization (TROSY)-based techniques leads to improved signal-to-noise and resolution for larger proteins as compared with backbone amide groups.[60-62] Chemical shift perturbations, nuclear Overhauser effect (NOE)-derived distances and relaxation dispersion-derived kinetic data on methyl groups have been used to study regulation and activity in a variety of protein systems ranging from 30 kDa to 1 MDa.[60, 63, 64] Detailed interpretation of the NMR data on methyl groups requires sequence-specific assignments. For favorable cases, the backbone resonance assignment can be extended to methyl resonances, as shown with Ile $C^{\delta 1}$, Leu C^{δ}, and Val C^{γ} (ILV) methyl assignments for the 81-kDa Malate Synthase G.[56] A "divide-and-conquer" approach was applied to a 670 kDa α7β7β7α7 20S proteasome, where methyl assignments were made for the individual α and β subunits and then mapped onto the larger protein complex and confirmed using methyl-methyl NOE data and mutagenesis.[58, 65] A high-throughput, systematic mutagenesis strategy has also been used to assign Ile and Ala methyls in the 468-kDa homododecameric PhTET2 protein.[57] This approach employs efficient methods for expression and purification of a large set of single-site mutations, which are then analyzed by 2D (^{13}C, ^{1}H) hetero-nuclear multiple quantum coherence (HMQC)-type spectra.

2.1.2. Structural-based Strategies for Methyl Assignments

Structure-based strategies have been developed for resonance assignments in proteins where the structure of the protein, or a homology model of the protein, has already been determined.[66-68]

Various programs have been developed for structure-based methyl resonance assignment in proteins that combine the structural data with experimental data and theoretical information including: distance information obtained from NOESY and/or paramagnetic relaxation enhancement (PRE) experiments, predictions of the ^{1}H and ^{13}C chemical shifts of methyl groups, labeling strategies that allow identification of amino-acid type or stereospecific assignment of methyls.[57, 69-76] Methods that employ PRE data require production of multiple constructs or mutant proteins, which is challenging for proteins that are not highly expressed in isotopically labeled media. Thus, to make NMR an accessible technique to a wider array of proteins, it is important to develop complementary methods that allow even partial methyl assignments with a minimum number of isotopically labeled protein samples.

2.1.3. Overview

Here we present a structure-based strategy for obtaining partial ILV side chain methyl assignments using 3D methyl-methyl NOESY and 3D through-bond methyl side chain "out-and-back" experiments on two different isotopically ILV methyl-labeled samples combined with the X-ray structure (Figure 2.1). This strategy was applied to the 42-kDa protein, extracellular signal-regulated kinase 2 (ERK2), which had no pre-existing ILV methyl assignments. This method yielded 60% of Ile, Leu and Val assignments, including 90% of Ile assignments. ERK2 is a critical component in the mitogen-activated protein (MAP) kinase signal cascade, where it helps regulate many cellular processes including proliferation, differentiation and gene expression.[77] Aberrant activation of ERK2 is found in multiple diseases, including cancer, diabetes and heart disease.[78] Previous studies yielded partial assignments (~50%) of the backbone amides in ERK2,[59] but these included few assignments of methyls. We previously studied conformational dynamics in both active and inactive ERK2 using ILV methyl probes[79] and the work here gives the detailed description of our methyl-assignment procedure. The structure-based method employed here bypasses the requirement for protein backbone

assignments. Thus, this method provides a valuable approach to obtaining methyl assignments in larger proteins, where the structure is known and backbone assignments are intractable. These assignments were also used to study binding of an ATP analogue and a peptide ligand to inactive and active ERK2.

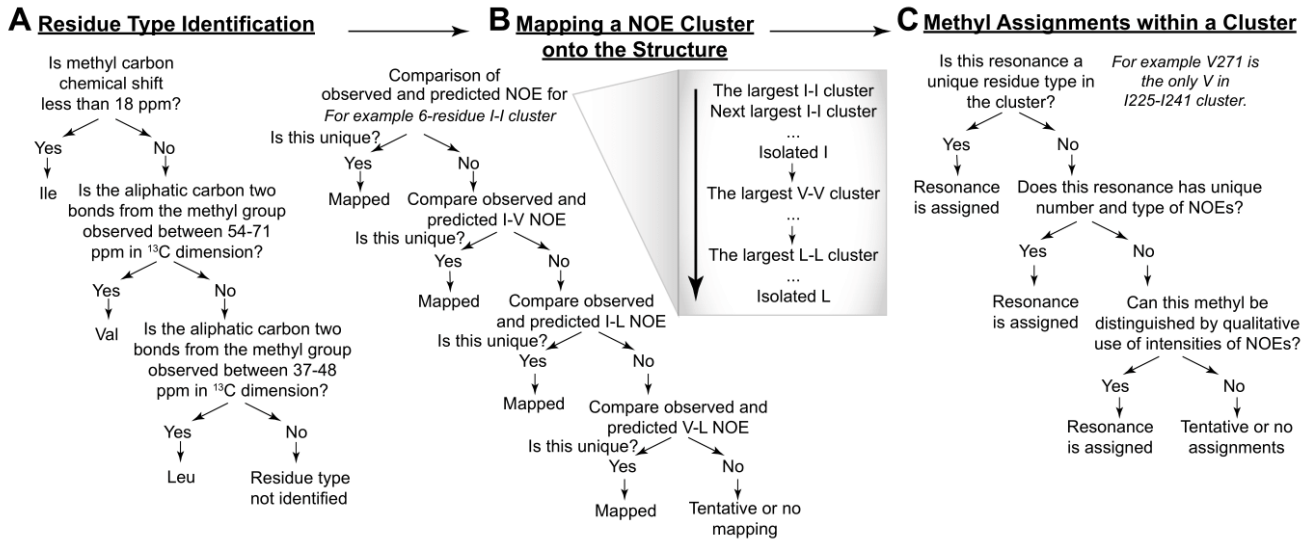

Figure 2.1. The hierarchical strategy for structure-based assignment of the ILV methyl resonances in ERK2. (A) Identification of methyl residue type (I, L, or V) utilizes both the ^{13}C chemical shifts and through-bond correlation experiments. (B) The predicted and observed Ile-Ile NOE clusters are analyzed first using a hierarchy of largest to smallest clusters. If there is only a single observed and predicted Ile cluster of a particular size, then this cluster can be uniquely mapped onto the X-ray structure. If a cluster cannot be uniquely mapped using only Ile-Ile NOEs then additional Ile-Val and Ile-Leu NOEs are progressively analyzed to try to uniquely map each cluster onto the structure. (C) Once specific clusters have been mapped onto the X-ray structure, the patterns and sizes of the predicted and observed methyl-methyl NOEs are qualitatively analyzed to assign individual methyl resonances within a cluster to specific residues in the sequence. In italics are examples for several criteria.

2.2. Materials and Methods

2.2.1. Protein Preparation

ILV methyl-protonated, U-[^{2}H,^{15}N] 0P-ERK2. The expression and purification of wild-type 0P-ERK2 in *E. coli* BL21(DE3) cells were performed as described.[79] A pET-23a plasmid containing the rat His_6-ERK2 sequence was transformed into *E. coli* BL21(DE3) cells [80]. A single colony was used to inoculate 1 mL of LB growth media containing 100 μg/mL carbenicillin and 34 μg/mL chloramphenicol, which was shaken overnight at 37 °C. Cells were spun down and re-suspended in 25 mL of unlabeled M9 minimal medium in H_2O. At an OD_{600} of 0.8, the cells were spun down and re-suspended in 200 mL M9 minimal media with D-glucose-d_7 in D_2O, shaking at 37 °C until OD_{600} ~0.6. Cells were then spun down and re-suspended in 1 L M9 minimal medium with 3 g/L D-glucose-d7 and 1 g/L $^{15}NH_4Cl$ for U-^{2}H, ^{15}N labeling, shaking at 37 °C. Precursors (α-keto-3-methyl-D3-butyric acid-4-^{13}C and 2-ketobutyric acid-4-^{13}C) for Ile ($^{13}C^{\delta}H_3$), Leu ($^{13}C^{\delta}H_3$,$^{12}C^{\delta}D_3$), Val ($^{13}C^{\gamma}H_3$,$^{12}C^{\gamma}D_3$) labeling[49, 50] were added to cells once the OD_{600} reached 0.8. After 1 h the cells were induced with isopropyl-β-D-1-thiogalactopyranoside and shaken at 18 °C for 16 h, after which cells were spun down. The cell pellets were re-suspended in lysis buffer (50 mM NaH_2PO_4/Na_2HPO_4 pH 8.0, 300 mM NaCl, 0.1% β-mercaptoethanol, 5 mM imidazole, 1x Halt protease inhibitor, 1 mg/mL lysozyme and 1 mM EDTA). The cell suspension was incubated at room temperature for 20 min and then sonicated and spun down at 4 °C. The supernatant was collected as cell lysate. Proteins were purified from cell lysate by Ni^{2+}-NTA affinity chromatography (Bio-Rad), PD-10 desalting (GE Healthcare), MonoQ FPLC (GE Healthcare), and Sephadex S200 size-exclusion chromatography (GE Healthcare)[81]. This procedure usually yields 100% unphosphorylated ERK2, confirmed using mass spectrometry of its trypsin-digested product. The peptide from the activation loop, VADPDHDHTGFLTEYVATR, was searched according to its mass-to-charge ratios (m/z) for unphosphorylated (0P), monophosphorylated

(1P), and dual phosphorylated (2P) forms. The relative peak area of each form yields the level of phosphorylation for the 0P-ERK2 sample. The NMR sample of 0P-ERK2 was concentrated to 0.3-0.4 mM, and exchanged into the NMR buffer (50 mM Tris pH 7.4, 150 mM NaCl, 5 mM $MgSO_4$, 0.1 mM EDTA, 5 mM DTT, 100% D_2O, and 2.5% (v/v) glycerol). This procedure yielded 0P-ERK2 sample that was uniformly $^2H/^{15}N$-labeled and selectively ILV-methyl-labeled on Ile ($^{13}C^{\delta}H_3$), Leu ($^{13}C^{\delta}H_3$, $^{12}C^{\delta}D_3$), Val ($^{13}C^{\gamma}H_3$, $^{12}C^{\gamma}D_3$) for the 2D (^{13}C, ^1H) HMQC and 3D NOESY experiments.

Constitutively active MKK1 (MKK-G7B). A constitutively active mutant MKK1 (MKK-G7B: ΔN4/S218D/M219D/N221D/S222D) in *E. coli* BL21(DE3) cells was expressed and purified as described[82], and used to phosphorylate 0P-ERK2 into 2P-ERK2 *in vitro*. A RSET plasmid containing the His_6-MKK-G7B sequence was transformed into *E. coli* BL21(DE3) cells [80]. A single colony was used to inoculate 20 mL of TB growth media containing 100 μg/mL ampicillin and 34 μg/mL chloramphenicol, which was shaken overnight at 37 °C. The 20 mL overnight culture was inoculated into 750 mL TB media with antibiotics, and grown at 30 °C until OD_{600} ~0.6. The cells were induced with 0.1 mM isopropyl-β-D-1-thiogalactopyranoside and shaken at 30 °C for 4 h, after which cells were spun down and cell pellets were frozen. The cell pellets were re-suspended in extraction buffer (10 mM KH_2PO_4/K_2HPO_4 pH 8.0, 10% glycerol, 0.25% Tween 20, 0.2% β-mercaptoethanol, 2 mM benzamidine and 1 mM PMSF). The cell suspension was sonicated and spun down at 4 °C. The supernatant was collected as cell lysate. Proteins were purified from cell lysate by TALON Cobalt Resin for His-tag purification, and DEAE Sephadex resin (GE Healthcare)[81]. The purified MKK-G7B, usually around 0.5-1 mg/mL, was immediately frozen with liquid nitrogen and stored at -80 °C till use.

ILV methyl-protonated, U-[^2H,^{15}N] 2P-ERK2. 2P-ERK2 was prepared from ILV methyl-protonated, U-[^2H,^{15}N]-labeled 0P-ERK2 purified through the MonoQ step, and phosphorylated *in vitro* using purified MKK-G7B. Each 1 mL of phosphorylation reaction contained 15 μg MKK-G7B,

170 μg ERK2, 200 μL of 5x ATP mixture, 1x EDTA-free Halt™ phosphatase inhibitor cocktail (Thermo Scientific) and H_2O. The 5x ATP mixture contained 20 mM ATP, 100 mM $MgCl_2$, 100 mM Hepes (pH 7.4) and 20 mM DTT. The phosphorylation reaction was performed in 30 °C water bath for 45 min before quenching with excess EDTA (e.g. 25-30 mM) and incubated on ice. Following the phosphorylation reaction, MKK-G7B was removed from 2P-ERK2 by a second MonoQ FPLC separation. The 2P-ERK2 sample is then trypsin digested for obtaining the level of phosphorylation using mass spectrometry. The peptide from the activation loop, VADPDHDHTGFLTEYVATR, was searched according to its mass-to-charge ratios (m/z) for dual phosphorylated (2P), monophosphorylated (1P), and unphosphorylated (0P) forms. The relative peak area of each form yields the level of phosphorylation for the 2P-ERK2 sample. If the 2P-ERK2 sample is >= 95% dual phosphorylated, it would be then further purified by Sephadex S200 size-exclusion chromatography to remove any aggregates. The resulting 2P-ERK2 was concentrated to 0.3-0.4 mM, and exchanged into the NMR buffer (50 mM Tris pH 7.4, 150 mM NaCl, 5 mM $MgSO_4$, 0.1 mM EDTA, 5 mM DTT, 100% D_2O, and 2.5% (v/v) glycerol). This procedure yielded a 2P-ERK2 NMR sample that was uniformly $^2H/^{15}N$-labeled and selectively ILV-methyl-labeled at Ile ($^{13}C^{\delta}H_3$), Leu ($^{13}C^{\delta}H_3$, $^{12}C^{\delta}D_3$), Val ($^{13}C^{\gamma}H_3$, $^{12}C^{\gamma}D_3$) for the 2D (^{13}C, ^1H) HMQC and 3D NOESY experiments.

ILV methyl-protonated, U-[^2H,^{15}N,^{13}C] 0P-ERK2. The preparation of ILV methyl-protonated, U-[^2H,^{15}N,^{13}C] 0P-ERK2 followed a very similar procedure as the preparation of ILV methyl-protonated, U-[^2H,^{15}N] 0P-ERK2. To achieve uniformed labeling of $^2H/^{15}N/^{13}C$, *E. coli,* cells were grown in 1 L M9 minimal medium with 3 g/L D-glucose-$^{13}C6$-d7 and 1 g/L $^{15}NH_4Cl$, shaking at 37 °C. Selective ILV-methyl-labeling on Ile ($^{13}C^{\delta}H_3$), Leu ($^{13}C^{\delta}H_3$, $^{12}C^{\delta}D_3$), Val ($^{13}C^{\gamma}H_3$, $^{12}C^{\gamma}D_3$) was achieved using the precursors 2-keto-3-(methyl-d_3)-1,2,3,4-$^{13}C_4$-3-d_1-butyrate and 2-keto-3,3-d_2-1,2,3,4-$^{13}C_4$-butyrate. This 0P-ERK2 sample was concentrated to 0.3-0.4 mM, and exchanged into

NMR buffer (50 mM Tris pH 7.4, 150 mM NaCl, 5 mM $MgSO_4$, 0.1 mM EDTA, 5 mM DTT, 100% D_2O, and 2.5% (v/v) glycerol). This procedure yielded a 0P-ERK2 NMR sample that was uniformly $^2H/^{15}N/^{13}C$-labeled and selectively ILV-methyl-labeled on Ile ($^{13}C^{\delta}H_3$), Leu ($^{13}C^{\delta}H_3$, $^{12}C^{\delta}D_3$), Val ($^{13}C^{\gamma}H_3$, $^{12}C^{\gamma}D_3$), and was used in the 3D (^{13}C, ^{13}C, ^1H) HMCM[CG]CBCA and an HNCA experiments.

ILV side chain-partial labeled, U-[^2H,^{15}N] 0P-ERK2. The preparation of a uniformly $^2H/^{15}N$-labeled with selective labeling of Ile ($^{13}C^{\delta}H_3$, $^{13}C^{\gamma}D_2$), Leu ($^{13}C^{\delta}H_3$, $^{12}C^{\delta}D_3$, $^{13}C^{\gamma}D$, $^{13}C^{\beta}D_2$), Val ($^{13}C^{\gamma}H_3$, $^{12}C^{\gamma}D_3$, $^{13}C^{\beta}D$, $^{13}C^{\alpha}D$) on 0P-ERK2 followed a similar procedure as the preparation of ILV methyl-protonated, U-[^2H,^{15}N] 0P-ERK2. The only difference was that to achieve such labeling, the precursors 2-keto-3-(methyl-d_3)-1,2,3,4-$^{13}C_4$-3-d_1-butyrate and 2-keto-3,3-d_2-1,2,3,4-$^{13}C_4$-butyrate[60] were used. This 0P-ERK2 sample was concentrated to 0.3-0.4 mM, and exchanged into the NMR buffer (50 mM Tris pH 7.4, 150 mM NaCl, 5 mM $MgSO_4$, 0.1 mM EDTA, 5 mM DTT, 100% D_2O, and 2.5% (v/v) glycerol). This 0P-ERK2 sample was used in the 3D (^{13}C, ^{13}C, ^1H) HMCMCBCA experiment.

ILV methyl-protonated, U-[^2H,^{15}N] 0P-ERK2 mutants. Ile, Leu or Val to Ala mutations (I101A, L105A, L110A, L113A, I124A, L154A, L155A, L161A, I196A, L198A, L235A, and I238A) were made from wild-type ERK2 using the QuikChange Mutagenesis Kit (Stratagene) and these 0P-ERK2 mutants were prepared using the same procedure as the ILV methyl-protonated, U-[^2H,^{15}N] 0P-ERK2 sample. All 0P-ERK2 mutant samples were exchanged into a buffer containing 50 mM Tris pH 7.4, 150 mM NaCl, 5 mM $MgSO_4$, 0.1 mM EDTA, 5 mM DTT, 10% D_2O and 2.5% (v/v) glycerol, and concentrated to 0.1-0.2 mM for 2D (^{13}C, ^1H) HMQC experiments.

2.2.2. NMR Experiments

2D (^{13}C, ^{1}H) TROSY HMQC experiments. 2D (^{13}C, ^{1}H) transverse relaxation-optimized spectroscopy (TROSY) HMQC experiments were performed on a Varian VNMRS 800 MHz spectrometer with a z-axis gradient cryoprobe at 25 °C using 0P, 2P and mutants samples of ILV methyl-protonated, U-[^{2}H,^{15}N] ERK2 in NMR buffer containing 10% or 100% D_2O. These were recorded using the pulse sequence "hmqc_c13_800_methyl_lek.c" (kindly provided by Dr. Lewis Kay, University of Toronto) or "hmqc_c13_800_methyl_bufsat.c". The sequence "hmqc_c13_800_methyl_bufsat.c" is a modification of "hmqc_c13_800_methyl_lek.c", but using an EBURP-1 shaped pulse to suppress the dithiothreitol (DTT) signal from the NMR buffer. The water signal was suppressed using an on-resonance water selective soft pulse and a gradient before the first HMQC pulse. After the water selective pulse, the ^{1}H carrier was moved to the methyl region (tof_me = 0.773 ppm). The ^{13}C carrier was usually placed between the Ile and Leu/Val regions (17.7 ppm). Some of the older spectra had placed ^{13}C carrier at 22.2 ppm (in the Leu/Val region), which could result in a peak that was originally at 7.5 ppm in ^{13}C dimension to be folded (depending on the spectral width and the position of ^{13}C carrier). The J-coupling of one bond methyl C-H is around 130 Hz, thus $1/(4J_{CH})$ (taua) was set to 1.8 ms. Typical spectra contain 2048 and 160 complex points over sweep widths of 12019.2 and 5429.6 Hz in the ^{1}H and ^{13}C dimensions. 8-64 transients were usually acquired with a delay time (d1) of 1.5 s, leading to 1-4 hours of acquisition time. The flag f1180 was set to 'y' so that t_1 starts at half dwell-time, and later during spectral processing require a zero- and first-order phase correction of (-90, 180) in t_1 (^{13}C) dimension. ^{13}C decoupling was applied with WALTZ-16 during the 85-ms acquisition period. Time-domain data in the ^{1}H dimension were apodized by a squared cosine window function and zero-filled prior to Fourier transformation. The indirect dimensions were also apodized by a cosine window function and zero-filled prior to Fourier transformation. Further

visualization and analysis of the spectra was performed using the program CcpNmr Analysis[83]. Table 2.1 lists the filenames and experimental parameters.

Table 2.1. Representative 2D (^{13}C, ^{1}H) TROSY HMQC experiment filenames, parameters and conditions.

Filename[a]	B_0	np	ni	sw	sw1	nt	d1
2H15N13CERK_13chmqc_121409.fid	800	2048	160	12019.2	5430	16	1.5
13Chmqc_2D_0PERK2_033111.fid	800	2048	160	12019.2	5430	16	1.5
2P-ERK2_smp021910_13Chmqc_021111.fid	800	2048	160	12019.2	5430	8	1.5
2P-ERK2_sample031611_ILV_D2O_25C_13Chmqc_100411.fid	800	2048	144	12019.2	5000	16	1.5
0p_ERK2_I101A_13Chmqc_022311.fid	800	2048	160	12019.2	5430	32	1.5
0p_ERK2_L105A_13Chmqc_022211.fid	800	2048	160	12019.2	5430	32	1.5
gHmqc_0p_ERK2_L110A_ILV_021811.fid	800	2048	160	12019.2	5430	8	1.5
hmqc13cILV_ERK2L113A_060710_9hours.fid	800	2048	160	12019.2	5430	64	2
0p_ERK2_I124A_hmqc_021711.fid	800	2048	160	12019.2	5430	8	1.5
0P-ERK2L154A_H2O_HMQC_25c_12172012.fid	800	2048	144	12019.2	5000	16	1.5
0p_ERK2_L155A_13Chmqc_022211.fid	800	2048	160	12019.2	5430	24	1.5
methylhmqc_ERK2_L161A_070610_9hour.fid	800	2048	160	12019.2	5430	64	1.5
hmqc_13cILV_ERK2I196A9hours_060410.fid	800	2048	160	12019.2	5430	48	2
hmqc_13cILV_ERK2I198A_9hours_060610.fid	800	2048	160	12019.2	5430	64	2
hmqcILVmethyl_ERK2L235A_9h_072410.fid	800	2048	160	12019.2	5430	64	1.5
hmqc13c_12hr_ERK2_I238A_060510.fid	800	2048	160	12019.2	5430	64	2

B_0 − magnetic field strength
np − number of complex points in t_2
ni − number of complex points in t_1
sw − sweep width in t_2 (Hz)
sw1 − sweep width in t_1 (Hz)
nt − number of scans per FID
d1 − interscan delay (s)
[a]Data directories in /yao/data/0P_ERK2_mutants/.

3D "out-and-back" experiments. The 3D (^{13}C, ^{13}C, ^{1}H) HMCM[CG]CBCA experiments on a ILV methyl-protonated, U-[^{2}H,^{15}N, ^{13}C] 0P-ERK2 sample and 3D (^{13}C, ^{13}C, ^{1}H) HMCMCBCA experiments on a ILV side chain-partial labeled, U-[^{2}H,^{15}N] 0P-ERK2 sample were performed as described,[56] on a Varian VNMRS 800 MHz spectrometer with a z-axis gradient cryoprobe at 25 °C. The 3D (^{13}C, ^{13}C, ^{1}H) HMCM[CG]CBCA experiment were acquired with 64 and 42 complex points (4 and 10.5 ms, respectively) in the t_1 (C_{aliph}) and t_2 (C_m) dimensions and 1024 complex points in acquisition period. ^{13}C decoupling was applied with WALTZ-16 during the 71-ms acquisition period. The 3D (^{13}C, ^{13}C, ^{1}H) HMCM[CG]CBCA used a pulse sequence "hmcmcgcbca_lek_800.c" (kindly provided by Dr. Lewis Kay, University of Toronto). In the experiment, the magnetization of methyl proton (H_m) is transferred to methyl carbon (C_m) through an insensitive nuclei enhanced by

polarization transfer (INEPT) sequence before the magnetization is transferred to aliphatic carbons through carbon-carbon J-coupling (J_{CC} = 35 Hz). A simplified scheme can be summarized as:

Val: C^{α} in-phase, C^{β} anti-phase

$$H_y^m \xrightarrow{INEPT} 2H_z^m C_x^m \xrightarrow{\frac{1}{2J_{CC}}} 4H_z^m C_y^m C_z^\beta \xrightarrow{90^\circ{}_x} 4H_z^m C_z^m C_y^\beta$$

$$\xrightarrow{\frac{1}{2J_{CC}}} (\xrightarrow{\frac{1}{2J_{C_m C^\beta}}} 2H_z^m C_x^\beta \xrightarrow{\frac{1}{2J_{C^\beta C^\alpha}}}) 4H_z^m C_y^\beta C_z^\alpha \xrightarrow{90^\circ{}_x} 4H_z^m C_z^\beta C_y^\alpha \xrightarrow{\frac{1}{4J_{CC}}} 2H_z^m C_x^\alpha$$

$$+ 4H_z^m C_z^\beta C_y^\alpha \xrightarrow{90^\circ{}_x} 2H_z^m C_x^\alpha + 4H_z^m C_y^\beta C_z^\alpha \rightarrow t_1$$

Leu: C^{β} in-phase, C^{α} and C^{γ} anti-phase

$$H_y^m \xrightarrow{INEPT} 2H_z^m C_x^m \xrightarrow{\frac{1}{2J_{CC}}} 4H_z^m C_y^m C_z^\gamma \xrightarrow{90^\circ{}_x} 4H_z^m C_z^m C_y^\gamma \xrightarrow{\frac{1}{2J_{CC}}} 4H_z^m C_y^\gamma C_z^\beta \xrightarrow{90^\circ{}_x} 4H_z^m C_z^\gamma C_y^\beta \xrightarrow{\frac{1}{4J_{CC}}} ($$

$$\xrightarrow{\frac{1}{4J_{C_m C^\beta}}} 2H_z^m C_x^\beta + 4H_z^m C_z^\gamma C_y^\beta \xrightarrow{\frac{1}{4J_{C^\beta C^\alpha}}} 2H_z^m C_x^\beta + 4H_z^m C_z^\gamma C_y^\beta + 4H_z^m C_y^\beta C_z^\alpha) \xrightarrow{90^\circ{}_x} 2H_z^m C_x^\beta$$

$$+ 4H_z^m C_y^\gamma C_z^\beta + 4H_z^m C_z^\beta C_y^\alpha \rightarrow t_1$$

These magnetizations were then transferred back to C_m and to H_m for acquisition. For a ILV methyl-protonated, U-[^{2}H, ^{15}N, ^{13}C]-labeled sample, chemical shifts of C^{α}, C^{β} and C^{γ} for Ile/Leu or C^{α}, C^{β} for Val were recorded in t_1, C_m and H_m were recorded in t_2 and t_3. The ^{13}C carrier for aliphatic carbons (t_1) was set to 40 ppm. A 1.2-s delay period was used with 20 scans, leading to a total acquisition time of 83 h. The HMCM[CG]CBCA experiment was acquired with 64 and 42 complex points (4 and 10.5 ms, respectively) in the t_1 (C_{aliph}) and t_2 (C_m) dimensions and 1024 complex points in acquisition period. ^{13}C decoupling was applied with WALTZ-16 during the 71-ms acquisition period. A 1.2-s delay period was used with 20 scans, leading to a total acquisition time of 83 h. Table 2.2 lists the filenames and experimental parameters.

The 3D (^{13}C, ^{13}C, ^{1}H) HMCMCBCA used a pulse sequence "hmcmcbca_lek_800.c" (kindly provided by Dr. Lewis Kay, University of Toronto). In this experiment, the magnetization of methyl

proton (H_m) is transferred to methyl carbon (C_m) through an insensitive nuclei enhanced by polarization transfer (INEPT) sequence before the magnetization is distributed to aliphatic carbons through carbon-carbon J-coupling (J_{CC} = 35 Hz). A over-simplified scheme can be summarized as:

Val: C^β in-phase, C_m and C^α anti-phase

$$H_y^m \xrightarrow{INEPT} 2H_z^m C_x^m \xrightarrow{\frac{1}{2J_{CC}}} 4H_z^m C_y^m C_z^\beta \xrightarrow{90^\circ x} 4H_z^m C_z^m C_y^\beta$$

$$\xrightarrow{\frac{1}{4J_{CC}}} (\xrightarrow{\frac{1}{4J_{C_m C^\beta}}} 4H_z^m C_z^m C_y^\beta + 2H_z^m C_x^\beta \xrightarrow{\frac{1}{4J_{C^\beta C^\alpha}}}) 4H_z^m C_z^m C_y^\beta + 2H_z^m C_x^\beta$$

$$+ 4H_z^m C_y^\beta C_z^\alpha \xrightarrow{90^\circ x} 4H_z^m C_y^m C_z^\beta + 2H_z^m C_x^b + 4H_z^m C_y^\beta C_z^\alpha \rightarrow t_1$$

Leu: C^γ in-phase, C_m and C^β anti-phase

$$H_y^m \xrightarrow{INEPT} 2H_z^m C_x^m \xrightarrow{\frac{1}{2J_{CC}}} 4H_z^m C_y^m C_z^\gamma \xrightarrow{90^\circ x} 4H_z^m C_z^m C_y^\gamma \xrightarrow{\frac{1}{4J_{CC}}} ($$

$$\xrightarrow{\frac{1}{4J_{C_m C^\gamma}}} 4H_z^m C_z^m C_y^\gamma + 2H_z^m C_x^\gamma \xrightarrow{\frac{1}{4J_{C^\gamma C^\beta}}} 4H_z^m C_z^m C_y^\gamma + 2H_z^m C_x^\gamma$$

$$+ 4H_z^m C_y^\gamma C_z^\beta \xrightarrow{90^\circ x} 4H_z^m C_y^m C_z^\gamma + 2H_z^m C_x^\gamma + 4H_z^m C_z^\gamma C_y^\beta \rightarrow t_1$$

These magnetizations were then transferred back to C_m and to H_m for acquisition. For ILV side chain-partial labeled, U-[^{2}H,^{15}N]-labeled samples, chemical shifts of C^γ and C_m for Ile, C^β and C^γ and C_m for Leu or C^α, C^β and C_m for Val were recorded in t_1, whereas C_m and H_m were recorded in t_2 and t_3. A 1.2-s delay period was used with 16 scans, leading to a total acquisition time of 63 h. The HMCMCBCA experiment was acquired with 60 and 44 complex points (3.3 and 8.1 ms, respectively) in the t_1 (C_{aliph}) and t_2 (C_m) dimensions and 2048 complex points in acquisition period. ^{13}C decoupling was applied with WALTZ-16 during the 71-ms acquisition period. Because the flags f1180 and f2180 were set to 'y' so that t_1 and t_2 both start at half dwell-time, and later during spectral processing require a zero- and first-order phase correction of (-90, 180) in both t_1 and t_2 (^{13}C) dimensions. Time-domain data in the ^{1}H dimension were apodized by a squared cosine window function and zero-filled prior to

Fourier transformation. The indirect dimensions were also apodized by a cosine window function and zero-filled prior to Fourier transformation. The spectra were further visualized and analyzed using the program CcpNmr Analysis[83].

Table 2.2. 3D "out-and-back" experiment filenames, parameters and conditions

Filename	B_0	np	ni	ni2	sw	sw1	sw2	nt	d1
0P-ERK2_f1f2f3hmcmcgcbca_smple_13C_13CILV_082911full.fid[a]	800	2048	60	44	14534.9	18002	5430	16	1.2
0P-ERK2_3Df1f2f3hmcmcbca_smple_080511_12C_13CILV.fid[b]	800	2048	64	42	14534.9	16000	4000	20	1.2

B_0 − magnetic field strength
np − number of complex points in t_3
ni − number of complex points in t_1
ni2 − number of complex points in t_2
sw − sweep width in t_3 (Hz)
sw1 − sweep width in t_1 (Hz)
sw2 − sweep width in t_2 (Hz)
nt − number of scans per FID
d1 − interscan delay (s)
[a]Data directories in /yao/data/ERK2_2011/0P-ERK2_smple_082411_1C_13CILV/.
[b]Data directories in /yao/data/ERK2_2011/0P-ERK2_smple_080411_12C_13CILV/.

3D NOESY experiments. The 3D (^{13}C, ^{13}C, ^{1}H) HMQC-NOESY-HMQC experiments [84] were performed on a Varian VNMRS 800 MHz spectrometer with a z-axis gradient cryoprobe at 25 °C on ILV methyl-protonated, U-[^{2}H,^{15}N] 0P- and 2P-ERK2 using a 350 ms mixing time (MIX). This experiment used the sequence "hmqc_c13_methyl_3dnoesy_ap_bufsat.c". The experiments on 0P-ERK2 were acquired with 54 and 52 complex points (15.9 and 15.3 ms, respectively) in the t_1 (^{13}C) and t_2 (^{13}C) dimensions, and 1024 complex points in the acquisition period. GARP1 ^{13}C decoupling was applied during the 73 ms acquisition period [85]. A 1.8 s delay period was used with 8 scans, leading to a total acquisition time of 56 h. The NOESY experiments for 2P-ERK2 were essentially the same, except that 64 and 64 complex points were used (18.8 and 18.8 ms, respectively) in the t_1 (^{13}C) and t_2 (^{13}C) dimensions, resulting in a total acquisition time of 82 h. Time-domain data in the ^{1}H dimension were apodized by a squared cosine window function and zero-filled prior to Fourier transformation. The number of points in both indirect dimensions was doubled using forward-backward linear prediction [86]. The indirect dimensions were then apodized by a cosine window function and zero-filled prior to Fourier transformation and baseline corrections were applied to both indirect dimensions. Table 2.3 lists the filenames and experimental parameters.

The 3D (^{1}H, ^{13}C, ^{1}H) HMQC-NOESY experiments[87] were performed on a Varian VNMRS 800 MHz spectrometer with a z-axis gradient cryoprobe at 25 °C on ILV methyl-protonated, U-[^{2}H,^{15}N] 0P-ERK2 with a mixing time of 300 ms (MIX) and total acquisition times of 96 h. This experiment used the sequence "hmqc_H1_c13_methyl_3dnoesy_ap_bufsat.c". The experiment was acquired with 75 and 84 complex points (34.1 and 18.6 ms, respectively) in the t_1 (^{1}H) and t_2 (^{13}C) dimensions, and 2048 complex points in the acquisition period. GARP1 ^{13}C decoupling was applied during the 73 ms acquisition period [85]. A 1.3 s delay period was used with 8 scans, leading to a total acquisition time of 56 h. The NMR data were processed with the NMRPipe software package.[88] The points in each indirect dimension was linear-predicted in a forward-backward manner,[86] and the time-domain data in all dimensions were apodized with a cosine bell and zero filled prior to Fourier transformation. Baseline corrections were applied after Fourier transformation as needed. The spectra were further visualized and analyzed using the program CcpNmr Analysis[83].

Table 2.3. 3D Methyl NOESY filenames, parameters and conditions

Filename[a]	B_0	mix	np	ni	ni2	sw	sw1	sw2	nt	d1
13c13c1hnoesy_3D_0PERK2_041011.fid[a]	800	0.35	2048	52	54	14044.9	3400	3400	8	1.8
2p_ERK2_sample031611_ILV_3d_13C13C1H_hmqcnoesy_032811.fid[b]	800	0.35	2048	64	64	14044.9	3400	3400	8	1.8
1h13c1hnoesy_2D_0PERK2_040411.fid[a]	800	0.3	2048	75	84	14044.9	3000	4500	8	1.3

mix − mixing time (s)
np − number of complex points in t_3
ni − number of complex points in t_1
ni2 − number of complex points in t_2
sw − sweep width in t_3 (Hz)
sw1 − sweep width in t_1 (Hz)
sw2 − sweep width in t_2 (Hz)
nt − number of scans per FID
d1 − interscan delay (s)
[a]Data directories in /yao/data/ERK2_2011/0pERK2_100D2O_033111/.
[b]Data directories in /yao/data/ERK2_2011/2pERK2_100D2O_031811/.

2.2.3. Analysis of X-ray Structure

Protons were added to the X-ray structure coordinates of ERK2 (PDB 1ERK) using the program http://spin.niddk.nih.gov/bax/nmrserver/pdbutil/sa. Distances between centers of the methyl protons were estimated using an in-house script. Empirically-derived cutoffs of 8.0 Å, 7.1 Å and 6.3 Å were used to define I-I, I-L/V, and V/L-V/L clusters, which take into account the lower intensities of L/V resonances in the samples used here. Solvent accessible surface areas for ERK2 were estimated using the server GETAREA[89] (http://curie.utmb.edu/getarea.html), with a 1.4 Å radius spherical water probe.

2.3. Results

2.3.1. Strategy for Assignment of ILV Methyls in Proteins with Known Structure

The strategy employed here for resonance assignment of an ILV $^{13}CH_3$-methyl labeled protein with a known X-ray structure is illustrated in Figure 2.1 and involves comparing the observed methyl-methyl NOEs with those predicted from the structure. To simplify this comparison, three levels of analysis were employed. The first level is identification of the methyl type (I, L or V) for both partners in each NOE using through-bond ^{13}C, ^{1}H correlation experiments (Figure 2.1A). The second level is that predicted and observed NOEs are compared in a hierarchical manner starting with Ile-Ile NOEs followed progressively by Ile-Val, Ile-Leu, Val-Val, Val-Leu, and Leu-Leu NOEs (Figure 2.1B). The rationale for this hierarchy is that NOEs involving Ile methyls have higher signal-to-noise than Val/Leu methyls in the labeling strategy used here, and generally there are fewer Ile or Val residues in a protein than Leu residues.[90] This level also involves ranking of the sizes of so-called "NOE clusters." A NOE cluster is defined as two or more methyls of the same residue type (e.g. Ile) that are linked through NOEs as well as methyls of other residue types (e.g. Leu/Val) that show NOEs to the methyls of the original residue type. For example, an Ile methyl is included in an Ile-NOE cluster if it shows an NOE to at least one other Ile and a Val/Leu residue is included in the cluster if its methyl(s) show NOEs to an Ile residue in the cluster. The number of methyls of a certain residue type within the cluster determines the size of a cluster. For example, an n-residue Ile cluster is a NOE cluster including n Ile methyls that are linked through NOEs. The hierarchical approach employed here analyzes the NOE clusters with largest number of Ile residues first. If there is a single n-residue Ile-cluster observed in the NOESY spectra and also predicted in the structure, then this cluster can be uniquely mapped onto the protein. When there is ambiguity in the mapping, the next step in the analysis involves comparison of predicted and observed Ile methyl to Val/Leu methyl NOEs within this cluster. As more

Ile-NOE clusters are mapped onto the structure, this reduces the number of possibilities for the remaining clusters.

The same approach is used to map Val-NOE clusters onto the protein followed by Leu-NOE clusters (Figure 2.1B). At this point, most of the methyls in a cluster have not been assigned to specific residues but have only been associated with one or more clusters in the structure. The next level of analysis involves qualitative comparison of the patterns and sizes of the NOEs with the predicted methyl-methyl distances from the X-ray structure (Figure 2.1C). This allows residue-specific resonance assignments for many methyl groups and ambiguous or tentative assignments for others. Additional information, such as NMR data on single-site ILV mutants, can then be used to confirm or extend the methyl resonance assignments. The application of this strategy for ERK2 was done manually, but this hierarchical NOE-cluster approach to ILV methyl resonance assignment is well suited to automation.

2.3.2. Identification of Amino Acid Type for ILV Methyls in 0P-ERK2

The first step in the assignment of the ILV methyls in 0P-ERK2 was to determine whether a resonance belonged to an Ile, Val or Leu residue. 2.2 shows the ILV methyl region of the 2D (^{13}C, ^{1}H) HMQC spectrum on an Ile$^{\delta 1}$-[$^{13}CH_3$], Leu$^{\delta}$/Val$^{\gamma}$-[$^{13}CH_3$,$^{12}CD_3$], U-[^{15}N,^{12}C,^{2}H]-labeled 0P-ERK2 sample that was generated as described in Methods. ERK2 has 144 Ile, Leu and Val methyls and 140 resonances (97%) were observed in the HMQC spectrum of 0P-ERK2 (2.2). The Ile C$^{\delta 1}$-methyl resonances were readily identified based on their distinctive ^{13}C-chemical shifts,[70] where the criteria used here were that methyls with ^{13}C chemical shifts < 18 ppm were identified as Ile. ERK2 has 28 Ile residues and 26 resolved peaks were observed in the Ile methyl region of the HMQC spectrum (2.2). Analysis of the HMQC spectra of mutants of ERK2 and the NOE patterns observed in wild-type ERK2

showed that 2 sets of Ile resonances were overlapped, therefore all 28 Ile methyls were observed in the HMQC spectrum of 0P-ERK2.

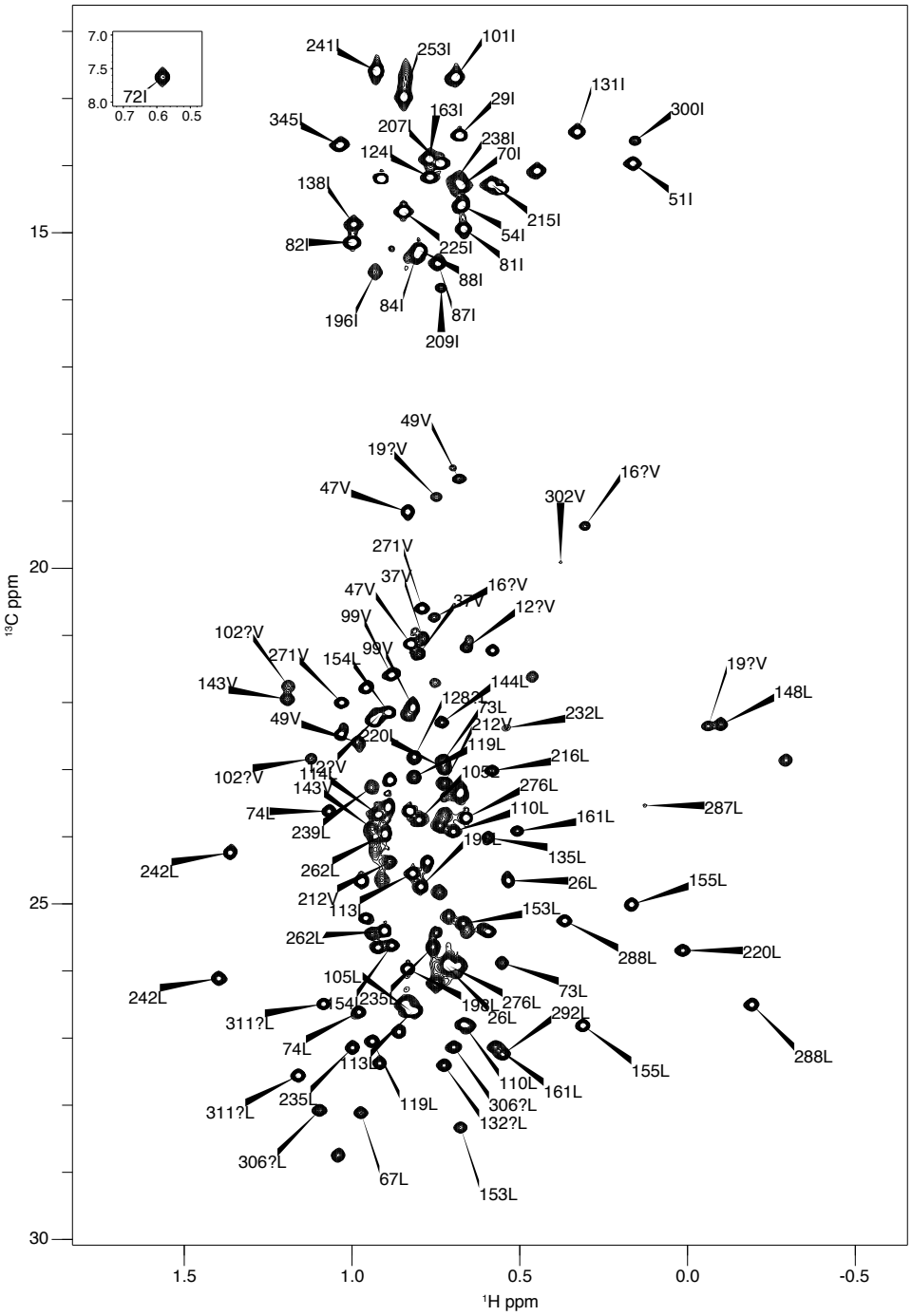

Figure 2.2. Methyl region of the 2D (^{13}C, ^{1}H) HMQC spectrum of ILV ^{13}CH3 methyl-labeled 0P-ERK2. The assigned methyls are labeled and tentative assignments are labeled with a question mark.

The next step in the resonance assignment was determining whether the non-Ile-methyl resonances originated from a Leu or Val residue. A total of 112 of the 116 expected Leu/Val-methyl resonances were observed in the HMQC spectrum of 0P-ERK2 (2.2). A 3D through-bond 'out-and-back' 3D (^{13}C, ^{13}C, ^{1}H) HMCM[CG]CBCA experiment[56] was used to distinguish Leu and Val residues in 0P-ERK2,[79] using a ILV methyl-protonated, U-[^{2}H,^{15}N, ^{13}C] 0P-ERK2 sample (Figure 2.3A). Leu and Val were distinct from each other because they yield different number of resonances from aliphatic carbons in this experiment (Figure 2.3B). A related through-bond 'out-and-back' 3D (^{13}C, ^{13}C, ^{1}H) HMCMCBCA experiment[56] was also employed here on a methyl protonated (Ile$^{\delta 1}$-[$^{13}CH_3$], Leu$^{\delta}$/Val$^{\gamma}$-[$^{13}CH_3$,$^{12}CD_3$]), and Ile$^{\gamma}$/Leu$^{\beta,\gamma}$/Val$^{\alpha,\beta}$-[^{13}C], U-[^{15}N,^{12}C,^{2}H]-labeled 0P-ERK2 (Figure 2.3C and Methods). This experiment correlates an individual Ile, Leu or Val-methyl group with aliphatic carbons on the same side chain. Only one non-methyl ^{13}C resonance is observed for an Ile residue in the ω_1 dimension of the HMCMCBCA spectrum, but up to two non-methyl resonances are observed for both Leu (C^{β}, C^{γ}) and Val (C^{α}, C^{β}) residues (Figure 2.3D). It is possible to determine the number of carbon-carbon bonds between the ^{13}C and the methyl group from analysis of both the sign and chemical shift of these ^{13}C resonances.[56] Many of the Leu and Val residues were distinguished by the distinct chemical shifts of their Leu C^{β} and Val C^{α} resonances (Figure 2.3D and BMRB[91]). This led to identification of 62 of the 88 Leu methyls and 25 of the 28 Val methyls in 0P-ERK2. For 12 Val and 19 Leu residues, the unique chemical shifts of the C^{α}, C^{β} (Val) or C^{β}, C^{γ} (Leu) resonances made it possible to assign both methyl resonances of the same residue. The labeling method employed here does not allow *a priori* stereospecific assignments of the pro-R and pro-S methyl groups in Leu or Val, although in some cases stereospecific assignment could be deduced by analysis of the NOE data and crystal structure. In addition, the labeling method for the “out-and-back” experiment here is not optimal for the 3D NOESY experiment, because the carbon one-bound away from the methyl carbon is also ^{13}C labeled,

thus each methyl resonance becomes a doublet due to carbon-carbon coupling (Figure 2.4). Representative data from "out-and-back" experiments of 0P-ERK2 were presented in Figure 2.5, Figure 2.6, and Figure 2.7.

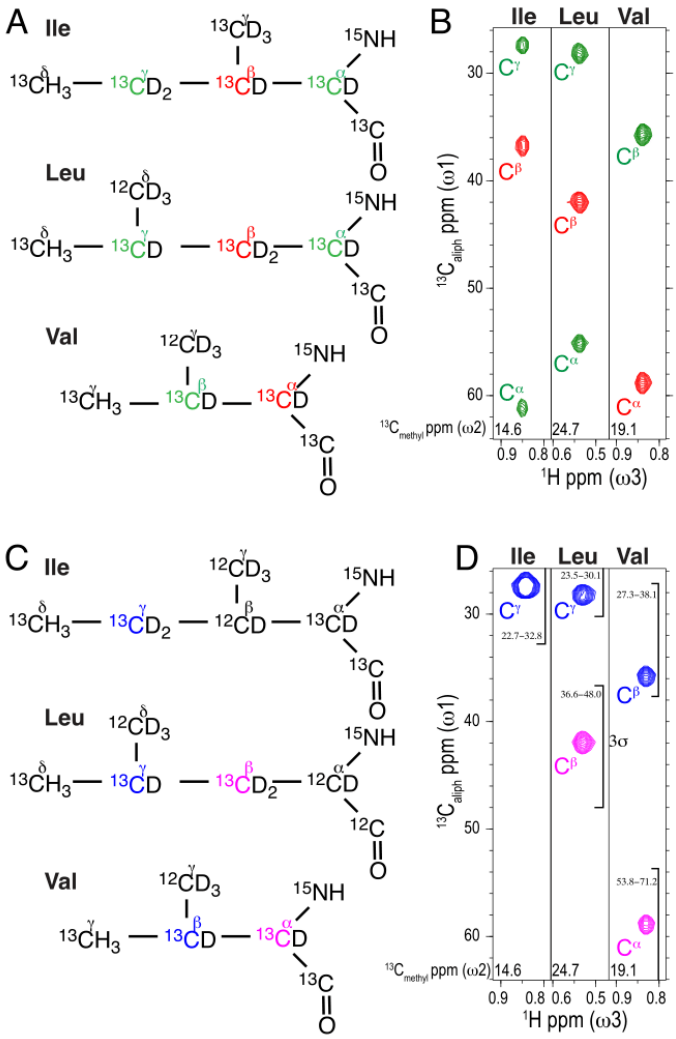

Figure 2.3. Identification of methyl residue type in ERK2 using ^{13}C chemical shifts and through-bond "out-and-back" spectra.
(A) The pattern of labeling for Ile, Leu and Val residues in the ILV methyl-protonated, U-[^{2}H,^{15}N, ^{13}C] 0P-ERK2. The aliphatic carbons colored green and red have opposite signs for their resonances in the 3D spectra. (B) Strip plots of the 3D HMCM(CG)CBCA spectrum for 0P-ERK2 showing distinct number of peaks from aliphatic carbons. (C) The pattern of ^{13}C-labeling for Ile, Leu and Val residues in the ILV side chain-partial labeled, U-[^{2}H,^{15}N] 0P-ERK2 sample. The aliphatic carbons colored blue and magenta have opposite signs for their resonances in the 3D spectra. (D) Strip plots of the 3D HMCMCBCA spectrum for 0P-ERK2 showing distinct chemical shifts for Leu and Val aliphatic carbons. In the aliphatic ^{13}C dimension, Ile residues have one peak, whereas two peaks are observed for Leu (C^{γ} and C^{β}) and Val (C^{β} and C^{α}) where the two are of opposite sign (colored blue and magenta here). The brackets denote the typical range of chemical shift (average ± 3σ, 99.7%) for a specific aliphatic carbon in I/L/V, using data from the BMRB[91]. The identity of Leu and Val was determined by the distinct chemical shifts of the Val C^{α} and the Leu C^{β} resonances.

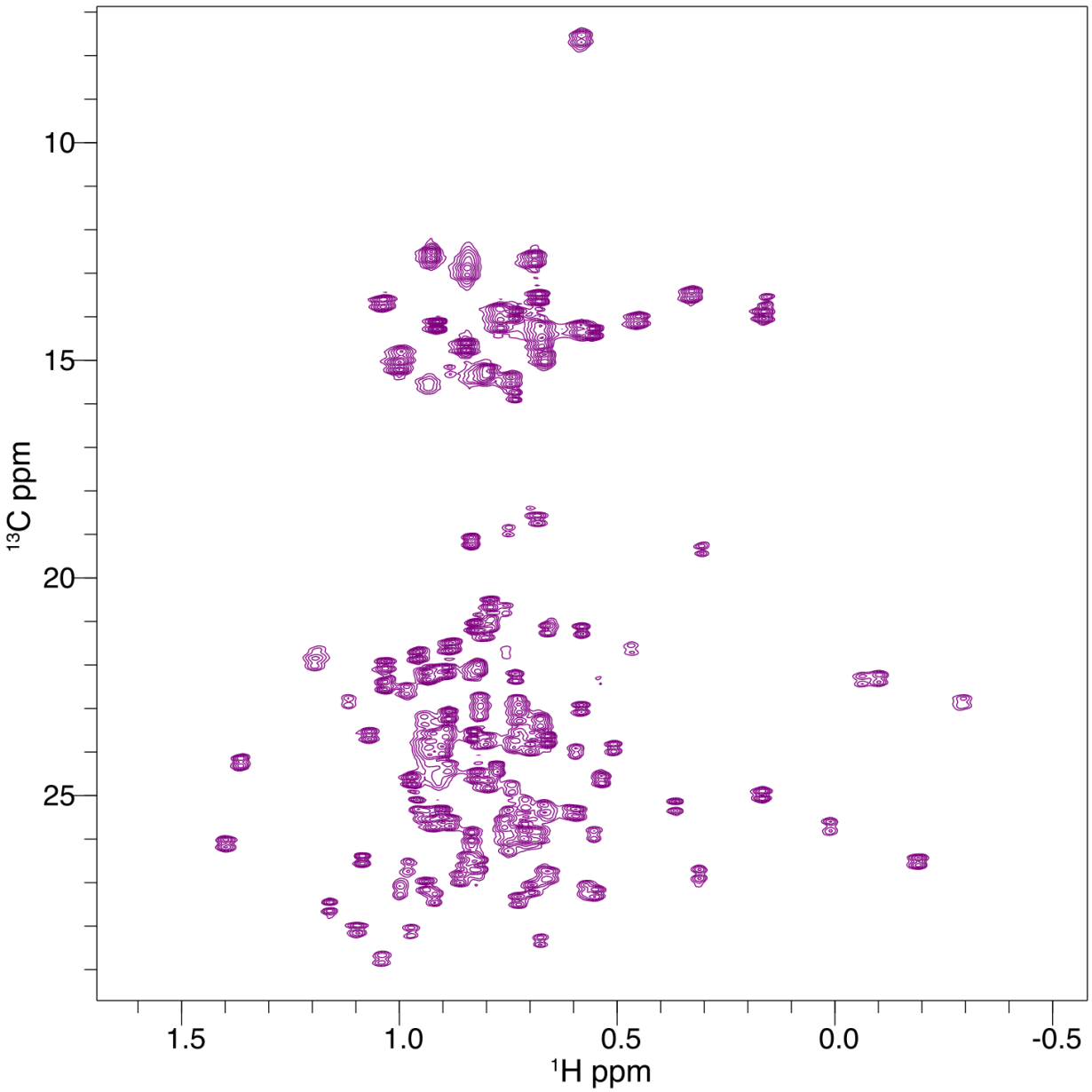

Figure 2.4. 2D (^{13}C, ^{1}H) HMQC spectra of a ILV side chain-partial labeled, U-[^{2}H,^{15}N] 0P-ERK2. Each methyl resonance in 0P-ERK2 shows a doublet because of carbon-carbon coupling (J_{CC} about 35 Hz).

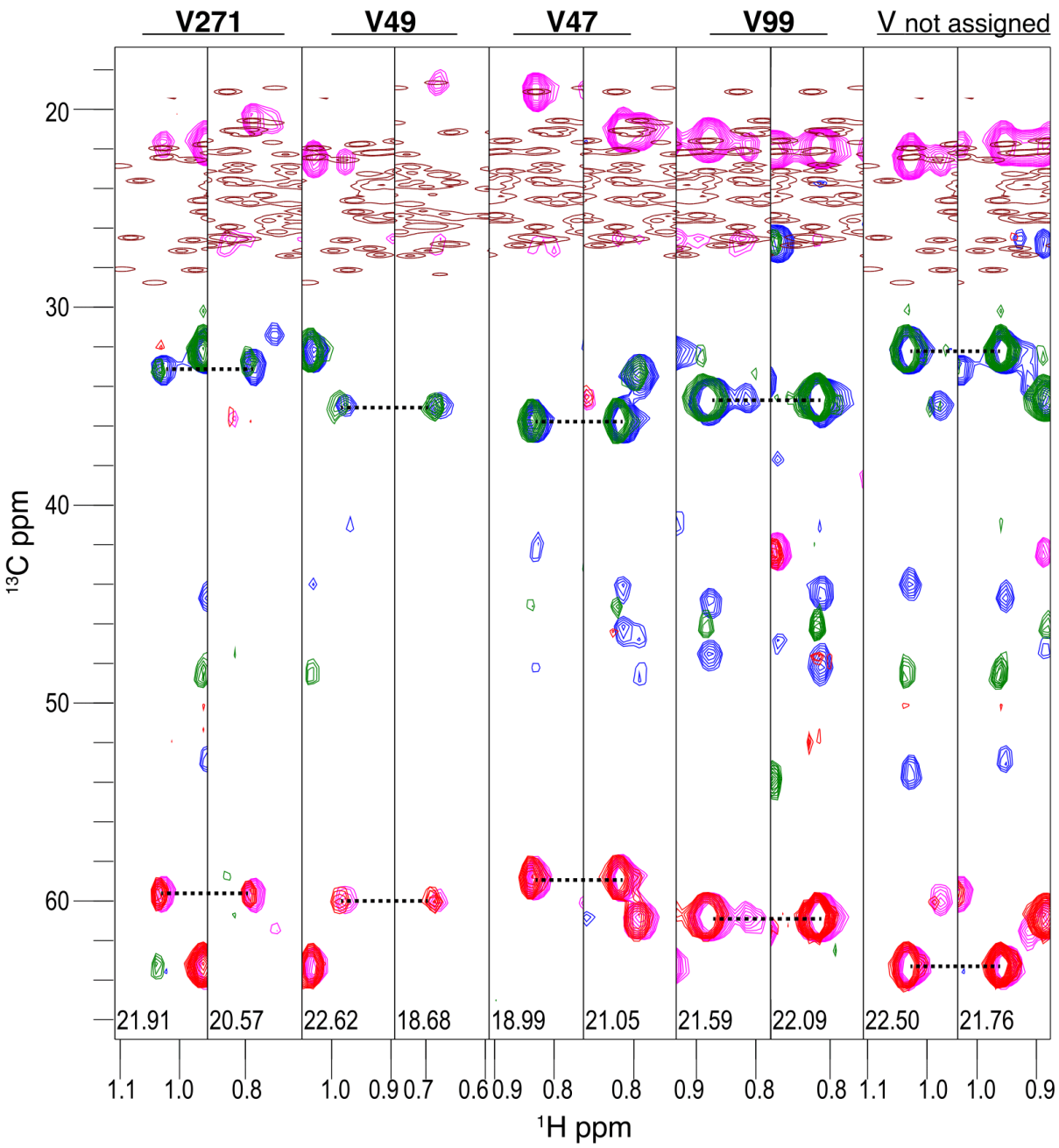

Figure 2.5. Representative Val in the "out-and-back" experiments.
Peaks from HMCMCBCA spectra were colored with blue and magenta to show their opposite phases. Peaks from HMCM(CG)CBCA spectra were colored with green and red to show their opposite phases. A 2D (^{13}C, ^{1}H) HMQC spectra of a ILV methyl-protonated, U-[^{2}H,^{15}N] 0P-ERK2 sample was colored in maroon to show the chemical shift positions of methyls. A methyl peak is recorded in t_1 of the HMCMCBCA but not in HMCM(CG)CBCA spectra. The C^{β} and C^{α} in the two "out-and-back" experiments were overlapped. The aliphatic carbon resonances from paired Val methyls were connected with dashes. The resonances that are weaker comparing with the peaks of interest (C_m, C^{β} and C^{α}) in the "out-and-back" experiments are either bleached through from other chemical shifts, or most likely a result of "multi-spin resonances".

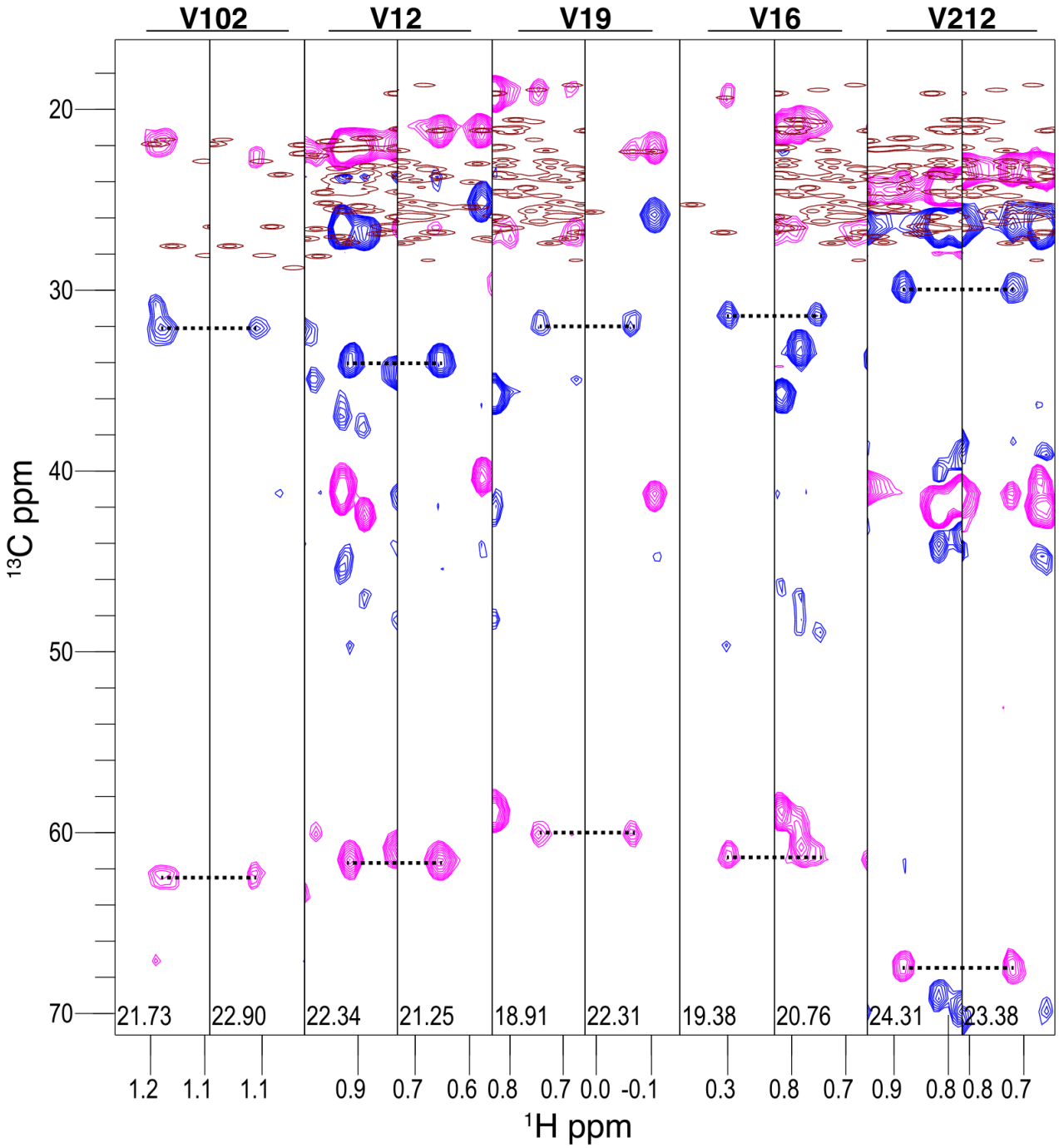

Figure 2.6. Representative Val in the HMCMCBCA experiment.
Peaks from HMCMCBCA spectra were colored with blue and magenta to show their opposite phases. A 2D (^{13}C, ^{1}H) HMQC spectra of a ILV methyl-protonated, U-[^{2}H,^{15}N] 0P-ERK2 sample was colored in maroon to show the chemical shift positions of methyls. The aliphatic carbon resonances from paired Val methyls were connected with dashes. The resonances that are weaker comparing with the peaks of interest (C_m, C^{β} and C^{α}) in the HMCMCBCA experiments are either bleached through from other chemical shifts, or most likely a result of "multispin resonances".

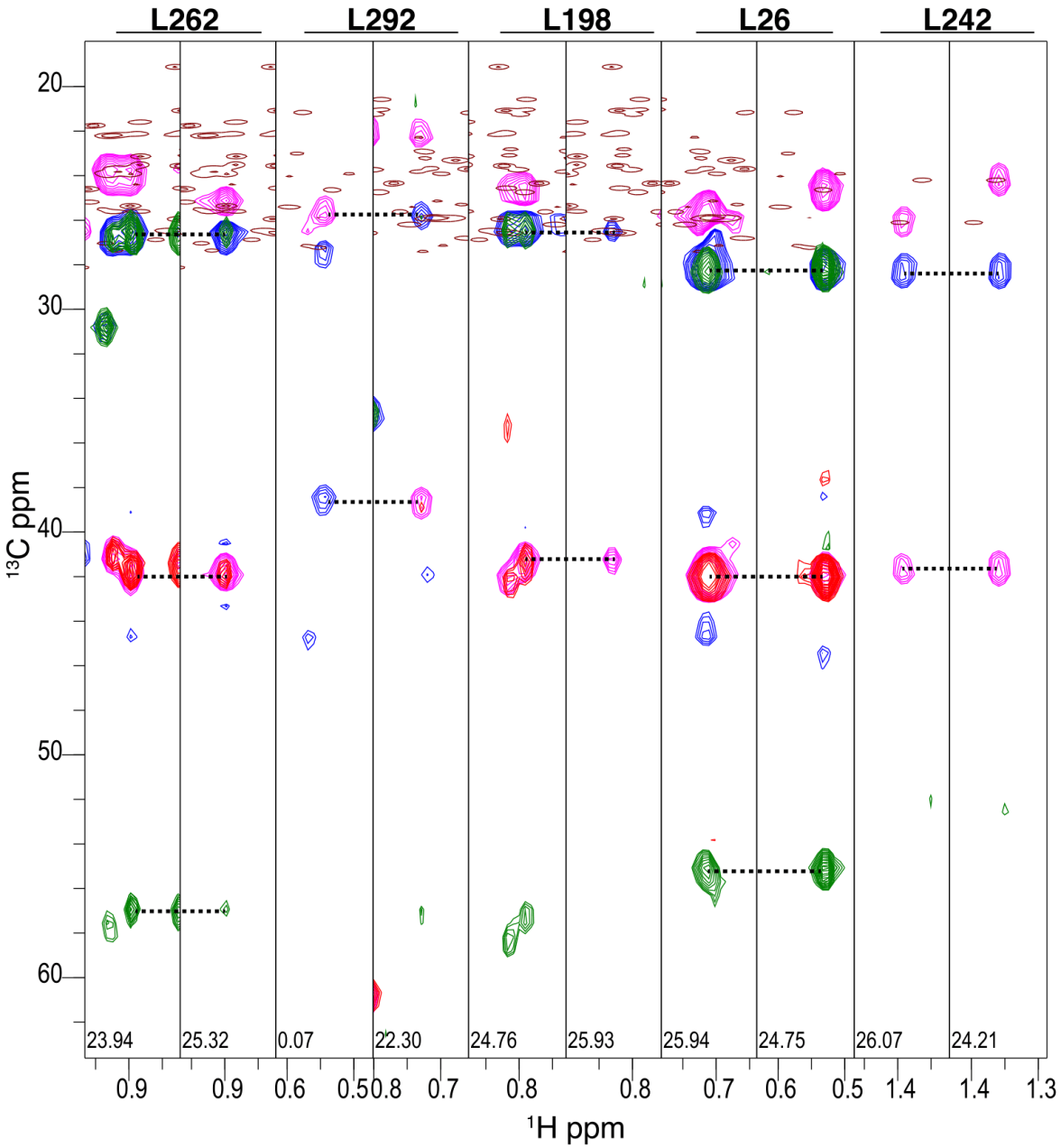

Figure 2.7. Representative Leu in "out-and-back"experiments.
Peaks from HMCMCBCA spectra were colored with blue and magenta to show their opposite phases. Peaks from HMCM(CG)CBCA spectra were colored with green and red to show their opposite phases. A 2D (^{13}C, ^{1}H) HMQC spectra of a ILV methyl-protonated, U-[^{2}H,^{15}N] 0P-ERK2 sample was colored in maroon to show the chemical shift positions of methyls. A methyl peak is recorded in t_1 of the HMCMCBCA but not in HMCM(CG)CBCA spectra. The C^{γ} and C^{β} in the two "out-and-back" experiments were overlapped. The C^{α} was observed in HMCM(CG)CBCA spectra (if signal-to-noise is good) but not in HMCMCBCA spectra. The aliphatic carbon resonances from paired Leu methyls were connected with dashes. The resonances that are weaker comparing with the peaks of interest (C_m, C^{β} and C^{α}) in the “out-and-back” experiments are either bleached through from other chemical shifts, or a result of “multispin resonances”.

2.3.3. Ile-NOE Clusters as the Starting Point for Methyl Resonance Assignments in 0P-ERK2

Identification of Ile-NOE clusters in the 3D NOESY spectra was the next step in resonance assignment in 0P-ERK2 (Figure 2.1B). The isotope-labeled sample used in the NOESY experiment have complete $^{13}CH_3$ labeling of the δ1 methyl on Ile, whereas the racemic mixture of the precursor metabolite results in $^{13}CH_3$-labeling of only one of two methyl groups on each Leu and Val residue in an individual protein.[49, 50] This leads to ≈50% lower signal-to-noise for the Leu or Val methyl resonances relative to Ile methyls in the HMQC spectrum. Thus, NOE clusters of Ile residues were used first because these methyls have more intense cross peaks than Val/Leu methyls (assuming equivalent relaxation and methyl-methyl distances) and because there is only one labeled methyl per residue, which avoids complications involving stereospecific assignments. Two 3D NOESY spectra were collected that had either (^{13}C, ^{13}C, ^{1}H) or (^{1}H, ^{13}C, ^{1}H) frequency labeling periods (see Methods). Every Ile methyl in the Ile-NOE cluster must show NOEs to at least one other Ile in the cluster but not all Ile methyls in a cluster will show NOEs to each other, especially for larger clusters.

Thirty Ile-Ile methyl cross peaks were observed in the 3D (^{13}C, ^{13}C, ^{1}H) NOESY spectrum of 0P-ERK2, arising from multiple Ile clusters. The largest Ile-NOE cluster in the 3D (^{13}C, ^{13}C, ^{1}H) NOESY spectrum of 0P-ERK2 consisted of 6 Ile residues, giving rise to 18 Ile-Ile cross peaks (Figure 2.8A). The second largest Ile-NOE cluster consisted of 3 Ile residues, with five pairs of 2-(Ile)-residue Ile-NOE clusters (referred to below as Ile-pairs).

The crystal structure of 0P-ERK2 was analyzed using an 8 Å cutoff to identify potential Ile-NOE clusters. This cutoff was empirically derived and is approximately the longest distance observed for methyl-methyl NOEs in the 350 ms mixing time 3D NOESY spectrum of ERK2. The largest Ile-methyl-cluster predicted in 0P-ERK2 involves Ile residues I54, I70, I84, I87, I101, I345 in the N-terminal lobe (Figure 2.8B), which was uniquely mapped to the 6-residue Ile-NOE cluster observed in

the NOESY spectra (Figure 2.8A, B). The second largest Ile cluster in the X-ray structure involved Ile residues I81, I138, I163, which could be uniquely mapped to the single 3-residue Ile-NOE cluster. 0P-ERK2 has five pairs of Ile methyls separated by less than 8 Å consisting of I51-I88, I131-I215, I196-I207, I225-I241, and I209-I300. These five Ile-pairs match the five 2-residue Ile-NOE clusters observed in the NOESY spectra (Figure 2.8A, B). Thus, 19 of the 28 Ile residues were found in the seven Ile-NOE clusters observed in the NOESY spectra (Figure 2.8B), whereas the other nine Ile methyls were too distant from other Iles to be involved in an Ile-NOE cluster.

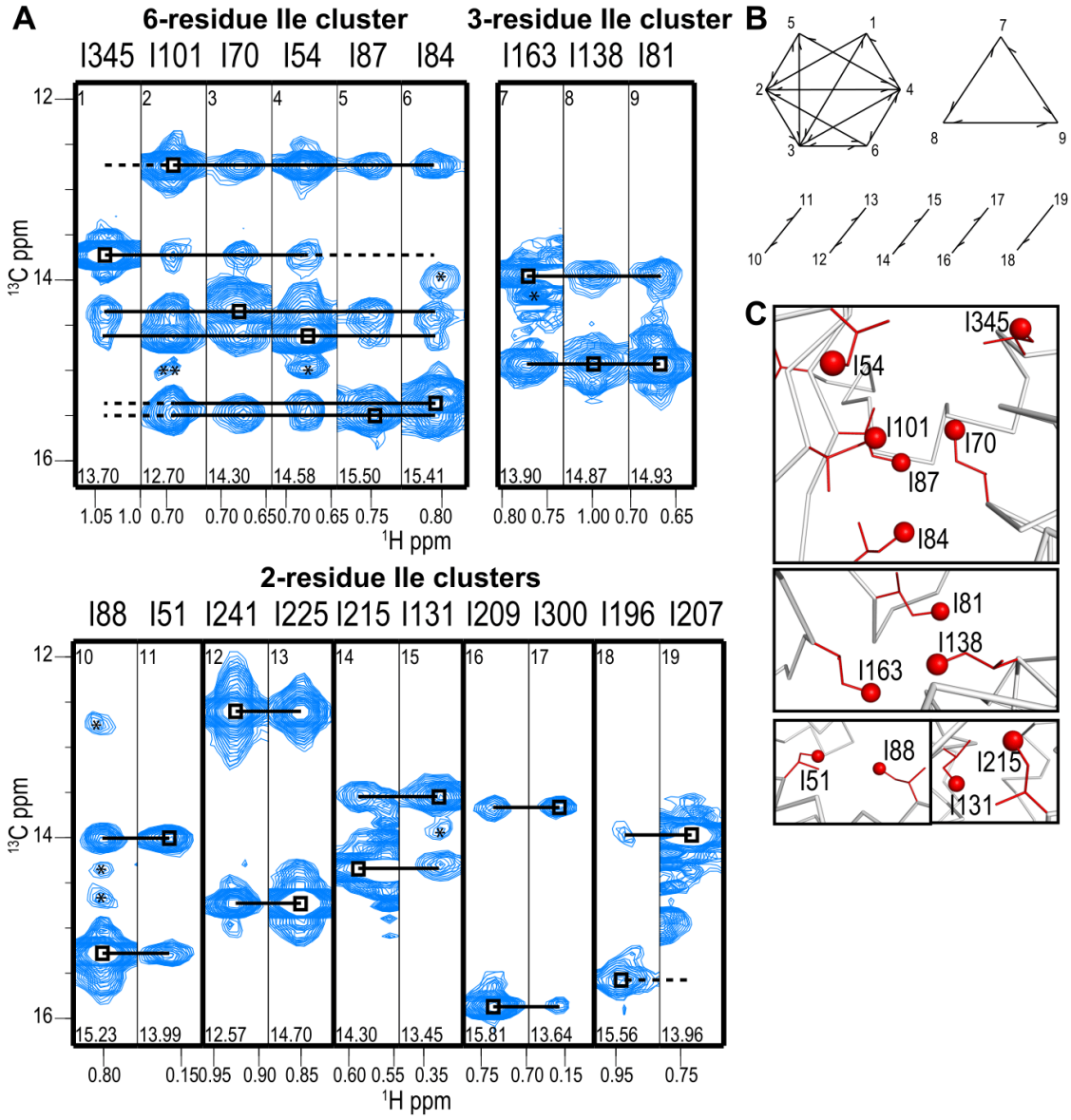

Figure 2.8. Mapping of Ile-NOE clusters onto the X-ray structure of ERK2.
(A) Strip plots of the 3D (^{13}C, ^{13}C, ^{1}H) HMQC-NOESY spectra for 0P-ERK2 illustrating the Ile-NOE clusters in the protein. Diagonal peaks are marked with squares, the horizontal solid lines indicate NOE cross peaks to other methyls and dashed lines indicate where a cross peak is not observed. Asterisks mark peaks that arise from bleed-through in the third dimension from a different methyl resonance and double asterisks indicate noise peaks or artifacts. The numbers at the bottom of each strip plot are the ^{13}C chemical shift for this methyl plane. (B) Geometry models illustrating the various Ile-NOE clusters in ERK2. The numbers at the vertex represent the methyl for that strip plot in (A) and a line connecting two vertices indicates an observed NOE between these two methyls with single and double headed arrows indicating that one and two cross peaks, respectively, were observed between the two methyl resonances. (C) Ile clusters in the X-ray structure of ERK2 that are consistent with geometry models in (B). The upper panel shows the only 6-residue Ile-methyl cluster (using an 8 Å cutoff), the middle panel shows the only 3-residue Ile-methyl cluster and the bottom two panels show two of the five 2-residue Ile-methyl clusters. Ile side chains are shown as red lines and their C$^{\delta}$ methyls are red spheres, and the backbone is a white ribbon.

The five 2-residue Ile-clusters in 0P-ERK2 could not be uniquely mapped using only Ile-Ile NOEs. This led to the next level of analysis that utilized Ile to Val/Leu methyl-methyl NOEs (Figure 2.1B). Due to the 50% $^{13}CH_3$-labeling of Val/Leu methyls, a slightly shorter cutoff of 7.1 Å was used to predict Ile to Leu or Val NOEs. Using the hierarchical approach (Figure 2.1B), the Ile-Val NOEs were analyzed first, since there are many fewer Val than Leu residues in ERK2. Only one Ile-pair had predicted and observed NOEs to 4 Val residues and could be uniquely mapped to I51-I81 (Figure 2.9). Three Ile-pairs had predicted and observed NOEs to one Val residue; thus, analysis of Ile-Leu and Val-Leu NOEs was performed next to map these Ile-clusters onto the structure. An Ile-pair had only one predicted and observed Ile-Leu NOE and no predicted or observed Ile-Val NOEs, which enabled unique mapping of this pair to I196-I207.

Three sets of 2-residue Ile clusters (I131-I215, I225-I241 and I209-I300) have the same number of predicted and observed I-V NOEs so the I-L and V-L NOEs were next analyzed. Among these three Ile-pairs, I131-I215 and I225-I241 both show NOEs to 5 Leu residues whereas the I209-I300 cluster shows a NOE to only 1 Leu residue (Figure 2.10). Thus, I209-I300 was uniquely mapped at this point. To map I131-I215 and I225-I241, the analysis was extended to V-L NOEs. V271 shows NOE to the I225-I241 cluster and it has predicted and observed NOE to only 1 Leu residue (Figure 2.11), allowing unique mapping of the I225-I241 cluster. Thus, the only remaining 2-residue Ile-NOE cluster that showed NOEs to one Val residue was mapped to I131-I215.

The seven observed Ile-NOE clusters were unambiguously mapped onto the structure as described above, but in practice additional information was used to confirm this mapping. For example, as seen in Figure 2.12, the single 3-residue Ile-cluster in 0P-ERK2 (I138-163-181) can be linked to the I131-I215 cluster because both show NOEs to two connecting Leu residues (L153 and L161). This

additional level of analysis lends confidence to the mapping and subsequent resonance assignments of residues in a cluster.

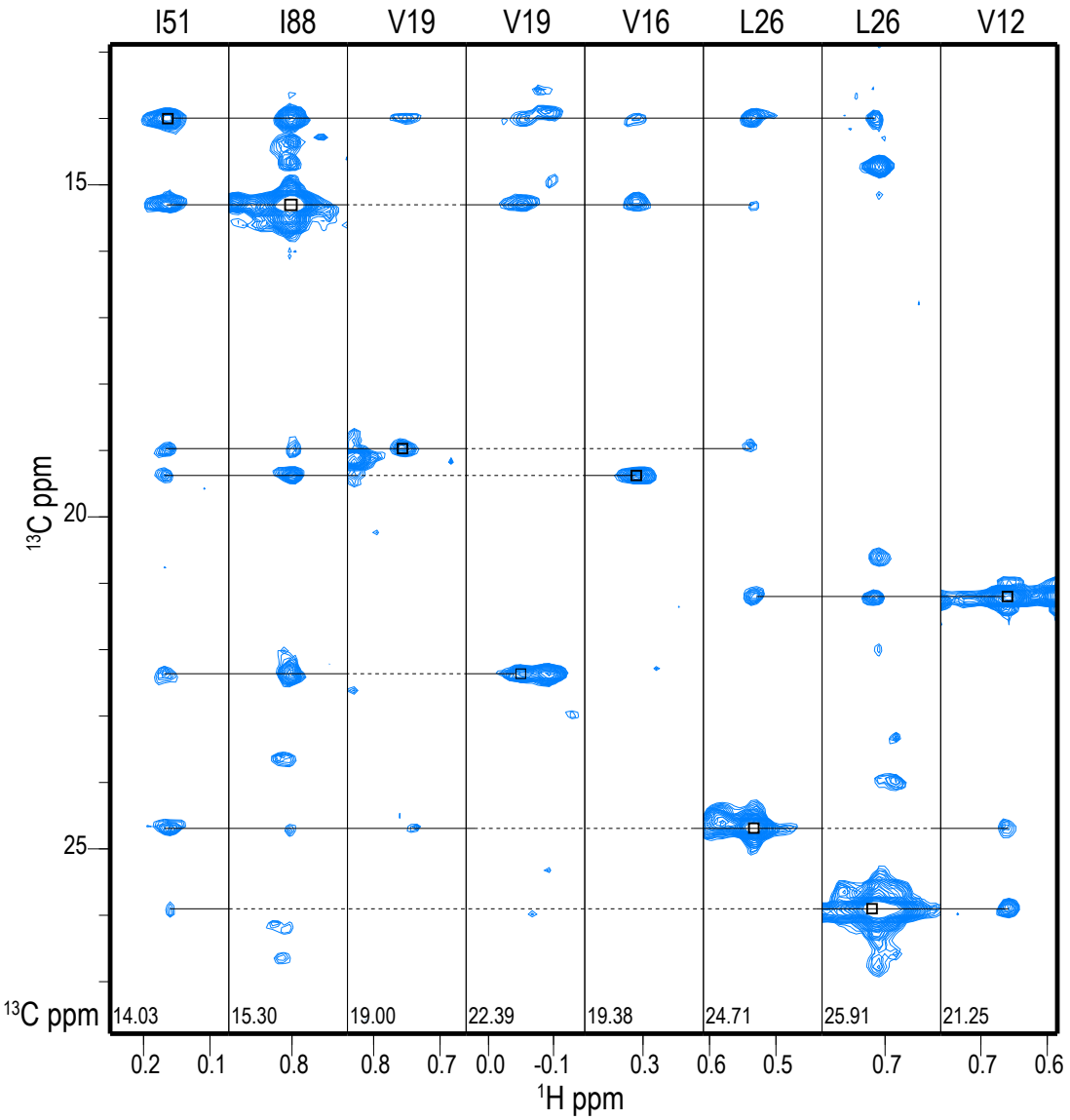

Figure 2.9. NOE data used in the mapping of a 2-residue Ile-NOE cluster.
Strip plots from the 3D (^{13}C, ^{13}C, ^{1}H) HMQC-NOESY spectrum of 0P-ERK2 illustrating that this 2-residue Ile-NOE cluster shows NOEs to 4 Val and 2 Leu methyls. Comparison with predicted NOEs allowed these two Ile methyls to be mapped to I51 and I81. Self peaks are marked with squares, the horizontal solid lines indicate observed NOE cross peaks and the dashed lines indicate no NOE was observed. The ^{13}C chemical shift (in ppm) of the third dimension is given in the lower corner of each strip plot.

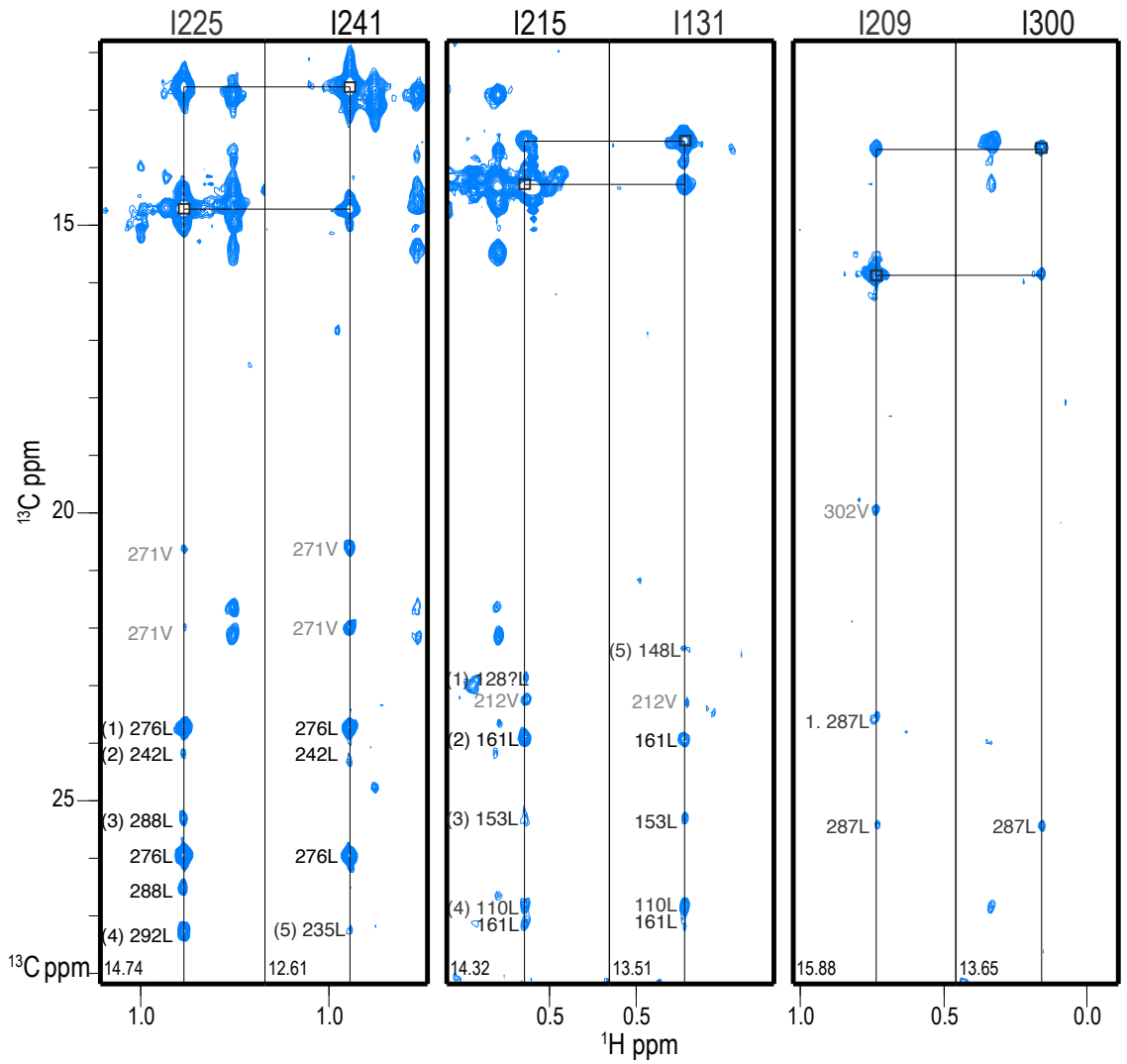

Figure 2.10. NOE data used in the mapping of three 2-residue Ile-NOE clusters.
Strip plots from the 3D (^{13}C, ^{13}C, ^{1}H) HMQC-NOESY spectrum of 0P-ERK2 for three 2-residue Ile-NOE clusters (I225-I241, I215-I131, and I209-I300). These three 2-residue Ile-NOE clusters show I-V NOEs to only 1 Val residue, but show I-L NOEs to 5, 5 and 1 Leu residues, respectively. Self peaks are marked with squares, and the vertical solid lines help trace the observed NOE cross peaks. I-L and I-V NOEs are labeled in black and grey, respectively and the numbers in parenthesis count the observed I-L NOEs. The ^{13}C chemical shift (in ppm) of the third dimension is given in the lower corner of each strip plot.

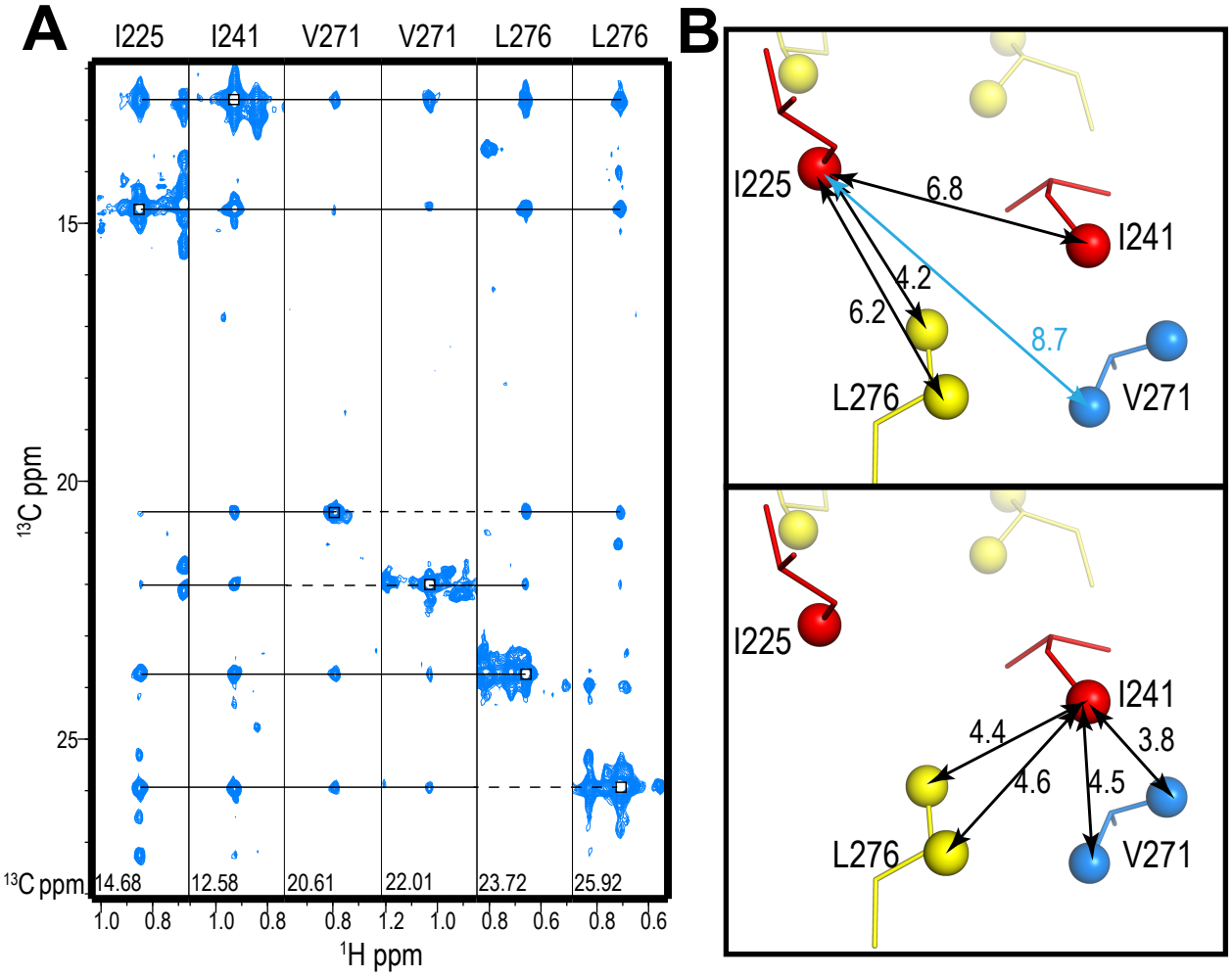

Figure 2.11. NOE and structural data used to assign the methyls in the I225-I241 cluster.
(A) Strip plots from the 3D (^{13}C, ^{13}C, ^{1}H) HMQC-NOESY spectrum of 0P-ERK2 showing the NOEs used to assign the I225-I241 Ile-cluster. Self peaks are marked with squares, the horizontal solid lines indicate observed NOE cross peaks and the dashed lines indicate no NOE was observed. The ^{13}C chemical shift (in ppm) of the third dimension is given in the lower corner of each strip plot. (B) The spatial arrangements of methyls for residues I225, I241, V271 and L276 in the structure of 0P-ERK2. Side chains of Ile (red), Leu (yellow) and Val (blue) are shown as lines and their methyls as spheres. Methyls with predicted and observed NOEs are connected with black arrows and the blue arrow indicates an observed NOE that was not predicted in the structure. The numbers on the connections are the inter-methyl distances.

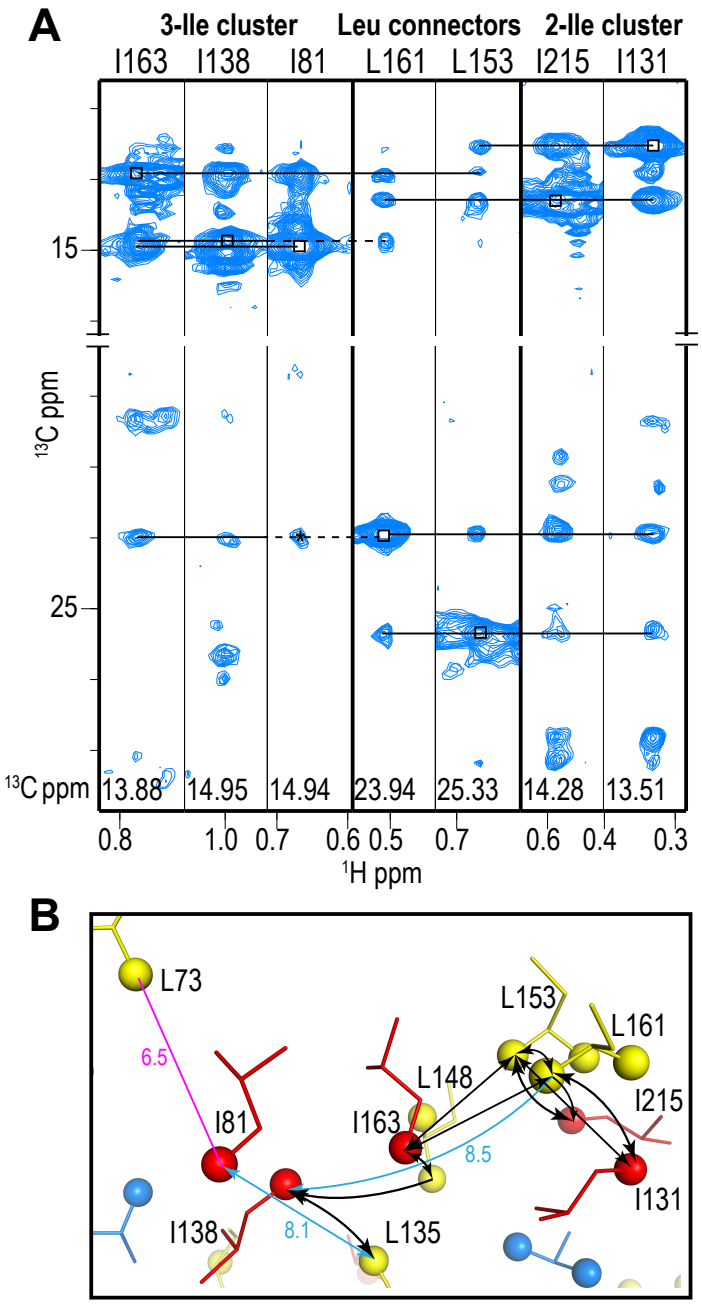

Figure 2.12. NOE and structural data used to assign the methyls in the 3-Ile cluster and one of the 2-Ile clusters. (A) Strip plots from the 3D (^{13}C, ^{13}C, ^{1}H) HMQC-NOESY spectrum of 0P-ERK2 illustrating that there are two Leu methyls that show NOEs to both the 3-residue Ile-NOE cluster and a 2-residue Ile-NOE cluster. Self peaks are marked with squares, the horizontal solid lines indicate observed NOE cross peaks and the dashed lines indicate no NOE was observed. The ^{13}C chemical shift (in ppm) of the third dimension is given in the lower corner of each strip plot. The asterisk in the I81 strip indicates a NOE signal to another methyl (L135) that has similar ^{13}C chemical shift with L161. (B) The spatial arrangements of methyls for these clusters in the structure of 0P-ERK2. Side chains of Ile (red), Leu (yellow) and Val (blue) are shown as lines and their methyls as spheres. Methyls with predicted and observed NOEs are connected with black arrows, the blue arrow indicates an observed NOE that was not predicted in the structure and magenta indicates where a NOE was predicted but not observed.

2.3.4. Isolated Iles Were Mapped and Assigned by Their Unique L/V Surroundings

An Ile residue was considered "isolated" here if it had no predicted or observed I-I NOEs. These residues were therefore mapped by their patterns of I-V, I-L or V-L NOEs. For example, two isolated Ile residues each showed predicted and observed NOEs to only 1 Val residue and 1 Leu residue, so they were associated with I29 and I72. They were further mapped (and immediately assigned) by the surrounding V-L NOEs. For example, as seen in Figure 2.13, the V37 and L105 methyls near I29 have predicted and observed NOEs to each other, whereas the Val and Leu methyls that show NOEs to I72 do not have predicted or observed V-L NOEs. The assignment of L105 was confirmed by the L105A 0P-ERK2 mutant (Figure 2.14). In addition to the NOE constraints, I72 showed a unique $^{13}C^{\delta 1}$ methyl chemical shift ≈7.6 ppm, significantly lower than the average $^{13}C^{\delta 1}$ methyl chemical shift of Ile residues (13.4 ppm, BMRB), possibly due to strong ring current effects. Thus, I72 is surrounded by 4 Phe side chains (F76, F166, F327, F329), which can lead to large ring current effects, consistent with its unique ^{13}C chemical shift.

I-L NOEs provided assignments for isolated Iles that have no predicted or observed NOE to any Val residue. For example, I82, I124, I238 and I253, have no predicted or observed I-V NOEs, but have predicted NOEs with 1, 3, 1, and 3 Leu residues, respectively. Four isolated Ile residues showed NOEs with 1, 4, 1, and 2 Leu residues, respectively, which differentiated I82 and I238 from I124 and I253. The methyls that have the same number of predicted I-L NOEs could then be mapped onto the structure by analysis of the number of L-L NOEs. In practice, residues I124, I238 and I253 were already assigned by expanding the L/V NOE network of the I225-I241 cluster. The assignments of I124 and I238 were confirmed by the I124A and I238A 0P-ERK2 mutants. Thus, the remaining isolated Ile residue was assigned to I82, which only has predicted and observed NOEs to L154 methyls (Figure 2.15A,B). This assignment was confirmed with the L154A 0P-ERK2 mutant. Residues I93,

I254, I322 could not be uniquely assigned due to lack of unique distance constraints. In summary, 25 out of 28 Ile methyls were assigned in 0P-ERK2.

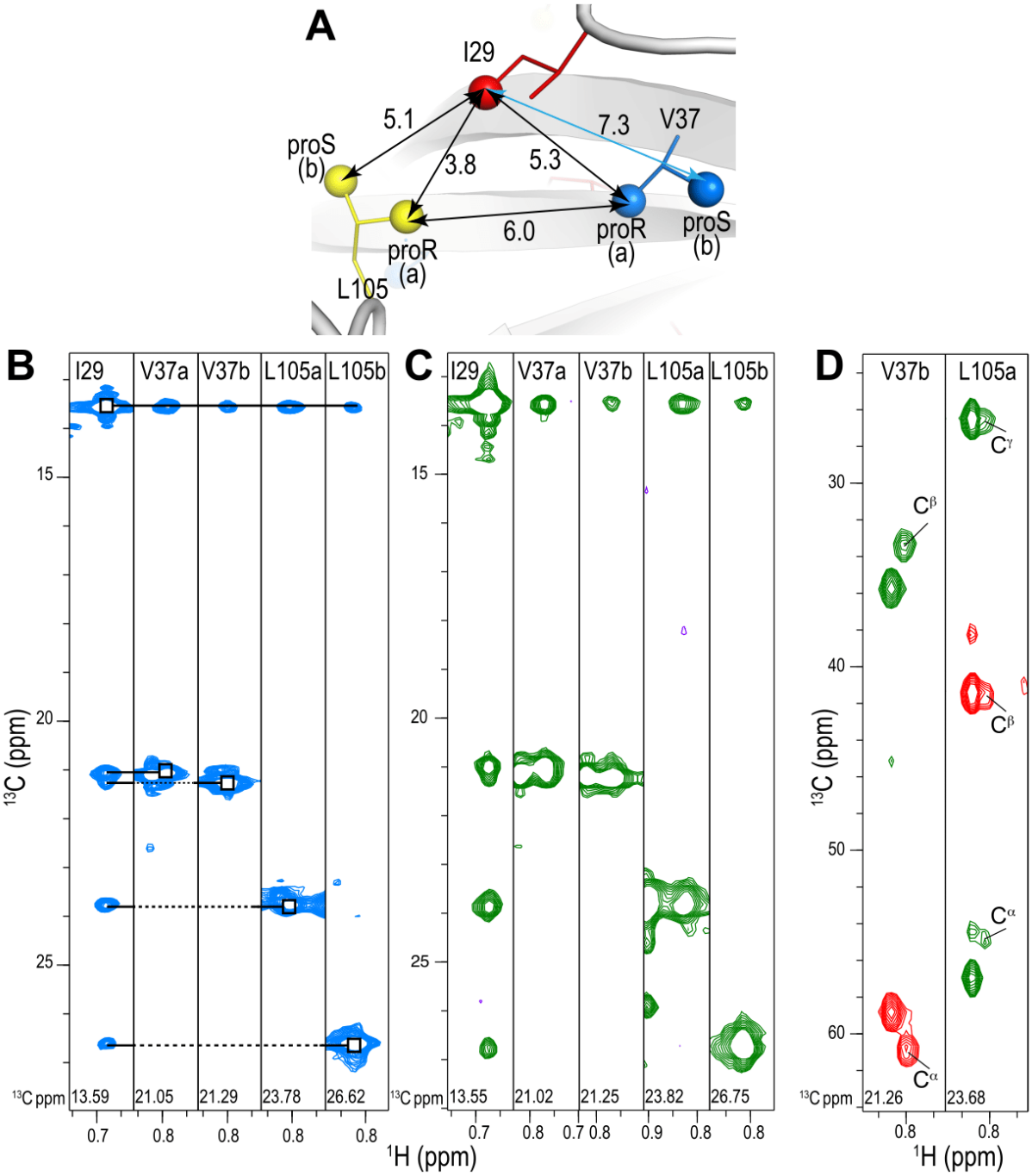

Figure 2.13. NOE and structural data used in the mapping and assignment of isolated Ile methyl I29. (A) The I29 region of the X-ray structure of 0P-ERK2 using the same color/labeling scheme as Figure 2.11. (B) Strip plots of the 3D (^{13}C, ^{13}C, ^{1}H) HMQC-NOESY spectrum of 0P-ERK2 illustrating the NOEs used to make assignments of I29, V37 and L105. (C) Similar NOEs in 2P-ERK2. (D) Strips from HMCM(CG)CBCA spectra showing aliphatic carbon chemical shifts for V37 and L105.

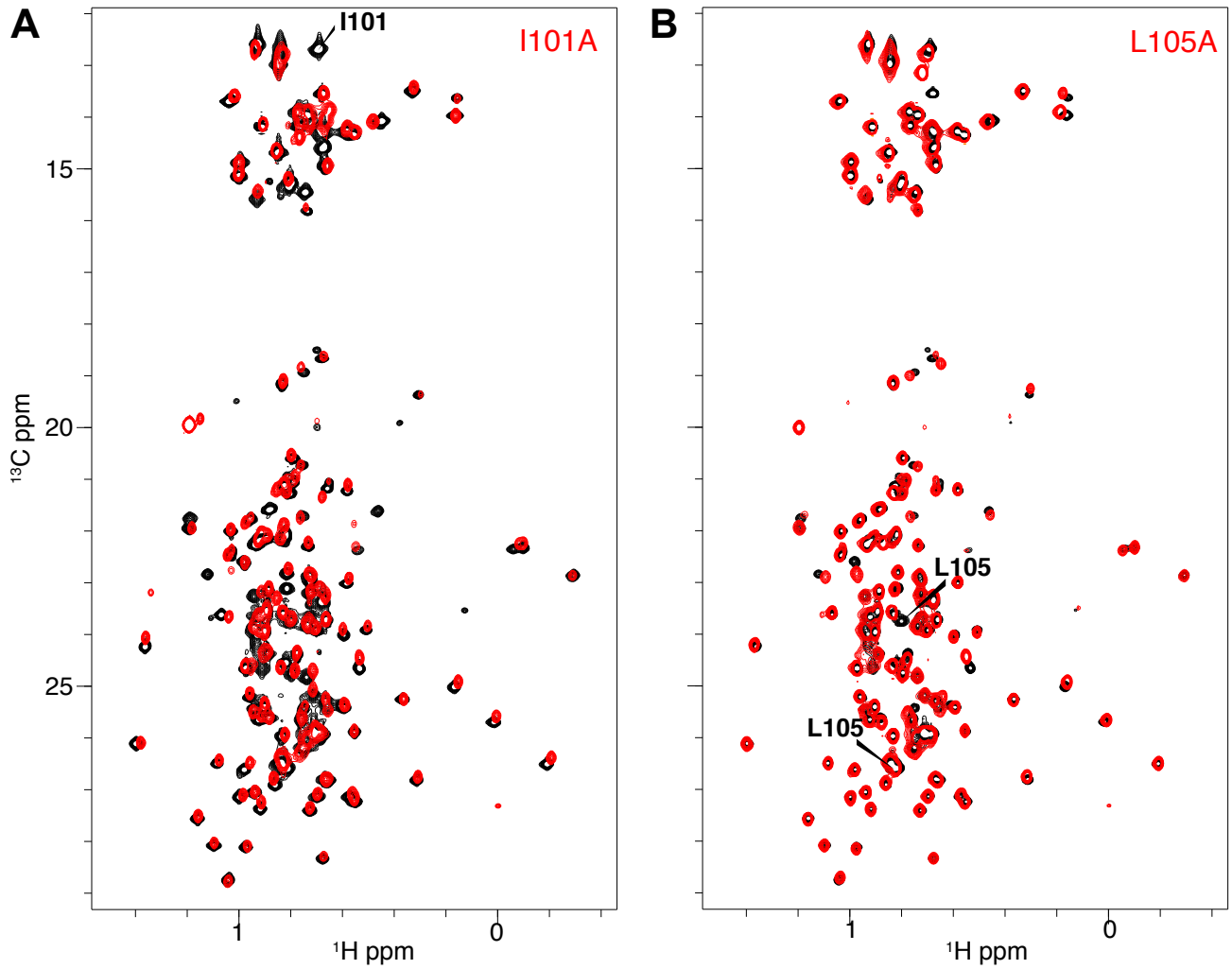

Figure 2.14. Overlay of 2D (^{13}C, ^{1}H) methyl TROSY HMQC spectra of wild type (black) and mutant (I101A, L105A) 0P-ERK2 (red).
(A) Spectra of I101A 0P-ERK2. (B) Spectra of I105A 0P-ERK2. Data were collected at 800 MHz and 25 °C on ILV methyl-protonated, U-[^{2}H,^{15}N] ERK2 samples. The resonances assigned as I101 and L105 were labeled. One of the L105 methyl peak with ^{13}C chemical shift at 27 ppm overlapped with other peaks.

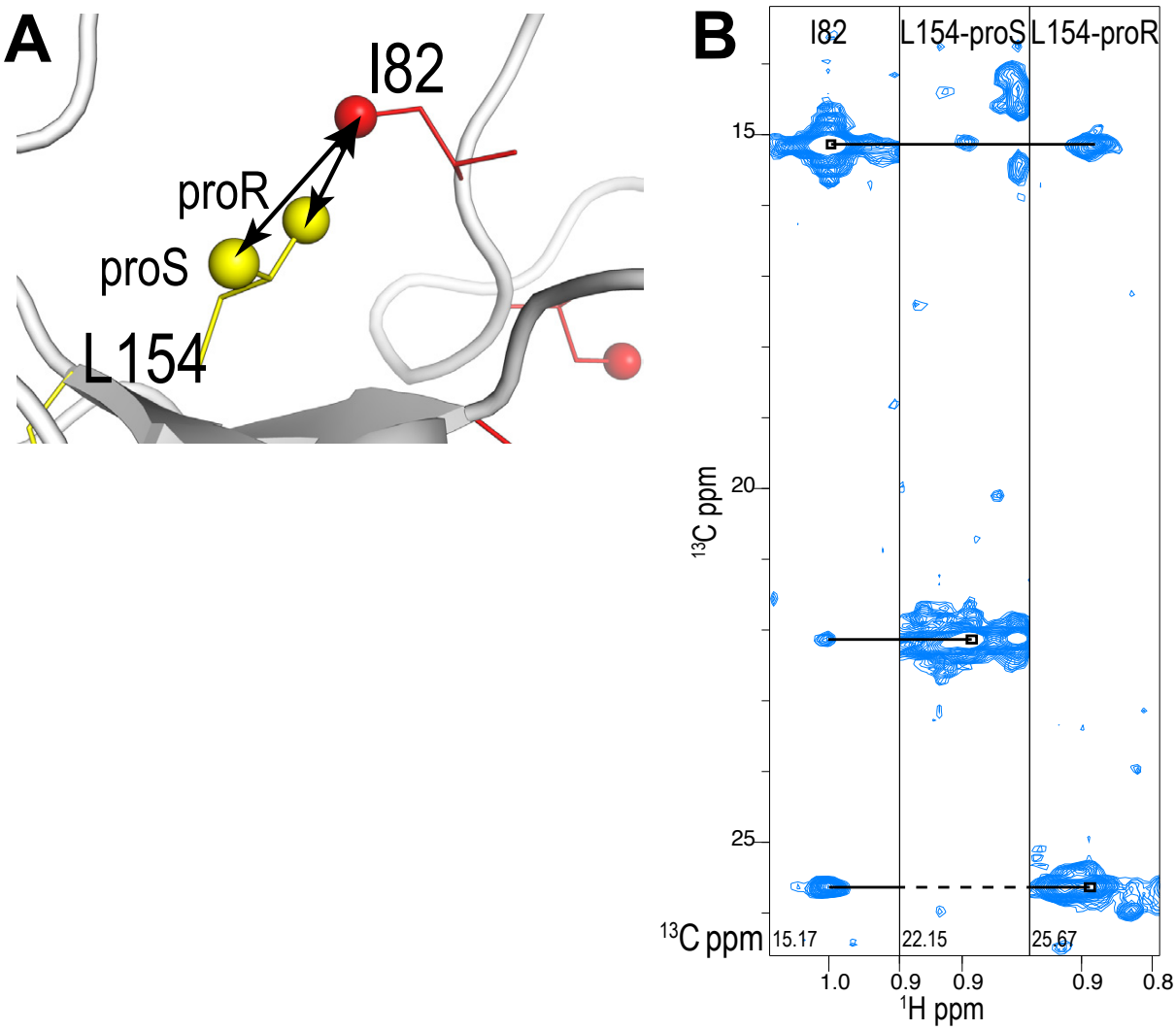

Figure 2.15. NOE and structural data used in the mapping and assignment of isolated Ile methyl I82. (A) The I82 region of the X-ray structure of 0P-ERK2 using the same color/labeling scheme as Figure 2.11. (B) Strip plots of 3D (^{13}C, ^{13}C, ^{1}H) HMQC-NOESY spectrum of 0P-ERK2 illustrating the NOEs used to make assignment for the methyls of I82 and L154.

2.3.5. Val/Leu Clusters Confirm Previous Mappings and Obtain More Mappings

V-V Clusters. After the analysis with Ile clusters, the next step is to utilize Val or Leu as starting points to confirm previous assignments or obtain more assignments. However, this often leads to tentative assignments due to the complexity of two methyls per L/V, and the high extent of predicted but missing NOE cross peaks that are probably due to weaker intensities of L/V compared with Ile. We began an analysis with V-V clusters because there were less Val than Leu (28 Val methyls *vs* 88 Leu methyls) in ERK2, thus it is more likely to identify a unique V-V cluster than a V-L or L-L cluster. For example, a Val methyl was observed to yield NOE to two methyls of the same Val residue, which turned out to be the only case of V-V NOE in ERK2 (Figure 2.16) and can be associated to V-V clusters (V47, V49, V102) or (V143, V171). V143 was pre-assigned in the analysis of isolated Ile, as a surrounding of I72. However, it didn't yield any NOE signal to other Val. Thus, the observed V-V NOE cross peaks was associated with (V47, V49, V102). These three methyl peaks were assigned to V47-proS and both methyls of V49 because none of them were missing in the 2D (^{13}C, ^{1}H) HMQC spectra of a V102A/Q103A mutant. In the structure, V49 is predicted to show NOE with both V47 and V102. However, we don't observe any NOE signal for the peaks that were tentatively assigned to V102 from the V102A/Q103A mutant. Also, V49 is predicted to show NOE with I51, but no V-I NOE was observed in any of the three Val methyls. This discrepancy might reflect a difference on the sheets β2 and β4 of N-terminal lobe between solution structure and X-ray structure.

V-L Clusters. After searching for V-V clusters, the analysis shifted to V-L clusters. We found a Leu methyl that shows NOEs to two methyls from two Val residues (Figure 2.9), which was associated with two V-L clusters: V212-L132/L135-V302 or V12/V16-L26-V19. Since V212 was pre-assigned as surrounding of I131-I215, this V-L cluster is mapped to V12/16-L26-V19. Methyls of L26 also showed NOE to two Ile methyls that were pre-assigned to I51 and I88, confirming the assignment of

I51-I88. Assignments of V12 (tentative), V16 (tentative) and V19 were obtained from qualitative comparison between the sizes of NOE and the distances to I51, I88 and L26.

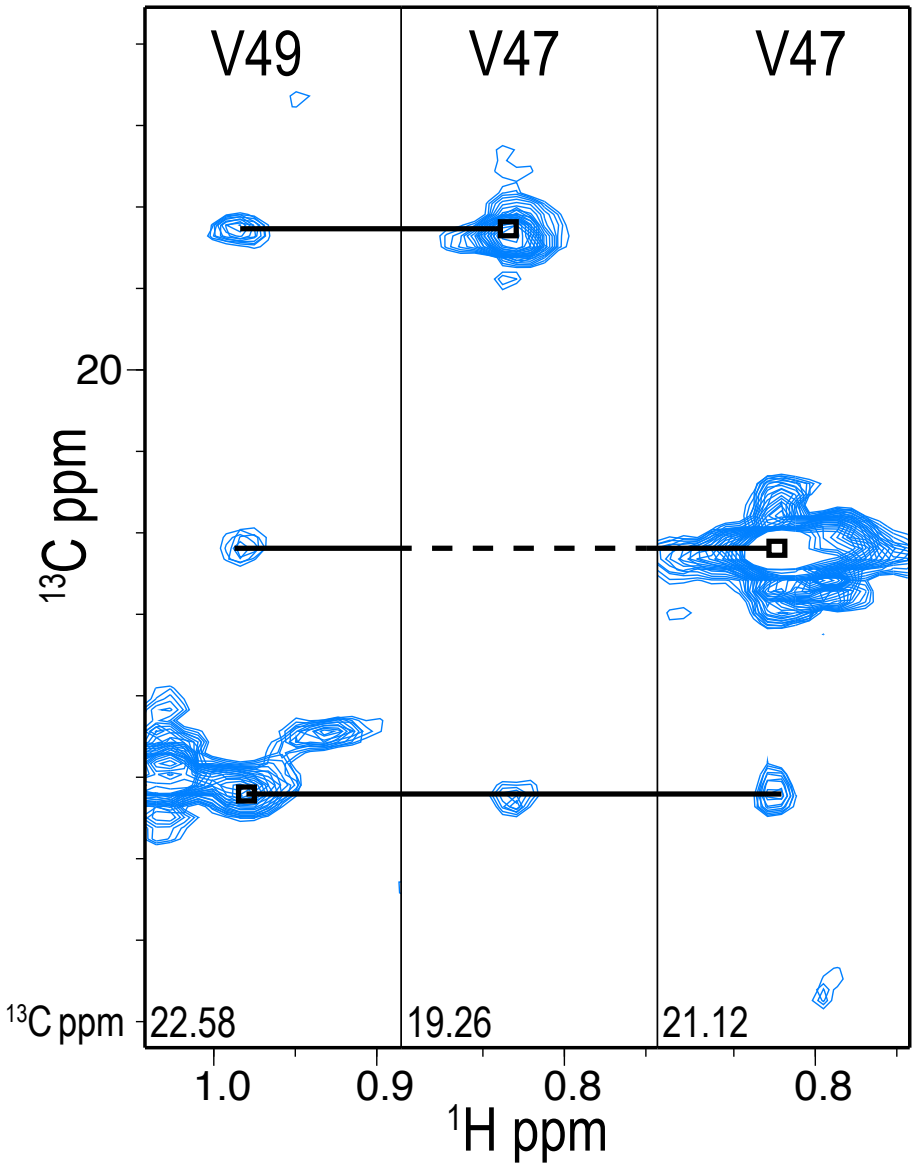

Figure 2.16. An example of a Val NOE cluster.
Strip plots of 3D (^{13}C, ^{13}C, ^{1}H) HMQC-NOESY spectrum of 0P-ERK2 illustrating the NOEs used to make assignment for the methyls of V47 and V49.

L-L Clusters. Leu methyls were enriched in three regions of ERK2: (1) β7-β8 region and αD-αE (DEJL motif binding site), extending to αF, αH and αI; (2) between αG and α1L14-α2L14 (MAP kinase insert); and (3) between αL16 and αC. Considering the large number of Leu methyls in ERK2 and their weaker intensity compared with Ile, the analysis of L-L clusters was set as the last step of the mapping procedure. Starting with the Leu clusters usually fall into a dead end due to lack of NOEs or unique NOEs, but the analysis of L-L clusters provides more assignments if it be expanded to a pre-assigned Ile/Val. For example, 8 unassigned Leu methyls build up NOE connectivity and 2 of them showed NOE to the pre-assigned I124. These were assigned to residues in αH and αI, including L128, L220, L306 (tentative) and L311 (tentative).

2.3.6. Assignments within Each Cluster

The observed and predicted methyl-methyl NOEs were next used to make sequence-specific resonance assignments in 0P-ERK2 (Figure 2.1C). A resonance of a unique residue type within a cluster is immediately assigned. For each methyl, a list of the NOE peak volumes was ranked from highest to lowest, and compared to a list of distances from other methyls in the cluster. The strongest NOE is assigned first to the methyl of shortest distance than weaker NOEs.

Example 1: 6-I Cluster. Assignment within each I-I NOE cluster was obtained by qualitative analysis of NOEs, including NOEs to and within the surrounding L/V methyls. The first step was assignment of methyls of a unique residue type. For example, two Val methyls in the 6-I cluster were assigned to V99 (Figure 2.17, Figure 2.18), the only Val residue in the cluster. Three Leu methyls showed NOEs to Ile methyls in 6-I cluster, and were associated with L74 and L67 (Figure 2.17). Since there were NOEs to more than one Leu residue, the second step was assignment of methyls with unique number or type of NOEs. Two of these Leu methyls were assigned to L74 because they showed NOEs to the same 3 Ile methyls in the cluster, but no NOEs to each other; consistent with the

prediction of NOEs from L74 to Ile methyls (Figure 2.18C, D). The third Leu methyl showed NOEs to only one Ile methyl, and was assigned to L67, which has a predicted NOE to I345 (and I70 for the pro-R methyl of L67) (Figure 2.18E, F).

The third step was qualitative analysis of NOE sizes with methyl-methyl distances. Here, methyls of V99, L74 and L67 were used as reference points for the comparison. Two Ile methyls showed strong NOEs to L74, but weak or no NOEs to the methyls of V99, indicating that they are close to L74 but farther from V99. Thus, these methyls were assigned to I84 and I87 (Figure 2.18A,B). The Ile methyl that showed stronger NOEs to the V99 methyls was assigned to I87, because I87 is closer to V99 than I84 (Figure 2.18A). This qualitative analysis was used to assign the remaining Ile methyls of the 6-I cluster. Similar NOE pattern was found in 2P-ERK2 (Figure 2.17C). The assignment of I101 resulted from this procedure was consistent with a missing I101 peak in the overlay of Ile region in 2D (^{13}C, ^{1}H) HMQC spectra of I101A and wild type ERK2 (Figure 2.14A), but several other peaks also showed significant changes in their chemical shifts. This general approach was then used to extend methyl resonance assignment to the rest of protein.

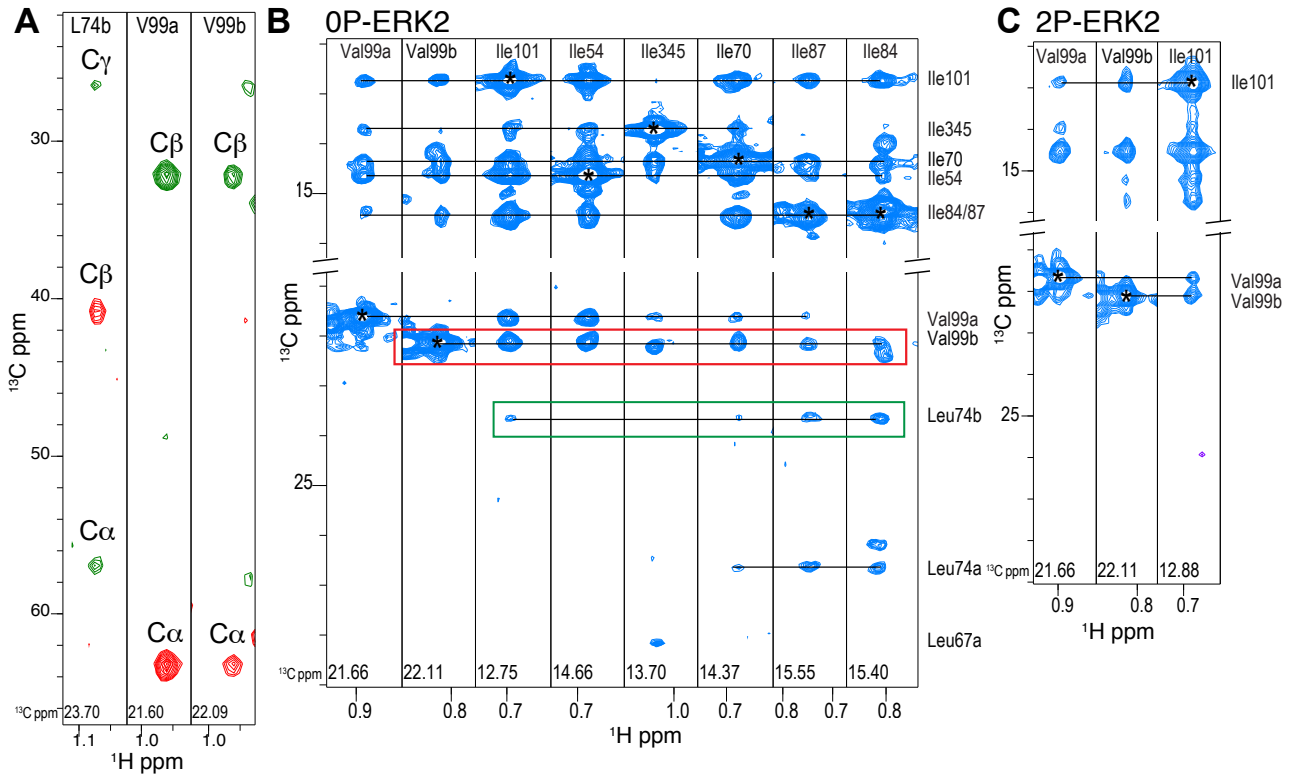

Figure 2.17. Assigning ILV methyls in the 6-I cluster.
(A) Through-bond intra-residue (HMCM[CG]CBCA) experiments allowed distinction of Val from Leu methyls. Strip plots [^{1}H, ^{13}C$_{aliph}$] of the 3D (^{13}C, ^{13}C, ^{1}H) HMCM[CG]CBCA spectra on a Ile (^{13}C$^{\delta}$H$_3$), Leu (^{13}C$^{\delta}$H$_3$,^{12}C$^{\delta}$D$_3$), Val (^{13}C$^{\gamma}$H$_3$,^{12}C$^{\gamma}$D$_3$) , and U-[^{15}N,^{13}C,^{2}H] sample of 0P-ERK2 acquired at 800 MHz at 25 °C, showing examples of Leu (L74) and Val (V99) residues. The chemical shifts (ppm) for the ^{13}C$_{methyl}$ dimension are labeled at the bottom of each strip. The signs of the peaks alternate as magnetization is transferred along the carbon chain (i.e. C$^{\alpha}$ is 180º out of phase with C$^{\beta}$ which is 180º out of phase with C$^{\gamma}$) as indicated by red and green contours. Val residues can be distinguished from Leu residues because the former only shows 2 carbon resonances (C$^{\alpha}$ and C$^{\beta}$) whereas the latter show 3 resonances (C$^{\alpha}$ and C$^{\beta}$ and C$^{\gamma}$). Both methyl groups in V99 share the same Cα and Cβ chemical shifts, which helps assign them to the same residue. (B) Strip plots [^{1}H, ^{13}C] from the 350 ms 3D (^{13}C, ^{13}C, ^{1}H) HMQC-NOESY spectrum of 0P-ERK2, illustrates that two Val methyl peaks (Val99a and Val99b) show NOEs to at least five Ile methyls (two of these Ile methyls have the same ^{13}C chemical shift). In addition, most of these Ile methyls show NOEs to each other. Three Leu methyl peaks, coming from at least two Leu residues, also show NOEs to a subset of the Ile methyls in this cluster. The chemical shifts (ppm) of the ^{13}C$_{methyl}$ dimension are labeled at the bottom of each strip and the asterisks highlight methyl self peaks. Cross peaks that were used in the assignment were aligned with the self-peak as indicated by the horizontal lines. Cross-peaks for V99b and L74b are highlighted in red and green boxes, respectively. (C) A similar pattern of NOE cross peaks is seen in 2P-ERK2; strip plots are shown only for NOEs between V99 and I101.

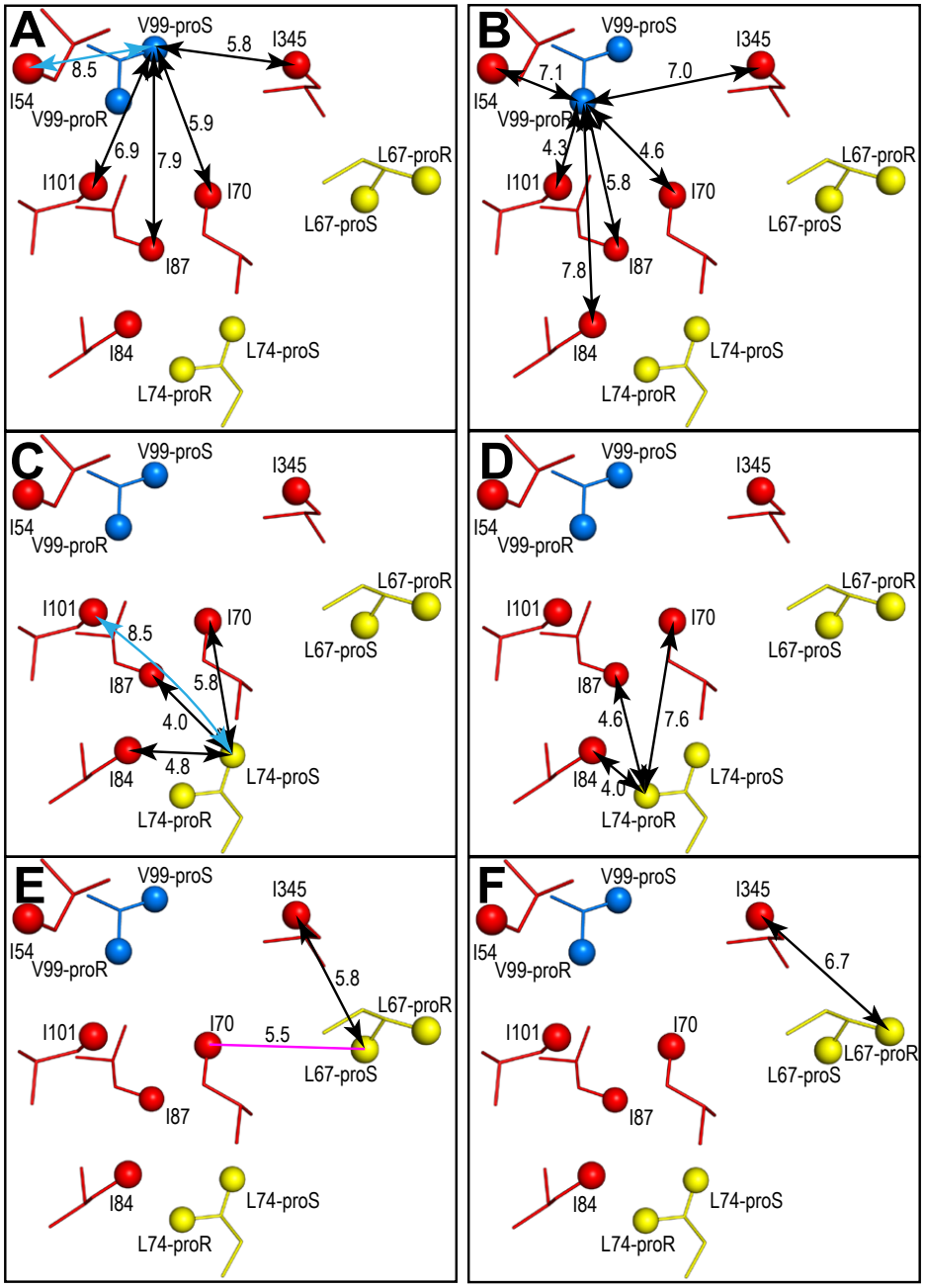

Figure 2.18. L/V surroundings of the 6-I cluster in the X-ray structure.
(A) V99-proS (blue sphere) is ≤ 7.1 Å to I70, I101, I345 (red spheres), and corresponding NOEs were observed (black arrow). The V99-proS methyl also showed NOE to I87 and I54 (blue arrows). The distances of the centers of two methyls from V99-proS to Ile in the 6-I cluster are labeled. Ile, Leu and Val side chains are colored in red (Ile), yellow (Leu) and blue (Val), with methyl groups highlighted with spheres. (B) V99-proR, which showed NOE to all the Ile in this Ile cluster, is ≤ 7.1 Å to all these Ile but I84 (7.8 Å). (C) L74-proS is ≤ 7.1 Å to I70, I84 and I87, and corresponding NOEs were observed. L74-proS also showed NOE to the next nearest Ile, I101. (D) L74-proS is ≤ 7.1 Å to I84 and I87, and corresponding NOEs were observed. L74-proS also showed NOE to the methyl of I70 (7.6 Å). (E) L67-proS is ≤ 7.1 Å to I70 and I345. The NOE of L67-proS to I70 was not observed (magenta line). (F) L67-proR is ≤ 7.1 Å to I345, and their NOE was observed.

Example 2: 3-I Cluster and I131-I215. The second largest Ile NOE-cluster is composed of 3 Ile, which yields NOE signal to each other based on 3D (^{13}C, ^{13}C, ^{1}H) NOESY (Figure 2.12A) and 3D (^{1}H, ^{13}C, ^{1}H) NOESY experiments (Figure 2.19). This 3-I NOE cluster was uniquely mapped to I81, I138, and I163 (Figure 2.12A). The methyl assignments of this 3-residue Ile cluster and a 2-residue Ile cluster I131-I215 were made together because they showed NOEs to the same Leu methyls (Figure 2.12A). The X-ray structure (Figure 2.12B) shows that methyls of L135, L148, L153, or L161 are in between the I131-I215 cluster and the 3-Ile cluster. One of these Leu methyls (L161) showed NOEs to 2 Ile methyls (I138, I163) in the 3-I cluster and 1 Ile methyl (I215) in the I131-I215 cluster (Figure 2.12). This leads to assignments of I215 and I131 in the I131-I215 cluster as well as assignment of I81. Another Leu methyl (L153) showed NOEs to 1 Ile methyl in 3-I cluster and both Ile methyls in I131-I215 (Figure 2.12), leading to assignments of I163 and I138.

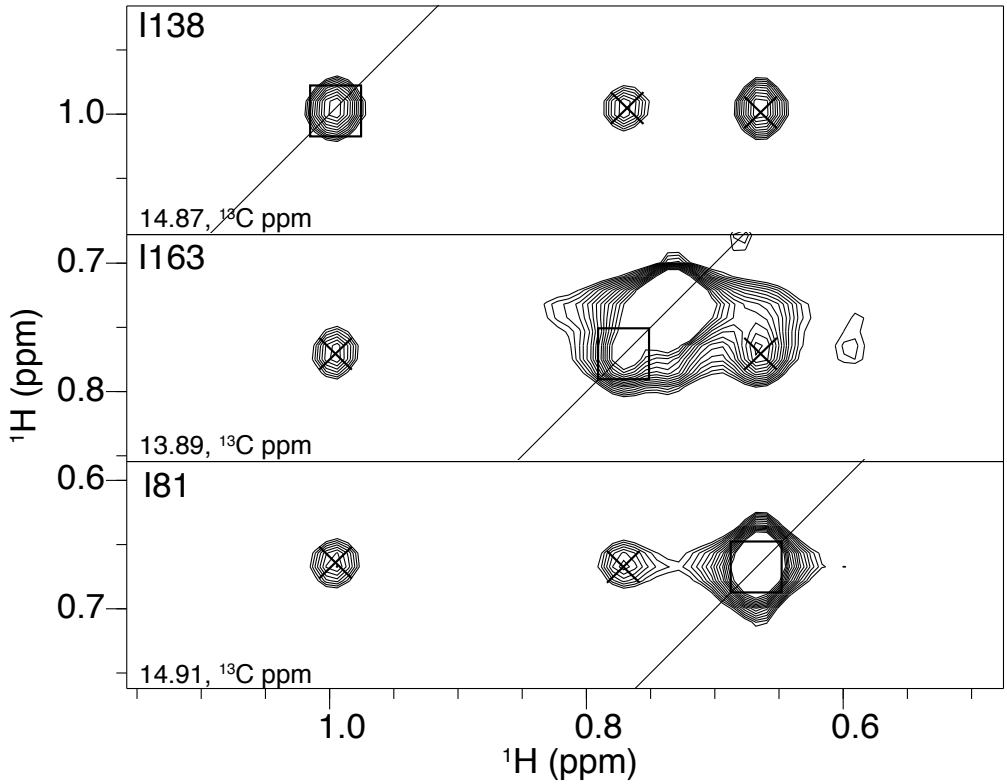

Figure 2.19. NOE data used in the mapping of I138, I163 and I81.
Strip plots from the 3D (^{1}H, ^{13}C, ^{1}H) HMQC-NOESY spectrum of 0P-ERK2 showing a 3-residue Ile-NOE cluster (I138, I163 and I81). Each methyl in this cluster shows NOEs to the other two Ile methyls, allowing mapping of this cluster on to the structure. Self peaks are marked with squares, cross peaks are marked with crosses, the oblique lines indicate equal chemical shifts in both ^{1}H dimensions.

Example 3: I225-I241 Pair. The methyl assignments of the I225-I241 cluster were obtained by qualitative analysis of NOEs (Figure 2.11A). The V residue close to this 2-residue I-I cluster has unique residue type and was assigned to V271. V271 and L276 methyls showed predicted and observed NOEs to each other, leading to the assignment of L276. The next step was assignment of the two Ile residues and, as seen in Figure 2.11, I225 has more predicted and predicted I-L/V NOE than I241. This assignment was confirmed by qualitative analysis of the NOE sizes where I225 and I241 both showed strong NOEs to L276 but I225 showed a weak NOE to V271 whereas I241 showed medium NOEs to V271. This is consistent with the structure, where I225 is more distant to V271 than I241 (Figure 2.11B). The V271 methyls only showed NOEs to I225, I241 and L276, consistent with their location in an isolated region of the protein. V271 is the only V in ERK2 that show predicted and observed NOE to 1 I and 1 L residue, reinforcing the assignment of I225-I241.

2.3.7. Single Site ILV Mutants Were Used to Confirm Resonance Assignments in 0P-ERK2

A set of 12 Ile, Leu or Val to Ala mutants of 0P-ERK2 was used to help confirm the methyl assignments obtained from the NOE data (Figure 2.20). In optimal cases, where there is little effect on the chemical shifts of other methyl resonances, a mutated I, L or V residue can be directly assigned from the loss of one (Ile) or two (Leu/Val) peak(s) in the 2D HMQC spectrum of the mutant when compared with the wild-type protein.[57] There was only one such case in 0P-ERK2 (I124A, Figure 2.20B) where unambiguous assignment could be confidently made solely from comparison of mutant and WT spectra. In most cases, the chemical shifts of other methyls were also perturbed by the mutation, and these spectra then represented additional data that complement the NOE- and structure-based resonance assignment procedure. For example, the overlay of the Ile region of the HMQC spectra of L161A and WT ERK2 (Figure 2.20C) showed significant chemical shift perturbations for the methyl resonances that had been assigned to I163, I131, and I215 based on NOE analysis. These perturbations are consistent with the X-ray structure (Figure 2.20D) where these 3 Ile methyls are in proximity to the L161 methyls. Thus, although mutants that only show loss of ILV methyl(s) with no perturbation of other methyls in their HMQC spectra are easy to interpret and directly lead to assignments, as illustrated by Boisbouvier and coworkers[57], mutants that show perturbations of other methyl resonances provide valuable information for structure-based assignment that complement the NOE data. The 2D HMQC spectral overlay of mutants and wild type 0P-ERK2 are listed in Figure 2.14, Figure 2.21, Figure 2.22, Figure 2.23, and Figure 2.24. The combined analysis of the HMQC spectra, NOE data, X-ray structure and mutagenesis led to confident resonance assignment for 60% of the ILV methyl resonances in 0P-ERK2 (Table 2.4), including 89% of Ile, 49% of Leu and 68% of Val methyls.

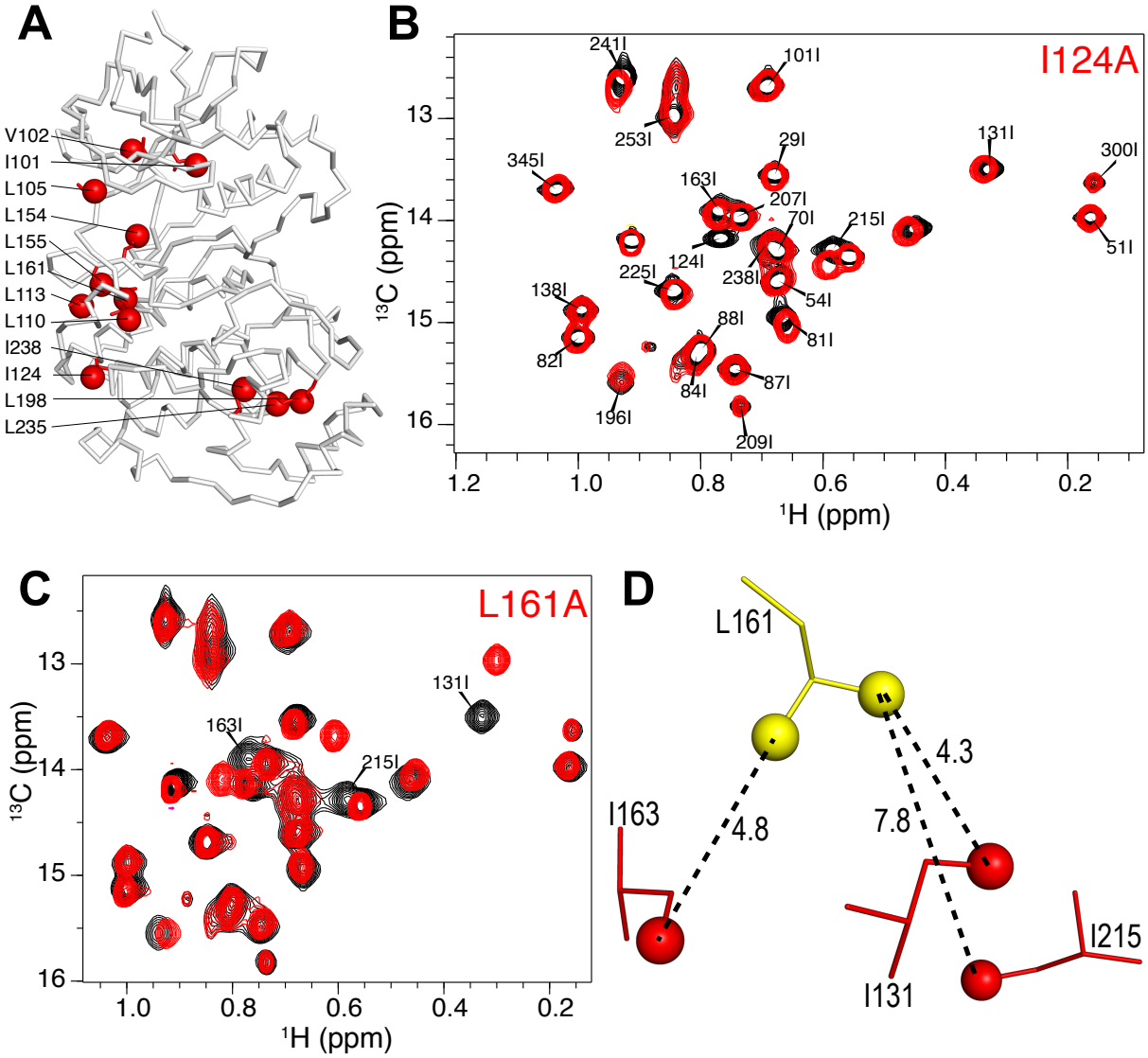

Figure 2.20. Ile, Val or Leu to Ala mutations used to confirm methyl assignments.
(A) Structure of ERK2 showing the sites of Ala mutations. The backbone is represented as a gray ribbon and side chains of mutation sites are shown in red with their methyls as spheres. (B) Overlay of the Ile region of the 2D (^{13}C, ^{1}H) HMQC spectra of mutant I124A (red) and wild-type 0P-ERK2 (black). The missing peak was unambiguously assigned to I124. (C) Overlay of the part of the Ile region of the HMQC spectra of mutant L161A (red) and wild-type 0P-ERK2 (black). Unambiguous assignment L161 methyls could not be made directly from these spectra because multiple Ile peaks (as well as Leu/Val peaks) showed chemical shift perturbations in the mutant. (D) The L161 region of the X-ray structure of 0P-ERK2 where the distances from the L161 methyl groups to nearby Ile methyls are shown.

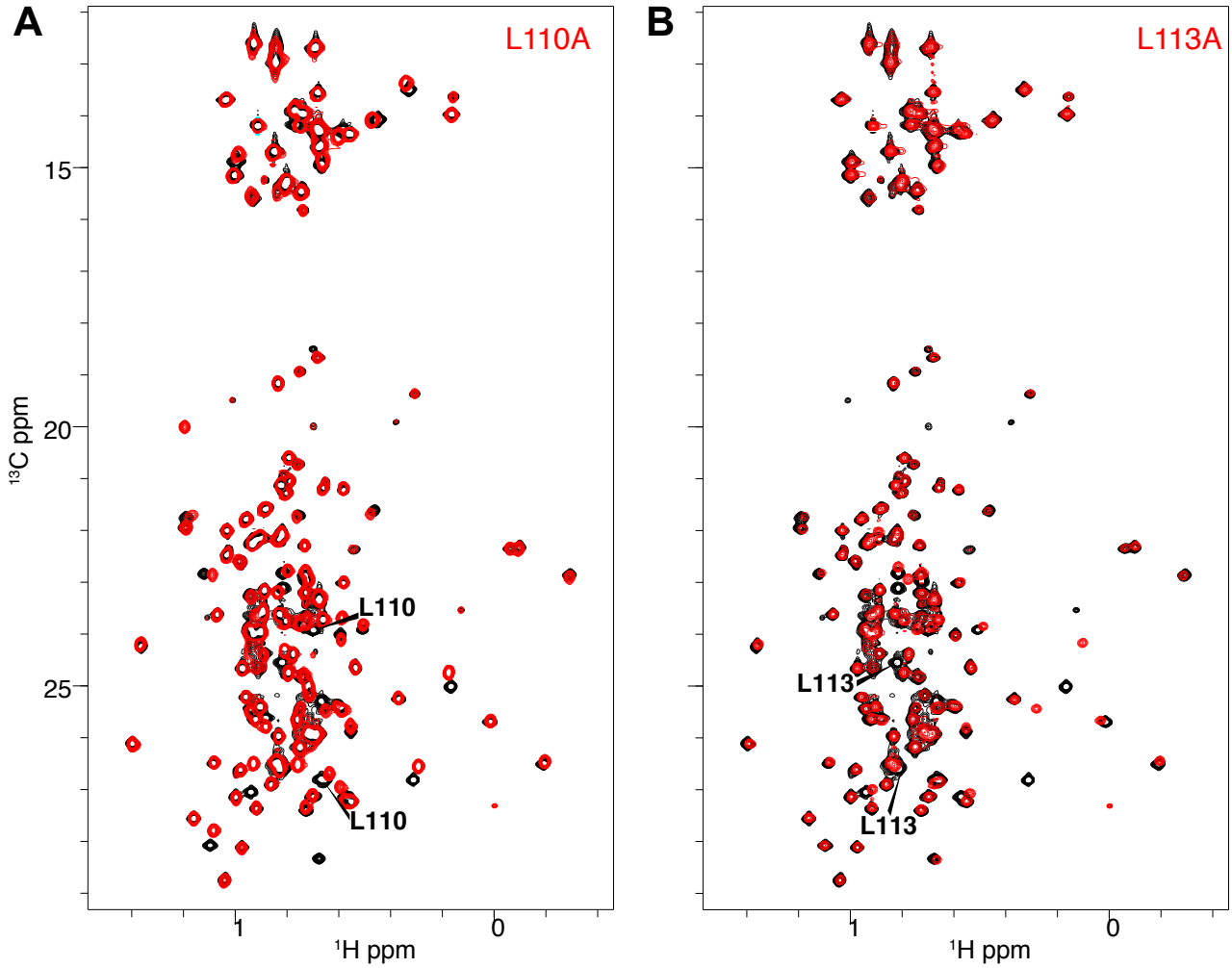

Figure 2.21. Overlay of 2D (^{13}C, ^{1}H) methyl TROSY HMQC spectra of wild type (black) and mutant (L110A, L113A) 0P-ERK2 (red).
(A) Spectra of L110A 0P-ERK2. (B) Spectra of L113A 0P-ERK2. Data were collected at 800 MHz and 25 °C on ILV methyl-protonated, U-[^{2}H,^{15}N] ERK2 samples. The resonances assigned as L110 and L113 were labeled.

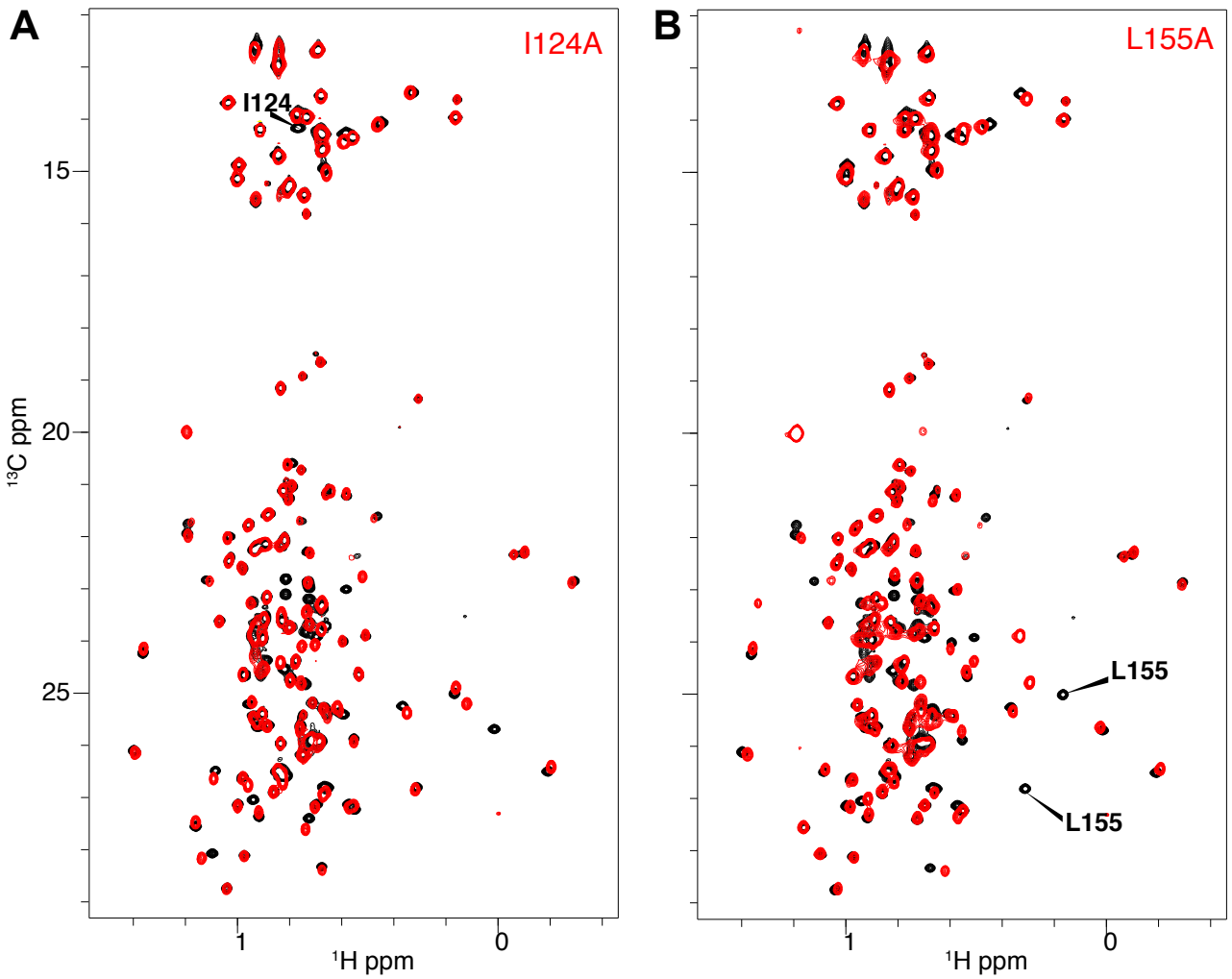

Figure 2.22. Overlay of 2D (^{13}C, ^{1}H) methyl TROSY HMQC spectra of wild type (black) and mutant (I124A, L155A) 0P-ERK2 (red).
(A) Spectra of I124A 0P-ERK2. (B) Spectra of L155A 0P-ERK2. Data were collected at 800 MHz and 25 °C on ILV methyl-protonated, U-[^{2}H,^{15}N] ERK2 samples. The resonances assigned as I124 and L155 were labeled.

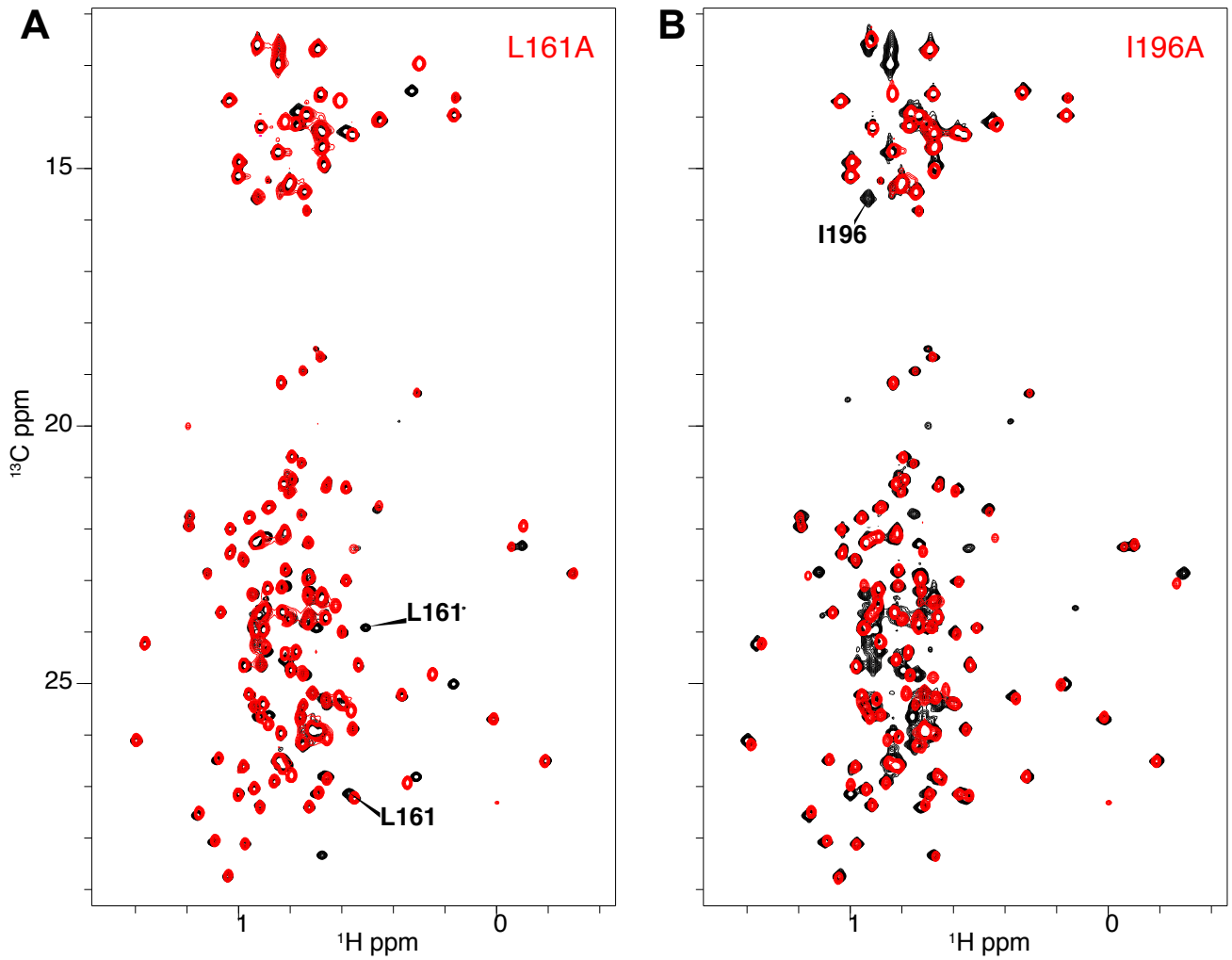

Figure 2.23. Overlay of 2D (^{13}C, ^{1}H) methyl TROSY HMQC spectra of wild type (black) and mutant (L161A, I196A) 0P-ERK2 (red).
(A) Spectra of L161A 0P-ERK2. (B) Spectra of I196A 0P-ERK2. Data were collected at 800 MHz and 25 °C on ILV methyl-protonated, U-[^{2}H,^{15}N] ERK2 samples. The resonances assigned as L161 and I196 were labeled.

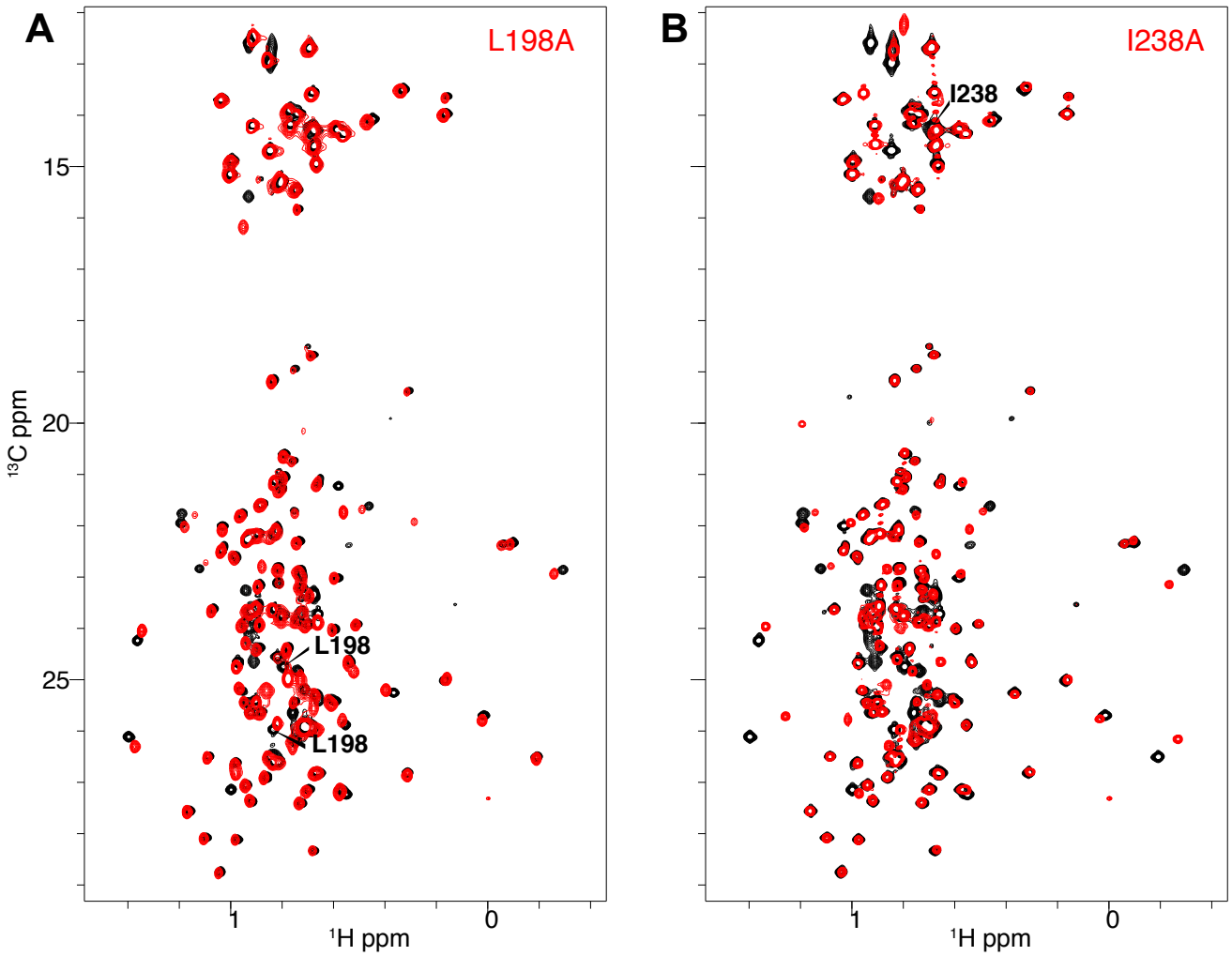

Figure 2.24. Overlay of 2D (^{13}C, ^{1}H) methyl TROSY HMQC spectra of wild type (black) and mutant (L198A, I238A) 0P-ERK2 (red).
(A) Spectra of L198A 0P-ERK2. (B) Spectra of I238A 0P-ERK2. Data were collected at 800 MHz and 25 °C on ILV methyl-protonated, U-[^{2}H,^{15}N] ERK2 samples. The resonances assigned as L198 and I238 were labeled.

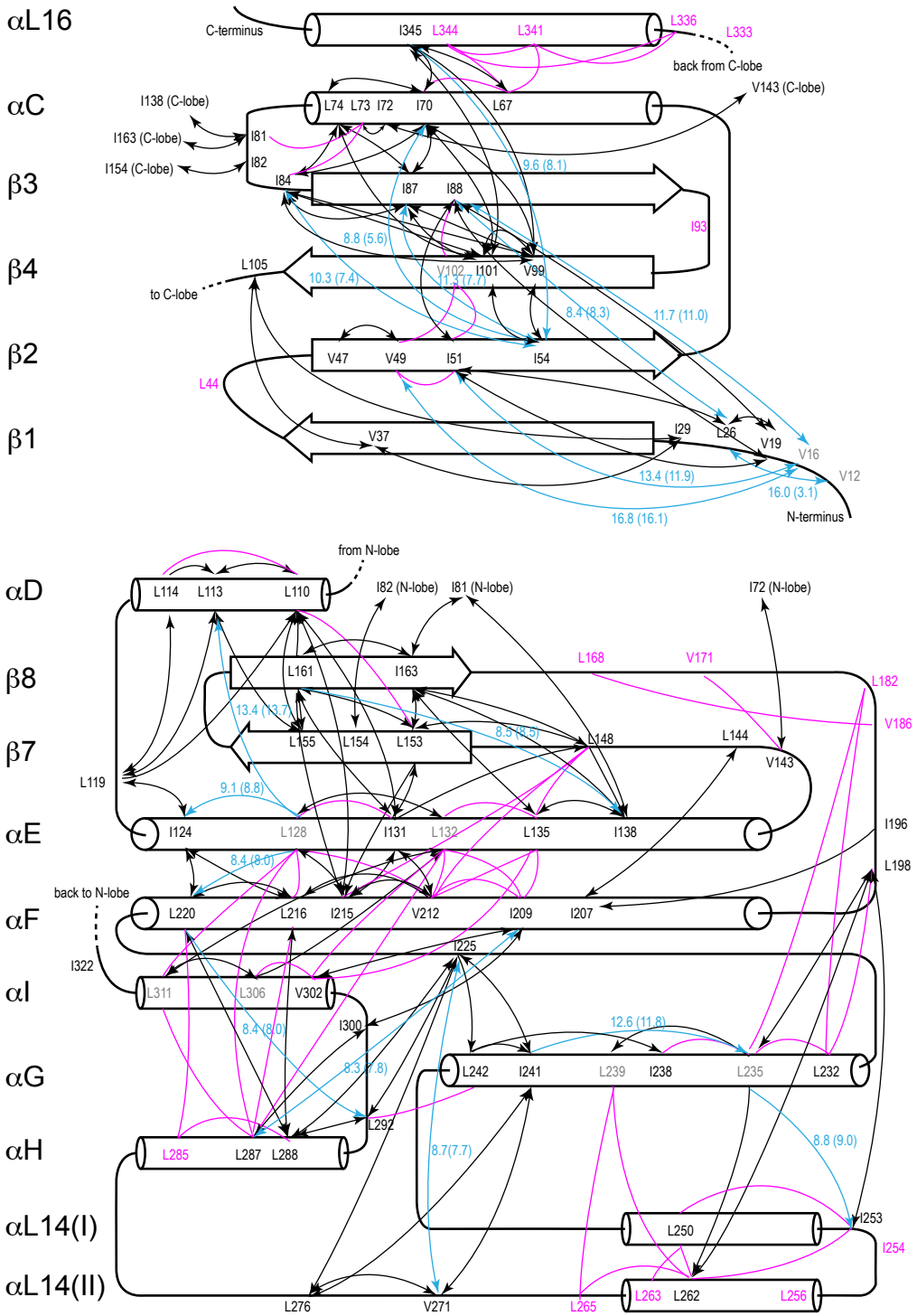

Figure 2.25. Observed and predicted NOE connectivities are mapped onto the topology diagram of ERK2. Methyls with predicted and observed NOEs in one (or both) directions are connected with single (or double)-headed arrows. Predicted but not observed NOEs are represented with a magenta connection. Observed but not predicted NOEs are represented with a blue connection and include inter-methyl distances measured in 0P-ERK2, with the distances for 2P-ERK2 in parentheses. Residues with at least one assigned methyl are in black. Residues with tentative assignments are in grey and unassigned residues are in magenta. The name of each secondary structure element is labeled on the left.

2.3.8. Resonance Assignments from 0P-ERK2 Were Transferred to 2P-ERK2

ILV methyl resonance assignments for 2P-ERK2 were obtained by transferring the assignments from 0P-ERK2 and were confirmed with NOE data from 3D NOESY spectra on 2P-ERK2. In 2P-ERK2, 137 out of 144 methyl resonances were observed and 80 of these were assigned (Figure 2.26, Table 2.4). Some resolved and assigned peaks in 0P-ERK2 were not observed in the HMQC spectrum of 2P-ERK2 possibly due to intermediate exchange between multiple conformations in the activated ERK2.[79] For example, a well-resolved Ile peak that was assigned as I196 was not observed in 2P-ERK2, although the volume of I196 was already small in 0P-ERK2 (about 10% of the peak of largest volume, Figure 2.28). Methyl chemical shift perturbations $|\Delta\delta|$ (in ppm) upon phosphorylation were also analyzed for the assigned residues in ERK2. From this analysis, we found that the chemical shift perturbations (in ppm) upon phosphorylation on ^{1}H dimension were significantly lower, almost negligible, comparing with the perturbation on ^{13}C dimension for most of the methyls (Figure 2.27). Thus, further analysis used the chemical shift difference on ^{13}C dimension, $|\Delta\delta^{13}C|$ (in ppm), as the reporter of local chemical environment change upon phosphorylation.

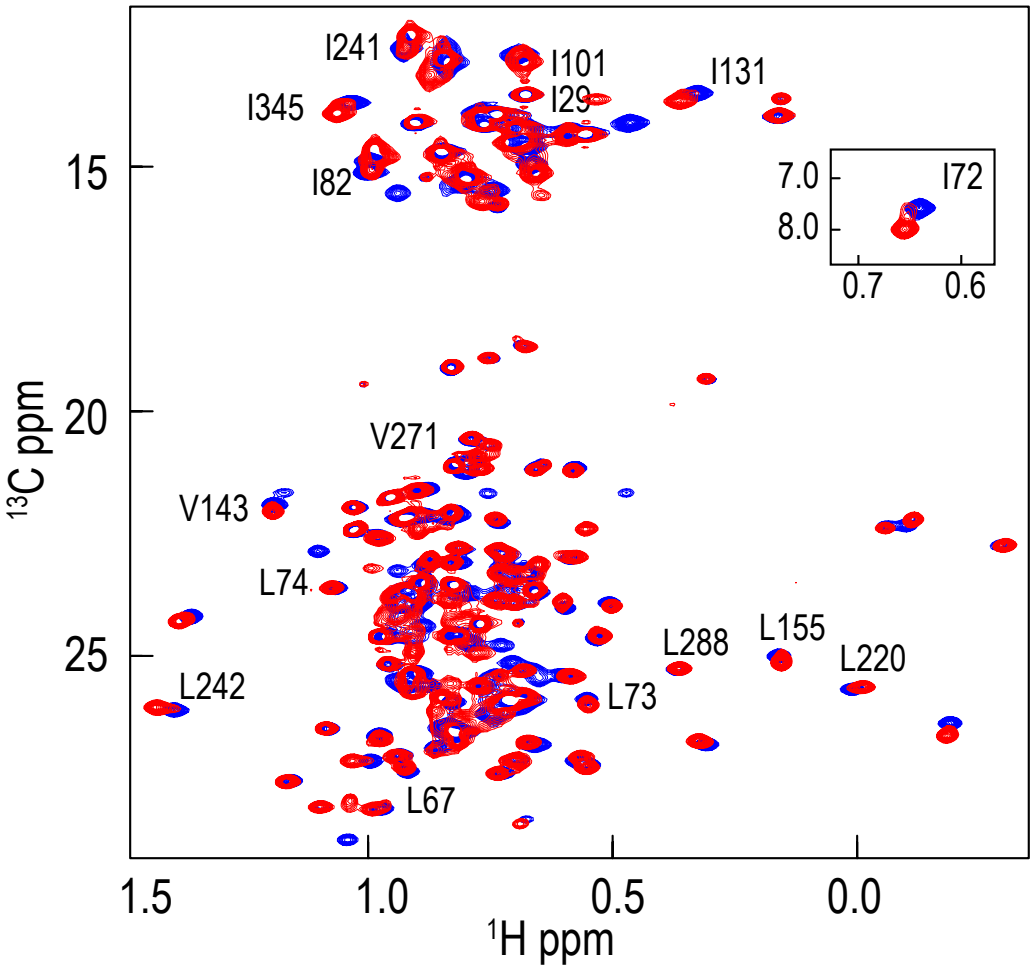

Figure 2.26. 2D (^{13}C, ^{1}H) HMQC spectra of ^{13}C ILV-methyl labeled 0P-ERK2 (blue) and 2P-ERK2 (red) recorded at 800 MHz and 25°C.

Table 2.4. ILV methyl assignments in 0P- and 2P-ERK2

	0P-ERK2		2P-ERK2									
Res ID	C^{methyl} (ppm)	H^{methyl} (ppm)	C^{methyl} (ppm)	H^{methyl} (ppm)	$\|\Delta\delta^{13}C\|$ (ppm)	$\|\Delta\delta^{1}H\|$ (ppm)	Notes	Mutant[c]	C^{β} (BB)[d]	C^{β} (Methyl)[e]	C^{α} (BB)[d]	C^{α} (Methyl)[e]
V12[a]	21.18	0.66	21.18	0.66	0.01	0.00	NOE - L26		33.29	33.89	61.22	61.50
V12[a]	22.18	0.92	22.19	0.92	0.00	0.00	NOE - L26		33.29	33.89	61.22	61.50
V16[a]	20.73	0.75	20.73	0.75	0.01	0.00	Same C_{aliph} as the other V16		31.61	31.31	63.02	61.28
V16[a]	19.37	0.31	19.33	0.31	0.04	0.00	I51-I88		31.61	31.31	63.02	61.28
V19	22.35	-0.06	22.38	-0.06	0.03	0.00	I51-I88		31.21	31.98	59.72	60.07
V19	18.94	0.75	18.92	0.75	0.02	0.00	I51-I88		31.21	31.98	59.72	60.07
L26	24.66	0.53	24.61	0.53	0.05	0.01	I51-I88		41.47	41.94	54.85	55.12
L26	25.89	0.72	25.85	0.71	0.04	0.01	I51-I88		41.47	41.94	54.85	55.12
I29	13.55	0.68	13.55	0.68	0.00	0.00	I29-V37-L105	L105A	38.54	38.87	62.37	62.63
V37	21.24	0.80	21.22	0.77	0.02	0.03	I29-V37-L105	L105A	32.79	33.39	60.65	60.86
V37	21.02	0.79	20.95	0.77	0.07	0.02	I29-V37-L105	L105A	32.79	33.39	60.65	60.86
V47	21.07	0.82	21.17	0.82	0.10	0.00	V47-V49	V102A			58.50	58.83
V47	19.16	0.83	19.14	0.84	0.02	0.00	V47-V49	V102A			58.50	58.83
V49	18.67	0.68	18.68	0.68	0.01	0.00	V47-V49	V102A				
V49	22.60	0.98	22.62	0.98	0.02	0.00	V47-V49	V102A				
I51	13.97	0.16	13.94	0.16	0.03	0.00	I51-I88					
I54	14.60	0.67	14.50	0.70	0.09	0.03	6-Ile cluster	I101A				
L67	28.12	0.97	28.10	0.98	0.02	0.01	6-Ile cluster		40.02	42.02	57.56	N.A.
I70	14.30	0.67	14.41	0.68	0.11	0.01	6-Ile cluster	I101A				
I72	7.58	0.58	7.99	0.61	0.41	0.03	I72-L73-V143, ^{13}C chemical shift					
L73	25.88	0.55	26.00	0.55	0.12	0.00	I72-L73-V143					
L73	22.88	0.73	22.83	0.73	0.04	0.01	I72-L73-V143					
L74	23.62	1.07	23.62	1.08	0.01	0.01	6-Ile cluster				56.42	56.96
L74	26.62	0.98	26.70	0.98	0.08	0.00	6-Ile cluster				56.42	N.A.
I81	14.94	0.67	15.13	0.66	0.18	0.01	3-Ile cluster				60.46	60.63
I82	15.15	1.00	14.68	0.99	0.47	0.01	I82-L154	L154A				
I84	15.33	0.81	15.23	0.79	0.10	0.02	6-Ile cluster				61.72	N.A.
I87	15.49	0.75	15.71	0.77	0.22	0.02	6-Ile cluster	I101A			60.60	60.84
I88	15.27	0.80	15.22	0.79	0.05	0.01	I51-I88 pair		40.15	40.62	59.71	59.97
V99	22.08	0.82	22.05	0.83	0.03	0.01	6-Ile cluster				60.50	60.78
V99	21.60	0.88	21.62	0.90	0.03	0.02	6-Ile cluster				60.50	60.78
I101	12.70	0.69	12.86	0.68	0.16	0.01	6-Ile cluster	I101A				
V102[a]	22.83	1.11	N.A.[b]				mutagenesis	V102A /Q103 A			60.96	62.36
V102[a]	21.68	1.18	N.A.[b]				mutagenesis	V102A /Q103 A			60.96	62.39
L105	23.75	0.80	23.90	0.84	0.15	0.04	I29-V37-L105	L105A				
L105	26.60	0.82	26.74	0.82	0.14	0.00	I29-V37-L105	L105A				
L110	23.93	0.70	23.91	0.70	0.01	0.00	Expanding[f] I131-I215	L110A				
L110	26.80	0.67	26.75	0.67	0.06	0.01	Expanding I131-I215	L110A				
L113	24.55	0.82	24.58	0.83	0.04	0.01	Expanding I131-I215	L113A			58.14	58.37
L113	26.60	0.82	26.55	0.82	0.05	0.00	Expanding I131-I215	L113A			58.14	N.A.
L114	23.67	0.92	23.65	0.92	0.02	0.00	Expanding I131-I215				55.82	
L119	27.05	0.94	27.06	0.94	0.01	0.01	Expanding I131-I215, I124-NOE	I124A	42.38	42.7	54.07	54.27
L119	23.11	0.82	23.18	0.83	0.07	0.01	Expanding I131-I215, I124-NOE	I124A	42.38	42.7	54.07	N.A.
I124	14.17	0.77	14.08	0.77	0.09	0.00	Expanding I131-I215, I225-I241	I124A			65.91	66.15

Table 2.4. ILV methyl assignments in 0P- and 2P-ERK2 (Continued)

	0P-ERK2		2P-ERK2									
Res ID	C^{methyl} (ppm)	H^{methyl} (ppm)	C^{methyl} (ppm)	H^{methyl} (ppm)	$\|\Delta\delta^{13}C\|$ (ppm)	$\|\Delta\delta^{1}H\|$ (ppm)	Notes	Mutant[c]	C^{β} (BB)[d]	C^{β} (Methyl)[e]	C^{α} (BB)[d]	C^{α} (Methyl)[e]
L128[a]	22.81	0.81	22.80	0.81	0.01	0.00	L-L cluster					
I131	13.50	0.33	13.64	0.36	0.14	0.03	I131-I215					
L132[a]	27.40	0.73	27.42	0.73	0.02	0.01	L-L cluster					
L135	24.02	0.59	23.92	0.60	0.10	0.01	I131-I215					
I138	14.88	0.99	14.80	0.98	0.07	0.02	3-Ile cluster					
V143	21.95	1.19	22.05	1.20	0.10	0.00	I72-L73-V143				N.A.	67.04
V143	23.88	0.94	23.81	0.95	0.07	0.01	I72-L73-V143				N.A.	67.05
L144	22.30	0.73	22.21	0.74	0.09	0.01	I196-I207				51.92	N.A.
L148	22.33	-0.10	22.20	-0.12	0.13	0.02	I131-I215					
L153	28.33	0.68	28.40	0.69	0.07	0.01	I131-I215					
L153	25.29	0.67	25.28	0.68	0.01	0.01	I131-I215					
L154	25.62	0.88	25.77	0.91	0.15	0.03	I82-L154	L154A			54.70	N.A.
L154	22.12	0.89	22.41	0.90	0.29	0.01	I82-L154	L154A			54.70	N.A.
L155	26.82	0.31	26.73	0.33	0.08	0.02	I131-I215	L155A			53.10	N.A.
L155	25.01	0.17	25.11	0.16	0.10	0.00	I131-I215	L155A			53.10	53.53
L161	23.92	0.51	23.99	0.50	0.07	0.01	I131-I215	L161A				
L161	27.13	0.67	27.08	0.56	0.05	0.11	I131-I215	L161A			62.01	62.17
I163	13.90	0.77	13.97	0.77	0.07	0.00	3-Ile cluster				62.01	62.17
I196	15.55	0.94	N.A.[b]				I196-I207	I196A				
L198	25.97	0.83	25.88	0.85	0.09	0.02	Expanding I225-I241	L198A				
L198	24.75	0.79	24.61	0.82	0.14	0.02	Expanding I225-I241	L198A				
I207	13.97	0.74	13.94	0.74	0.03	0.00	I196-I207	I196A				
I209	15.83	0.73	15.76	0.73	0.06	0.00	I209-I300					
V212	23.20	0.72	23.27	0.73	0.07	0.01	Expanding I131-I215					
V212	24.38	0.89	24.49	0.91	0.11	0.02	Same C_{aliph} as the other V212					
I215	14.28	0.58	14.36	0.59	0.08	0.01	I131-I215 pair					
L216	23.02	0.58	22.99	0.58	0.03	0.01	I124-NOE	I124A				
L220	22.98	0.72	22.96	0.72	0.02	0.00	I124-NOE	I124A			56.44	56.15(?)
L220	25.70	0.01	25.65	-0.01	0.04	0.02	I124-NOE	I124A			56.44	N.A.
I225	14.69	0.85	14.74	0.85	0.05	0.00	I225-I241					
L232	22.38	0.54	22.45	0.56	0.07	0.03	Expanding I225-I241					
L235[a]	27.15	1.00	27.17	1.03	0.02	0.03	Expanding I225-I241	L198A, L235A, L238A				
L235[a]	25.65	0.76	25.65	0.77	0.00	0.01	Expanding I225-I241	L198A, L235A, L238A				
I238	14.22	0.69	14.24	0.70	0.02	0.01	Expanding I225-I241	L198A, L235A, L238A				
L239[a]	23.27	0.94	23.25	0.99	0.02	0.04	Expanding I225-I241					
I241	12.57	0.93	12.31	0.91	0.26	0.01	I225-I241				61.88	66.05
L242	26.11	1.40	26.06	1.43	0.05	0.03	I225-I241				56.50	N.A.
L242	24.24	1.36	24.31	1.39	0.07	0.02	I225-I241				56.50	N.A.
I253	13.13	0.87	12.88	0.84	0.25	0.04	Expanding I225-I241				59.59	N.A.
L262	25.40	0.90	25.42	0.92	0.02	0.01	Expanding I225-I241				57.62	N.A.
L262	23.92	0.90	23.80	0.91	0.12	0.01	Expanding I225-I241				57.62	58.13
V271	20.60	0.79	20.56	0.79	0.04	0.00	I225-I241				59.30	59.62
V271	22.00	1.03	22.00	1.04	0.01	0.00	I225-I241				59.30	59.60
L276	25.91	0.71	25.95	0.71	0.04	0.00	I225-I241				56.09	56.35

Table 2.4. ILV methyl assignments in 0P- and 2P-ERK2 (Continued)

	0P-ERK2		2P-ERK2									
Res ID	C^{methyl} (ppm)	H^{methyl} (ppm)	C^{methyl} (ppm)	H^{methyl} (ppm)	$\lvert\Delta\delta^{13}C\rvert$ (ppm)	$\lvert\Delta\delta^{1}H\rvert$ (ppm)	Notes	Mutant[c]	C^{β} (BB)[d]	C^{β} (Methyl)[e]	C^{α} (BB)[d]	C^{α} (Methyl)[e]
L276	23.72	0.66	23.66	0.66	0.06	0.00	I225-I241				56.09	56.36
L287	23.54	0.13	23.51	0.12	0.02	0.00	Expanding I225-I241					
L288	25.26	0.36	25.24	0.36	0.01	0.00	Expanding I225-I241					
L288	26.51	-0.19	26.60	-0.19	0.10	0.00	Expanding I225-I241					
L292	27.24	0.55	27.28	0.55	0.04	0.00	Expanding I225-I241					
I300	13.63	0.16	13.60	0.15	0.03	0.00	I209-I300				62.29	N.A.
V302	19.91	0.38	19.87	0.38	0.05	0.00	I209-I300				66.69	N.A.
L306[a]	25.65	0.92	25.59	0.91	0.06	0.01	L-L cluster					
L306[a]	27.14	0.70	27.12	0.70	0.02	0.01	L-L cluster					
L311[a]	26.49	1.08	26.48	1.09	0.01	0.00	L-L cluster					
L311[a]	27.56	1.16	27.57	1.17	0.00	0.01	L-L cluster					
I345	13.70	1.04	13.91	1.06	0.21	0.03	6-Ile cluster	I101A			65.69	N.A.

[a]Residues in italics are tentative assignments as a result of insufficient distance constraints or mutagenesis that induced chemical shift perturbation of multiple methyls.
[b]Assignment was not available in 2P-ERK2 because the resonance was not observed or not resolved.
[c]Mutants that help confirm the assignment from a shifted/unobserved peak.
[d]The C^{β} and C^{α} values from the backbone assignments of ERK2 reported by the Ghose group[59].
[e]The C^{β} and C^{α} values from the "out-and-back" experiments of ERK2.
[f]Methyls that were noted as "expanding a I-I cluster" have no direct NOE to these Ile methyls, and can be assigned by propagation of NOEs from these Ile methyls.

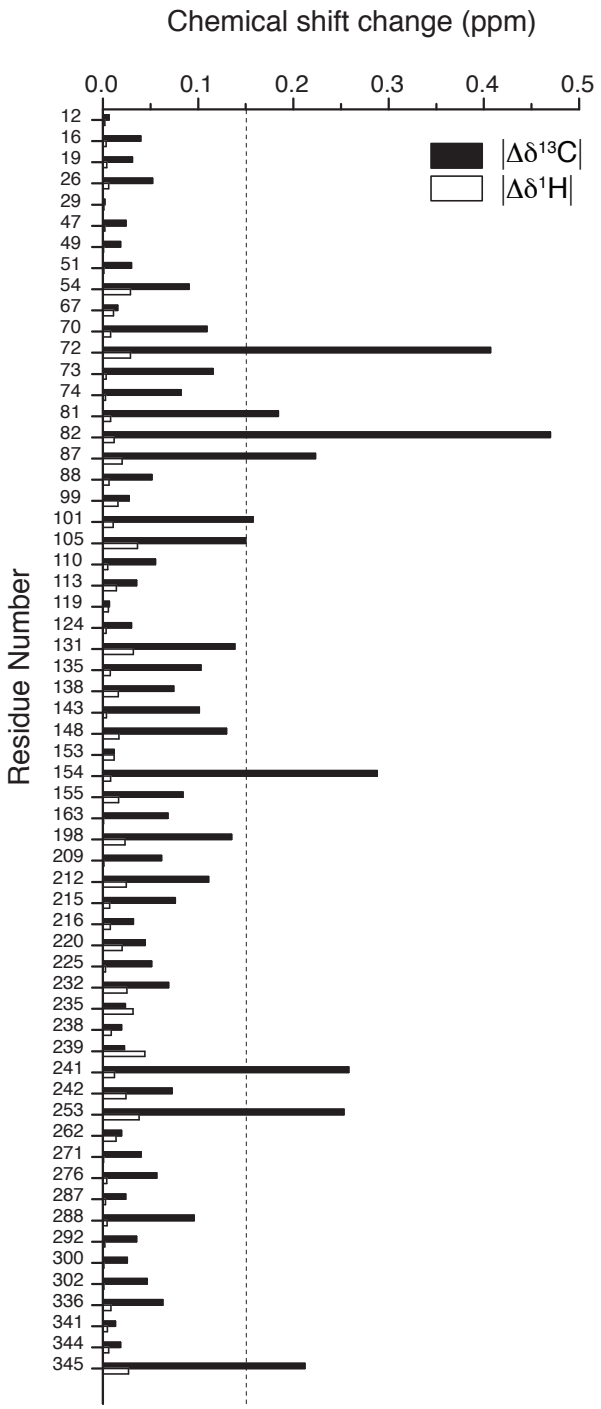

Figure 2.27. Changes in chemical shifts and chemical environment between 0P-ERK2 and 2P-ERK2.
Plot of the changes in carbon $|\Delta\delta^{13}C|$ (solid bars) and proton $|\Delta\delta^{1}H|$ (open bars) chemical shifts for the assigned methyl groups in 0P- and 2P-ERK2. The dashed line indicates a threshold of $|\Delta\delta| = 0.15$ ppm, which highlights methyls with the largest chemical shift changes induced by phosphorylation.

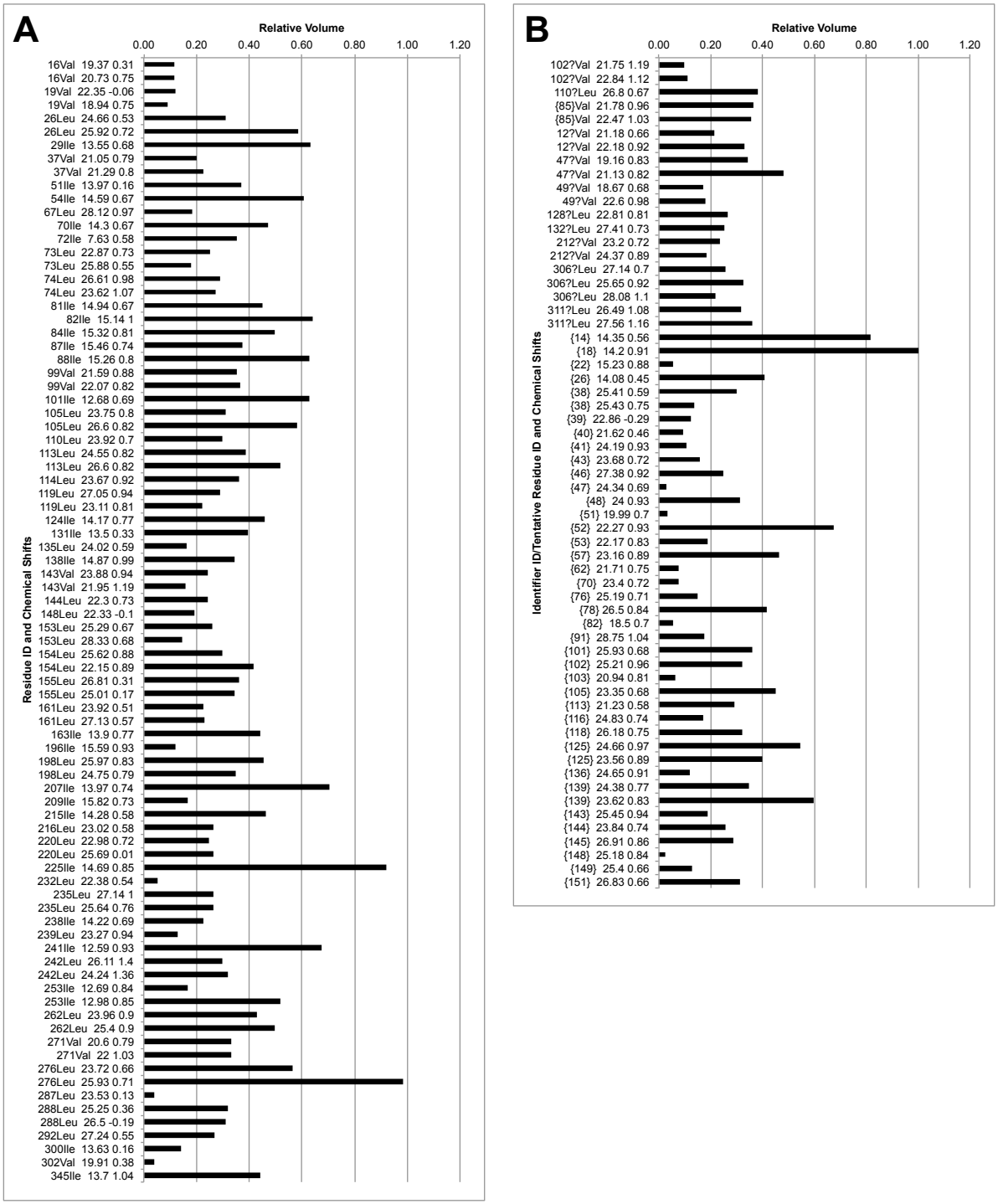

Figure 2.28. Peak volume variation among methyls in a representative 2D (^{13}C, ^{1}H) HMQC spectra of 0P-ERK2. (A) Relative peak volumes for assigned methyls. Assigned methyls were labeled with the assignment and chemical shifts of ^{13}C and ^{1}H dimensions. (B) Relative peak volumes for tentatively assigned or unassigned methyls. The volume of each peak was normalized to the peak of largest volume. Tentatively assigned methyls were labeled with the tentative assignment with a question mark and chemical shifts of ^{13}C and ^{1}H dimensions. The unassigned methyls were labeled using an arbitrary number within pair of curly brackets and chemical shifts of ^{13}C and ^{1}H dimensions.

2.3.9. Structural Mapping of Chemical Shift Perturbation on 2P-ERK2 vs 0P-ERK2

The differences in ^{13}C-methyl chemical shifts between 0P- and 2P-ERK2 (in ppm), $|\Delta\delta^{13}C|$, provide a sensitive probe of changes in local environment. Eight residues showed significant chemical shift differences between the two forms of ERK2, ranging between 0.15-0.47 ppm, whereas 16 residues showed moderate changes, ranging between 0.1-0.15 ppm (Figure 2.27, Figure 2.29A). Two of the three residues with largest $|\Delta\delta^{13}C|$ were I82 and L154 (0.47 and 0.29 ppm, respectively), which interact with the hinge that links the N- and C-terminal domains. L154 is located in the β7-strand, and I82 is located in the αC-β4 loop. These form hydrophobic contacts with each other as well as with M106 at the hinge (Figure 2.29B). Large chemical shift changes at these residues were surprising, given their distance from the site of phosphorylation. The X-ray structures showed no significant conformational differences between 0P and 2P-ERK2 around these residues (Figure 2.29B). Significant $|\Delta\delta^{13}C|$ were also observed at I72 near the ATP binding site in helix αC; I241 in helix αG; and I253 in the MAPK insert (0.41, 0.26, 0.25 ppm, respectively). Other residues with measurable $|\Delta\delta^{13}C|$ are shown in Figure 2.27. Based on the X-ray structures, chemical shift changes were expected in the activation loop and C-terminal L16 loop, but could not be determined due to incomplete assignments. Overall, the NMR chemical shift data reported significant changes in the chemical environment of ILV methyl side chains at the hinge, the ATP binding site, and MAPK insert, upon phosphorylation of ERK2.

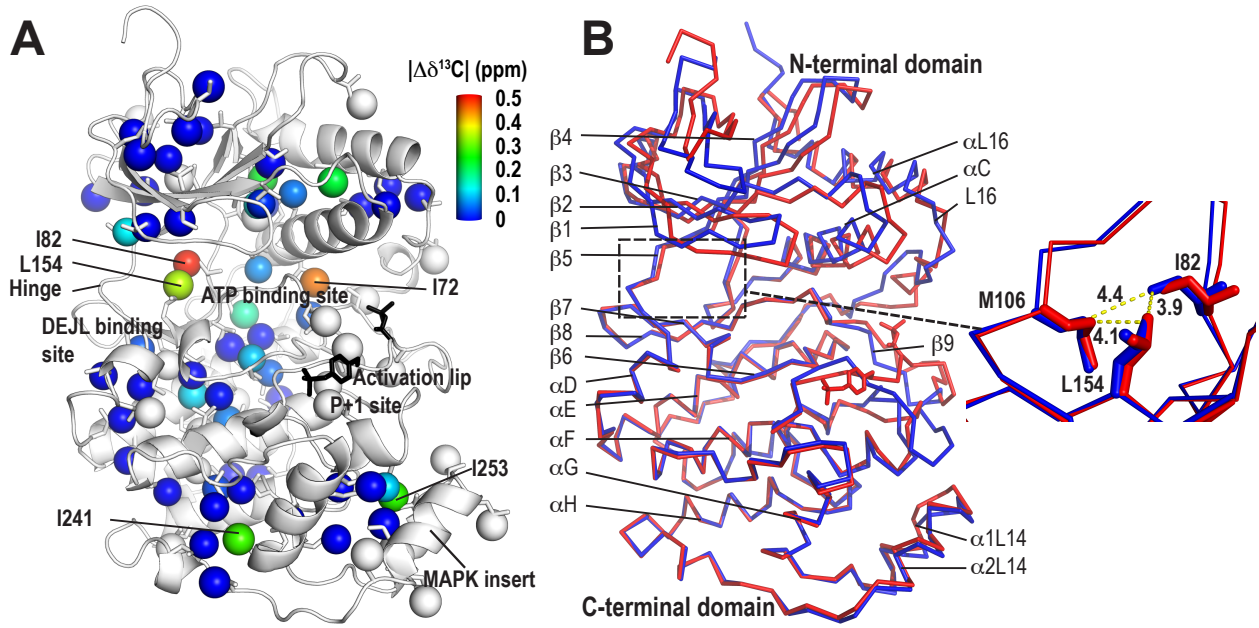

Figure 2.29. ERK2 phosphorylation induces chemical shift changes at the hinge region.
(A) X-ray structure of 0P-ERK2 (PDB:1ERK) showing spheres representing positions of ILV methyls, with ^{13}C chemical shift differences ($|\Delta\delta^{13}C|$) between 0P-ERK2 and 2P-ERK2 indicated by the color scale (also see Figure 2.27). Unassigned ILV methyls are represented by white spheres. (B) Structural alignment of 0P-ERK2 (blue) and 2P-ERK2 (red). The expansion shows that the side chains of L154 and I82, which have two of the largest $|\Delta\delta^{13}C|$ (see (B)), form hydrophobic interactions with each other and with M106 at the hinge. Structure images were prepared using PYMOL (**www.pymol.org**).

2.4. Discussion

The ability to understand the detailed mechanism of action of proteins usually requires the combination of both structural and biochemical information. In many cases, analysis of the biochemical data with only static X-ray structures does yield insight into the mechanism. This is because static structures are often blind to conformational dynamics required for activity of many proteins, especially enzymes. Thus, there are a growing number of examples where X-ray structures are complemented with experimental or theoretical techniques that probe protein motions, such as NMR relaxation experiments or molecular dynamic simulations.[92-94] For studies of dynamics by NMR, the bottleneck is often resonance assignment, especially as the size of the protein increases. Here we report a structure-based strategy that yielded assignment of ~60% of the ILV methyl resonances in inactive (0P-) and active (2P-) ERK2. Two perdeuterated and selectively ILV $^{13}C^{1}H_3$-methyl labeled samples of 0P-ERK2 were used, one for determining methyl residue type using through-bond correlation experiments and the other for collecting methyl-methyl NOE data. The approach here employs a hierarchical analysis of the predicted and observed methyl "NOE-clusters", where NOEs involving Ile methyls are analyzed first followed by Ile-Val, Ile-Leu, etc. (Figure 2.1).

2.4.1. Methyl Assignments of ERK2 through a "Hierarchical Search of Uniqueness"

The first step in the structure-based ILV-methyl assignment procedure is identification of methyl type. A 2D (^{13}C, ^{1}H) HMQC spectrum was used to determine the number of resolved methyl resonances and also to distinguish Ile $C^{\delta 1}$ methyls from Leu/Val methyls based on the distinctive ^{13}C chemical shifts of the Ile $C^{\delta 1}$ methyl resonances. For a larger protein, there are often fewer methyl peaks than expected, due to resonance overlap. Overlapping peaks can often be identified by collecting spectra at different temperatures or by analysis of the NOE patterns, both of which were used here for ERK2. The Leu and Val methyl resonances were next distinguished using through-bond information

such as HMCMCBCA or HMCM[CG]CBCA experiments,[56] which correlate the Leu or Val methyl resonances with their other side chain carbon resonances (Figure 2.3). The identification of residue type is a key component of the NOE-cluster-based assignment process. In 0P-ERK2, all the Ile $C^{\delta 1}$ methyl resonances and 89% and 70% of the Val and Leu methyl resonances, respectively, were identified by residue type, with low signal-to-noise usually being the limiting factor in identification. If higher percentage of residue-type identification for the ILV methyls is required, methyl correlation experiments can be employed that direct magnetization to a single C^{γ}, C^{β}, or C^{α} resonance leading to higher single-to-noise.[95] In favorable cases, it is possible to identify methyl groups belonging to the same Leu or Val residue based on the chemical shifts of aliphatic carbon resonances. For 0P-ERK2, ~53% of methyl groups (86% of V, 43% of L) that belong to the same residue were unambiguously paired based on HMCMCBCA experiment. If higher-resolution structural information is desired, stereospecific assignments for the methyl groups of Leu or Val can be obtained using procedures that that employ chirally-labeled precursors[72, 96] or partial ^{13}C enrichment.[97] Methods for efficient $^{13}C^{1}H_3$ labeling of Ala, Met, and/or Thr methyls have also been developed, which give additional NOE data and more NMR probes.[49, 50, 54, 55, 98]

Structure-based assignment procedures have a long history in protein NMR. One of the earliest examples was the main-chain-directed assignment procedure developed by Englander & Wand in 1987 where patterns of ^{1}H-^{1}H NOEs in 2D NOESY spectra were compared with distances predicted for secondary structure motifs derived from a set of X-ray structures.[66] The two protons in the NOEs were also identified by atom type: H^{N}, H^{α} or H^{β}. The structure-based methods were largely replaced by triple-resonance hetero-nuclear through-bond correlation experiments with the advent of efficient procedures for production of $^{13}C/^{15}N$-labeled proteins. These through-bond experiments eliminate the ambiguities inherent in through-space NOE connectivities. Thus, triple-resonance backbone

assignment experiments on $^{13}C/^{15}N$-labeled proteins are generally the method of choice for resonance assignment of small-to-medium sized proteins. However, faster relaxation leading to poor magnetization transfer and therefore low signal-to-noise limits the application of the triple resonance backbone assignment experiments. Thus, structure-based assignment methods are being more commonly used for studies of larger proteins with known structures or for studies on homologous or mutant proteins.

The current structure-based methods for assignment of methyl groups are conceptually similar to the original main-chain-directed procedure; however, there have been tremendous experimental, algorithm and computational improvements, which allow larger and more complex systems to be studied. NOE distance data still represent the primary type of experimental data for structure-based assignments, because a complete set of NOE-derived methyl-methyl distance data can be obtained using a single perdeuterated, $^{13}C^{1}H_3$-labeled sample. Deuteration helps reduce ^{1}H-^{1}H spin-diffusion, which further simplifies the analysis of the NOE data in larger proteins. The NOE data are most valuable when there is a high density of methyl groups, such as on the interior of protein but are less useful for residues on the surface where fewer methyl-methyl NOEs are observed. For example, 70% of ILV methyls on the hydrophobic interior of ERK2 were assigned (Accessible Surface Area or ASA < 1 Å^2) whereas only 50% of the partially exposed methyls (ASA > 9 Å^2) and 20% of the highly exposed methyls (ASA > 30 Å^2) were assigned. One of the disadvantages of using NOE data is that there is generally no reference point from which to begin making unambiguous assignments. The hierarchical approach employed here helps to overcome this issue by mapping uniquely sized methyl-methyl NOE clusters onto the X-ray structure.

In addition to NOEs, other structural information such as PREs,[74] pseudocontact shifts,[99] stereospecific assignments for chiral centers,[73, 74] residual dipolar couplings[100] and chemical shifts[69]

have been used in structure-based methyl assignment methods. The PRE distance data are a natural complement to the methyl-methyl NOEs, where the paramagnetic label is usually placed on a surface residue where the bulky nitroxide or metal is less likely to perturb the structure. In addition, the spin-label then represents a known reference point in the structure, allowing assignment of isolated methyls (especially surface exposed methyls) where no methyl-methyl NOE is observed. The PRE data can therefore provide a unique starting point for resonance assignment; this is extremely helpful in reducing the combinatorial problem inherent in structure-based methyl assignments, as discussed below.

One of the major challenges for structure-based assignment of methyls is that for proteins with large numbers of methyls (>100) the problem becomes computationally intractable and therefore it is not possible to exhaustively search all possible combinations of methyl resonance assignments. Thus, various mathematical methods that have been applied to help overcome this problem including: graph theory, fuzzy math/logic, nuclear vector representation, clustering algorithms and probabilistic techniques.[68, 69, 71, 73, 74, 100-103] A number of programs have been developed for automated structure-based assignment of methyl resonances, including MAP-XS (II)[69, 73], FLAMEnGO(2.0)[71, 74] and a PRE-based program[104]. These programs first all employ residue-type identification to reduce the complexity of the search and then employ NOE and/or PRE constraints as their primary experimental data. To identify residue types, MAP-XS and FLAMEnGO employ through-bond techniques similar to the approaches used here. The PRE-based program[104] did not employ through-bond assignment methods for distinguishing methyl-type, instead 3 samples were prepared where only the methyls on Ile, Ala, or Met residues were $^{13}C^{1}H_3$-labeled. Once methyls have been identified by residue-type, the next step is comparison of predicted distances with the experimental short-range (NOE) or long-range (PRE) distance information. The highest agreement between distance constraints and the structure is

assumed to be the best assignment, or in some programs this is a set of possible assignments. However, even assuming complete residue-type identification, a complete search is computationally impossible (e.g. ERK2 has at least $N_{res}(I)! \times N_{res}(L)! \times N_{res}(V)! = 28! \times 44! \times 14! = 10^{95}$ possible assignments even if methyls were only assigned to individual residues). Therefore various approaches are used to reduce the size of the search. The most common way is to introduce known assignments, which not only reduces the size of the search but also provides reference points for performing fragment searches where only a subset of the structure is searched. The NOEnet program[101] utilizes a complementary strategy that reduces the complexity of the search by ruling out impossible assignments (instead of the more common approach of introducing unambiguous assignments). This approach yields an ensemble of assignments that are consistent with the experimental data and structure. The search process in NOEnet is further simplified by a fragmentation approach involving analysis of the largest networks first, similar to the hierarchical clustering approach employed in this study. As discussed above, the hierarchical analysis here eliminates the brute force search of all possible assignments by instead mapping the largest (e.g. I-I) cluster onto the structure, which can then be used as unique starting point to extend assignments.

We attempted to make assignments of ERK2 using both MAP-XSII and FLAMEnGO, but not the PRE-based program (because we did not collect any PRE data) or NOEnet (because it is not yet set up for methyl groups and therefore has issues with stereospecific assignments of the Val/Leu methyl-methyl NOEs). Our input to the former programs included a chemical shift list of methyl resonances of ERK2 from 2D (^{13}C, ^{1}H) HMQC spectra with the identified residue types, a chemical shift list predicted from the program CH3shift,[70] a protonated structure of ERK2 (PDB 1ERK) and a list of (^{13}C, ^{13}C, ^{1}H) NOEs. Twenty trials were performed on each of these programs using distance cutoff of 8.0 Å. The five trials with best scores yielded a low percentage (<20%) of confident assignment, indicating

a low-level of convergence for the methyls assignment. Thus, we did not pursue further structure-based assignment with these automated programs.

2.4.2. Long Range Chemical Shift Perturbation upon Phosphorylation of ERK2

Phosphorylation is a common post-translation modification that regulates multiple cellular signaling events, usually through controlling enzyme activities. Thus, the conformational perturbation induced by phosphorylation, which may provide mechanism for the enzyme activation, has been of broad interest. The activity of ERK2 relies on the dual-phosphorylation at the activation loop. Here, we showed that phosphorylation induced significant chemical shift perturbations on methyls around the hinge (Figure 2.29A), 20 Å away from the sites of phosphorylation, based on the partial assignments of methyls in 0P- and 2P-ERK2. Because only partial assignment was obtained on ERK2 and no methyl is assigned on the activation loop, we don't know if these perturbations on the hinge are the largest throughout the structure. However, this significant chemical shift perturbation detected using solution NMR was not reflected in the structural overlay of side chains around the hinge from crystal structures of 0P- and 2P-ERK2 (Figure 2.29B). Instead, the crystal structure overlay of 0P- and 2P-ERK2 showed most evident conformational perturbation on the activation loop, where the phosphoryl groups on the activation loop form inter- and intra-domain ion pairs with Arg side chains. In contrast to the long-range perturbation observed on the phosphorylation of ERK2, previous solution NMR study on a phosphocarrier protein HPr from Bacillus subtilis showed only localized structural changes upon phosphorylation [105]. Further study in Chapter 3 using NMR relaxation experiment may provide some insights on how the dual-phosphorylation (and maybe formation of ion pairs) of ERK2 induces such long-range perturbations.

2.5. Summary

This study describes a hierarchical approach that simplifies the structure-based methyl assignments of proteins. The approach identifies methyl type and then compares observed methyl-methyl NOEs with those predicted from the X-ray structure. The NOE-methyl clusters of specific type are identified, and if this cluster is unique it is mapped onto the structure. This approach provided 60% of Ile, Leu and Val methyl assignments of the MAP kinase ERK2. The assignments were then used to study binding of a docking-motif peptide from substrate and ATP analog to both inactive and active ERK2. Although the approach here was applied to assignments of Ile, Leu and Val methyls, it is applicable to proteins with selective methyl labeling of other residues. The approach here relies on observation of methyl-methyl NOEs, thus it is most useful for assignment of methyls on the interior of the protein, since there are generally fewer methyl-methyl NOEs on the protein surface. PRE[104] and/or mutagenesis[57] of surface methyls could be used to complement the NOE data to obtain higher percentage of assignments. The hierarchical cluster-type analysis employed here is amenable to automation and could be incorporated into existing structure-based assignment programs.

Chapter 3. ERK2 Conformational Dynamics upon Activation

3.1. Introduction

3.1.1. Structural Changes of ERK2 upon Activation

ERK2 can be activated by MAP kinase kinases 1 and 2 (MKK1, 2) through dual phosphorylation of Thr and Tyr residues located at the activation loop (Thr183 and Tyr185, numbered in rat ERK2) [106, 107]. Phosphorylation at both sites is required for kinase activation, resulting in increased phosphoryl transfer rate and enhanced affinity for ATP and substrate [31].

Conformational changes accompanying the activation of ERK2 have been documented by X-ray structures of the inactive, unphosphorylated (0P-ERK2) and the active, dual-phosphorylated (2P-ERK2) forms [32, 33]. Phosphorylation rearranges the activation loop, leading to new ion-pair interactions between pThr and pTyr residues and basic residues in the N- and C-terminal domains of the kinase core structure. This leads to a repositioning of active site residues surrounding the catalytic base, enabling recognition of the Ser/Thr-Pro sequence motif at phosphorylation sites, and exposing a recognition site for interactions with docking sequences in substrates and scaffolds [34].

3.1.2. Motions at the Hinge Are Regulated upon Activation of ERK2

Less is known about how changes in internal motions contribute to kinase activation. Previous studies using hydrogen-exchange mass spectrometry (HX-MS) and electron paramagnetic resonance spectroscopy [81, 108, 109] led to a model where conformational mobility at the hinge linking the N- and C-terminal domains is increased by phosphorylation, therefore releasing constraints needed for activation. Such a model differs from other types of autoinhibitory mechanisms in protein kinases, which involve interactions with domains outside the kinase core [110, 111]. However, how the hinge flexibility regulates ERK2 is unknown.

3.1.3. Millisecond Conformational Exchange Measured using NMR CPMG Experiments

NMR relaxation dispersion methods enable protein dynamics to be monitored by measuring exchange between conformational states [93]. In particular, Carr-Purcell-Meiboom-Gill (CPMG) relaxation dispersion experiments report on motions on slow (100-2000 s^{-1}) timescales [37], which are often important for enzymatic function [37, 112-114]. In the CPMG experiment, exchange between different conformational states is probed with varying times between "refocusing" pulses. Conformational exchange leads to imperfect refocusing, thus decreasing the intensity of the NMR signal. Increasing the pulse frequency allows less chance for conformational exchange between pulses, and therefore increased NMR signal intensity. For a given pulse frequency, analysis of the signal intensity yields the effective relaxation rate for the resonance, $R_{2,eff}$. This is typically plotted as a relaxation dispersion curve, which can be fit to a two-state exchange process (e.g., $A \rightleftharpoons B$ interconversion). Under optimal conditions, fitting extracts the populations and the exchange rates between states as well as the chemical shift difference between the interconverting states, thus reflecting the thermodynamics and kinetics of the exchanging system [38, 115].

3.1.4. Overview

Here, we performed CPMG relaxation dispersion experiments at multiple field strengths to compare the dynamic properties of ^{13}C-methyl labeled ERK2 in its phosphorylated and unphosphorylated states. The results demonstrate that phosphorylation causes a significant change in exchange dynamics throughout the kinase core, consistent with a global domain motion. Increasing hinge mobility by introducing mutations at the hinge also promotes domain motion within the core, but with differing kinetics and populations. Taken together, the results show that large changes in dynamics accompany ERK2 phosphorylation, which are influenced by conformational mobility at the hinge. We propose that the activation of ERK2 involves removing inhibitory constraints to domain motion, which are conferred by the internal architecture of the kinase.

3.2. Materials and Methods

3.2.1. Protein Preparation

ILV methyl-protonated, U-[^{2}H,^{15}N] 0P-, 2P- and mutants ERK2. The general procedure of preparing a ILV methyl-protonated, U-[^{2}H,^{15}N] 0P-ERK2 was presented in Chapter 2. Briefly, a pET-23a plasmid containing the rat His$_6$-ERK2 sequence was transformed into *E. coli* BL21(DE3) cells [80]. The cells were grown at 37 °C sequentially in LB media, then in unlabeled M9 minimal medium in H_2O, followed by M9 minimal media with D-glucose-d$_7$ in D_2O, and finally in 1 L M9 minimal medium with 3 g/L D-glucose-d7 and 1 g/L $^{15}NH_4Cl$ for U-^{2}H, ^{15}N labeling. Ile ($^{13}C^{\delta}H_3$), Leu ($^{13}C^{\delta}H_3$,$^{12}C^{\delta}D_3$), Val ($^{13}C^{\gamma}H_3$,$^{12}C^{\gamma}D_3$) labeling were achieved with precursors (α-keto-3-methyl-D3-butyric acid-4-^{13}C and 2-ketobutyric acid-4-^{13}C) [49, 50]. Cells were induced with isopropyl-β-D-1-thiogalactopyranoside until harvest. Cell lysis was performed with a buffer containing lysozyme, followed by sonication, which also breaks down genomic DNA. Proteins were purified from cell lysate by Ni^{2+}-NTA affinity chromatography (Bio-Rad), PD-10 desalting (GE Healthcare), MonoQ FPLC (GE Healthcare), and Sephadex S200 size-exclusion chromatography (GE Healthcare)[81]. 2P-ERK2 was prepared from 0P-ERK2 after the MonoQ step, phosphorylated *in vitro* using constitutively active mutant MKK1 (MKK-G7B: ΔN4/S218D/M219D/N221D/S222D) as described in Chapter 2[82], and further purified by Sephadex S200 size-exclusion chromatography. The NMR samples of 0P-ERK2 and 2P-ERK2 were concentrated to 0.3-0.4 mM, and exchanged into the NMR buffer (50 mM Tris pH 7.4, 150 mM NaCl, 5 mM $MgSO_4$, 0.1 mM EDTA, 5 mM DTT, 100% D_2O, and 2.5% (v/v) glycerol) for NMR experiments. Mutants of 0P-ERK2 M106E107/GG and L154A were created by site-directed mutagenesis of ERK2 using the QuikChange Mutagenesis Kit (Stratagene), confirmed by DNA sequencing, and purified in the same way as wild type 0P-ERK2. The mutants were concentrated down to a final concentration of ~0.4 mM in the NMR buffer containing 5% D_2O.

3.2.2. Constant Time CPMG Relaxation Dispersion Experiments

Multiple-Quantum CPMG experiments. Methyl side chain dynamics were measured using 2D (^{13}C, ^{1}H) multiple-quantum (MQ) CPMG relaxation dispersion experiments [38, 115] on 0.3 mM ILV methyl-protonated, U-[^{2}H,^{15}N] 0P- and 2P-ERK2, performed at 25 °C, 17.5 °C, and 10 °C on Varian 600, 800 and 900 MHz NMR spectrometers. The datasets of 800, and 900 MHz were collected on Varian VNMRS 800 and 900 MHz NMR spectrometers equipped with z-axis gradient cryoprobes. The 600 MHz datasets were collected on a Varian INOVA 600 MHz NMR spectrometer equipped with a room temperature probe. These experiments were recorded using the pulse sequence "hmqc_CH3_exchange_bigprotein_800_lek_v4.c" (kindly provided by Dr. Lewis Kay, University of Toronto). These experiments were arrayed with different delays (2τ) between ^{13}C refocusing pulses, with constant relaxation time (total time of CPMG trains) of 20 ms (T_{relax}, or time_T2)[115]. The experiment for 2P-ERK2 at 800 MHz was acquired with 12 different τ times corresponding to CPMG frequencies (ν_{CPMG}) ranging from 50 Hz – 1000 Hz. Several τ times were collected twice to estimate errors in the measurements. A set of 160 complex points in the t_1 (^{13}C) dimension, and 1024 complex points in the acquisition period were collected. A 2 s delay period was used with 8 scans, leading to a total acquisition time of 21 h. WURST-40 ^{13}C decoupling was applied during the 85 ms acquisition period [116]. This experiment, with slightly different values of τ and numbers of complex points in the t_1 period, was repeated for 2P-ERK2 at 600 and 900 MHz, as well as for 0P-ERK2 at all three field strengths. These experiments execute an array of "phase, ncyc_cp" (occasionally set to "ncyc_cp, phase"), in which the "phase" array is an outer loop of the "ncyc_cp" array. According to the setup of the array, each CPMG experiment was separated into a series of 2D spectra so that two phases are associated with each ncyc_cp value, using an in-house script "fid_cut_mf_ppc" or "fid_cut_mf_intel". The cleaved 2D spectra for each τ were processed using NMRPipe[88], similar to 2D HMQC spectra

described in Chapter 2. Peak intensities were measured using the program FuDA (Function and Data Analysis, http://pound.med.utoronto.ca/software). The effective decay rate ($R_{2,eff}$) was calculated by this following equation[117] using an in-house script (CPMG.py, written by Dr. D. F. Hansen and provided by Dr. Michael Latham):

$$R_{2,eff} = -\frac{1}{T} ln \frac{I(\nu_{CPMG})}{I(0)} \quad \text{(Equation 3.1)}$$

where $\nu_{CPMG} = 1/(4\tau)$ and 2τ is the interval between successive 180° ^{13}C refocusing pulses, $I(\nu_{CPMG})$ and $I(0)$ are the intensities of peaks recorded with and without the CPMG period, respectively. Uncertainties in $R_{2,eff}$ were estimated in parallel using CPMG.py by this following equation:

$$\Delta R_{2,eff} = -\frac{1}{T} \frac{\Delta I(\nu_{CPMG})}{I(\nu_{CPMG})} \quad \text{(Equation 3.2)}$$

where $\Delta I(\nu_{CPMG})$ is the standard deviation of the peak intensities that came out of duplicate measurements at the same CPMG frequency or the fitted lineshape using FuDA. If $\Delta R_{2,eff}$ from this calculation is less than 2% of $R_{2,eff}$, then $\Delta R_{2,eff}$ is set to the value that is 2% of $R_{2,eff}$.

Two-state Exchange Fitting of MQ-CPMG experiments. The MQ-CPMG dispersion profiles of 0P-, 2P- and ME/GG-ERK2 were fit on a per methyl basis to a two-state exchange process[35, 115, 118, 119], obtaining exchange rate constant ($k_{ex} = k_{AB} + k_{BA}$), populations of the two exchanging states (p_A, p_B), and ^{13}C chemical shift changes (in ppm) between states A and B ($|\Delta\delta_{CPMG}{}^{13}C|$, assuming $|\Delta\delta_{CPMG}{}^{1}H| = 0$)[120]. This was performed using a modified version of the program CATIA (Cpmg, Anti-trosy, and Trosy Intelligent Analysis, http://pound.med.utoronto.ca/software), which was provided by Dr. Michael Latham to allow fitting MQ-CPMG experiments. A "calculated $R_{2,eff}$ ($R_{2,cal}$)" is obtained by numerically simulating the evolution matrix (EM) of the spin system that undergoes two-state chemical exchange during the CPMG experiment[121]:

$$EM = \begin{pmatrix} -R_{2A} - k_{ex}p_B & k_{ex}p_A \\ k_{ex}p_B & -R_{2B} - k_{ex}p_A + i\Delta\omega_{AB} \end{pmatrix} \quad \text{(Equation 3.3)}$$

where R_{2A} and R_{2B} are the transverse relaxation rate of state A and B, respectively, and $\Delta\omega$ is the magnitude of chemical shift difference (in Hz) between these two exchanging states A and B, which have populations of p_A and p_B, respectively. The best fit of exchanging parameters is then obtained by a least-square minimization of a chi-squared (χ^2) function which is a comparison between experimental and calculated $R_{2,eff}$ [118, 119]:

$$\chi^2 = \sum \frac{(R_{2,cal} - R_{2,eff})^2}{(\Delta R_{2,eff})^2} \qquad \text{(Equation 3.4)}$$

The advantage of this fitting method is that no time regime assumption (e.g. fast exchange limit) has to be made. However, since the estimated errors of the individual fittings assumed a two-state exchange process, they could be underestimated due to the existence of more than two states. In addition, non-linear least-squared fitting using the simplified, fast exchange limit Carver-Richards equation[35]:

$$R_{2,eff} = R_{2,0} + \frac{p_A p_B \Delta\omega_{AB}{}^2}{k_{ex}} \left(1 - \frac{2 \tanh\left[\frac{k_{ex}\tau_{CP}}{2}\right]}{k_{ex}\tau_{CP}}\right) \qquad \text{(Equation 3.5)}$$

was performed to estimate the term $p_A p_B \Delta\omega^2$ for methyls in 0P-ERK2 and ME-GG ERK2. $R_{2,0}$ is the relaxation decay rate in absence of exchange. τ_{CP} is the interval between successive 180° ^{13}C refocusing pulses (2τ). Table 3.2 lists the filenames and experimental parameters.

Single-Quantum CPMG experiments. 2D (^{13}C, ^{1}H) single-quantum CPMG measurements [117] on 0P- and 2P-ERK2 were carried out at 25 °C on 800 and 900 MHz NMR spectrometers, in parallel with 2D ^{13}C-^{1}H MQ CPMG experiments. These experiments were recorded using the pulse sequence "HtoC_CH3_exchange_800_lek_ILV_ap.c" (kindly provided by Dr. Lewis Kay, University of Toronto). The experiment for 2P-ERK2 at 800 MHz was acquired with 15 different τ times corresponding to CPMG frequencies (ν_{CPMG}) ranging from 100 Hz – 1000 Hz. Several τ times were collected twice to estimate errors in the measurements. It should be noted that in this experiment all the

"ncyc_cp" values are set to even numbers because this pulse sequence contains a P-element in the middle of the CPMG period[122]. For this reason, the SQ-CPMG may not provide enough data at early CPMG frequencies, especially for a slow exchanging process that is quickly quenched. In the experiment of 2P-ERK2 at 800 MHz, a set of 128 complex points in the t_1 (^{13}C) dimension, and 1024 complex points in the acquisition period were collected. A 1.5 s delay period was used with 48 scans, leading to a total acquisition time of 84 h. WALTZ-16 ^{13}C decoupling was applied during the 85 ms acquisition period [116]. This experiment, with slightly different values of τ and numbers of scans, was repeated for 2P-ERK2 at 900 MHz, as well as for 0P-ERK2 at these field strengths. The data processing was performed in a similar manner to the MQ-CPMG spectra. The effective decay rates ($R_{2,eff}$) were plotted as a function of CPMG frequencies (ν_{CPMG}). Table 3.3 lists the filenames and experimental parameters.

3.2.3. 2D (^{13}C, ^{1}H) TROSY HMQC Experiments

0P- and 2P-ERK2 at Various Temperatures. Slow exchange in 2P-ERK2 was probed from analysis of methyl peaks in TROSY HMQC spectra, collected on a Varian 800 MHz spectrometer with cryoprobe, at 5, 10, 15, 20, and 25 ºC for 2P-ERK2. In parallel, 2D (^{13}C, ^{1}H) HMQC spectra at 5, 10, 15 and 25 ºC for 0P-ERK2 were also collected on the same spectrometer. These HMQC experiments were processed using NMRPipe[88], similar to the HMQC experiments described in Chapter 2. The peak volumes of slow exchanging peaks were estimated using CCPNMR Analysis software [83]. Equilibrium constants of two-state exchange (K_{eq}) were calculated from the volume ratios of the two slow-exchanging peaks. Information on standard enthalpy ($\Delta H°$) and standard entropy ($\Delta S°$) was extracted for each slow exchanging peak using the following Van't Hoff equation:

$$\ln K_{eq} = -\frac{\Delta H°}{R}\frac{1}{T} + \frac{\Delta S°}{R} \qquad \text{(Equation 3.6)}$$

where T is temperature in Kelvin, and R is the ideal gas constant (2.0 cal $K^{-1}mol^{-1}$). Table 3.4 lists the filenames and experimental parameters.

ME/GG and L154A mutants of 0P-ERK2. 2D (^{13}C, ^{1}H) HMQC spectra of ME/GG and L154A mutants of ERK2 were collected on the 800 MHz spectrometer at 25 ºC. Both spectra contain 2048 and 144 complex points over sweep widths of 12019.2 and 5500 Hz in the ^{1}H and ^{13}C dimensions. 16 transients were acquired with a delay time (d1) of 1.5 s. These spectra were processed and visualized as described in Chapter 2. Table 3.4 lists the filenames and experimental parameters.

3.2.4. 1D Line Shape Simulation using Spinworks 3

The software Spinworks 3 was used to simulate 1D spectra using a given set of k_{ex}, population and chemical shifts of two exchanging species of a spin. A detailed manual was found at the link www.scribd.com/doc/67818925/91/DNMR-Tutorial. A template file for "AB to CD Non-mutual exchange" was loaded by reading spin system file from C:\Program Files\Spinworks_3\Spin systems\example 4, or C:\Program Files\Spinworks\dnmr\dnmr_test4.ss. The directory of the template file may change, depending on the system. Upon loading the template file, chemical shifts of the two exchanging species can be defined by clicking the menu "Spin System", and select for "Edit chemical shifts", where a table shows up for modification. For simulation of a two-state exchange process of a spin, an example of the parameters on "group 1" and "group 2" is summarized in Table 3.1, whereas all the inputs of "group 3" and "group 4" need to be empty.

Table 3.1. Chemical shifts of the two exchanging species are defined in Spinworks 3.

	Spins	label	species	spin	Shift (Hz)
Group 1	1	a	1	½	340
Group 2	1	b	2	½	450

To change the J-coupling, go to Spin System → Edit Scalar Couplings. For our purpose we make sure the J-couplings between the exchanging species to 0. Simulation options can be modified by

opening the tab “Spin system” and click on “Simulation options and DNMR parameters”. The parameter RC(1,2) (1/s) defines the exchange rate constant of group 1 and 2, the parameter “Pop 1” and “Pop 2” defines the populations of the two states (e.g. Pop 1 = 0.5). If it is two-state exchange between states 1 and 2, then the “mutual exchange” box is not checked. Other parameters that may need adjustment include “Spectrometer frequency”, which I usually set to 800 (500 by default), and T2, which I usually set to 0.02 (0.5 by default). To run a DNMR3 simulation, the simulation mode DNMR3 is selected by “Simulation → Simulation Mode → DNMR3/MEXICO”. The simulation is performed by “Simulation → Run DNMR3 simulation”.

Table 3.2. Multiple-Quantum CPMG Experiment Filenames, Parameters and Conditions

Filename	Sample	Temp (°C)	B_0	np	ni	sw	sw1	nt	d1	#ncyc	ncyc_cp	dof (ppm)
0P-ERK2_13CILV_D2O_CPMG_ILE_25carry_123011-rich.fid[a]	0P-ERK2	25	600	4096	128	12019.2	4500	48	1.6	13	1 3 9 10 4 15 7 5 0 2 6 4 3	13.8
0P-ERK2_13CILV_D2O_CPMG_ILE_17C_ncycarry_011212.fid[a]	0P-ERK2	17.5	600	4096	128	12001.2	4500	48	1.6	9	0 1 2 10 19 5 8 3 4	13.8
0P-ERK2_13CILV_D2O_CPMG_Val_10C_ncyc_arry_012411.fid[a]	0P-ERK2	10	600	4096	128	12001.2	4500	48	1.7	13	0 1 19 2 3 5 6 7 8 10 12 14 5	24.9
0P-ERK2_13CILV_D2O_CPMGarry_Val_10C_010312.fid[a]	0P-ERK2	10	600	4096	128	12019.2	4500	32	1.6	12	0 1 2 3 4 5 6 8 10 15 5 19	23.6
2P-ERK2_13CILV_D2O_CPMGarry_Val_021412.fid[a]	2P-ERK2	25	600	4096	128	12001.2	4500	48	1.6	14	1 3 9 10 4 15 7 5 0 2 6 4 3 19	13.8
2P-ERK2_13CILV_D2O_CPMGarry_ILE_17C_030112.fid[a]	2P-ERK2	17.5	600	4096	128	12001.2	4500	48	1.6	14	0 1 19 10 4 7 2 6 3 8 15 2 5 4	13.9
2P-ERK2_13CILV_D2O_CPMGarry_10C_ILE_05032012.fid[a]	2P-ERK2	10	600	4096	128	12004.8	4500	48	1.6	13	0 1 19 10 4 2 6 3 8 15 2 5 4	13.9
2P-ERK2_13CILV_D2O_CPMGarry_10C_Leu_04272012.fid[a]	2P-ERK2	10	600	4096	128	12001.2	4000	48	1.6	15	1 3 9 10 4 15 7 5 0 2 6 4 3 19 12	18.2
0P-ERK2_13CILV_D2O_CPMG_Leu_arry_600_122511.fid[a]	0P-ERK2	25	600	4096	128	12019.2	4500	48	1.7	12	1 3 9 10 4 15 7 5 0 2 6 4	25.5
0PERK2_smple033111_25C_13CCPMGLeu_101711.fid[a]	0P-ERK2	25	800	2048	128	12019.2	5500	8	1.8	10	1 0 20 2 3 7 10 5 4 15	22.1
0PERK2_smple033111_17C_13CCPMGLeu_101611.fid[a]	0P-ERK2	17.5	800	2048	128	12019.2	5500	8	1.8	10	1 0 20 2 3 7 10 5 4 15	22.1
0P-ERK2_smple18_D2O_10C_13cCPMGValLeu_100411.fid[a]	0P-ERK2	10	800	2048	144	12019.2	5500	8	1.8	12	1 0 20 3 7 10 2 5 15 4 2 4	22.1
2H12C15NILV_2P-ERK2_smple0318_25c_13CCPMGLeu_101511.fid[a]	2P-ERK2	25	800	2048	160	12019.2	5500	8	2.0	14	1 0 20 2 3 7 10 2 5 15 4 2 4 12	22.1
2H12C15NILV_2P-ERK2_smple0318_17c_13CCPMGLeu_101611.fid[a]	2P-ERK2	17.5	800	2048	128	12019.2	5500	8	1.8	10	1 0 20 2 3 7 10 5 4 15	22.1
2H12C15NILV_2P-ERK2_CPMGLeu_10C_1001011.fid[a]	2P-ERK2	10	800	2048	144	12019.2	5500	8	2.0	12	1 0 20 3 7 10 2 5 15 4 2 4	22.1
0P-ERK2_smp18_900_13C_CPMG_Val_arry_25c_021712.fid[a]	0P-ERK2	25	900	2048	128	12019.2	5500	16	1.8	13	0 2 3 4 5 6 8 10 15 20 5 1 2	21.5
0P-ERK2_smp18_900_CPMGarry_Val_Ile_17c_021912.fid[a]	0P-ERK2	17.5	900	2048	128	12019.2	5500	16	1.8	16	0 5 15 3 2 8 10 1 6 20 7 2 4 18 1 12	21.5
0P-ERK2_smp18_900_CPMGarry_Val_Ile_10c_022112.fid[a]	0P-ERK2	10	900	2048	128	12019.2	5500	8	1.8	19	0 5 15 3 2 8 10 1 6 20 7 2 4 18 1 12 3 0 16	14.1
2P-ERK2_smp3-18-11_D2O_13C_CPMG_VAL_ncyc_arry_25c_122811_900.fid[a]	2P-ERK2	25	900	2048	128	12019.2	5500	16	1.8	13	0 2 3 4 5 6 8 10 15 20 5 1 2	21.5
2P-ERK2_smp3-18-11_900_CPMGarry_Val_17c_010312.fid[a]	2P-ERK2	17.5	900	2048	80	12019.2	5500	16	1.8	12	0 2 3 4 5 6 8 10 15 20 5 1	21.5
2P-ERK2_smp3-18-11_900_CPMGarry_Val_10c_010212.fid[a]	2P-ERK2	10	900	2048	80	12019.2	5500	16	1.8	13	0 2 3 4 5 6 8 10 15 20 5 1 2	21.5
2P-ERK2_smp3-18-11_900_CPMGarry_Ile_10c_123111.fid[a]	2P-ERK2	10	900	2048	128	12019.2	5500	16	1.8	13	0 2 3 4 5 6 8 10 15 20 5 1 2	14.1
0P-ERK2_MEGGh2o_900_CPMG_Val_arry_25c_121712.fid[b]	MEGG	25	900	2048	120	12019.2	5500	16	1.8	11	0 5 15 1 3 2 10 20 2 4 8	18.2
0P-ERK2_MEGGh2o_900_CPMG_Val_arry_17p5c_121712.fid[b]	MEGG	17.5	900	2048	120	12019.2	5500	16	1.8	11	0 5 15 1 3 2 10 20 2 4 8	18.2
0P-ERK2_MEGGh2o_900_CPMG_Val_arry_10c_121712.fid[b]	MEGG	10	900	2048	128	12019.2	5500	16	1.8	11	0 5 15 1 3 2 10 20 2 4 8	18.2
0P_ERK2_MEGGh2o_methylCPMG_3pts_12132012.fid[b]	MEGG	25	800	2048	144	12019.2	5000	16	2.0	3	3 10 15	17.6
0P_ERK2_MEGGh2o_methylCPMG_5pts_12132012.fid[b]	MEGG	25	800	2048	144	12019.2	5000	16	2.0	5	1 0 19 2 5	17.6
0P_ERK2_MEGGh2o_methylCPMG_8pts_17p5C_12132012.fid[b]	MEGG	17.5	800	2048	140	12019.2	5000	16	2.0	8	1 0 19 2 5 3 10 15	17.6
0P-ERK2_L154Ah2o_900_CPMG_Val_arry_25c_122212.fid[b]	L154A	25	900	2048	128	12019.2	5500	16	1.8	12	0 5 15 1 3 2 10 20 2 4 8 6	18.2
0P-ERK2_L154Ah2o_900_CPMG_Val_arry_17p5c_122212.fid[b]	L154A	17.5	900	2048	128	12019.2	5500	16	1.8	12	0 5 15 1 3 2 10 20 2 4 8 6	18.2
0P-ERK2_L154Ah2o_900_CPMG_Val_arry_10c_122212.fid[b]	L154A	10	900	2048	128	12019.2	5500	16	1.8	12	0 5 15 1 3 2 10 20 2 4 8 6	18.2
0P_ERK2_L154Ah2o_methylCPMG_9pts_12172012.fid[b]	L154A	25	800	2048	140	12019.2	5000	16	2.0	9	2 0 1 3 10 15 19 4 5	17.6
0P_ERK2_L154Ah2o_methylCPMG_9pts_17p5C_12172012.fid[b]	L154A	17.5	800	2048	140	12019.2	5000	16	2.0	9	2 0 1 3 10 15 19 4 5	17.6
0P_ERK2_L154Ah2o_methylCPMG_12pts_10C_12172012.fid[b]	L154A	10	800	2048	144	12019.2	5000	32	2.0	12	0 2 1 3 10 15 19 4 5 8 6 12	17.6

B_0 – magnetic field strength
np – number of complex points in t_2
ni – number of complex points in t_1

sw − sweep width in t_2 (Hz)
sw1 − sweep width in t_1 (Hz)
nt − number of scans per FID
d1 − interscan delay (s)
#ncyc − number of elements in the ncyc_cp array
ncyc_cp − number of CPMG cycles
[a]Data directories in /yao/data/ERK2_2011/methylCPMG2011/. Experiments collected at the field strengths of 600, 800 and 900 MHz are in the folder 800 and 900, respectively.
[b]Data directories in /yao/data/ERK2_2012/mqCPMG/.

Table 3.3. Single-Quantum CPMG Experiment Filenames, Parameters and Conditions[a]

Filename[b]	Sample	B_0	nt	array	time_T2	#ncyc	ncyc_cp	dof (ppm)
0P-ERK2_D2O_800_CPMG_SQ_20ms_ncycarray_Val_Ile_25c_060112.fid	0P-ERK2	800	48	ncyc_cp,phase	0.02	15	0 2 22 4 12 6 10 8 2 16 4 18 14 20 6	22.1
2P-ERK2_smp3-18-11_800_CPMG_SQ_20ms_ncycarray_Val_Ile_25c_052612.fid	2P-ERK2	800	48	ncyc_cp,phase	0.02	15	0 2 22 4 12 6 10 8 2 16 4 18 14 20 6	22.1
0P-ERK2_smp18_900_CPMG_SQ_20ms_ncycarraya_Val_Ile_25c_022512.fid	0P-ERK2	900	28	phase,ncyc_cp	0.02	10	0 2 22 4 12 6 10 8 2 16	21.5
0P-ERK2_smp18_900_CPMG_SQ_20ms_ncycarrayb_Val_Ile_25c_022812.fid	0P-ERK2	900	28	phase,ncyc_cp	0.02	10	0 2 22 4 12 6 10 8 2 16	21.5
0P-ERK2_smp18_900_CPMG_SQ_30ms_ncycarray_Ile_25c_030712.fid	0P-ERK2	900	40	phase,ncyc_cp	0.03	13	2 0 16 20 4 8 16 10 6 12 22 4 2	13.5
2P-ERK2_smp3-18-11_900_CPMG_SQ_20ms_ncycarray_Val_Ile_25c_051812.fid	2P-ERK2	900	48	phase,ncyc_cp	0.02	12	0 2 22 4 12 6 10 8 2 16 4 18	21.5

B_0 − magnetic field strength!
nt − number of scans per FID
time_T2 − total time for CPMG trains
Array − if equals "phase, ncyc_cp", then "phase" array is an outer loop of "ncyc_cp" array
#ncyc − number of elements in the ncyc_cp array
ncyc_cp − number of CPMG cycles
[a]All of these experiments were collected at 25 °C, and have np (number of complex points in t_2) = 2048, ni (number of complex points in t_1) =128, sw (sweep width in t_2, in Hz) = 12019.2, sw1 (sweep width in t_1, in Hz)= 5333, d1 (interscan delay, in s) = 1.5.
[b]Data directories in /yao/data/ERK2_2011/methylCPMG2011/. Experiments collected at the field strengths of 800 and 900 MHz are in the folder 800 and 900, respectively.

Table 3.4. 2D (^{13}C,^{1}H) TROSY HMQC Experiment Filenames, Parameters and Conditions[a]

Filename	Sample	Temp (°C)	Solvent[b]	B_0	sequence	np	ni	sw	sw1	nt
13Chmqc_2D_0PERK2_033111.fid[c]	0P-ERK2	25	D2O	800	hmqc_c13_800_methyl_lek.c	2048	160	12019.2	5430	16
0P-ERK2_D2O_HMQC_25c_10082012.fid[d]	0P-ERK2	25	D2O	800	hmqc_c13_800_methyl_bufsat.c	2048	144	12019.2	5000	16
0P-ERK2_D2O_HMQC_15c_10082012.fid[d]	0P-ERK2	15	D2O	800	hmqc_c13_800_methyl_bufsat.c	2048	144	12019.2	5000	16

0P-ERK2_13CILV_D2O_HMQC_10c_122911.fid[e]	0P-ERK2	10	D2O	600	hmqc_c13_800_methyl_bufsat.c	4096	144	12001.2	4000	8
0P-ERK2_D2O_HMQC_10c_10082012.fid[d]	0P-ERK2	10	D2O	800	hmqc_c13_800_methyl_bufsat.c	2048	144	12019.2	5000	16
0P-ERK2_D2O_HMQC_5c_10082012.fid[d]	0P-ERK2	5	D2O	800	hmqc_c13_800_methyl_bufsat.c	2048	144	12019.2	5000	16
2P-ERK2_sample031611_ILV_D2O_25C_13Chmqc_100411.fid[f]	2P-ERK2	25	D2O	800	hmqc_c13_800_methyl_bufsat.c	2048	144	12019.2	5000	16
2P-ERK2_sample031611_ILV_D2O_20C_13Chmqc_100411.fid[f]	2P-ERK2	20	D2O	800	hmqc_c13_800_methyl_bufsat.c	2048	144	12019.2	5000	16
2P-ERK2_sample031611_ILV_D2O_17pt5C_13Chmqc_100511.fid[f]	2P-ERK2	17.5	D2O	800	hmqc_c13_800_methyl_bufsat.c	2048	144	12019.2	5000	16
2P-ERK2_sample031611_ILV_D2O_15C_13Chmqc_100411.fid[f]	2P-ERK2	15	D2O	800	hmqc_c13_800_methyl_bufsat.c	2048	144	12019.2	5000	16
2P-ERK2_sample031611_ILV_D2O_10C_13Chmqc_100411.fid[f]	2P-ERK2	10	D2O	800	hmqc_c13_800_methyl_bufsat.c	2048	144	12019.2	5000	16
2P-ERK2_sample031611_ILV_D2O_5C_13Chmqc_100411.fid[f]	2P-ERK2	5	D2O	800	hmqc_c13_800_methyl_bufsat.c	2048	144	12019.2	5000	16
0P-ERK2MEGG_H2O_HMQC_25c_12142012.fid[d]	MEGG	25	H2O	800	hmqc_c13_800_methyl_bufsat.c	2048	144	12019.2	5000	16
0P-ERK2L154A_H2O_HMQC_25c_12172012.fid[d]	L154A	25	H2O	800	hmqc_c13_800_methyl_bufsat.c	2048	144	12019.2	5000	16

B_0 − magnetic field strength
np − number of complex points in t_2
ni − number of complex points in t_1
sw − sweep width in t_2 (Hz)
sw1 − sweep width in t_1 (Hz)
nt − number of scans per FID
[a]All of these experiments were collected with an interscan delay of 1.5 s.
[b]Solvent is either 95% -99% D2O (labeled as D2O) or 5% D2O (labeled as H2O).
[c]Data directories in /yao/data/ERK2_2011/0pERK2_100D2O_033111/
[d]Data directories in /yao/data/ERK2_2012/HMQCs/
[e]Data directories in /Users/yao/data/ERK2_2011/methylCPMG2011/600/HMQCs/
[f]Data directories in /Users/yao/data/ERK2_2011/2pERK2_100D20_031811/

3.3. Results

3.3.1. Accurate Peak Intensity Were Obtained by Peak Fitting using FuDA

Conformational dynamics of ILV methyl groups were examined in 0P- and 2P-ERK2 using ^{13}C-^{1}H multiple-quantum CPMG relaxation dispersion experiments [115]. Methyl groups undergoing conformational exchange in the μs-ms timescale showed changes in their effective relaxation rate $R_{2,eff}$, measured as a function of the frequency of the refocusing pulses (ν_{CPMG}). Accurate determination of peak intensities (volumes) is a prerequisite to obtain reliable $R_{2,eff}$ values or any further dynamic information from the CPMG dispersion curves. However, the peak fitting in overlapped regions of the 2D spectra could be highly skewed, resulting in inaccurate peak intensities. Here we show that good peak fitting could be obtained using FuDA, especially on the overlapping peaks (Figure 3.1 and Figure 3.2). A function in FuDA called "OVERLAP_PEAKS" is specified for fitting overlapping peaks. To use this function, a line is added to the input file for FuDA "param.fuda": OVERLAP_PEAKS=(peak1;peak2). The peak fitting result was examined by visualizing for each peak before plotting the CPMG relaxation curves, to ensure that each CPMG relaxation curve is based on accurate peak intensity measurements.

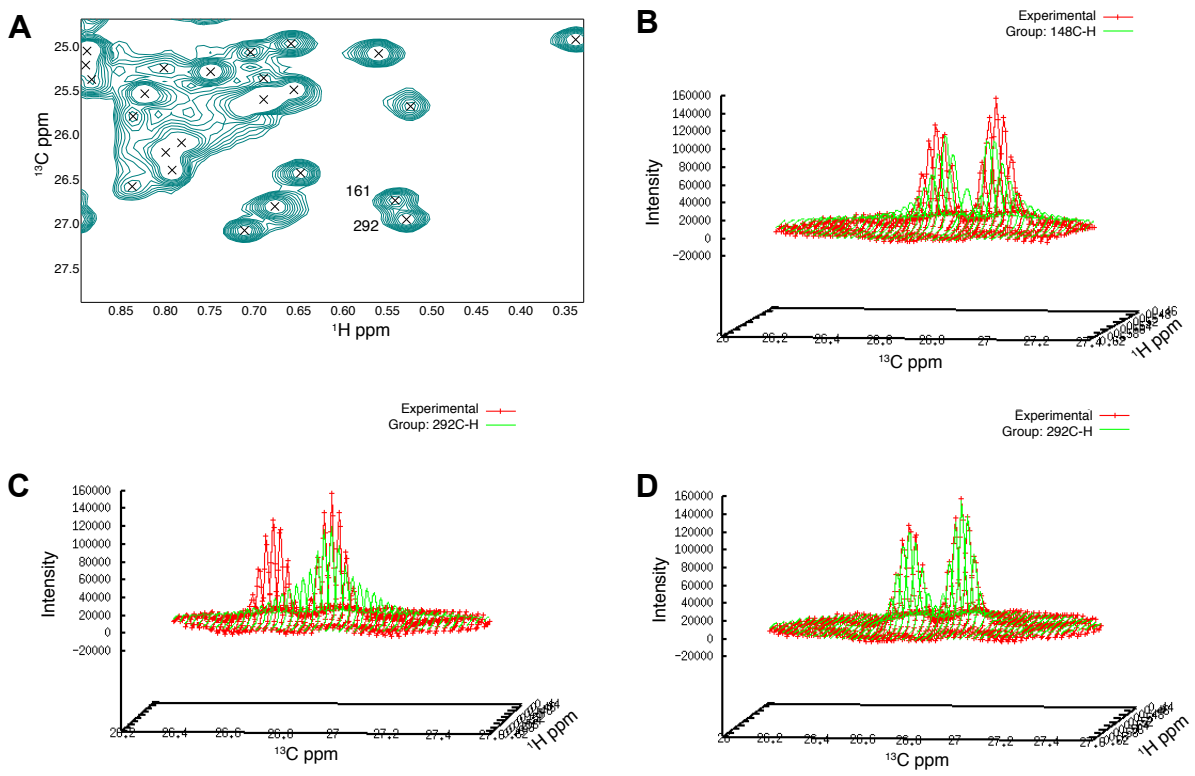

Figure 3.1. Peak fitting of L161 and L292 methyls using FuDA.
(A) A multiple-quantum CPMG spectra without CPMG trains (ncyc_cp = 0) of 2P-ERK2 highlighting resonances L161 and L292 that were partially overlapping on the spectra. (B) Peak fitting of L161 without the "OVERLAP_PEAKS" function. The experimental line shapes were in red, the fitted line shapes were in green. (C) Peak fitting of L292 without the "OVERLAP_PEAKS" function. (D) Peak fitting of L161 and L292 after applying the "OVERLAP_PEAKS" function on L161 and L292.

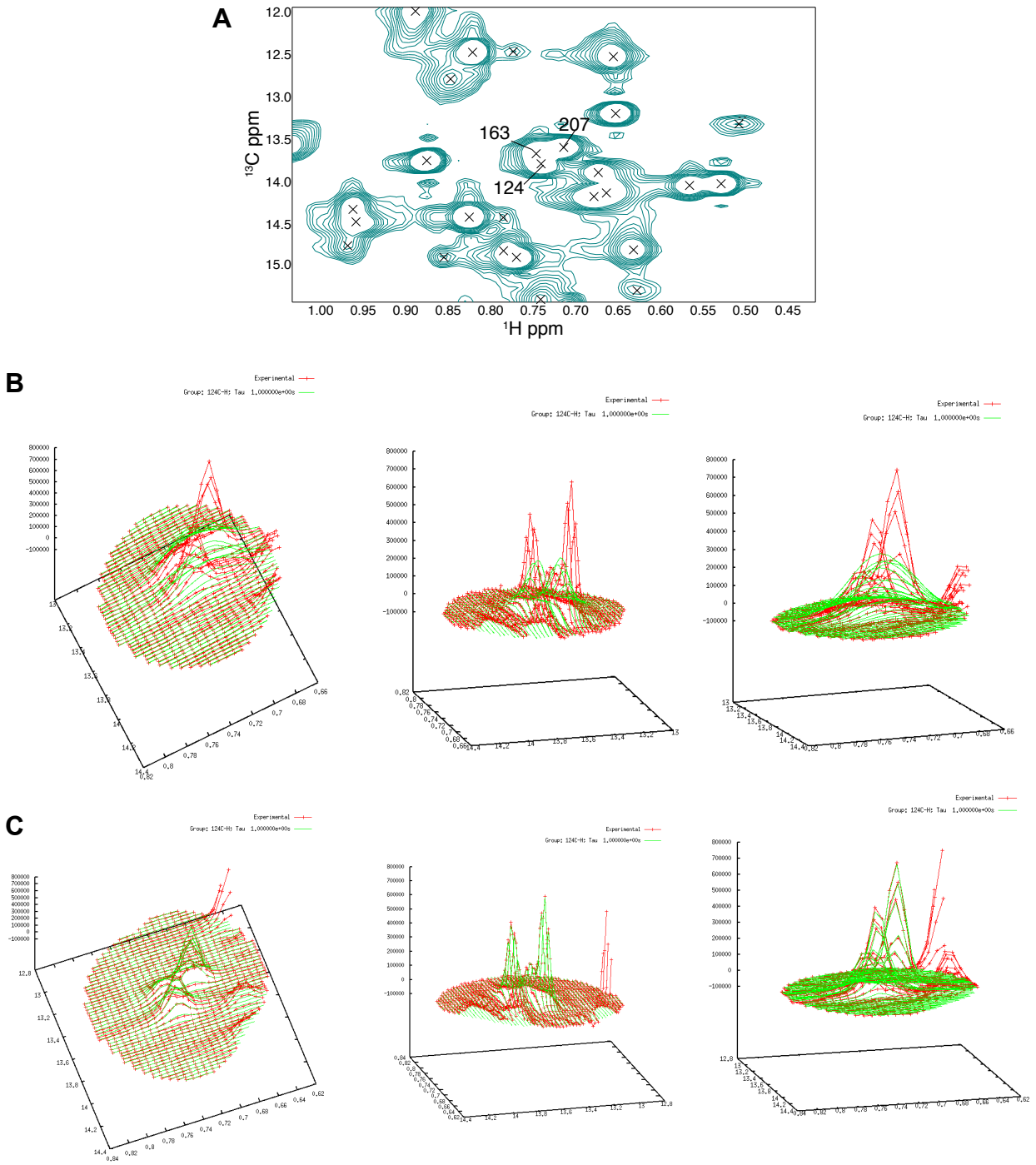

Figure 3.2. Peak fitting of I124, I163 and I207 methyls using FuDA.
(A) A multiple-quantum CPMG spectra without CPMG trains (ncyc_cp = 0) of 2P-ERK2 highlighting resonances I124, I163 and I207 that were partially overlapping on the spectra. (B) Different views of peak fitting of I124 without applying the "OVERLAP_PEAKS" function. The experimental line shapes were in red, the fitted line shapes were in green. (C) Peak fitting of I124 after applying the "OVERLAP_PEAKS" function on I124, I163 and I207.

3.3.2. Residues in 0P-ERK2 Show Local Conformational Dynamics

To examine the μs-ms conformational dynamics in 0P-ERK2, the relaxation dispersion curves collected at 25 ºC and at three field strengths (600, 800 and 900 MHz) are plotted in Figure 3.3 and Figure 3.4. Dynamics were indicated when R_{ex}, the contribution to $R_{2,eff}$ from exchange, was significant (> 4 s^{-1}), yielding curvature in the plot of $R_{2,eff}$ *vs* ν_{CPMG} (Figure 3.3 and Table 3.5). No evidence for dynamics on this timescale was indicated when $R_{ex} \approx 0$ s^{-1}. For individual ILV methyl groups, the dispersion curves at 600, 800 and 900 MHz were fit to a two-state exchange model ($A \rightleftharpoons B$), yielding exchange rate constants ($k_{ex}= k_{AB} + k_{BA}$) [38, 115]. Under optimal conditions, the populations (p_A and p_B), and the chemical shift differences between the two states (in Hz), $|\Delta\omega|$, were obtained for individual methyl groups [38, 115]. However, the analysis on the multiple-quantum CPMG dispersion data immediately gets complicated because both $|\Delta\delta_{CPMG}{}^{13}C|$ (in ppm) and $|\Delta\delta_{CPMG}{}^{1}H|$ (in ppm) contribute to the dispersion curvature. To be specific, a methyl with two well-populated states separated by their $|\Delta\delta_{CPMG}{}^{13}C|$ that are exchanging in the μs-ms timescale would show flattened dispersion curvature if they have large $|\Delta\delta_{CPMG}{}^{1}H|$, whereas a large dispersion curve would be observed if $|\Delta\delta_{CPMG}{}^{1}H| = 0$ ppm (Figure 3.5).

To simplify the fitting on CPMG data, the assumption is made that $|\Delta\delta_{CPMG}{}^{1}H|$ (in ppm) ≈ 0, so that we only need to consider $|\Delta\delta_{CPMG}{}^{13}C|$ in the estimation of population and rate constants. To validate this assumption, a set of single quantum ^{13}C CPMG experiment was collected at 25 ºC for both 0P- and 2P-ERK2 to compare with the multiple-quantum CPMG experiment using the same conditions, because the single quantum ^{13}C CPMG data will not affected by $|\Delta\delta_{CPMG}{}^{1}H|$. The results showed dispersion curves (Figure 3.6 and Figure 3.7) from the single quantum CPMG experiment comparable to multiple-quantum CPMG experiments, validating the assumption that $|\Delta\delta_{CPMG}{}^{1}H|$ is ≈ 0.

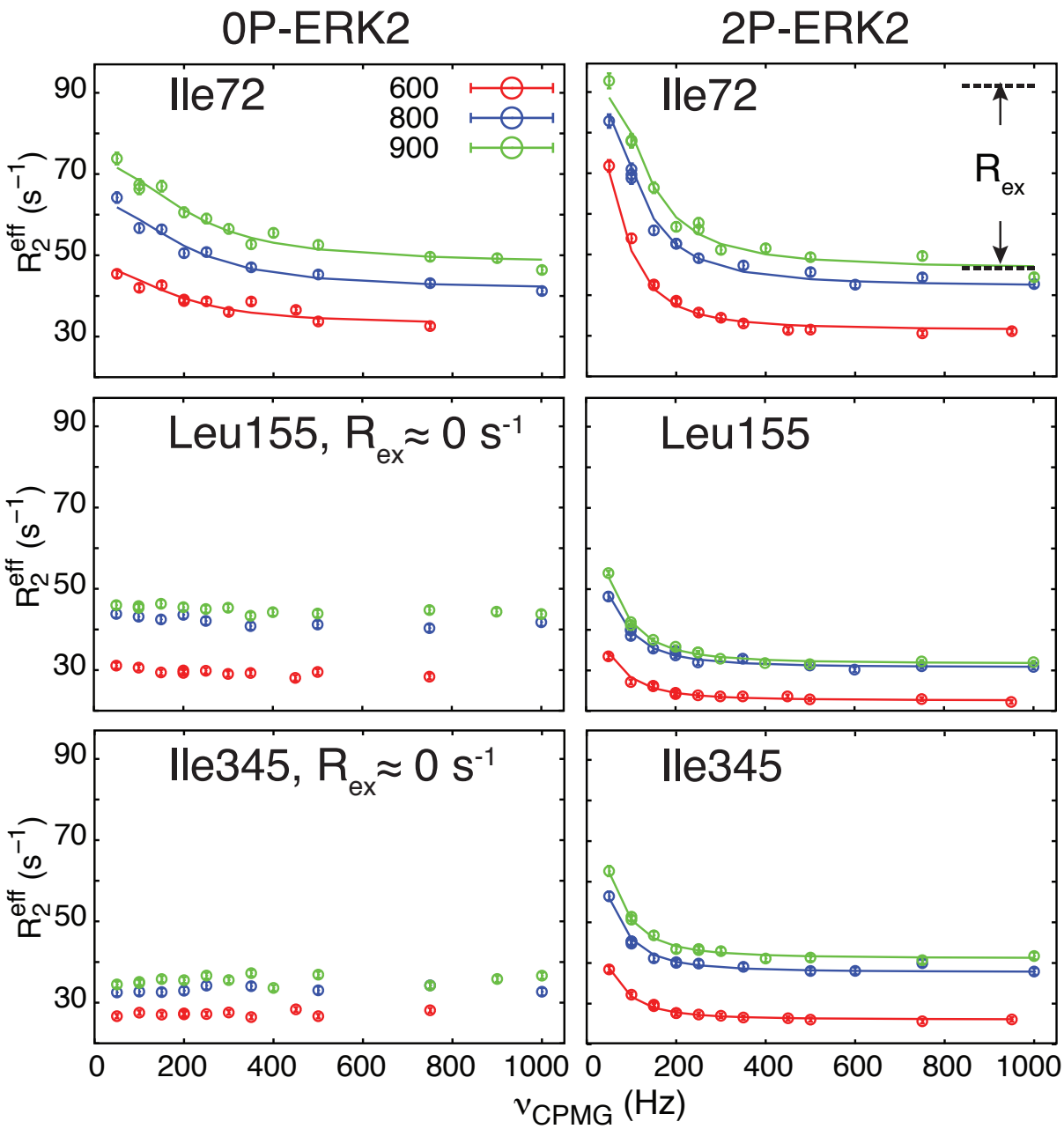

Figure 3.3. CPMG dispersion experiments show changes in methyl dynamics following ERK2 phosphorylation. The dispersion curves measured at 25 °C and 900 (green), 800 (blue), and 600 (red) MHz are shown for representative residues in 0P-ERK2 (left) and 2P-ERK2 (right). The R_{ex} is shown for I72 in 2P-ERK2 at 800 MHz. Lines show individual fits and the error bars were estimated from peak intensities of duplicate measurements.

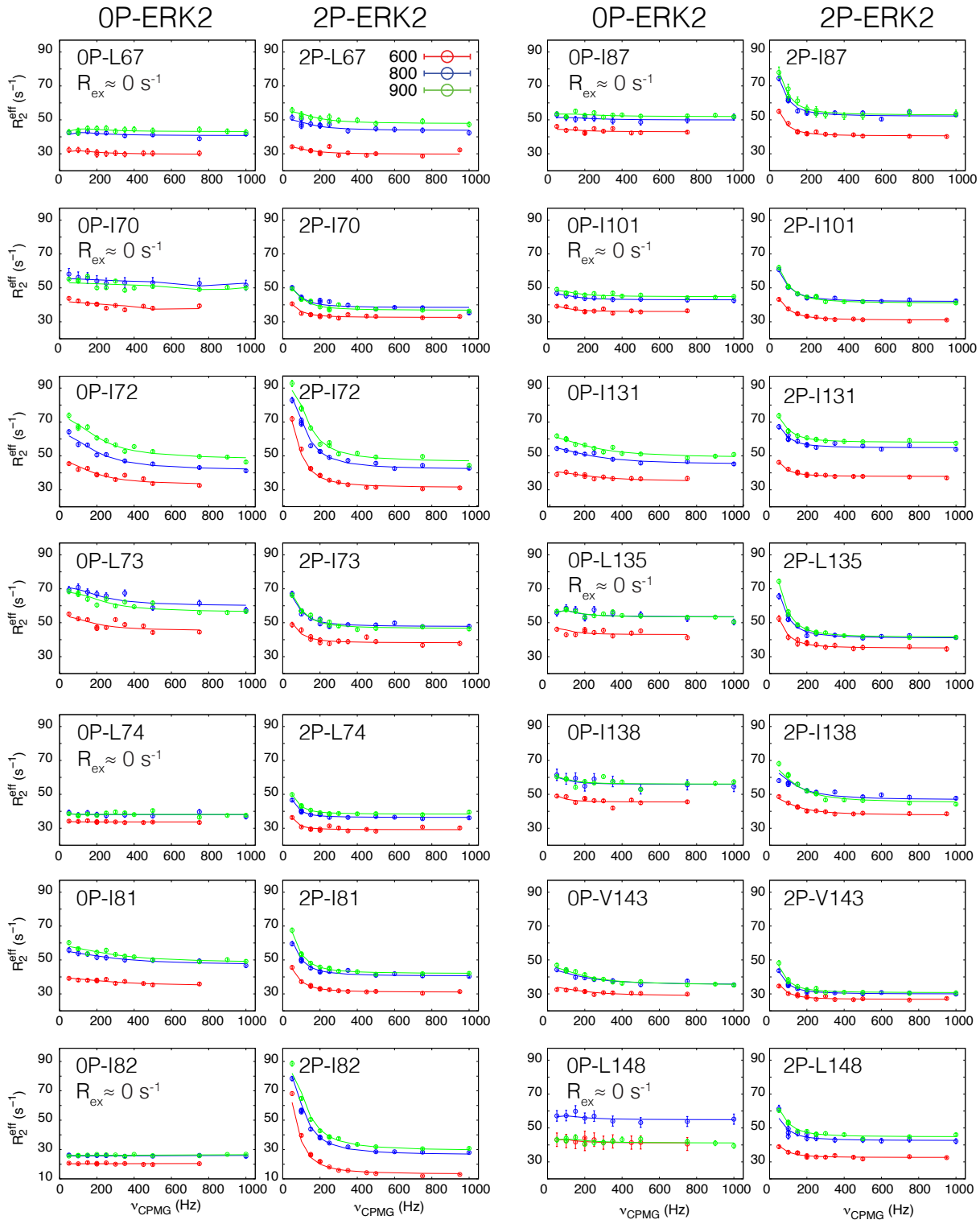

Figure 3.4**.** CPMG relaxation dispersion curves for 0P- and 2P-ERK2.
Relaxation dispersion curves at 25 °C and 900 (green), 800 (blue), and 600 (red) MHz are plotted for all residues that showed significant R_{ex} in either 0P-ERK2 (left) or 2P-ERK2 (right). Curves labeled ("$R_{ex} \approx 0$") are residues where the dispersion was too small to confidently fit, meaning they had $R_{ex} < 4\ s^{-1}$. Lines show individual fits and the error bars were estimated from peak intensities of duplicate experiments.

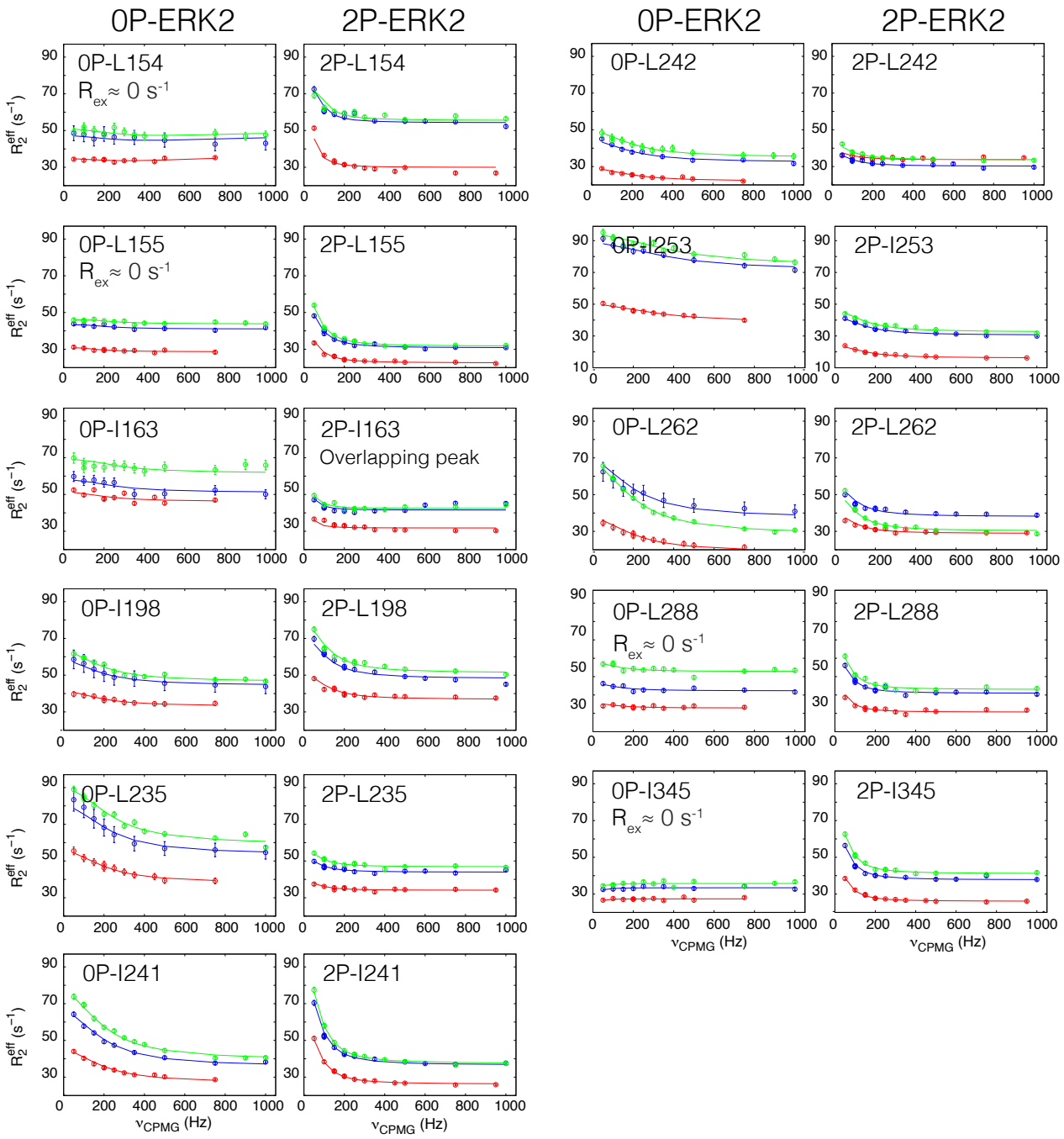

Figure 3.4. (Continued) CPMG relaxation dispersion curves for 0P- and 2P-ERK2.
Relaxation dispersion curves at 25 °C and 900 (green), 800 (blue), and 600 (red) MHz are plotted for all residues that showed significant R_{ex} in either 0P-ERK2 (left) or 2P-ERK2 (right). Curves labeled ("$R_{ex} \approx 0$") are residues where the dispersion was too small to confidently fit, meaning they had $R_{ex} < 4\ s^{-1}$. Lines show individual fits and the error bars were estimated from peak intensities of duplicate experiments.

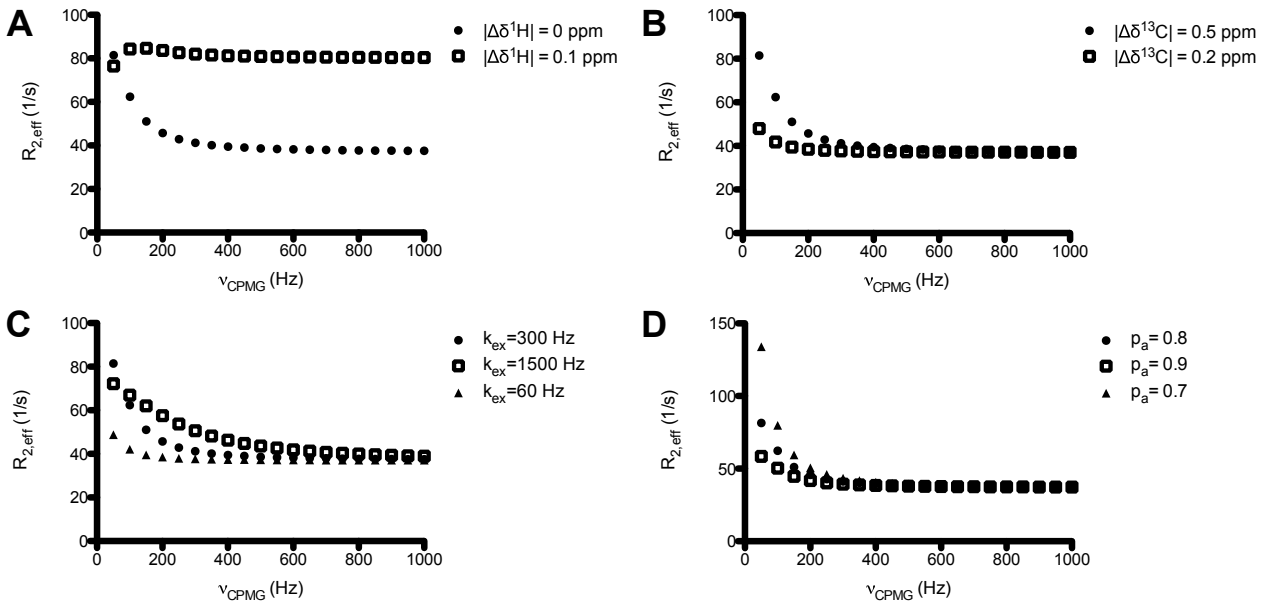

Figure 3.5. Simulations of multiple-quantum CPMG dispersion curves.
The simulations were performed using a total time of CPMG trains (time_T2) of 0.02 s, with the number of CPMG cycles ranging from 1 to 20. A simulated two-state exchange scenario where $p_a = 0.8$, $p_b=0.2$, $k_{ex} = 300\ s^{-1}$, $|\Delta\delta^{13}C| = 0.5$ ppm, $|\Delta\delta^1H| = 0$ ppm is used as an template, and individual parameters ($|\Delta\delta^1H|$, $|\Delta\delta^{13}C|$, k_{ex} and p_a) are varied. (A) $|\Delta\delta^1H| = 0$ ppm (solid circle) or $|\Delta\delta^1H| = 0.1$ ppm (empty square). (B) $|\Delta\delta^{13}C| = 0.5$ ppm (solid circle) or $|\Delta\delta^{13}C| = 0.2$ ppm (empty square). (C) $k_{ex} = 300\ s^{-1}$ (solid circle), $k_{ex} = 1500\ s^{-1}$ (empty square), or $k_{ex} = 60\ s^{-1}$(solid triangle). (D) $p_a = 0.8$ (solid circle), $p_a = 0.9$ (empty square), or $p_a = 0.7$ (solid triangle)

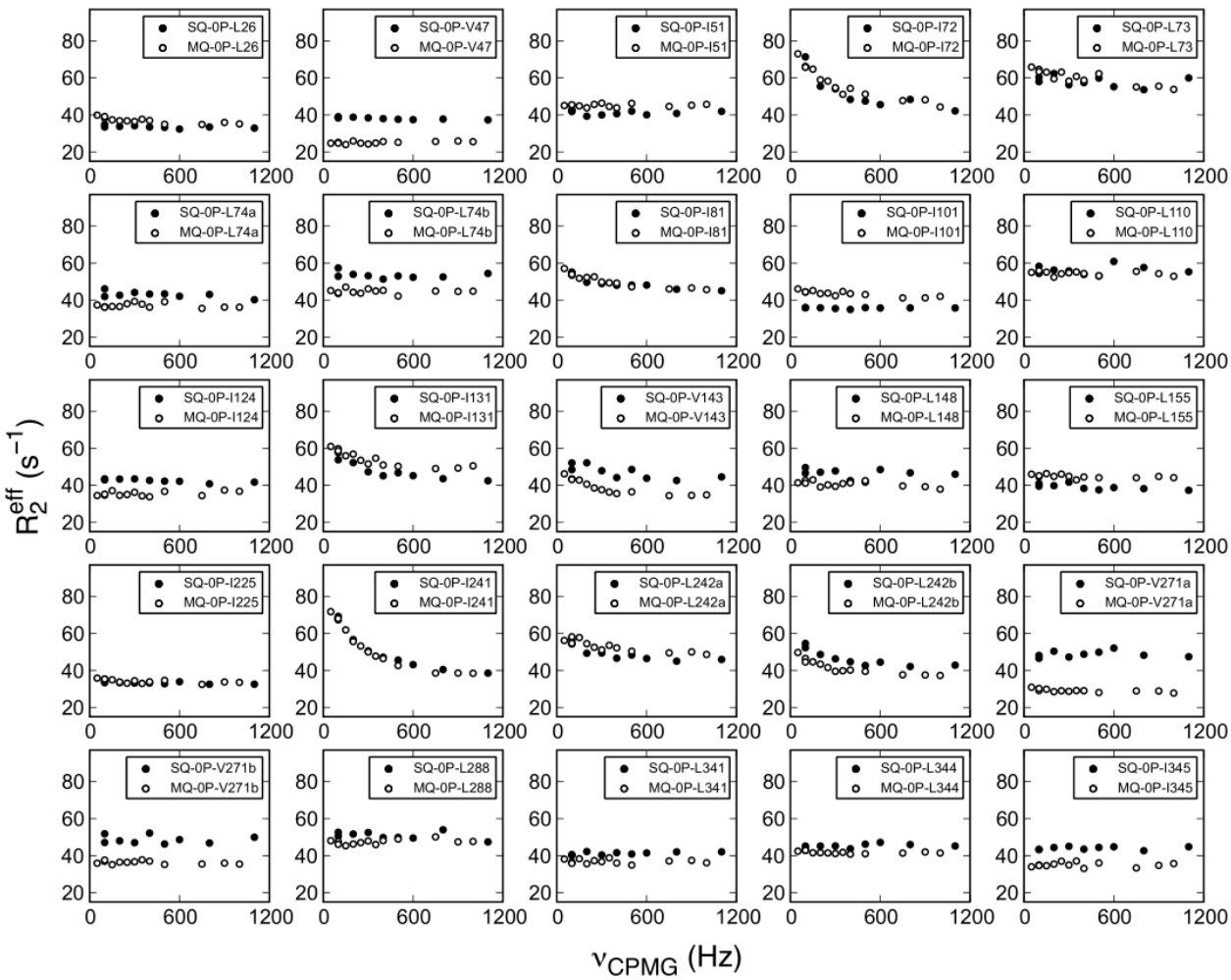

Figure 3.6. Single-quantum CPMG experiments show dispersion profiles similar to multiple-quantum CPMG experiments.

CPMG dispersion curves were comparable between 2D (^{13}C,^{1}H) single-quantum CPMG experiments (SQ, solid circles) and 2D (^{13}C, ^{1}H) multiple-quantum CPMG experiments (MQ, empty circles), for 0P-ERK2. Each set of experiments was carried out at 900 MHz and 25°C.

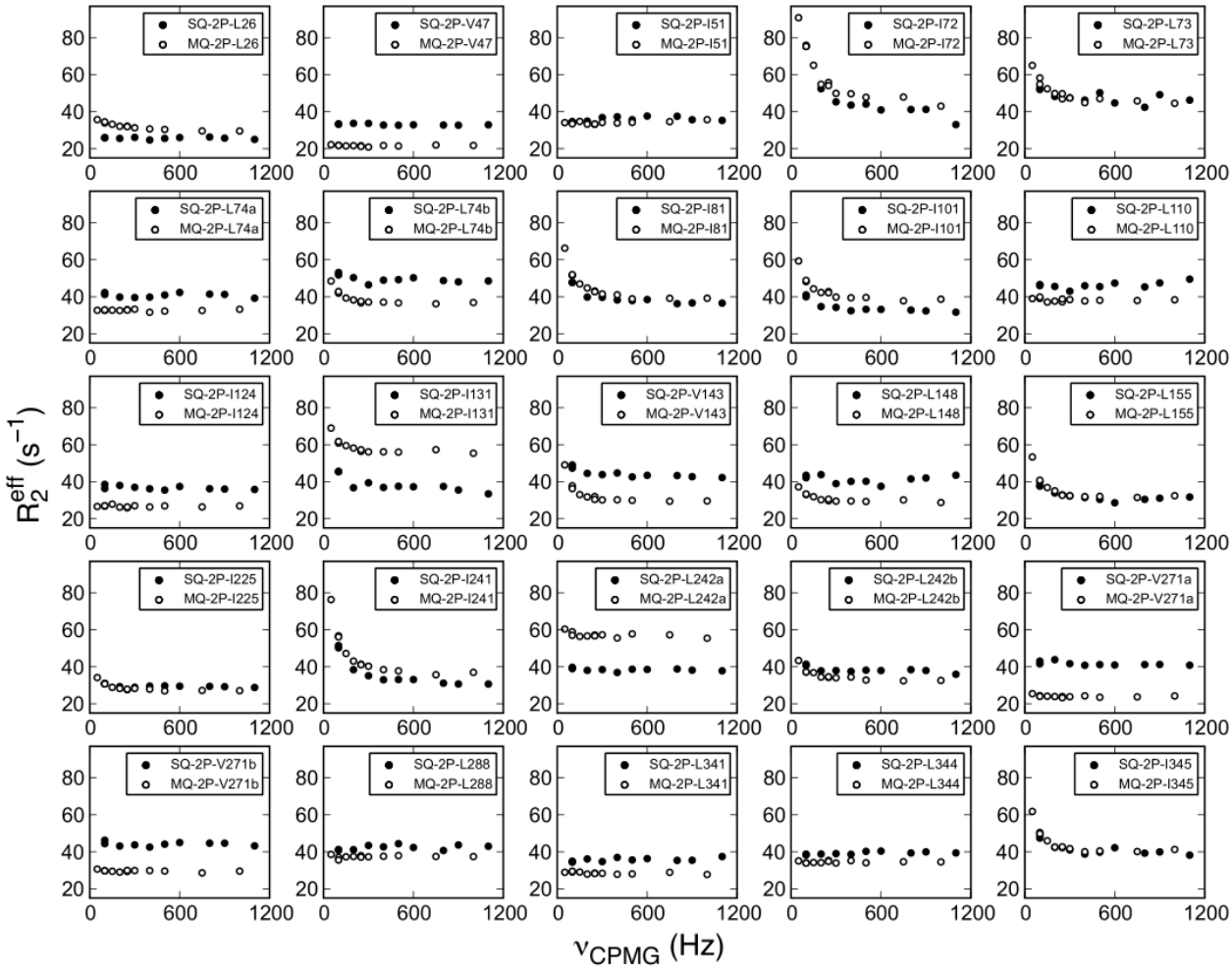

Figure 3.7. Single-quantum CPMG experiments show dispersion profiles similar to multiple-quantum CPMG experiments.

CPMG dispersion curves were comparable between 2D (^{13}C,^{1}H) single-quantum CPMG experiments (SQ, solid circles) and 2D (^{13}C, ^{1}H) multiple-quantum CPMG experiments (MQ, empty circles), for 2P-ERK2. Each set of experiments was carried out at 900 MHz and 25°C.

Table 3.5. Exchange parameters for methyl groups in 0P-ERK2, fitted individually*

Residue	Parameters			
	$k_{ex}(s^{-1})$ †	$R_{ex}(800)$ (s^{-1}) ‡	$p_A p_B(\Delta\omega^{13}C)^2$ (s^{-2}) §	χ^2/DF¶
Kinase core				
Ile72	1400 ± 400	23	32000 ± 5000	2.2
Leu73	900 ± 700	12	16000 ± 8000	3.2
Ile81	2000 ± 600	9	26000 ± 9000	0.8
Ile131	1700 ± 700	9	26000 ± 10000	0.9
IIe138‖	N.D.	7	N.D.	N.D.
Val143	1100 ± 600	9	11000 ± 4000	1.0
Ile163‖	N.D.	10	N.D.	N.D.
Ile241	1100 ± 200	26	40000 ± 2000	1.0
Leu242	1500 ± 300	13	19000 ± 3000	0.8
MAPK insert				
Leu198	1300 ± 300	15	10000 ± 2000	0.4
Leu235	1200 ± 200	29	45000 ± 3000	1.0
Ile253	2200 ± 300	20	62000 ± 15000	0.9
Leu262	1400 ± 300	22	34000 ± 3000	0.5

*These parameters were all obtained from MQ-CPMG dispersion data collected at 25°C.
†The k_{ex} values were obtained by fitting CPMG dispersion data collected at 600, 800 and 900 MHz to a two-state exchange process using Carver-Richards equation on a per-methyl basis. The errors were estimated from fits using the CATIA program and may be underestimated if the data are not well described by a two-state exchange process (see Methods).
‡$R_{ex}(800)$ was estimated using the equation $R_{ex} = R_{2,eff}(50\ Hz) - R_{2,eff}(1000\ Hz)$ from 800 MHz CPMG dispersion data.
§This term was estimated assuming a two-state exchange model under fast-exchange limit using 800 MHz CPMG dispersion data (see Methods).
¶The χ^2/DF (reduced chi-square) describes the quality of the fit for the experimental data. DF is the degrees of freedom and was calculated by DF= (number of experimental data points – number of parameters –1) for each methyl in the dataset.
‖Individual fits were not determined due to large errors, but the R_{ex} could still be estimated.

Methyl peaks from 13 residues in 0P-ERK2, showed significant conformational exchange dynamics (Figure 3.8A, Table 3.5). These residues were clustered in three regions located in the cleft between N- and C-terminal domains, including the αC-β4 loop, the β7-β8 loop, and helix αE. Other regions with significant exchange were located near the activation loop and the P+1 loop, helix αG, and helices in the MAP kinase insert, α1L14/α2L14. Individual fits of the relaxation dispersion data, yielded k_{ex} ranging between 900-2200 s^{-1} (Table 3.5). These exchange processes were fast on the NMR chemical shift timescale (i.e., $k_{ex} > |\Delta\omega^{13}C|$); therefore, it was not possible to confidently extract populations and chemical shift differences for individual methyls. Attempts to globally fit all or subsets of residues resulted in poorly defined populations. Thus, relaxation dispersion measurements on 0P-ERK2 were inconsistent with ILV residues undergoing a single exchange process. Instead, they reported fast conformational exchange processes in subdomains of the kinase, with little or no evidence for coupling between residues, including those with interacting methyl groups (Figure 3.8A).

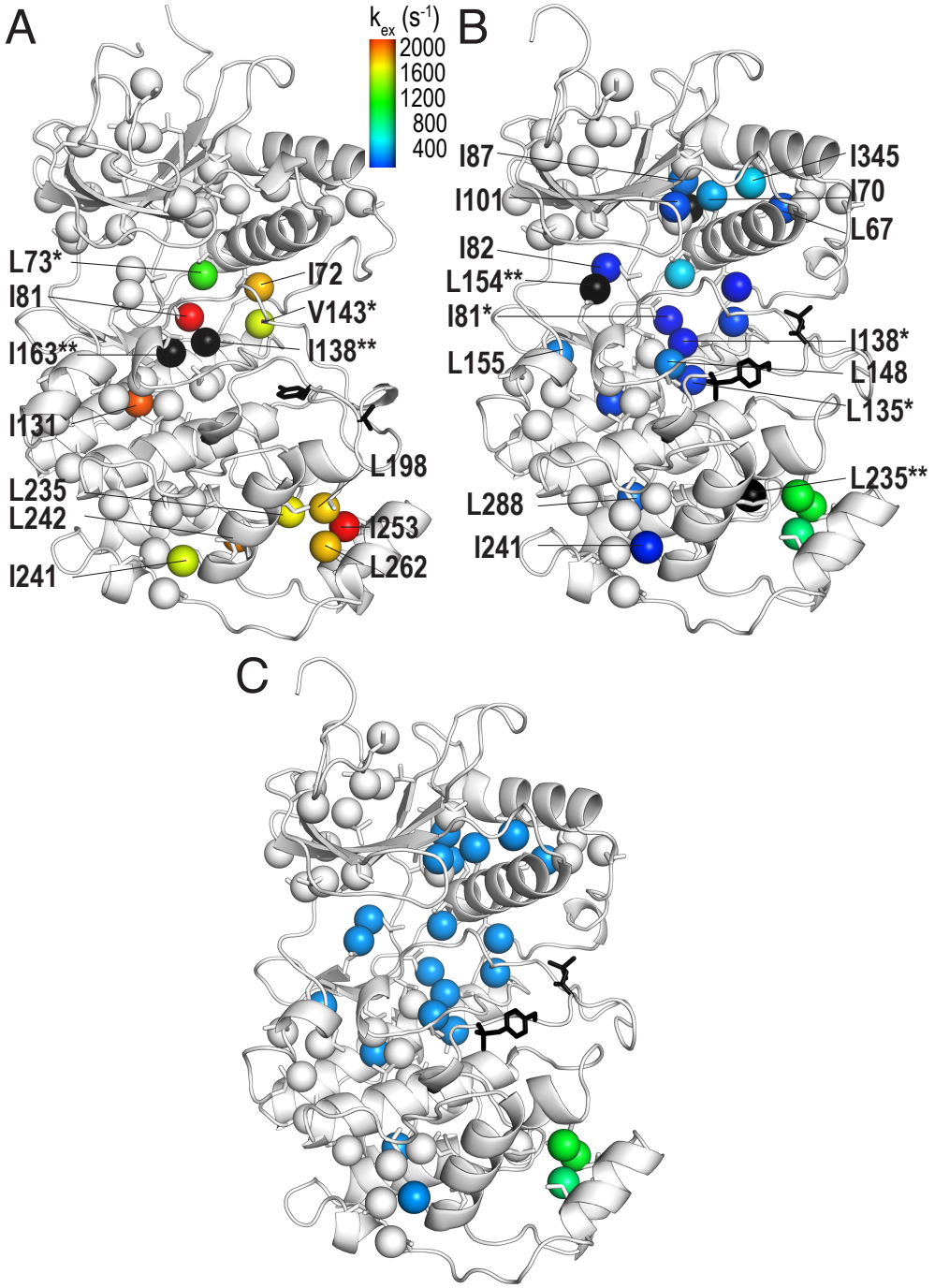

Figure 3.8. ERK2 phosphorylation induces global conformational exchange in the kinase core.
(A) Assigned methyls in 0P-ERK2 are shown as spheres with k_{ex} values indicated by the color scale for individual fits of methyls that have $R_{ex} > 4\ s^{-1}$. The asterisks and double asterisks indicate methyls having errors in $k_{ex} > 50$ and >100%, respectively, with the latter methyls shown as black spheres. Methyls with no observable dynamics ($R_{ex} \approx 0\ s^{-1}$) are shown as white spheres. Thr183 and Tyr185 are shown as black sticks. (B) Residues in 2P-ERK2 with observable dynamics each fitted individually, colored as in (A). (C) In 2P-ERK2, 19 methyls could be fit globally to a single rate constant ($k_{ex} = 300 \pm 10\ s^{-1}$) and population ($p_A/p_B = 80\%/20\% \pm 0.6\%$), demonstrating global domain motion for residues throughout the kinase core. Residues in the MAP kinase insert subdomain could not be fit by a global process.

3.3.3. Phosphorylation of ERK2 Induces Large-scale Conformational Exchange Dynamics

Significant changes in conformational exchange dynamics were observed between 0P-ERK2 and 2P-ERK2, as reflected by differences in their dispersion curves (Figure 3.3). Methyls from 22 residues in 2P-ERK2 showed significant R_{ex}. For many ILV methyls, the values of k_{ex}, populations, and $|\Delta\delta^{13}C|$ could be confidently fit for individual residues (Figure 3.8B, Table 3.6). Nineteen residues throughout the kinase core and in the catalytic pocket could be globally fit (Figure 3.8C), consistent with a single exchange process with $k_{ex} = 300 \pm 10\ s^{-1}$ and p_A and p_B populations of 80% and 20% (± 0.6%). They included residues at the hinge, the αC-β4 loop, and β5 which formed the hydrophobic cluster at the cleft between N- and C-terminal domains; N-terminal domain residues located at the interface between αC and β3-β4 strands; C-terminal domain residues at the interface between αE and αF; and C-terminal domain residues between αF and αG (Figure 3.8C). In contrast, residues in the MAP kinase insert could not be fit globally, but individual fits yielded k_{ex} values of 640 - 750 s^{-1}, significantly lower than the corresponding k_{ex} values of 1200 - 2200 s^{-1} in 0P-ERK2. The results revealed that phosphorylation of ERK2 induces a dramatic change in dynamics, where internal motions become dominated by a slow exchange process characterized by interconversion between two major conformational states with populations of 80% and 20%.

Table 3.6. Exchange parameters for methyl groups in 2P-ERK2, fitted individually*

Residue	Parameters					
	$k_{ex}(s^{-1})$ †	p_B (%) †	$\lvert\Delta\delta^{13}C_{CPMG}\rvert$ (ppm) †	$R_{ex}(800)$ (s^{-1})‡	χ^2/DF§	$\lvert\Delta\delta^{13}C_{global}\rvert$ (ppm) ¶
Kinase core						
Leu67	550 ± 400	2 ± 1 %	0.6 ± 0.3	9	2.3	0.1 ± 0.01
Ile70	210 ± 100	8 ± 2 %	0.4 ± 0.09	15	2.3	0.2 ± 0.01
Ile72	150 ± 60	28 ± 8 %	0.7 ± 0.07	40	2.7	0.6 ± 0.02
Leu73	230 ± 80	13 ± 2 %	0.4 ± 0.06	19	1.3	0.3 ± 0.01
Leu74‖	N.D.	N.D.	N.D.	10	N.D.	0.2 ± 0.01
Ile81	110 ± 60	17 ± 6 %	0.5 ± 0.09	19	0.7	0.3 ± 0.01
Ile82	140 ± 60	35 ± 12 %	0.7 ± 0.08	50	8.3	0.6 ± 0.02
Ile87	200 ± 90	19 ± 4 %	0.4 ± 0.1	22	0.9	0.3 ± 0.01
Ile101	220 ± 50	13 ± 2 %	0.4 ± 0.05	18	0.6	0.3 ± 0.01
Ile131	190 ± 50	11 ± 2 %	0.4 ± 0.05	13	0.5	0.2 ± 0.01
Leu135	180 ± 90	18 ± 3 %	0.4 ± 0.1	24	0.6	0.3 ± 0.01
IIe138	110 ± 90	8 ± 6 %	0.9 ± 0.1	10	2.1	0.3 ± 0.01
Val143	190 ± 50	16 ± 6 %	0.3 ± 0.06	14	0.8	0.2 ± 0.01
Leu148	290 ± 60	16 ± 6 %	0.3 ± 0.04	19	1.1	0.2 ± 0.01
Ile154‖	N.D.	N.D.	N.D.	20	N.D.	0.3 ± 0.01
Leu155	290 ± 50	13 ± 3 %	0.4 ± 0.05	17	1.6	0.3 ± 0.01
Ile241	160 ± 50	21 ± 3 %	0.5 ± 0.06	33	0.8	0.4 ± 0.01
Leu288	260 ± 220	15 ± 18 %	0.3 ± 0.3	16	1.7	0.2 ± 0.01
Ile345	380 ± 30	20 ± 20 %	0.1 ± 0.01	19	0.6	0.3 ± 0.01
Global fitting	**300 ± 10**	**80 ± 0.6 %**			**1.0**	**See above**
MAPK insert						
Leu198	750 ± 340	20 ± 100%	0.3 ± 0.7	25	2.0	
Leu235‖	N.D.	N.D.	N.D.	5	N.D.	
Ile253	750 ± 130	5 ± 3 %	0.5 ± 0.2	11	0.8	
Leu262	640 ± 80	60 ± 70 %	0.1 ± 0.04	11	0.8	

*These parameters were all obtained from MQ-CPMG dispersion data collected at 25°C.

†These parameters were obtained by fitting CPMG dispersion data collected at 600, 800 and 900 MHz to a two-state exchange process using Carver-Richards equation on a per-methyl basis. The errors were estimated from fits using the CATIA program and may be underestimated if the data are not well described by a two-state exchange process (see Methods).

‡$R_{ex}(800)$ was estimated using the equation $R_{ex} = R_{2,eff}(50\ Hz) - R_{2,eff}(1000\ Hz)$ from 800 MHz CPMG dispersion data.

§The χ^2/DF (reduced chi-square) describes the quality of the fit for the experimental data. DF is the degrees of freedom and was calculated by DF= (number of experimental data points – number of parameters –1) for each methyl in the dataset.

¶The $\lvert\Delta\delta^{13}C_{global}\rvert$ is obtained by a global fitting of the methyls in the kinase core that showed $R_{ex}(800) > 4\ s^{-1}$ using CATIA.

‖Individual fits were not determined due to large errors, but the R_{ex} could still be estimated.

3.3.4. Phosphorylation Shifts the Equilibrium between Two Conformational States

We next examined the temperature dependence of the HMQC spectra of 2P-ERK2. Several methyls appeared as two discrete peaks at 5 ºC, indicating two conformational states in slow exchange on the NMR chemical shift timescale (Figure 3.9A). These methyls showed similar populations of the two states, varying from 50%:50% at 5 °C to 80%:20% at 25 °C. Importantly, the populations at 25 °C matched those obtained from the global fits of the relaxation dispersion experiments (Table 3.6). The similarity in population from these two independent experiments let us ask the question if they were reporting the same conformational exchange process of 2P-ERK2. To confirm this, we performed several 1D line shape simulations based on the populations, line width and chemical shift difference of the two states of the I72 methyl on the HMQC spectra, and varied k_{ex} values around 300 s^{-1}. The simulation showed excellent line shape fit of I72 using parameters k_{ex} = 150 s^{-1}, p_A/p_B =80%/20%, line width = 30 Hz, and $\Delta\omega$ = 100 Hz. This consistency demonstrates that the conformational exchange process reflects two discrete conformers, which shift their populations with temperature.

Thermodynamic parameters determined from van't Hoff plots were most accurately measured for I72 because the two exchanging populations of I72 methyl could be estimated at all of the five temperatures (5 °C, 10 °C, 15 °C, 20 °C and 25 °C). This estimation yielded $\Delta H°$ = 9.7 ± 1.1 kcal/mol and $\Delta S°$ = 37 ± 2 cal/mol/K (Figure 3.11A) for the reaction A ⇌ B, where A denotes for the minor state, and B denotes for the major state in 2P-ERK2 at 25 °C. Thermodynamic parameters estimated for other residues (e.g. I72, I131 and L288, Table 3.7) were consistent with these values, indicating that the same conformational exchange processes underlies dynamics throughout most of the molecule. The exception was I241, located within helix αG, which gave $\Delta H°$ = 5.8 ± 1.1 kcal/mol and $\Delta S°$ = 22 ± 3 cal/mol/K (Figure 3.11B), indicating a distinct process.

In 0P-ERK2, each methyl group appeared as one peak in the HMQC spectra. In each case, peaks from 0P-ERK2 overlapped well with those corresponding to the minor conformational state in 2P-ERK2 (i.e., with 20% population at 25 °C) (Figure 3.9B). Thus, based on chemical shifts, the major state in 0P-ERK2 corresponds to the minor state in 2P-ERK2. In 0P-ERK2, the single observed conformer (population >99.5%) exchanges with an unobservable conformer (population < 0.5%), from which $\Delta G°$ can be estimated as > +3.1 kcal/mol. In 2P-ERK2, interconverting conformers represent two states with populations of 80% and 20%, yielding $\Delta G° = -0.8$ kcal/mol.

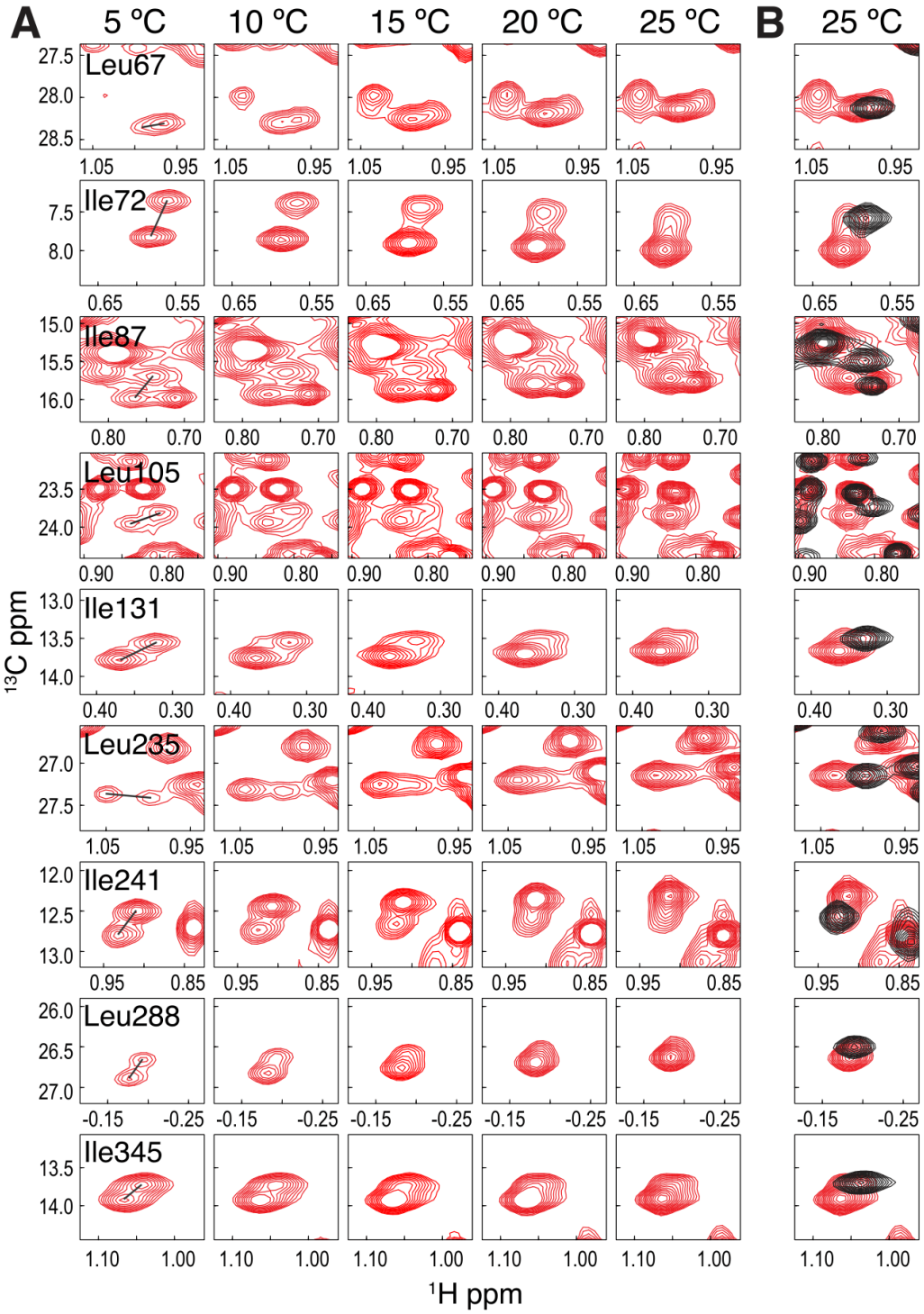

Figure 3.9. Methyl peaks reveal a slow conformational exchange process in 2P-ERK2.
(A) 2D (^{13}C, ^{1}H) methyl HMQC spectra of 2P-ERK2 from 5-25 °C show that many methyls have two distinct peaks that are undergoing slow conformational exchange on the NMR chemical shift timescale. The black lines on the 5°C spectra highlight the two exchanging peaks, indicating two well-populated states. (B) Overlay of spectra from 0P- (black) and 2P-ERK2 (red) at 25 °C shows that the higher populated state in 0P-ERK2 corresponds to the lower populated state in 2P-ERK2.

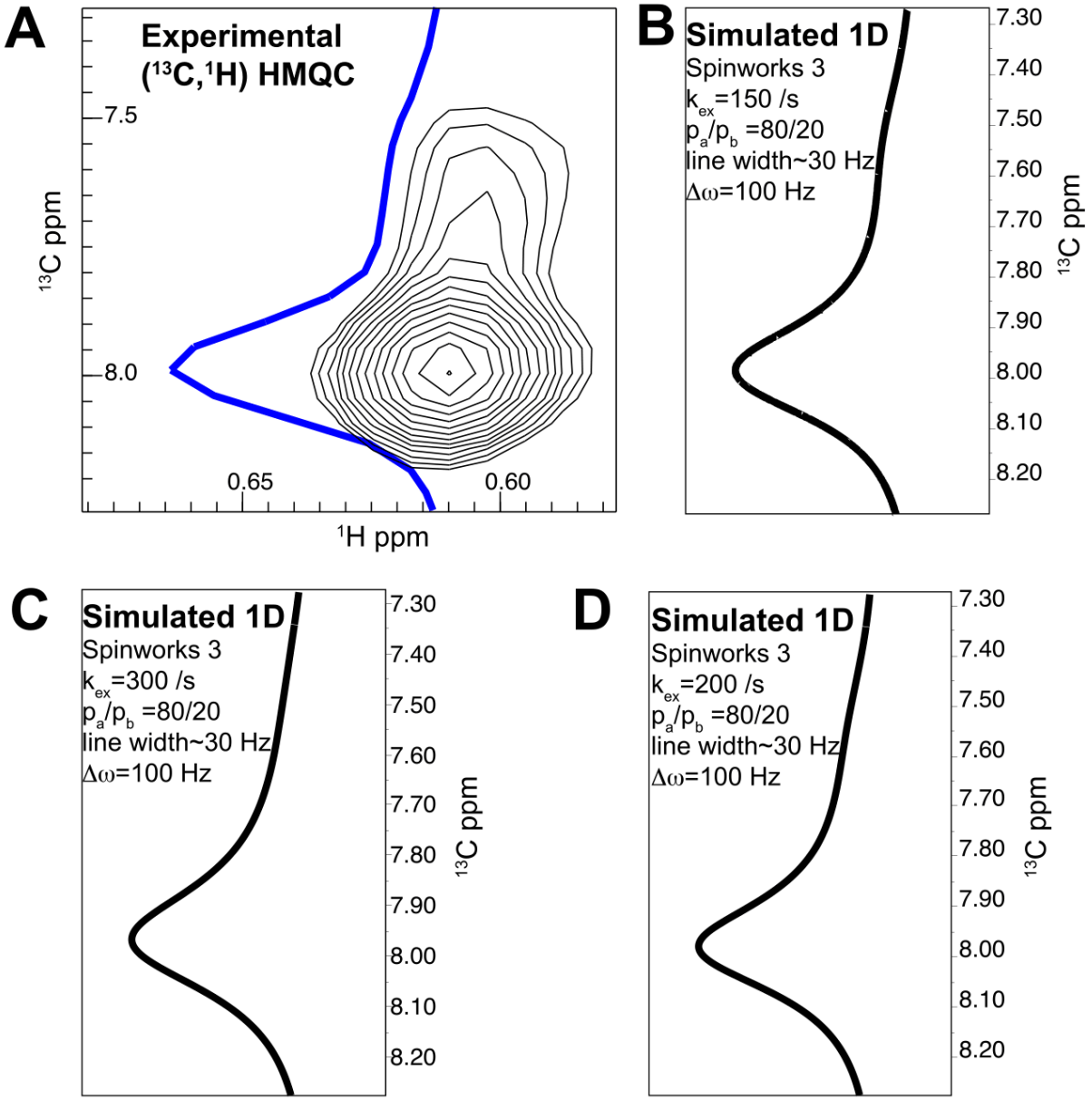

Figure 3.10. 1D Line shape simulation of I72 methyl peak in 2P-ERK2.
(A) 2D (^{13}C,^{1}H) HMQC spectra showing I72 methyl of 2P-ERK2, with a 1D side trace displayed using CcpNmr. (B) The experimental side trace is best mimicked by a simulation with parameters k_{ex} = 150 s^{-1}, p_A/p_B =80%/20%, line width = 30 Hz, and Δω = 100 Hz. (C) Simulation was performed using the same settings as (B) except k_{ex} = 300 s^{-1}. (D) Simulation was performed using the same settings as (B) except k_{ex} = 200 s^{-1}.

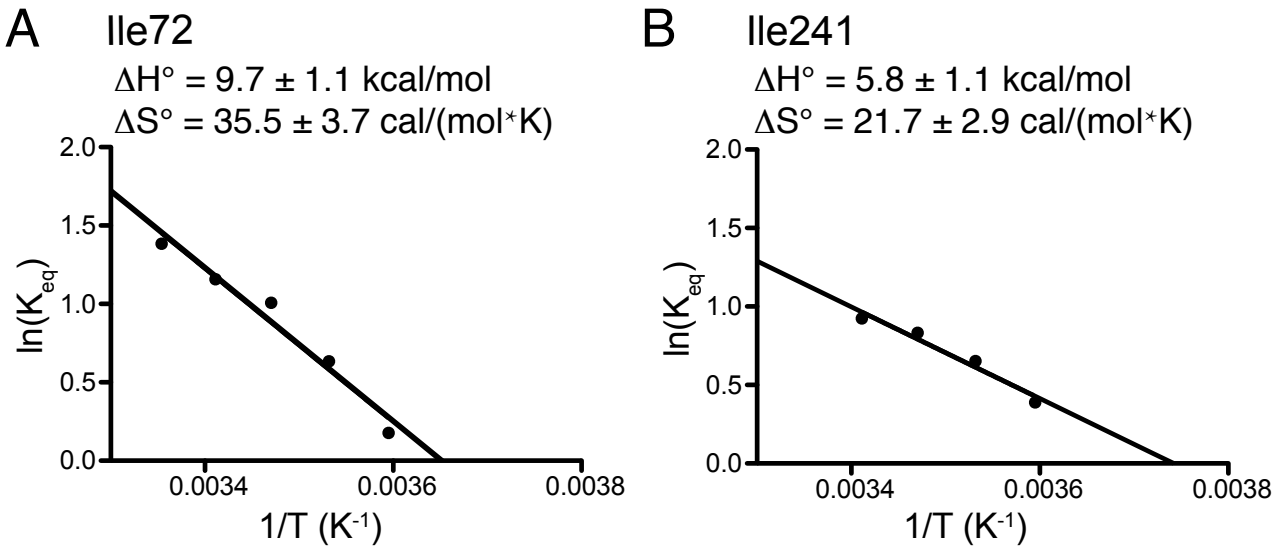

Figure 3.11. Enthalpies and entropies estimated from 2D (^{13}C, ^{1}H) HMQC spectra.
Van't Hoff plots for (A) I72 and (B) I241 where the K_{eq} values were estimated from the volumes of the two peaks that showed slow exchange for individual methyls in the HMQC spectra at different temperatures (Figure 3.9).

Table 3.7. Summary of thermodynamic properties of slow exchanging peaks

Residue ID	ΔH°, kcal/mol	ΔS°, kcal/(mol•K)	N[a]
Ile72	9.7 ± 1.1	35.5 ± 3.7	5
Ile131[b]	10.8 ± 1.2	39.3 ± 4.1	3
Ile345[b]	11.1 ± 1.2	39.8 ± 4.2	3
Ile87[b]	9.8 ± 1.1	35.0 ± 3.7	3
Leu288[b]	9.9 ± 1.1	35.7 ± 3.8	2
Ile241	5.8 ± 1.1	21.7 ± 2.9	4
Leu235[b]	7.9 ± 1.1	29.0 ± 3.0	2
Leu105[b]	8.8 ± 1.1	31.4 ± 3.3	2

[a]N denotes for the number of points used in the calculation. Each point is the ratio of the two populations under one temperature.
[b]Standard deviations were calculated from percent error on Ile72, which has the most points.

We have shown in the previous section that the two-exchanging states of a methyl group showed similar populations and exchange rate constants from both HMQC and CPMG experiment, supporting that these two experiments report the same process of A ⇌ B. Here, we wanted to further test if there is any correlation between the chemical shift differences of two-exchanging states for individual methyls, in order to determine if HMQC spectra and CPMG experiments agree[39]. Because the two exchanging states A (20%) and B (80%) in 2P-ERK2 fell into the slow-intermediate regime, the "real" chemical shift difference ($|\Delta\omega_{BA}|$ in Hz, or $|\Delta\delta_{HMQC}{}^{13}C|^*$ in ppm) is larger than the observed chemical shift difference, and needs some adjustment. To adjust for the chemical shift difference of the two slow exchanging states A and B $|\Delta\omega_{BA}|$ on the HMQC spectra of 2P-ERK2, Ω_B is solved using the following equation that comes from a numerical solution to the Bloch-McConnell equation for two-state exchange, assuming equal transverse relaxation rate constants between the two states ($R_{2A}^0 = R_{2B}^0$)[35]:

$$\Omega_{ex} = \frac{\Omega_A+\Omega_B}{2} \pm \frac{1}{\sqrt{8}}\left\{\Delta\omega_{BA}{}^2 - k_{ex}^2 + \left[\left(k_{ex}^2 + \Delta\omega_{BA}{}^2\right)^2 - 16p_Ap_B\Delta\omega_{BA}{}^2k_{ex}^2\right]^{\frac{1}{2}}\right\}^{\frac{1}{2}}$$

and $|\Delta\omega_{BA}| = |\Omega_B - \Omega_A|$ (Equation 3.7)

where Ω_A and Ω_B are the chemical shifts of the two exchanging states A and B in 2P-ERK2, Ω_{ex} is the observed dominant chemical shift, k_{ex} is the rate constant for the exchange, and p_A and p_B are populations of state A and B respectively. To solve for the chemical shift of state B (Ω_B), from which $|\Delta\omega_{BA}|$ or $|\Delta\delta_{HMQC}{}^{13}C|^*$ can be immediately obtained, parameters Ω_A, Ω_{ex}, k_{ex}, and p_A need to be known. We set Ω_A equal to the ^{13}C chemical shift of 0P-ERK2 at 25 °C, because it is hard to determine the observed chemical shift of the 20% population state in 2P-ERK2. We set Ω_{ex} equal to the observed ^{13}C chemical shift of 2P-ERK2 at 25 °C. The exchange rate constant k_{ex} is set to 300 s^{-1}, and populations p_A and p_B were set to 80% and 20%. To confirm that the CPMG relaxation data and the

slow exchange in HMQC spectra reflect the same process, the chemical shift difference of individual methyls in the two-exchanging states from the global fitting of CPMG experiment ($|\Delta\delta_{CPMG}{}^{13}C|$) was compared with the HMQC spectra ($|\Delta\delta_{HMQC}{}^{13}C|^*$) of 2P-ERK2 (Figure 3.12). Although one methyl (I72) with the largest chemical shift difference (~0.6 ppm) in the CPMG analysis also showed the large chemical shift difference (~0.45 ppm) in the HMQC analysis, the rest of the methyls had too small chemical shift differences to extract any reliable correlation.

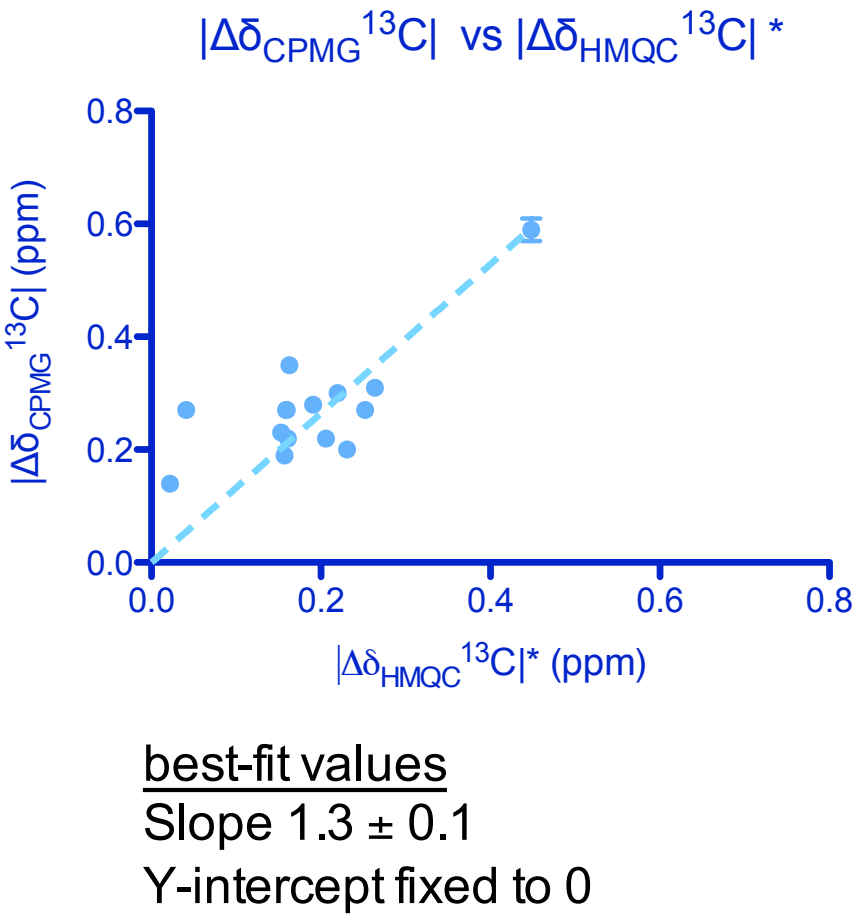

Figure 3.12. Comparison of the chemical shift difference of methyls from the global fitting of CPMG experiment ($|\Delta\delta_{CPMG}{}^{13}C|$) with the corrected chemical shift difference of methyls that undergoes slow exchange in the HMQC spectra ($|\Delta\delta_{HMQC}{}^{13}C|^*$)of 2P-ERK2.
Chemical shift differences of the two states from the HMQC spectra were adjusted (labeled with the asterisk) for the comparison. Error bars are the errors of individual $|\Delta\delta_{CPMG}{}^{13}C|$. The dashed line represents a linear regression of these data points with Y-intercept fixed to zero.

3.3.5. Global Dynamics of 2P-ERK2 at Varied Temperatures

Relaxation dispersion experiments were performed on 2P-ERK2 at lower temperatures (17.5 and 10 °C). Global fitting of the 17.5 °C dispersion data into a two-state exchange process could be performed with 16 methyls (res.id. 67, 70, 72, 73, 74, 81, 87, 101, 131, 135, 138, 143, 148, 155, 241 and 345; Figure 3.13) yielding k_{ex} = 160 ± 20 s^{-1} and p_A and p_B populations of 19% and 81%, respectively (each ± 2%). Similar k_{ex} and population values were obtained when a subset of methyls surrounding the active site were fit globally (res.id. 70, 72, 73, 74, 81, 87, 101, 138, 143, 148, 155 and 345) to a two-state exchange process, yielding a k_{ex} = 150 ± 20 s^{-1} and p_A and p_B populations of 21% and 79% (± 2%). From this, we estimate k_{AB} =120 s^{-1}, and k_{BA}=30 s^{-1}. Thus, from 25 °C to 17.5 °C, the k_{AB} decreased by 2-fold from 240 to 120 s^{-1}, and k_{BA} decreased by 2-fold from 60 to 30 s^{-1}.

At 10 °C, global fitting of the relaxation dispersion data for 2P-ERK2 to a two-state exchange model did not yield a well-defined k_{ex} when p_A (or p_B) was set to a variable, due to the smaller magnitude of R_{ex} at low temperature. But because slow exchange was observed for several methyls of 2P-ERK2, the populations of the two states could be estimated. For example, the methyl peak for I72 showed p_A:p_B=65:35 at 10 °C. This was used to fix p_B to 35% in the global fitting of the 10 °C dispersion data, which included 9 methyls (res.id. 70, 72, 81, 101, 135, 138, 143, 155 and 345; Figure 3.14). This yielded a k_{ex} = 50 ± 2 s^{-1}, with k_{AB} =32 s^{-1} and k_{BA}=18 s^{-1}. Therefore, from 25 °C to 10 °C, the k_{AB} decreased by 8-fold from 240 to 32 s^{-1}, and k_{BA} decreased by 3-fold from 60 to 18 s^{-1}. This provides information on the activation energies for the reaction A ⇌ B in 2P-ERK2.

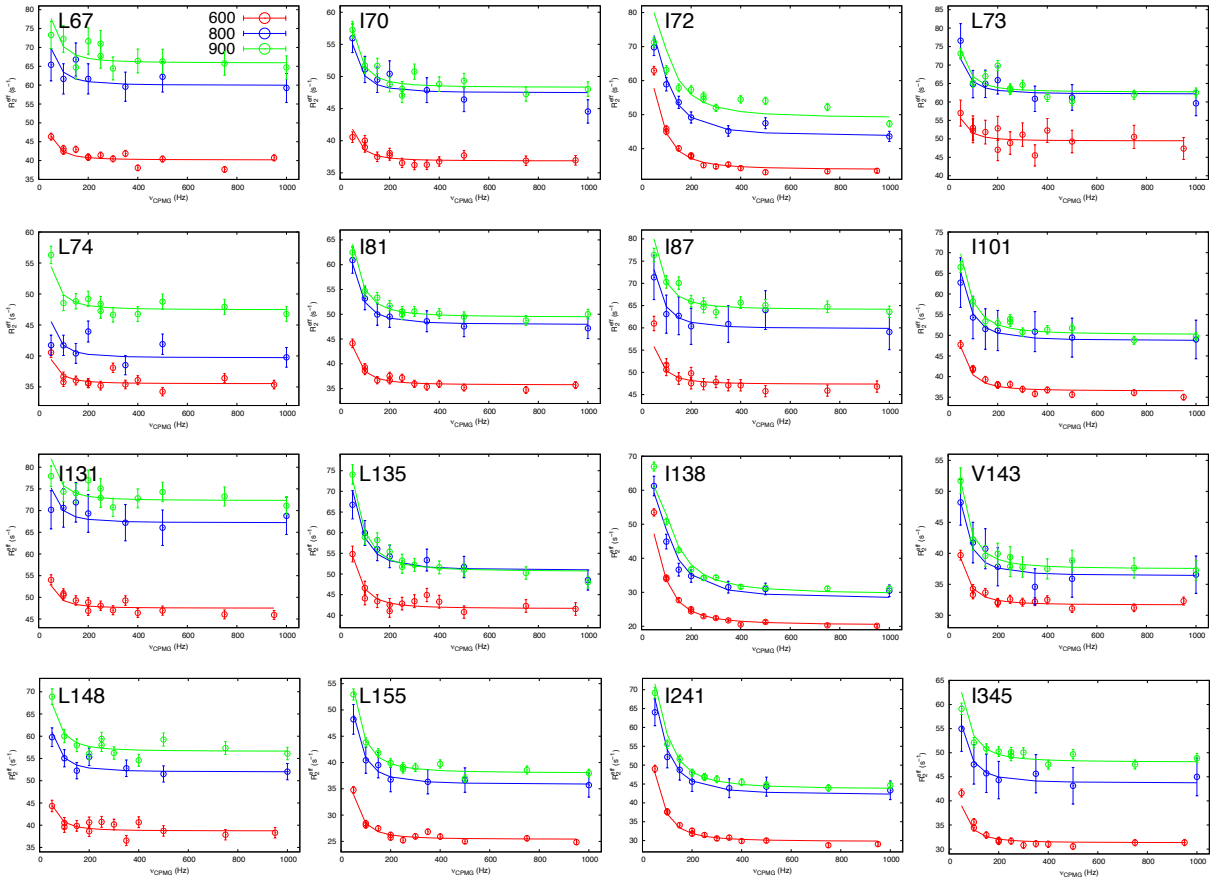

Figure 3.13. CPMG relaxation dispersion curves of 2P-ERK2 at 17.5 °C.
Relaxation dispersion curves at 17.5 °C and 900 (green), 800 (blue), and 600 (red) MHz are plotted for all residues that showed significant R_{ex} in 2P-ERK2. Lines show a global two-state exchange fit with all the above methyls and the error bars were estimated from peak intensities of duplicate experiments.

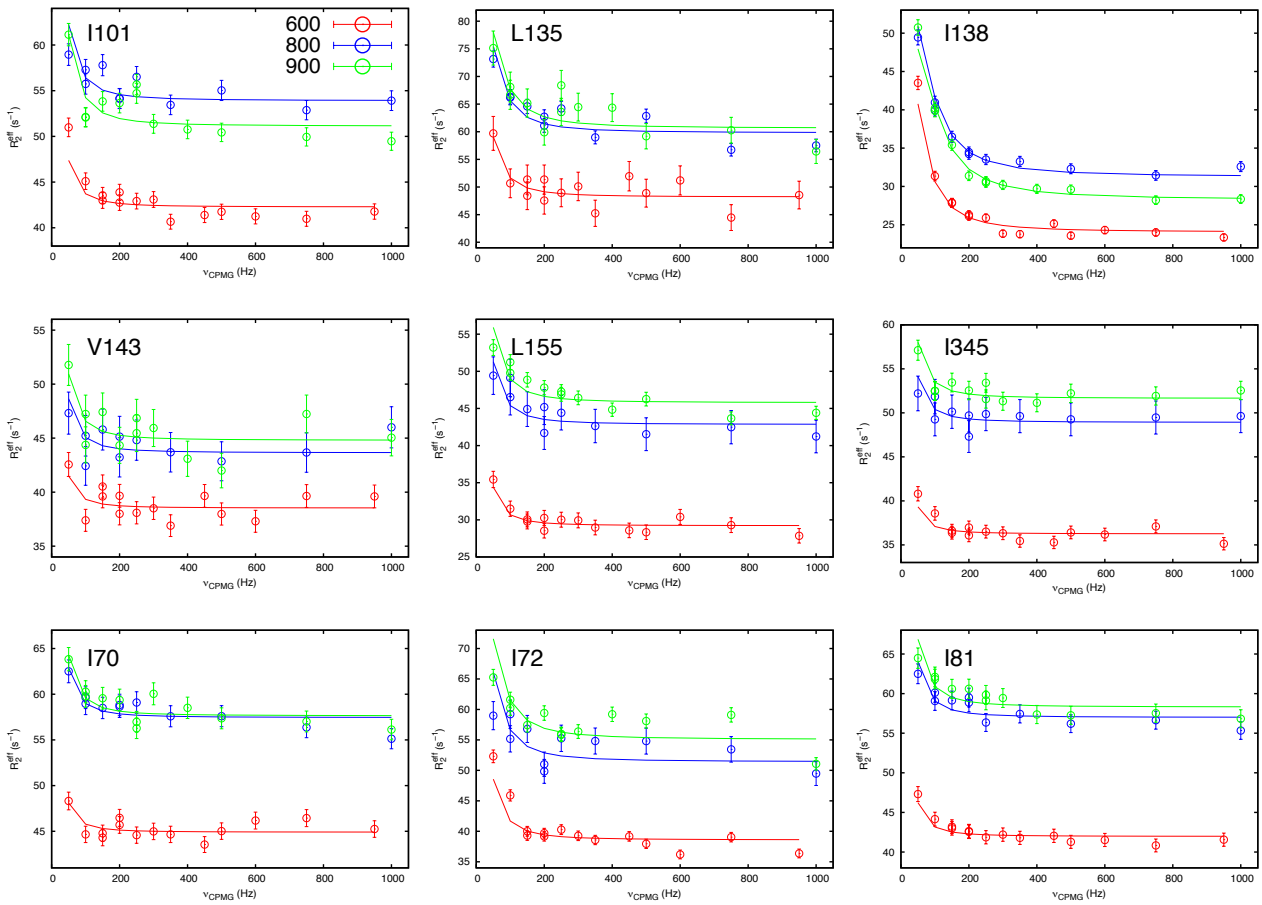

Figure 3.14. CPMG relaxation dispersion curves of 2P-ERK2 at 10 °C.
Relaxation dispersion curves at 17.5 °C and 900 (green), 800 (blue), and 600 (red) MHz are plotted for all residues that showed significant R_{ex} in 2P-ERK2. Lines show a global two-state exchange fit with all the above methyls and the error bars were estimated from peak intensities of duplicate experiments.

The temperature dependence of rate constants for 2P-ERK2 was used to depict the energy landscape of the transition state for the conformational exchange process. The activation energy of the exchange process (E_a) was estimated by fitting k_{AB} and k_{BA} values *vs* 1/T according to the following Arrhenius equation[123]:

$$\ln(k) = \frac{-E_a}{R}\frac{1}{T} + \ln(A) \qquad \text{(Equation 3.8)}$$

where R is the gas constant, A is the pre-exponential factor that is related to molecular collision, and T is the temperature in Kelvin. Linear fitting of k_{AB} and k_{BA} measured at three temperatures (Figure 3.15) yielded estimates of $E_{a,\,AB} \approx 24$ kcal/mol, and $E_{a,\,BA} \approx 14$ kcal/mol. Alternatively, the k_{AB} and k_{BA} values could be used to estimate the enthalpy of activation ($\Delta H^{\ddagger}$), the entropy of activation ($\Delta S^{\ddagger}$) and the Gibbs energy of activation ($\Delta G^{\ddagger}$) using the following Eyring equation[123]:

$$\ln\left(\frac{k}{T}\right) = \frac{-\Delta H^{\ddagger}}{R}\frac{1}{T} + \ln\left(\frac{k_B}{h}\right) + \frac{\Delta S^{\ddagger}}{R} \qquad \text{(Equation 3.9)}$$

where R is the gas constant, k_B is the Boltzmann constant, and h is the Plank constant. Linear fitting of k_{AB} and k_{BA} values at three temperatures (Figure 3.16) yielded estimates of $\Delta H^{\ddagger}_{AB} \approx 23.2$ kcal/mol, $\Delta H^{\ddagger}_{BA} \approx 13.5$ kcal/mol, $\Delta S^{\ddagger}_{AB} \approx 30.2$ cal/mol/K ($T\Delta S^{\ddagger}_{AB} \approx 9.0$ kcal/mol), and $\Delta S^{\ddagger}_{BA} \approx -5.5$ cal/mol/K ($T\Delta S^{\ddagger}_{BA} \approx -1.6$ kcal/mol) at 298 K (25 °C). The Gibbs energy of activation ($\Delta G^{\ddagger}$)[123] is estimated by the following equation:

$$\Delta G^{\ddagger} = \Delta H^{\ddagger} - T\Delta S^{\ddagger} \qquad \text{(Equation 3.10)}$$

from which we estimated $\Delta G^{\ddagger}_{AB} \approx 14.2$ kcal/mol, and $\Delta G^{\ddagger}_{BA} \approx 15.1$ kcal/mol. Thus, the difference in free energy between the two conformations is approximately -0.9 kcal/mol, calculated using the activation free energy ($\Delta\Delta G = \Delta G^{\ddagger}_{AB} - \Delta G^{\ddagger}_{BA}$), which is consistent with the $\Delta G°$ of -0.8 kcal/mol measured from the populations of the two conformations at 25 °C. These values are summarized as an energy landscape in Figure 3.17.

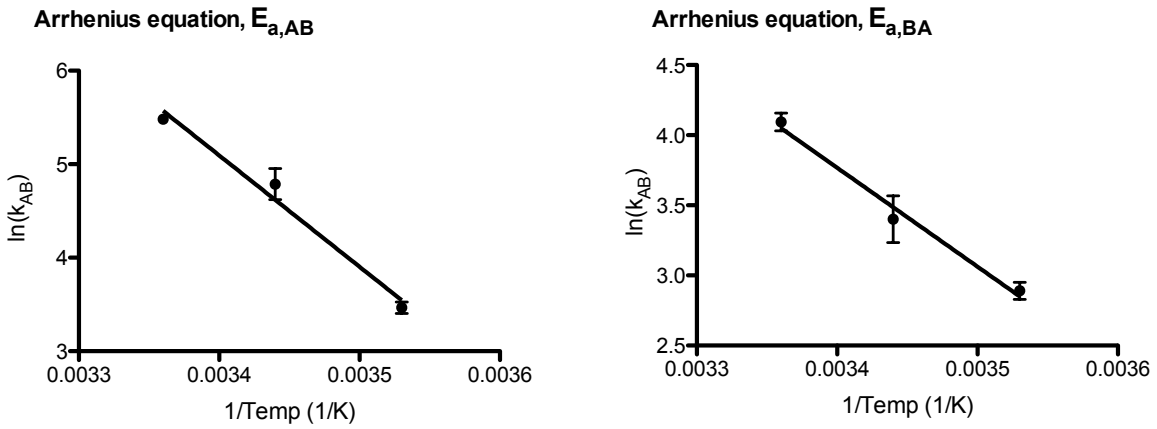

Figure 3.15. Activation energy was estimated from rate constants at varied temperatures.
Natural logarithm of the rate constants (k_{AB}, k_{BA}) were plotted against the inverse of temperature (1/T), using rate constants obtained from CPMG experiments at 283 K (10 °C), 290.5 K (17.5 °C) and 298 K (25 °C). The line shows the linear regression fit of these 3 data points. The error of k_{AB} or k_{BA} was propagated from k_{ex} and populations obtained in the CATIA fitting. The slope and Y-intercept of this linear regression were labeled underneath the plot.

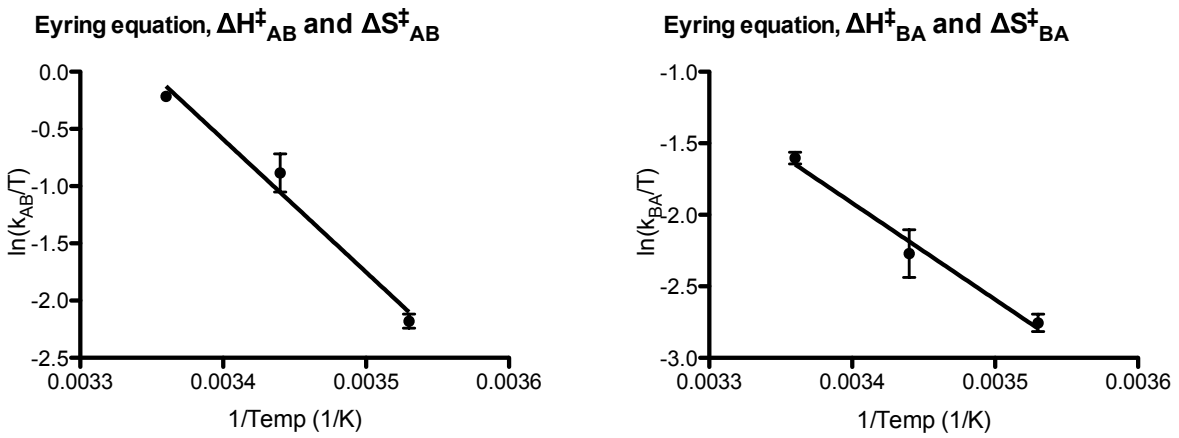

Figure 3.16. Activation enthalpy and entropy were estimated from rate constants at varied temperatures. Natural logarithm of the ratio of rate constants (k_{AB}, k_{BA}) and temperature (T) were plotted against 1/T, using rate constants obtained from CPMG experiments at 283 K (10 °C), 290.5 K (17.5 °C) and 298 K (25 °C). The line shows the linear regression fit of these 3 data points. The error of k_{AB} or k_{BA} was propagated from k_{ex} and populations obtained in the CATIA fitting. The slope and Y-intercept of this linear regression were labeled underneath the plot.

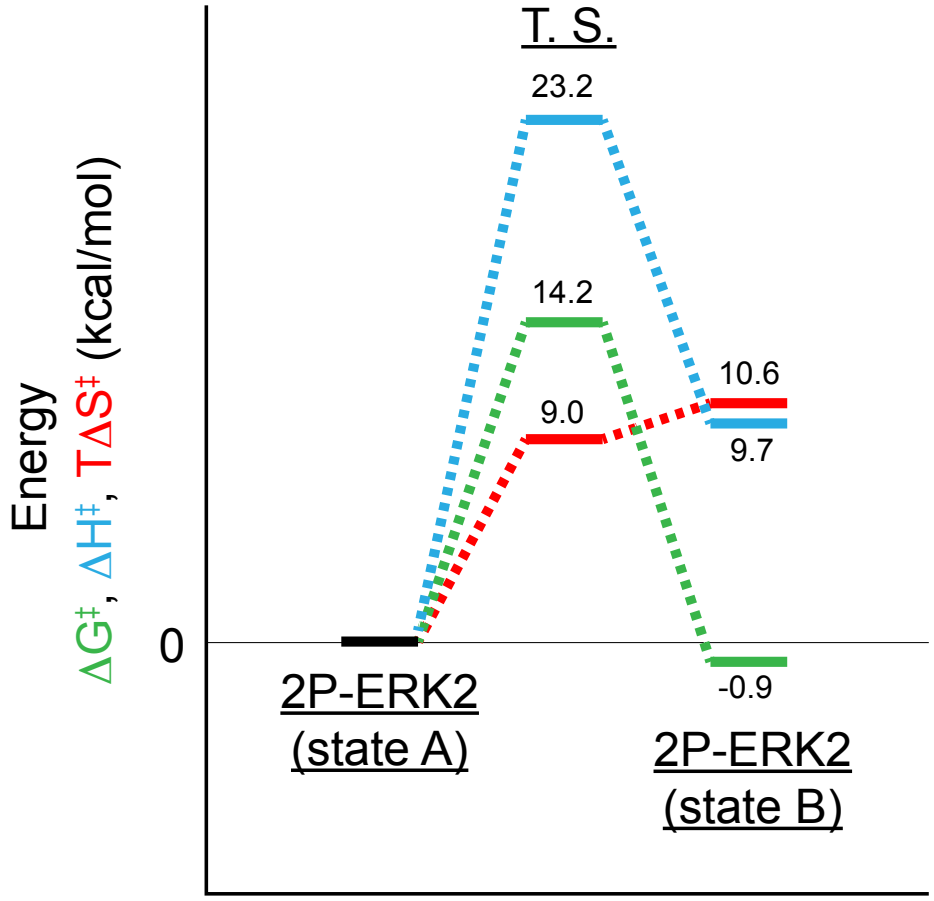

Figure 3.17. Energy landscape of the conformational exchange in 2P-ERK2.
Energy barriers at 298 K were calculated using the temperature dependence of the exchange rate constants. The minor state in 2P-ERK2 (state A) at 298 K is arbitrarily set to 0 kcal/mol as a reference. T.S. represents the transition state of the conformational exchange between state A and B.

3.3.6. The Conformational Switch Is Perturbed by Hinge Residues

We next asked what type of dynamics might be reflected by a large-scale two-state exchange process involving residues throughout the consensus kinase core. This is not likely to be inter-molecular motion from a dimerization process, because both 0P-ERK2 and 2P-ERK2 showed Stokes radii consistent with monomeric forms (Figure 3.18) using size exclusion chromatography. Prior HX-MS studies suggested that phosphorylation of ERK2 leads to enhanced backbone flexibility at the hinge, reducing the constraint for interdomain motion between N- and C-terminal domains [109]. We therefore asked whether increased hinge motion could affect the conformational exchange process, as measured by NMR.

To address this, mutations were engineered to increase conformational mobility at the hinge, by replacing residues M106-E107 with G-G to create a "ME/GG-ERK2" mutant. HMQC spectra were acquired on the ^{13}C-methyl-ILV labeled ME/GG-ERK2 and assigned as described in Methods. The chemical shifts of the methyls in ME/GG-ERK2 overlaid well with wild-type 0P-ERK2, except for residues near the mutation site where structural changes would be expected (Figure 3.19 and Figure 3.20).

Relaxation dispersion experiments on unphosphorylated ME/GG-ERK2 showed that methyl groups of 21 ILV residues had significant dynamics, and were located throughout the enzyme (Figure 3.19C, Table 3.8). These corresponded to 12 of the 13 residues with significant R_{ex} in 0P-ERK2, and 14 of 22 residues with significant R_{ex} in 2P-ERK2. Importantly, 16 residues throughout the kinase core could be fit to a single exchange model, indicating a global motion with $k_{ex} = 500 \pm 60\ s^{-1}$ and populations of 97% and 3% (± 0.2%) (Figure 3.19C). The similar chemical shifts for ME/GG-ERK2 and 0P-ERK2, especially for the methyls that showed large dispersions (e.g. V99, I72, and I131) means that the dominant state is similar in both proteins. Within the MAPK insert of ME/GG-ERK2,

k_{ex} values of 1200-1600 s^{-1} were observed, comparable to the rate constants in 0P-ERK2. Therefore, ME/GG partially mimics the shift in conformational exchange dynamics induced by phosphorylation and activation of ERK2.

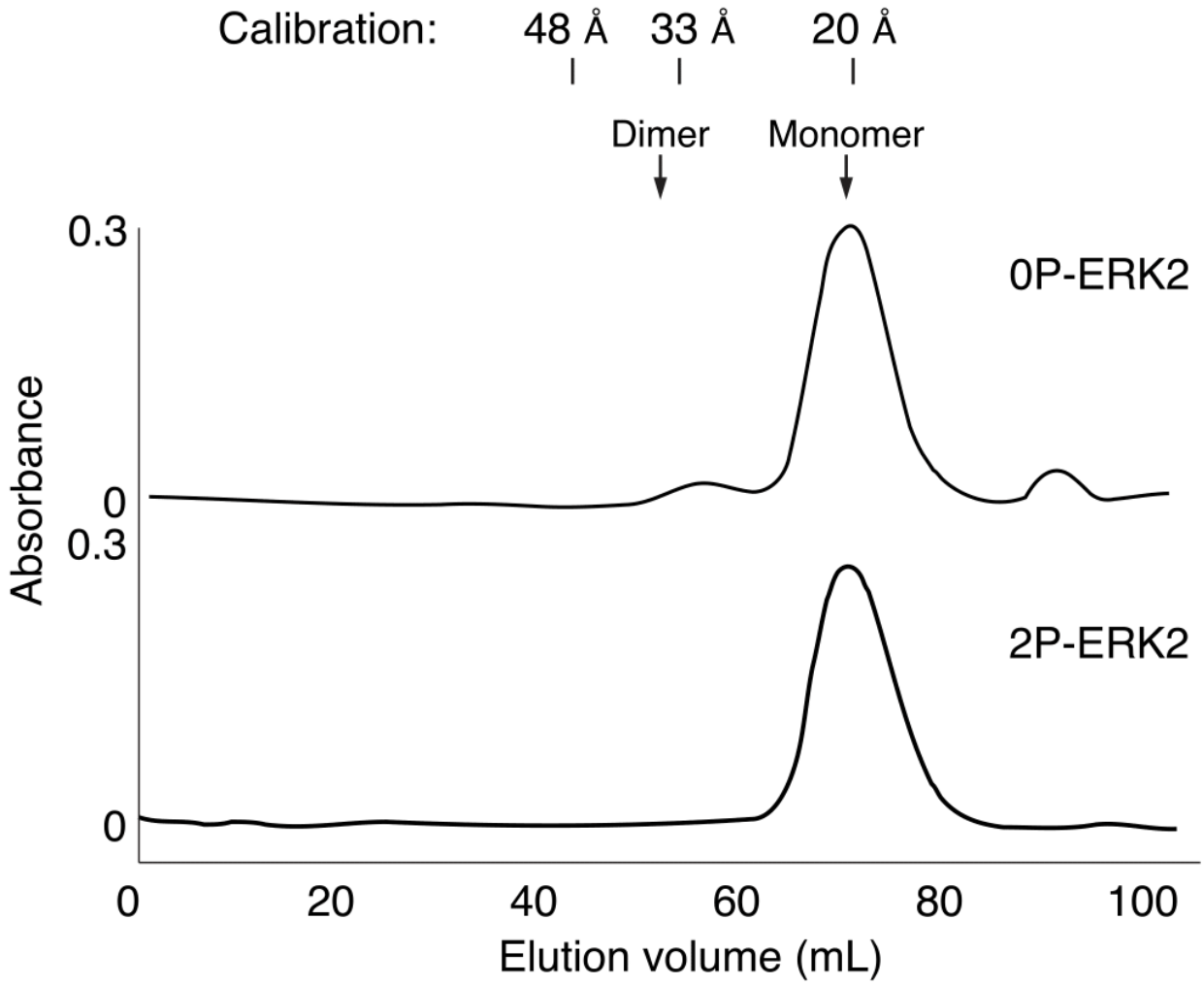

Figure 3.18. 0P-ERK2 and 2P-ERK2 are monomeric.
Size exclusion chromatography (Sephacryl S200) of the $^{1}H,^{13}C$-ILV-methyl-labeled 0P-ERK2 and 2P-ERK2 samples used in NMR experiments. Both forms of ERK2 show elution volumes consistent with monomeric protein, as measured against the Stokes radii of protein calibration standards (γ-globulin, 48 Å; ovalbumin, 33 Å; myoglobin, 20 Å). The apparent Stokes radii of the ERK2 monomer and dimer were previously measured as 24 Å and 35 Å, respectively.[124]

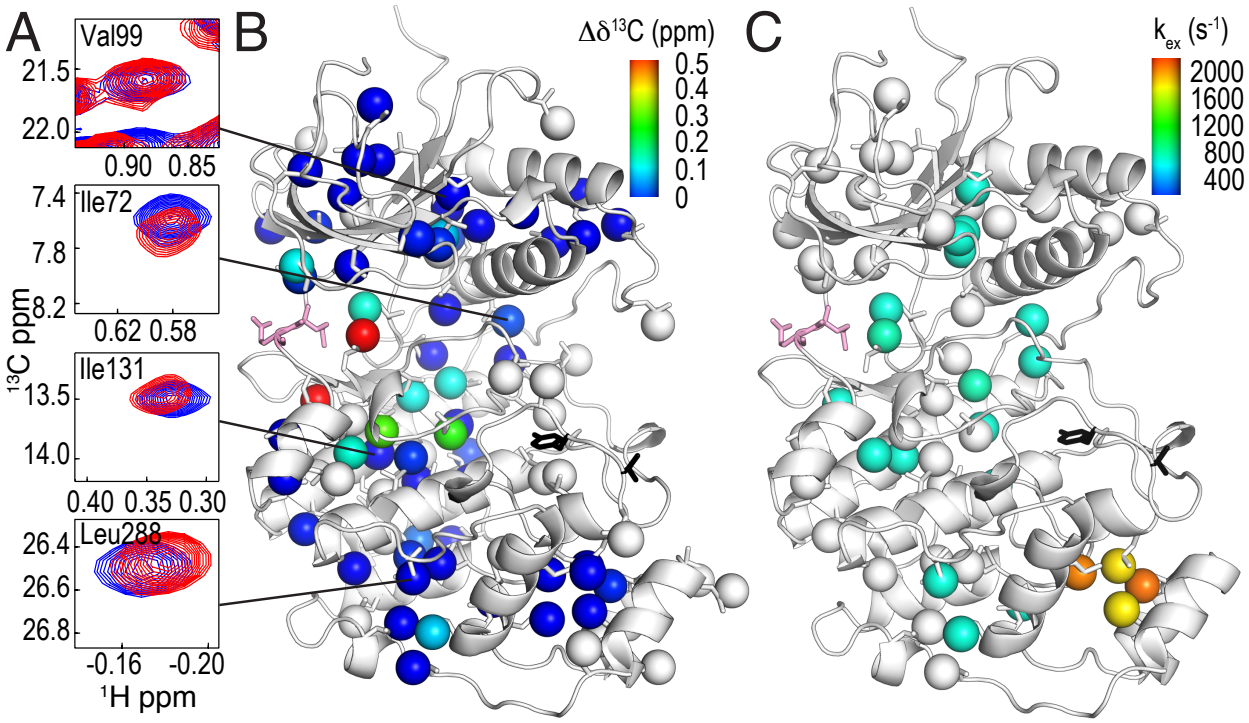

Figure 3.19. ME/GG hinge mutations induce conformational exchange in the kinase core, but not the MAP kinase insert.

(A) Overlays of several methyl regions of the 2D HMQC spectra showing similar chemical shifts for these methyls in 0P-ERK2 (blue) and ME/GG-ERK2 (red). (B) The $|\Delta\delta^{13}C|$ between 0P-ERK2 and ME/GG-ERK2 indicated by the color scale and unassigned ILV methyls are represented by white spheres. The $|\Delta\delta^{13}C|$ between 0P-ERK2 and ME/GG-ERK2 are small throughout the protein, except for residues close to the mutated M106 and E107 (shown in pink). (C) Sixteen methyls in ME/GG-ERK2 could be globally fit with k_{ex} (500 ± 60 s^{-1}, shown as cyan spheres) and population (97%, 3% ± 0.2%), indicating a single exchange process throughout the kinase core, similar to 2P-ERK2. The assigned methyls in the MAPK insert are shown as spheres, with k_{ex} values indicated by the color scale.

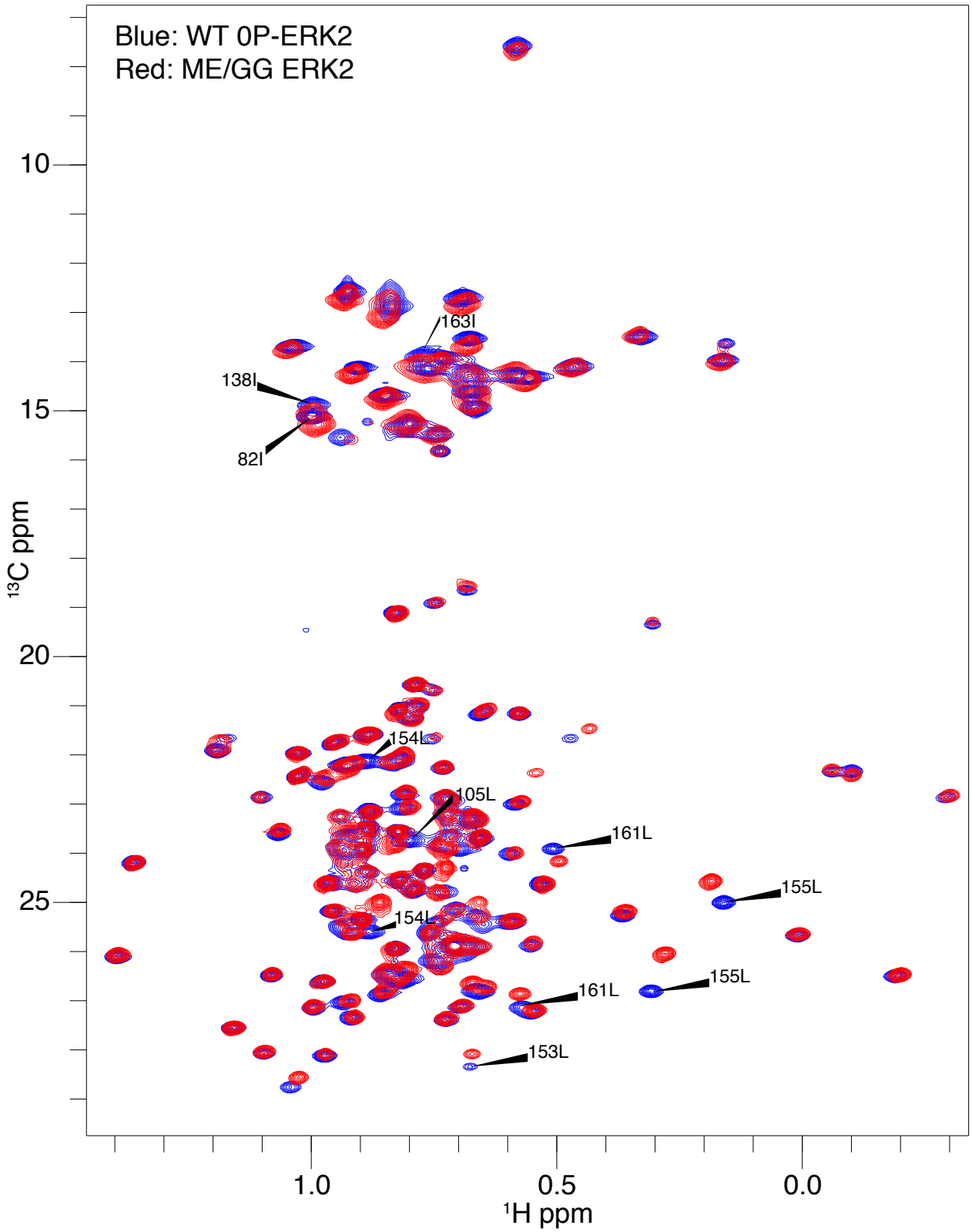

Figure 3.20. 2D (^{13}C, ^{1}H) HMQC spectra overlay of ME/GG (red) and 0P-ERK2 (blue). Methyls that showed clear chemical shift are labeled with assignments.

Table 3.8. Exchange parameters for methyl groups in ME/GG-ERK2, fitted individually*

Residue	Parameters				
	$k_{ex}(s^{-1})$†	$R_{ex}(800)$ (s^{-1}) ‡	$p_A p_B(\Delta\omega^{13}C)^2$ (s^{-2}) §	χ^2/DF¶	$\lvert\Delta\delta^{13}C_{global}\rvert$ (ppm) ‖
Kinase core					
Ile54	900 ± 500	9	7000 ± 1000	1.2	0.4 ± 0.05
Ile72	1100 ± 800	13	28000 ± 12000	0.9	1 ± 0.1
Ile82	500 ± 100	6	4400 ± 800	0.3	0.3 ± 0.04
Ile84**	N.D.	7	N.D.	N.D.	0.3 ± 0.04
Val99**	N.D.	6	N.D.	N.D.	0.3 ± 0.04
Ile101	1000 ± 300	8	10000 ± 2000	0.9	0.5 ± 0.05
Leu105**	N.D.	4	N.D.	N.D.	
Leu110	800 ± 300	13	31000 ± 10000	0.4	1.1 ± 0.1
Ile113**	N.D.	4	N.D.	N.D.	
Ile124	200 ± 170	4	3400 ± 800	0.2	
Ile131	1700 ± 700	12	50000 ± 45000	4	0.9 ± 0.1
Leu135**	N.D.	6	N.D.	N.D.	0.5 ± 0.04
Ile138**	N.D.	7	N.D.	N.D.	0.4 ± 0.04
Val143	500 ± 200	8	7500 ± 3200	1.0	0.3 ± 0.05
Leu148**	N.D.	4	N.D.	N.D.	
Leu154	1400 ± 800	8	16000 ± 3000	0.9	0.7 ± 0.05
Leu155	1900 ± 600	8	31000 ± 15000	0.8	0.4 ± 0.04
Leu209	200 ± 100	6	3600 ± 400	2.7	0.3 ± 0.04
Leu225	400 ± 100	6	4700 ± 700	0.2	0.3 ± 0.04
Ile241	700 ± 200	17	26000 ± 2000	0.1	0.9 ± 0.1
Leu242**	N.D.	8	N.D.	N.D.	0.4 ± 0.03
Global fitting	**500 ± 60**		**p_B =3 ± 0.2 %**	**1.0**	**See above**
MAPK insert					
Leu198	1200 ± 300	11	21000 ± 3000	0.9	
Leu235	1400 ± 800	20	34000 ± 4000	1.4	
Ile253	1600 ± 1200	11	36000 ± 18000	0.6	
Leu262	1300 ± 600	28	95000 ± 25000	4.6	

*These parameters were all obtained from MQ-CPMG dispersion data collected at 25°C.
†These parameters were all obtained by fitting CPMG dispersion data collected at 600, 800 and 900 MHz to a two-state exchange process using Carver-Richards equation on a per-methyl basis. The errors were estimated from fits using the CATIA program and may be underestimated if the data are not well described by a two-state exchange process (see Methods).
‡$R_{ex}(800)$ was estimated using the equation $R_{ex} = R_{2,eff}(50\ Hz) - R_{2,eff}(1000\ Hz)$ from 800 MHz CPMG dispersion data.
§This term was estimated assuming a two-state exchange model under fast-exchange limit using 800 MHz CPMG dispersion data (see Methods).
¶The χ^2/DF (reduced chi-square) describes the quality of the fit for the experimental data. DF is the degrees of freedom and was calculated by DF= (number of experimental data points – number of parameters –1) for each methyl in the dataset of ME/GG-ERK2.
‖The $\lvert\Delta\delta^{13}C_{global}\rvert$ is obtained by a global fitting of the methyls in the kinase core that showed $R_{ex}(800) > 4\ s^{-1}$ using CATIA.
**Individual fits were not determined due to large errors, but the R_{ex} could still be estimated.

3.3.7. The Conformational Dynamics of Mutant L154A-ERK2

In the structure of ERK2, the side chain of residue L154 packs against that of M106 in the ME hinge sequence. Mutating L154 to Ala is likely to reduce these side chain interactions, increasing hinge flexibility at the hinge region. We were therefore interested in determining whether the L154A mutation might mimic any effect seen with ME/GG. The 2D (^{13}C, ^{1}H) HMQC spectral overlay of L154A and wild type 0P-ERK2 (Figure 3.21) showed decreased peak intensity at I82, located ~4 Å away from L154, as well as chemical shift perturbations around the hinge and the DEJL binding site, similar to our findings with ME/GG. However, the chemical shift perturbations induced by L154A mutation were smaller than the chemical shift perturbations induced by ME/GG. The ILV side chain methyl dynamics were also measured for L154A using relaxation dispersion experiments (Table 3.9). Similar to ME/GG, L154A also showed strong evidence for changes in side chain motions within the DEJL binding site, probably due to the increased space in the hinge region. However, attempts to globally fit dispersion data for L154A-ERK2 into a two-state exchange process using similar methyls as in ME/GG (res.id. 72, 81, 84, 99, 101, 110, 113, 143, 155, 212, 225, 241 and 242) did not yield well-defined populations. Thus, the motions observed for L154A-ERK2 cannot be simply described by a single two-state exchange process.

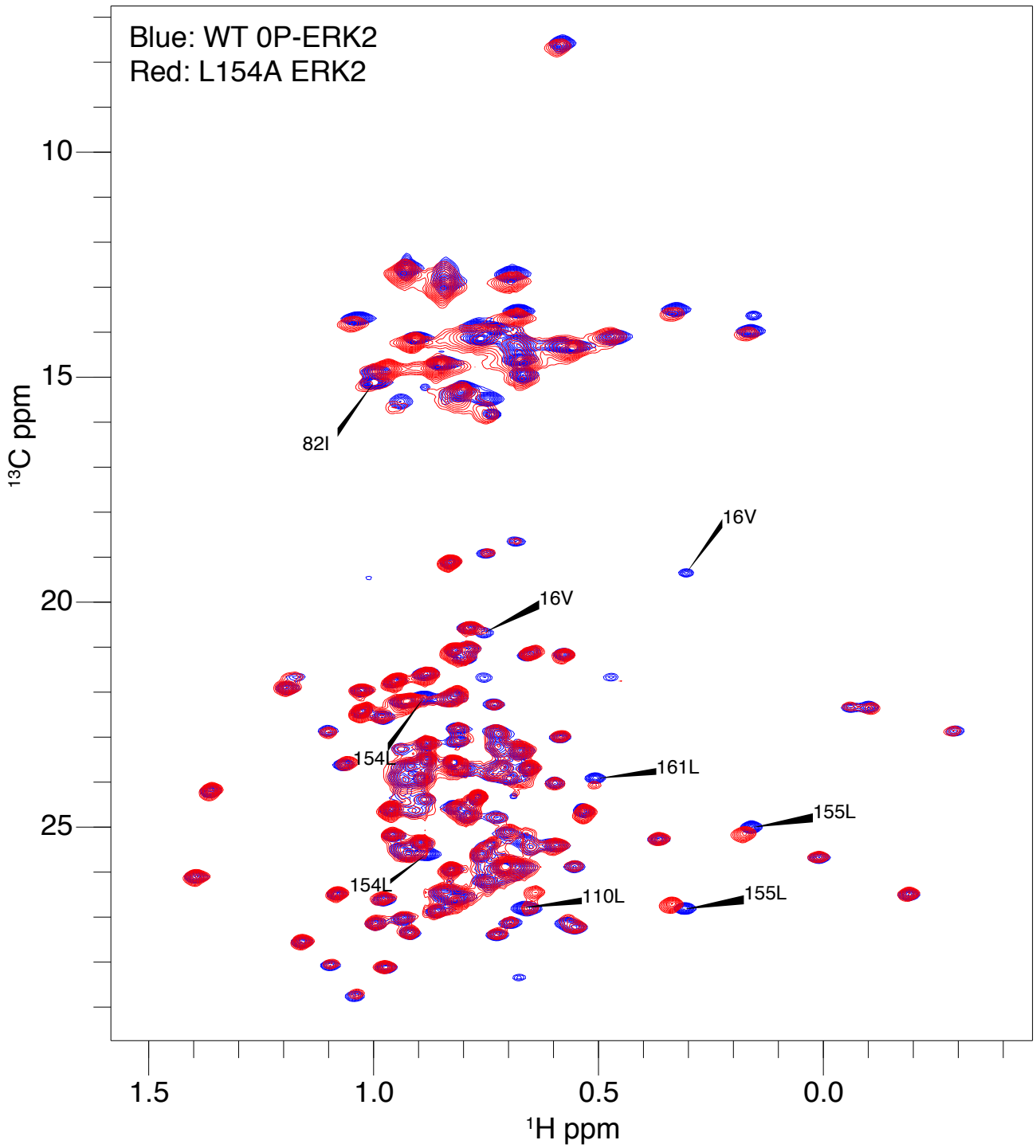

Figure 3.21. 2D (^{13}C, ^{1}H) HMQC spectra overlay of L154A (red) and 0P-ERK2 (blue). Methyls that showed clear chemical shift are labeled with assignments.

Table 3.9. Exchange parameters for methyl groups in L154A-ERK2, fitted individually*

Residue	Parameters			
	$k_{ex}(s^{-1})$ †	$R_{ex}(800)$ (s^{-1}) ‡	$p_A p_B(\Delta\omega^{13}C)^2$ (s^{-2}) §	χ^2 /DF¶
Kinase core				
Ile72‖	N.D.	16	N.D.	N.D.
Ile84‖	N.D.	4	N.D.	N.D.
Val99‖	N.D.	5	N.D.	N.D.
Ile101‖	N.D.	8	N.D.	N.D.
Leu110‖	N.D.	6	N.D.	N.D.
Ile113‖	N.D.	4	N.D.	N.D.
Ile131‖	N.D.	11	N.D.	N.D.
Val143‖	N.D.	10	N.D.	N.D.
Leu153	1400 ± 800	11	29000 ± 17000	1.2
Leu155‖	N.D.	3	N.D.	N.D.
Leu212‖	N.D.	6	N.D.	N.D.
Leu225	400 ± 100	5	N.D.	N.D.
Ile241	900 ± 500	26	21000 ± 1600	1.0
Leu242	800 ± 200	13	9000 ± 1000	1.8
Leu276	700 ± 500	5	6000 ± 1000	0.4
MAPK insert				
Leu198	1000 ± 700	9	25000 ± 6000	0.9
Leu235	1000 ± 600	18	6800 ± 6000	1.3
Ile253	N.D.	13	N.D.	N.D.
Leu262	1200 ± 400	13	20000 ± 3000	0.3

*These parameters were all obtained from MQ-CPMG dispersion data collected at 25°C.
†The k_{ex} values were obtained by fitting CPMG dispersion data collected at 800 and 900 MHz to a two-state exchange process using Carver-Richards equation on a per-methyl basis. The errors were estimated from fits using the CATIA program and may be underestimated if the data are not well described by a two-state exchange process (see Methods).
‡$R_{ex}(800)$ was estimated using the equation $R_{ex} = R_{2,eff}(50\ Hz) - R_{2,eff}(1000\ Hz)$ from 800 MHz CPMG dispersion data.
§This term was estimated assuming a two-state exchange model under fast-exchange limit using 800 MHz CPMG dispersion data (see Methods).
¶The χ^2/DF (reduced chi-square) describes the quality of the fit for the experimental data. DF is the degrees of freedom and was calculated by DF= (number of experimental data points – number of parameters –1) for each methyl in the dataset.
‖Individual fits were not determined due to large errors, but the R_{ex} could still be estimated.

3.4. Discussion

Our study demonstrates that the catalytic activation of a eukaryotic protein kinase elicits significant changes in protein dynamics. In 0P-ERK2, side chains show fast, localized motions on μs-ms timescale, with little evidence for coupling. In the phosphorylated enzyme, side chain motions are dominated by a global exchange process involving residues throughout the kinase core. The NMR data demonstrate that large-scale interdomain motion, with an exchange rate constant of 300 s^{-1}, accompanies phosphorylation and activation. Motions within the MAP kinase insert indicated a separate process, illustrating that independent subdomain motion occurs outside the consensus kinase core. The results support a model, illustrated in Figure 3.22A, in which unphosphorylated ERK2 is stabilized in the inactive conformer by an inhibitory constraint. This is released upon phosphorylation, allowing a global shift in equilibrium between conformational states, illustrated here as a hypothetical domain movement.

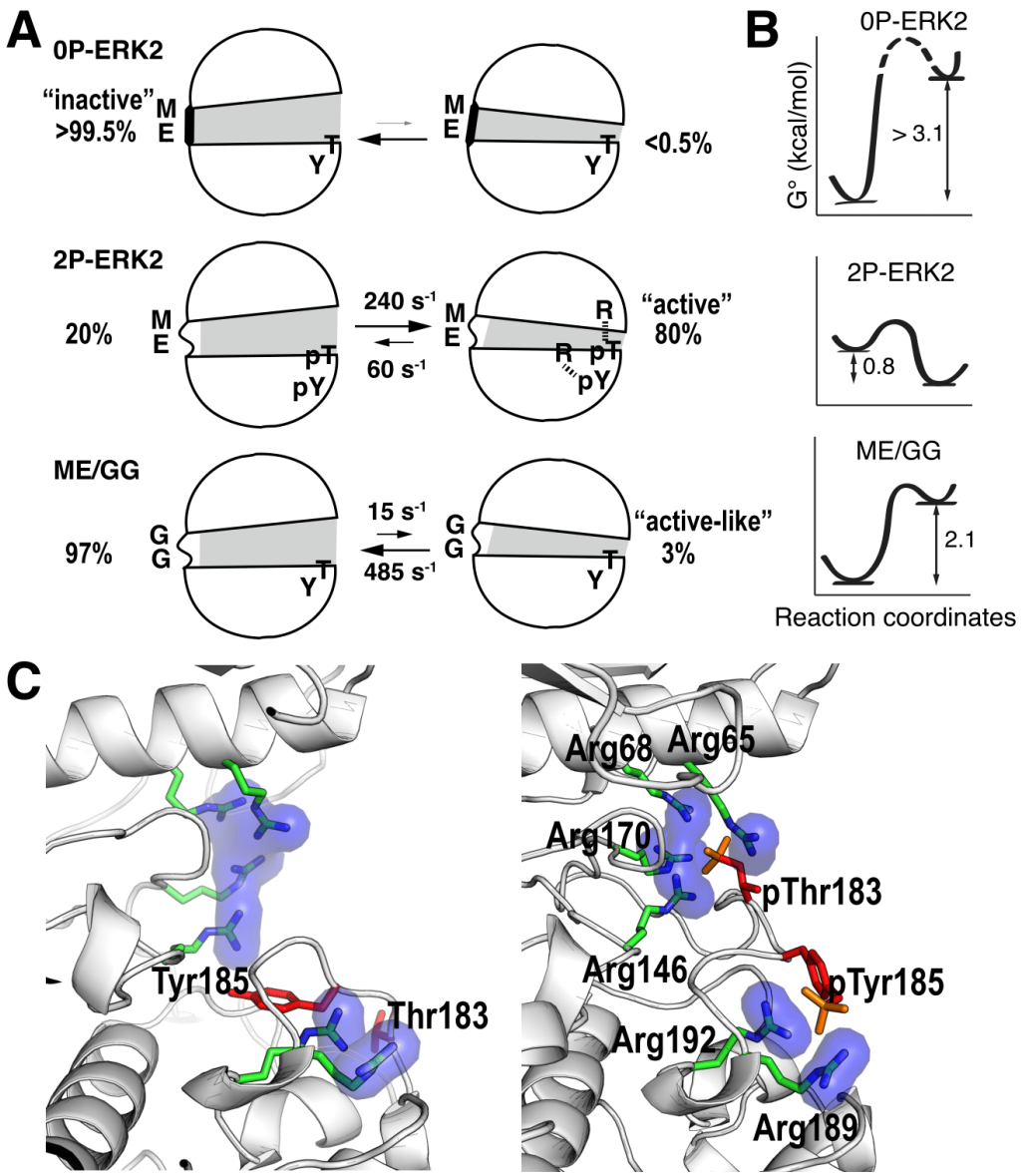

Figure 3.22. Model for activation of ERK2, involving the release of constraints to domain movement and change in energy landscape induced by phosphorylation.
(A, B) Prior to phosphorylation, 0P-ERK2 is in an "inactive" conformation that is constrained from domain motion, involving rigidity at the hinge (illustrated by the straight thick line between hinge residues ME). The CPMG dispersion data show no evidence for additional conformations indicating they must have low populations (< 0.5%), reflecting a $\Delta G° > +3.1$ kcal/mol. Phosphorylation enhances hinge mobility (illustrated by the wavy thin line) and shifts the equilibrium to favor the "active" conformer with $\Delta G°$ of -0.8 kcal/mol and rate constants of $k_{AB} = 240\ s^{-1}$ and $k_{BA} = 60\ s^{-1}$. The ME/GG mutation partially relieves the constraint to domain motion by increasing mobility at the hinge, sampling of the "active-like" conformer (3%), and reducing $\Delta G°$ to +2.1 kcal/mol. The activation energy is not known for 0P-ERK2, indicated by the dashed line in (B). (C) 0P-ERK2 and 2P-ERK2 structures show how phosphorylation at the activation loop promotes interactions between N- and C-terminal domains through ion pairing between pT183 and Arg65/68 in helix αC, which may stabilize the active form. The ERK2 backbone is colored in white, phosphates are colored orange, Thr183 and Tyr185 are colored red, Arg side chains are represented as sticks and surfaces are shown for the guanidinium groups.

3.4.1. Domain Movement in 2P-ERK2

Lateral or rotational movements between the N- and C-terminal domains provide one conceptual model to describe the global motions observed in active ERK2. Interconversions between "open" and "closed" domain conformations have been noted in other enzymes, including protein kinases [21, 125]. In the cAMP-dependent protein kinase catalytic subunit (PKA-C), the X-ray structure of the apo form shows an open conformation, whereas a binary complex with Mg^{2+}-AMP-PNP shows a closed conformation formed by rotation of the N-terminal domain by 18 degrees and closure of the catalytic cleft around the nucleotide [126, 127]. NMR relaxation measurements of backbone amides in the nucleotide-PKA-C binary complex show global exchange behavior in residues lining the catalytic core [128, 129], which are absent in apo PKA-C, and have been interpreted as an equilibrium shift to a closed conformation. Thus, PKA-C and active ERK2 share characteristics consistent with interconversion between open and closed conformers, with rates of conformational exchange on the same time scale ($k_{ex} \approx 200\ s^{-1}$ in PKA-C and $300\ s^{-1}$ in 2P-ERK2). This suggests that the nucleotide-induced domain closure observed in PKA-C may not adequately describe the dynamics in ERK2, where global exchange is allosterically stabilized by phosphorylation, but not by ligand binding.

Other models are possible, for example, one involving rotation of secondary structures within the N-terminal domain. In X-ray structures of ERK2, phosphorylation induces rearrangement of the activation loop, which in turn directs movement of helices αC and αL16 and refolding of the C-terminal L16 extension [32, 33]. A network of hydrogen bond and hydrophobic residue interactions throughout the N-terminal domain enable communication between these structures as well as connectivity with residues in the β3-β5 strands. It is possible that this network extends to the hinge through connections with the αC-β4 loop, and that the large chemical shift changes induced by

phosphorylation within this region reflect environmental changes due to rotational movements in the N-terminal domain.

The exchange rate constants between the two conformational states in 2P-ERK2 each decreased with reductions in temperature, indicating slower domain movements at low temperatures. At 10 °C, the $k_{ex} \approx 50\ s^{-1}$ approaches the limit of detection for CPMG relaxation dispersion experiments. Under conditions of similar populations and chemical shift differences, exchange rate constants that are lower than this value yields no significant R_{ex} and thus no reliable exchange parameters may be extracted. However, the rate constants measured between 10-25 °C were sufficient to show the energy landscape to the transition state for the two-state conformational exchange in 2P-ERK2. In 2P-ERK2, the major state (B) at 25 °C had significantly higher entropy compared with the minor state (A) (Figure 3.17). Because state A was dominant in 0P-ERK2, the result implies that 2P-ERK2 is less ordered than 0P-ERK2. In addition, the major state in 2P-ERK2 had slightly lower free energy than the minor state (A) at 25 °C. The the activation energy barrier for ERK2 ($\Delta G^{\ddagger}$ = 14 kcal/mol) is on the same order of magnitude with the thermodynamics of conformational exchange described for other proteins, including interconversion between "closed" and "occluded" states in dihydrofolate reductase (DHFR):ligand complexes ($\Delta G^{\ddagger}$ = 16 kcal/mol)[130], and inactive and active states in nitrogen regulatory protein C ($\Delta G^{\ddagger}$ = 6 kcal/mol)[131].

3.4.2. Effect of Hinge Flexibility to Domain Movement

An important finding from our study was that the unphosphorylated ME/GG hinge mutant induced a global exchange process, similar to that of 2P-ERK2. This involved residues as widely spread across the kinase core as in 2P-ERK2, strongly implying that the constraints to global exchange in 0P-ERK2 can be released by enhancing hinge flexibility. Mechanically, ERK2 might be conceptualized as having a strong spring constant at the hinge, which is weakened either upon

phosphorylation or mutation thus leading to a change in population of the conformational states. Figure 3.22A illustrates this model, where the ME/GG mutation bypasses the constraint to domain movement in 0P-ERK2 by mimicking the effect of phosphorylation on conformational mobility at the hinge. This increase in hinge flexibility lowers the barrier to domain movement relative to 0P-ERK2. However, unlike 2P-ERK2, ME/GG-ERK2 showed a smaller population (3%, instead of 80%) of the "active-like" conformer (Figure 3.22). Under the assumption that the two exchanging states in ME/GG- and 2P-ERK2 are the same, the chemical shift difference, $|\Delta\delta_{CPMG}{}^{13}C|$, should be the same for each methyl in ME/GG or 2P-ERK2. Thus, a comparison between the chemical shift differences of the two-exchanging states of individual methyls from CPMG fittings of 2P-ERK2 and ME/GG-ERK2 could be used to evaluate whether the assumption is valid. This comparison showed a slope that is significantly different from 1 (Figure 3.23), in specific, the $|\Delta\delta_{CPMG}{}^{13}C|$s for ME/GG-ERK2 methyls are usually larger than those of 2P-ERK2. Thus, it is more likely that the "active-like" conformer in ME/GG-ERK2 has some differences from the "active" conformer of 2P-ERK2.

The specific activity of ME/GG-ERK2 (0.06 nmol/min/mg) was comparable to that of 0P-ERK2 (0.08 nmol/min/mg), both order of magnitudes lower than 2P-ERK2 (264 nmol/min/mg). The NMR relaxation dispersion data summarized in Figure 3.22A show no correlation of the kinase activity with the kinetics or populations for any of the studied forms of ERK2. Instead, the data support a model where multiple events take place following the phosphorylation of ERK2. One event involves removal of a constraint to global exchange dynamics, illustrated by domain movement, which can be induced by either ME/GG or phosphorylation. A second event involves stabilization of the "active" conformation in 2P-ERK2, illustrated by ionic interactions that promote interactions between the N- and C-terminal domains (Figure 3.22C). Further work is needed to understand the details of the

conformational transitions, as well as the kinetic and thermodynamic contributions, that occur upon activation of ERK2.

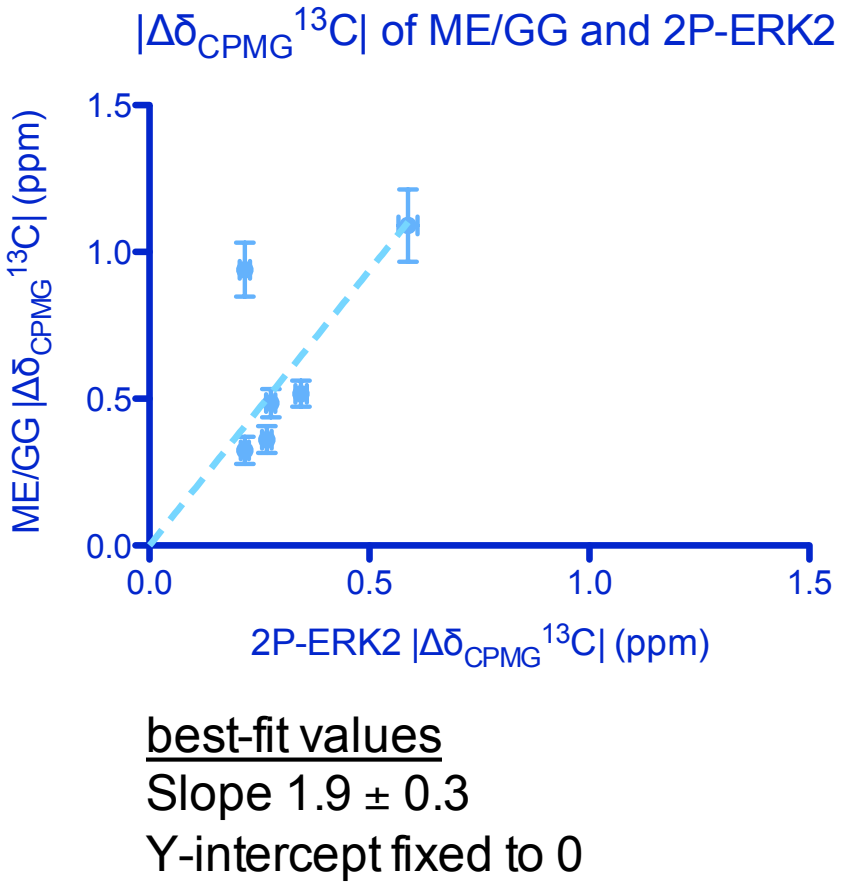

Figure 3.23. Comparison of chemical shift differences from global fitting of CPMG experiments ($\Delta\delta_{CPMG}$ ^{13}C) between ME/GG-ERK2 and 2P-ERK2.
This comparison included methyls of I101, I131, I135, I138, I143 and I72. Error bars are the errors of individual chemical shift differences from the global fitting of CPMG experiment. The dashed line represents a linear regression of these data points with Y-intercept fixed to zero.

In contrast to ME/GG, a global two-state exchange process could not be demonstrated with L154A. Although non-zero R_{ex} could be observed at multiple methyls, most of the methyl groups yielded large errors on exchange kinetics when fit individually and could not be reported. It is most likely that L154A shows local fluctuations or motions on the μs-ms timescale, which are poorly described by a single two-state exchange model. This implies that L154, although interacting with the hinge, does not significantly contribute to the constraints at the hinge that prevent release of dynamics. An alternative possibility is that the global two-state exchange process exists for L154A, but the process cannot be detected, for example, because the population of the activated state is too low to be observed using the CPMG experiment.

3.5. Summary

Compared to the large amount of structural information on protein kinases, the understanding of how kinases are regulated at the level of internal protein motions is much less well developed. A major conclusion of this study is that, prior to phosphorylation, ERK2 is maintained in its inactive form by a mechanism that imposes constraints on protein dynamics. Unlike autoinhibitory mechanisms that involve intra- or inter-molecular occlusion at the catalytic site in other kinases, the constraints in ERK2 involve the hinge region, distal from the site of phosphorylation. The importance of hinge mobility has been suggested in other protein kinases. For example, allosteric communication between the activation loop and hinge was reported in FGFR2, which forms an autoinhibitory "molecular brake" involving a triad of interacting residues at the hinge, the αC-β4 loop and the β8 strand [132]. Structural studies also showed an extensive hydrogen bond network accompanied by reduced hinge flexibility in ZAP-70, which was proposed to maintain the kinase inactive form [133]. Finally, molecular dynamics calculations suggested local unfolding of the hinge in the catalytic domain of EGFR, which was proposed as an intermediate step towards the transition from the inactive to active state [134, 135].

However, in contrast to FGFR2, ZAP-70 and EGFR, the X-ray structures of ERK2 show no significant conformational changes around the hinge upon phosphorylation [32, 33]. Likewise, both inactive and active X-ray structures of ERK2 show a properly formed catalytic site and an intact "hydrophobic spine" network, whose misalignment underlies the mechanism of inactivation in many protein kinases [20, 28]. Thus, the mechanism of communication from the activation loop to the hinge most likely involves subtle reorganization of residues, suggesting that the autoinhibitory regulation in ERK2 involves architectural features that may be unique to this kinase. Our findings now set the stage for future studies to define the details of this architecture and understand its prevalence across the protein kinase superfamily.

Chapter 4. Effects of Ligand Binding to ERK2

4.1. Introduction

4.1.1. ERK2 Is an Important Therapeutic Target

The mitogen-activated protein kinase (MAPK) signaling pathway is a compelling target for anticancer therapy given the prevalence of oncogenic Ras and B-Raf in many cancer types. For example, about 50% of the melanoma patients have the B-Raf^{V600E} activating mutation,[13] leading to the therapeutic development of ATP-binding site inhibitors of B-Raf^{V600E} (e.g. vemurafenib and dabrafenib) and of MAP kinase kinase MKK1/2 (e.g. trametinib). Although these inhibitors showed remarkable clinical efficacy in the B-Raf^{V600E} patients, their benefit is limited by the clinical relapse of patients after 6-7 months of individual inhibitor treatment,[14, 15] or 11-12 months of combined B-Raf^{V600E} + MKK inhibitors treatment.[16] The transient nature of the "progression-free" period motivates the development of inhibitors of their downstream kinase ERK2. The ATP-binding site inhibitors of ERK2, e.g. ERKi, an inhibitor based on Vertex-11e and SCH772984, are shown to be effective against cells with acquired resistance to BRAF and MKK inhibitors,[17, 18] supporting the potential of ERKs as attractive targets for therapeutics. These findings motivate both a deep understanding of the regulation of ERK during catalysis, as well as careful characterizations of the binding mode for ERK inhibitors.

4.1.2. ERK2 Catalysis Is Rate-Limited by Phosphoryl Transfer and Product Dissociation

ERK2 is activated by dual phosphorylation at Thr and Tyr residues within the activation loop, with both events catalyzed by MKK1/2.[106] X-ray structures of unphosphorylated ERK2 (0P-ERK2) and dual-phosphorylated ERK2 (2P-ERK2) show that phosphorylation rearranges the activation loop to organize residues in the active site and allow productive recognition of protein/peptide substrates containing the phosphorylation motif, Pro-Xxx-Ser/Thr-Pro.[32, 33] Upon dual phosphorylation, 2P-ERK2 efficiently catalyzes the phosphoryl transfer from the γ-phosphate of ATP to a Ser/Thr residue

on the phosphorylation motif of the substrate, with the coordination of Mg^{2+}. Active ERK2 has a broad range of protein substrates in the cytoplasm and in the nucleus, regulating various cellular activities such as transcription[136] and chromatin remodeling.[137] However, to date, only a handful of ERK2 and substrate interactions have been structurally or kinetically studied.

The mechanism by which ERK2 recognizes and recruits its substrates is still incompletely understood. Two consensus sequence docking motifs are commonly found on the substrates of ERK2.[138] One motif is called the "docking site for ERK and JNK, LXL (DEJL)"-motif, and it interacts with the DEJL-motif binding site on ERK2.[139] This motif is commonly found on other ligands of EKR2 besides substrates, such as scaffolds (e.g. MP1/p14),[140] phosphatases[141, 142] (e.g. MKP3, HePTP) and upstream kinases[143] (e.g. MKK1/2). A second consensus motif, called "docking site for ERK, FXF (DEF)" motif, binds a DEF-motif binding site (DEF-site) on 2P-ERK2.[138] The affinity for this interaction is strengthened upon dual phosphorylation of ERK2, due to steric blocking of the DEF-site by the activation loop in 0P-ERK2.[34] For example, the transcription factor Elk1 contains DEJL and DEF motifs, and thus can bind to both docking sites at the same time in 2P-ERK2,[144] but only binds the DEJL-site in 0P-ERK2. Some ERK2 substrates contain only one docking motif, such as ribosomal S6 kinase 1 (DEJL-motif only) and c-Fos (DEF-motif only).[145] Other ERK2 ligands lack either canonical DEJL- or DEF-motif (e.g. the ERK2 substrate Ets-1[146, 147] or the cytoplasmic scaffold PEA-15[148]); these may be recruited to ERK2 in a non-canonical manner, which might involve partial engagement of these two sites.

The rate of turnover (k_{cat}) of 2P-ERK2 for various protein substrates are on the timescale of millisecond-second, e.g. 10 s^{-1} for myelin basic protein (MBP)[31] and 25 s^{-1} (or 37 s^{-1}) for the transcription factor Ets-1(1-138)[149]. The phosphorylation reaction on MBP was rate-limited by the phosphoryl transfer step of 12 s^{-1}, followed by a faster (56 s^{-1}) product release step.[31] In contrast, the

phosphorylation of Ets-1(1-138) was rate limited by two steps: the phosphoryl transfer step (110 s^{-1}) and the product release step (56 s^{-1}).[149] The relatively slow observed rate of turnover in ERK2 leads to a hypothesis that one or more of the catalytic rate-limiting steps are governed by conformational exchange processes of the protein kinase.

4.1.3. Tight Binding of ATP-Competitive Inhibitors of ERK2

So far, only a handful of ATP-binding site inhibitors of ERK2 have been publically described, with various affinities in the nM to μM range.[17, 150-154] For example, there are Vertex-11e, SCH772984 and GDC-0994 (Figure 4.1), each with up to 10^6-fold tighter affinity than ATP (K_d ~500 μM)[34]. Vertex-11e, a compound that is closely related to ERK-i, has been reported to be potent inhibitor of 2P-ERK2 *in vitro* (K_d = 0.28 nM, K_i = 0.34 nM) and *in vivo* (IC_{50} = 48 nM).[153] SCH772984 showed similar potency against 2P-ERK2 from both *in vitro* (K_d = 0.11 nM, K_i = 0.12 nM) and *in vivo* (IC_{50} = 60 nM) measurements.[17] Recent findings on GDC-0994, another tight inhibitor of 2P-ERK2 that is advancing to a Phase 1 clinical trial, reported a K_i value of 0.3 nM, comparable to Vertex-11e and SCH772984.[154] A previous study reported $k_{on,ATP}$ = 0.015 $\mu M^{-1}s^{-1}$ and $k_{off, ATP}$ = 0.5 s^{-1} for formation of the ternary MBP-bound complex of Tyr-185 phosphorylated (pY) ERK2.[155] This is only 10-100 fold slower than the k_{on} values of Vertex-11e (0.2 $\mu M^{-1}s^{-1}$) or SCH772984 (2.8 $\mu M^{-1}s^{-1}$). Thus, the tight affinities of these inhibitors mainly arise from their slow dissociation rate constants from 2P-ERK2 (k_{off} values of 5.8×10^{-5} s^{-1} for Vertex-11e and 3.0×10^{-4} s^{-1} for SCH772984), in comparison with faster dissociation rate constant of ATP (k_{off} value in the magnitude of 10^2 s^{-1}).

These inhibitors exhibited differences in their biochemical properties and physiological effects. Vertex-11e (K_i = 2.5 nM) for 0P-ERK2 shows 10-fold weaker inhibition than SCH772984 (K_i = 0.12 nM) for 0P-ERK2. In addition, although both compounds show comparable affinities for 2P-ERK2, the values of k_{on} and k_{off} for Vertex-11e are 10-fold slower than SCH772984. In contrast to SCH772984,

which inhibits ERK2 phosphorylation by MKK,[17] GDC-0994 and Vertex-11e do not alter cellular levels of 2P-ERK2.[154, 156] Together the results indicate distinct modes of inhibition by these molecules. However, to date, the differences in how these inhibitors interact with ERK2 remains unknown.

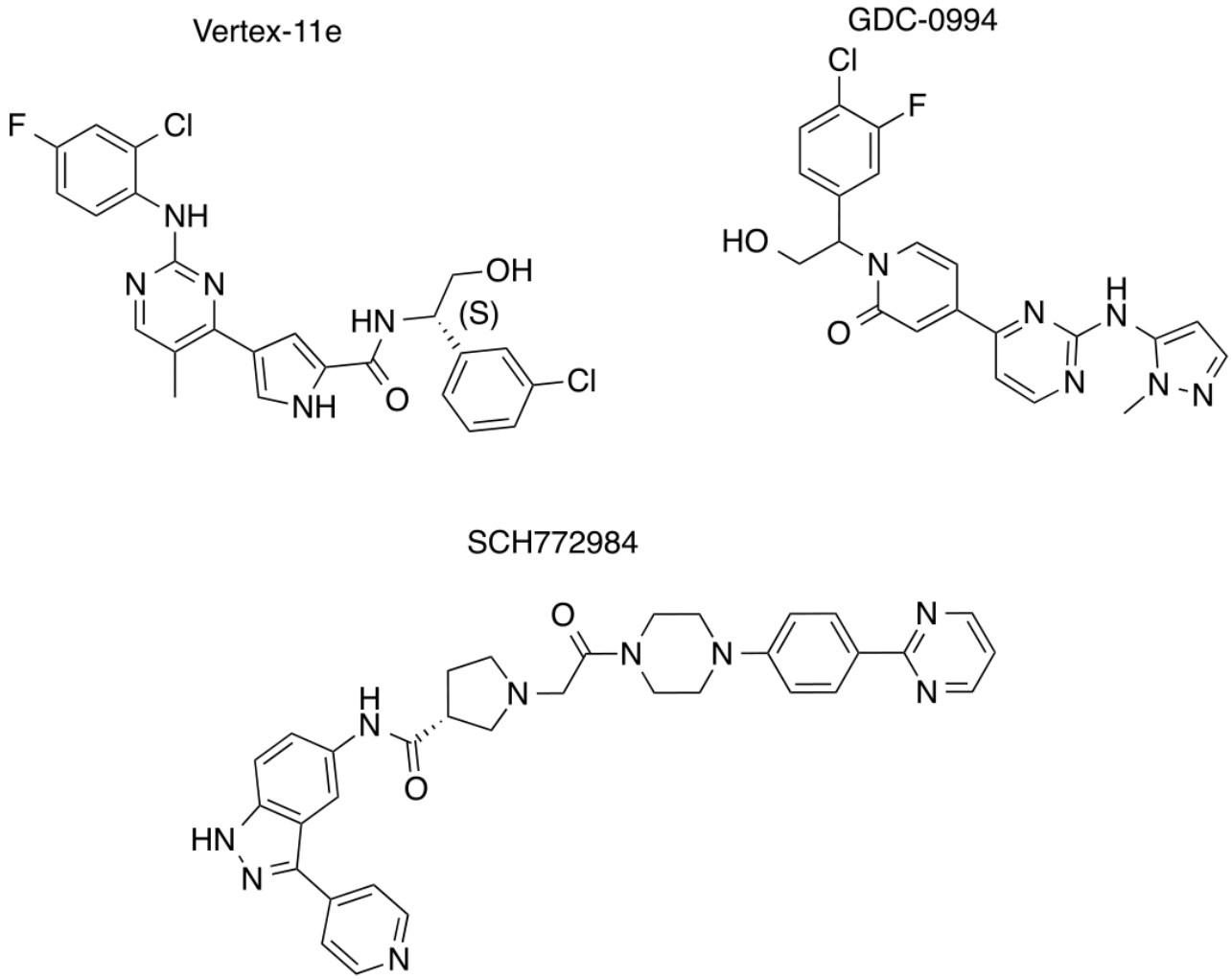

Figure 4.1. Structures of ERK2 inhibitors Vertex-11e, GDC-0994 and SCH772984.

4.1.4. ERK2 Shows Altered Conformational Dynamics upon Phosphorylation

As described in the Chapter 3 of this Thesis, we have previously discovered that dual phosphorylation of ERK2 induces significant changes in the dynamics of the enzyme, using NMR relaxation dispersion experiments.[79] Whereas 0P-ERK2 exists as one major conformer, 2P-ERK2 exists in two separate conformers that exchange on a millisecond time scale. The minor (20%, T)

conformer in 2P-ERK2 corresponds to the conformer seen in 0P-ERK2 (100%, T), whereas the major (80%, R) conformer in 2P-ERK2 represents another form that is energetically hard to access for 0P-ERK2. However, the role of these two conformers in ERK2 catalysis remained unclear. For example, if the two-state T⇌R conformational exchange for 2P-ERK2 represents an interconversion between active (R, 80% in 2P-ERK2) and inactive (T, 100% in 0P-ERK2) forms, would saturation of 2P-ERK2 with ATP-Mg^{2+} shift the equilibrium completely to the R state?

Such allosteric behavior of ERK2 might be exploited by inhibitors with conformational selective properties. Conformational selection is emerging as an important property of certain kinase inhibitors, termed "Type II", which work by trapping nonproductive active site conformers. This was first shown for BCR-ABL kinase inhibitors (e.g., imatinib and posatinib), which induce a "DFG flip" where Asp and Phe side chains in the conserved DFG motif swap positions to form an inactive "DFG-out" conformer.[157, 158] In contrast to " DFG-out", the EGF receptor inhibitor lapatinib binds an inactive "helix αC-out" conformer, disrupting the Mg^{2+}-coordinating Lys-Glu ion pair.[27, 159] In each case, the allosteric effects of Type II inhibitors reinforce their ATP competitive effects.

4.1.5. Purpose/Overview

In this chapter, NMR methyl chemical shifts were used to probe the binding interaction between ligand and ERK2, using the Elk1D docking motif peptide. Then, we characterized the effects of binding other ERK2 ligands, including the ATP analogues (AMP-PNP, AMP-PCP) and ADP (or analogue AMP-CP), to mimic ERK2 conformations in its catalytically relevant intermediates. A ternary complex of ERK2 with AMP-PCP and a substrate peptide, sub-D, was also formed to mimic the substrate-bound Michaelis complex of ERK2. The substrate peptide, sub-D, has an N-terminal DEJL motif derived from yeast STE7, and is linked to a C-terminal MAP kinase phosphorylation consensus sequence by a flexible hydrophobic linker.[160, 161] It has been shown to be an excellent

substrate for 2P-ERK2, with k_{cat} = 3-15 s^{-1} and k_{cat}/K_m of ~5 $\mu M^{-1}s^{-1}$, comparable to those values seen with the Ets-1(residue 1-138) protein as substrate.[160, 161] The binding of AMP-PNP and ADP showed slow exchange on the chemical shift time scale for the binding to 2P-ERK2, which was unexpected for a binding interaction with a high K_d value of 200-500 μM. In contrast, the binding of the substrate peptide, sub-D, or docking peptide, Elk1D, showed mostly fast exchange on the chemical shift time scale, but with tighter affinities. The results of these binding experiments show that 2P-ERK2 does not shift to 100% R conformation in its catalytically relevant forms, bound to ATP analogues. Instead, the T⇌R conformational equilibrium in 2P-ERK2 showed a small increase on the population of the T state when bound to ATP or ADP analogues.

In addition, the three inhibitors with highest cellular efficacy (Vertex-11e, SCH772984 and GDC-0994), each induced distinct effects on the conformational equilibrium of 2P-ERK2. NMR methyl-TROSY-HMQC experiments showed that the T⇌R conformational equilibrium in 2P-ERK2 shifted completely to the R state upon Vertex-11e binding, completely to the T state upon SCH772984 binding, and was comparable to apoenzyme upon GDC-0994 binding. Our results suggest that phosphorylation-induced dynamics represent an allosteric property of ERK2 that can be exploited for conformation selective inhibition.

4.2. Materials and Methods

4.2.1. Binding of Elk1D to ERK2

The peptide Elk1D[34] (NH-QKGRKPRDLELPLSPSL-OH, ANASPEC) was prepared in the same buffer as the ERK2 protein. Elk1D was titrated into 0P- (50 μM) or 2P-ERK2 (80 μM) where 5 h 2D (^{13}C, ^{1}H) TROSY HMQC spectra at 25 °C were collected and analyzed for each titration point (Table 4.1). The titration was stopped when there were no further changes in the chemical shift of the complex were observed. The combined chemical shift perturbation ($CSP_{C,H}$) of each methyl was calculated using the following equation:[162]

Equation 4.1

$$CSP_{C,H} = \sqrt{CSP_H^2 + (0.25CSP_C)^2}$$

where CSP_H and CSP_C are the chemical shift perturbations (in ppm) of ERK2 in the ^{1}H and ^{13}C dimensions. The K_d values were estimated by globally fitting $CSP_{C,H}$ with the following the equation:

Equation 4.2

$$CSP_{C,H}([Elk1D]) = CSP_{C,H(max)} \times \frac{K_d + [Elk1D] + [ERK2] - \sqrt{(K_d + [Elk1D] + [ERK2])^2 - 4[Elk1D][ERK2]}}{2[ERK2]}$$

where $CSP_{C,H(max)}$ is the maximum chemical shift perturbation between free and bound ERK2, and [Elk1D] and [ERK2] are the total concentrations of Elk1D and ERK2 for each titration point. A single K_d was fit for all the methyls with individual $CSP_{C,H(max)}$ values for each methyl resonance.

Table 4.1. 2D (^{13}C,^{1}H) TROSY HMQC Experiment Filenames, Parameters and Conditions in Elk1D Titrations with 2P- and 0P-ERK2

Filename	Sample	Temp (°C)	Solvent[a]
Elk1D to 2P-ERK2[b]			
2P-ERK2_H2Osmp021911_HMQC_25c_5hr_05012014_RTprobe.fid	2P-ERK2	25	H2O
2P-ERK2_H2Osmp021911_HMQC_5c_9hr_05012014_RTprobe.fid	2P-ERK2	5	H2O
2P-ERK2_H2Osmp021911_titr1_0p04mMElk1D_HMQC_25c_5hr_05012014_RTprobe.fid	2P-ERK2	25	H2O
2P-ERK2_H2Osmp021911_titr1_0p04mMElk1D_HMQC_5c_9hr_05012014_RTprobe.fid	2P-ERK2	5	H2O
2P-ERK2_H2Osmp021911_titr2_0p08mMElk1D_HMQC_25c_5hr_05032014_RTprobe.fid	2P-ERK2	25	H2O
2P-ERK2_H2Osmp021911_titr2_0p08mMElk1D_HMQC_5c_9hr_05032014_RTprobe.fid	2P-ERK2	5	H2O
2P-ERK2_H2Osmp021911_titr3_0p16mMElk1D_HMQC_25c_5hr_05042014_RTprobe.fid	2P-ERK2	25	H2O
2P-ERK2_H2Osmp021911_titr3_0p16mMElk1D_HMQC_5c_9hr_05042014_RTprobe.fid	2P-ERK2	5	H2O
2P-ERK2_H2Osmp021911_titr4_0p32mMElk1D_HMQC_25c_5hr_05052014_RTprobe.fid	2P-ERK2	25	H2O
2P-ERK2_H2Osmp021911_titr4_0p32mMElk1D_HMQC_5c_9hr_05052014_RTprobe.fid	2P-ERK2	5	H2O
2P-ERK2_H2Osmp021911_titr5_0p48mMElk1D_HMQC_25c_5hr_05062014_RTprobe.fid	2P-ERK2	25	H2O
2P-ERK2_H2Osmp021911_titr5_0p48mMElk1D_HMQC_5c_9hr_05062014_RTprobe.fid	2P-ERK2	5	H2O
2P-ERK2_H2Osmp021911_titr6_0p80mMElk1D_HMQC_25c_5hr_05132014_RTprobe.fid	2P-ERK2	25	H2O
Elk1D to 0P-ERK2[c]			
0P-ERK2_D2O_Elk1D_0mM_HMQC_25c_05102014.fid	0P-ERK2	25	D2O
0P-ERK2_D2O_Elk1D_23uM_HMQC_25c_05102014.fid	0P-ERK2	25	D2O
0P-ERK2_D2O_Elk1D_69uM_HMQC_25c_05112014.fid	0P-ERK2	25	D2O
0P-ERK2_D2O_Elk1D_115uM_titr3_HMQC_25c_05112014.fid	0P-ERK2	25	D2O
0P-ERK2_D2O_Elk1D_161uM_titr4_HMQC_25c_05122014.fid	0P-ERK2	25	D2O
0P-ERK2_D2O_Elk1D_253uM_titr5_HMQC_25c_05122014.fid	0P-ERK2	25	D2O
0P-ERK2_D2O_Elk1D_345uM_titr6_HMQC_25c_05122014.fid	0P-ERK2	25	D2O

[a]Solvent is either 95% - 99% D2O (labeled as D2O) or 5% D2O (labeled as H2O).
[b]These experiments were conducted on the 800 MHz NMR spectrometer with pulse sequence "hmqc_c13_800_methyl_bufsat", np (number of complex points in t_2) = 2048, ni (number of complex points in t_1) = 144, sw (sweep width in t_2, Hz) = 12019.2, sw1 (sweep width in t_1, Hz) = 5000, nt (number of scans per FID) = 40 (25 °C) or nt = 72 (5 °C) and d1=1.5 s. Data directories in /yao/data/ERK2_2014/2PERK2_800/.
[c]These experiments were conducted on the 800 MHz NMR spectrometer with pulse sequence "hmqc_c13_800_methyl_bufsat", np = 2048, ni = 144, sw = 12019.2, sw1= 5000, nt = 56 and d1=1.5 s. Data directories in /yao/data/ERK2_2014/0PERK2_800/.

4.2.2. Binding of AMP-PNP to ERK2

A 50 mM β,γ-imidoadenosine 5'-triphosphate (AMP-PNP, Sigma Aldrich) stock solution was prepared in the same buffer as the ERK2 sample, and the pD was adjusted to 7.0 (pH = 7.4). Two sets of 0P- and 2P-ERK2 samples were used to perform the binding experiment with AMP-PNP (Table 4.2). The first set of samples was prepared using the same procedure as described in Chapter 2; however, they were prepared approximately 36 months before the experiment and might not provide accurate concentrations. In addition, the AMP-PNP concentrations used during titration with 2P-ERK2 were not well controlled. Thus, I used this dataset only to compare saturated *vs* free ERK2, to measure any changes in the T⇌R populations between these two forms. A second set of samples was prepared similarly to the previous one expect that the cells were grown to produce protein in a protonated

background, thus yielding a broader line width and greater difficulty in extracting the T⇌R populations. Thus, this dataset was used only to show the chemical shift perturbations during the AMP-PNP titration. AMP-PNP was titrated into ERK2 samples, and a set of 5 h 2D (^{13}C, ^{1}H) TROSY HMQC spectra were collected using the 800 MHz NMR spectrometer. A series of 0, 0.1, 0.2, 0.3, 1.0, 2.1 and 4.2 mM AMP-PNP were titrated with ~0.26 mM 0P-ERK2, and 0, 0.15, 0.3, 0.6, 1.2 and 2.4 mM AMP-PNP were titrated with ~0.30 mM 2P-ERK2. The combined chemical shift perturbation ($CSP_{C,H}$) for individual methyls was calculated using Equation 4.1.

Table 4.2. 2D (^{13}C,^{1}H) TROSY HMQC Experiment Filenames, Parameters and Conditions in AMP-PNP Titrations with 2P- and 0P-ERK2

Filename	Sample	Temp (°C)	Solvent
AMP-PNP to D_2P-ERK2[a]			
2P-ERK2_D2O_HMQC_25c_10312013.fid	2P-ERK2	25	D2O[b]
2P-ERK2_D2O_HMQC_25c_AMPPNPtitra1_11012013.fid	2P-ERK2	25	D2O
2P-ERK2_D2O_HMQC_25c_AMPPNPtitra2_11022013.fid	2P-ERK2	25	D2O
2P-ERK2_D2O_HMQC_25c_AMPPNPtitra3_11032013.fid	2P-ERK2	25	D2O
2P-ERK2_D2O_HMQC_25c_AMPPNPtitra4_11042013.fid	2P-ERK2	25	D2O
2P-ERK2_D2O_HMQC_25c_AMPPNPtitra5_11052013.fid	2P-ERK2	25	D2O
2P-ERK2_D2O_HMQC_25c_AMPPNPtitra6_11062013.fid	2P-ERK2	25	D2O
2P-ERK2_D2O_HMQC_5c_10hr_10312013.fid	2P-ERK2	5	D2O
2P-ERK2_D2O_HMQC_5c_10hr_AMPPNPtitr1_11012013.fid	2P-ERK2	5	D2O
2P-ERK2_D2O_HMQC_5c_10hr_AMPPNPtitr2_11022013.fid	2P-ERK2	5	D2O
2P-ERK2_D2O_HMQC_5c_10hr_AMPPNPtitr3_11032013.fid	2P-ERK2	5	D2O
2P-ERK2_D2O_HMQC_5c_10hr_AMPPNPtitr4_11042013.fid	2P-ERK2	5	D2O
2P-ERK2_D2O_HMQC_5c_10hr_AMPPNPtitr5_11052013.fid	2P-ERK2	5	D2O
2P-ERK2_D2O_HMQC_5c_10hr_AMPPNPtitr6_11062013.fid	2P-ERK2	5	D2O
AMP-PNP to D_0P-ERK2[c]			
0P-ERK2_D2O_HMQC_25c_11272013.fid	2P-ERK2	25	D2O
0P-ERK2_D2O_AMPPNPtitr1_HMQC_25c_11302013.fid	2P-ERK2	25	D2O
0P-ERK2_D2O_AMPPNPtitr2_HMQC_25c_11302013.fid	2P-ERK2	25	D2O
0P-ERK2_D2O_AMPPNPtitr3_HMQC_25c_12012013.fid	2P-ERK2	25	D2O
0P-ERK2_D2O_AMPPNPtitr4_HMQC_25c_12022013.fid	2P-ERK2	25	D2O
0P-ERK2_D2O_AMPPNPtitr5_HMQC_25c_12032013.fid	2P-ERK2	25	D2O
0P-ERK2_D2O_AMPPNPtitr6_HMQC_25c_12042013.fid	2P-ERK2	25	D2O
0P-ERK2_D2O_HMQC_5c_11272013.fid	2P-ERK2	5	D2O
0P-ERK2_D2O_AMPPNPtitr1_HMQC_5c_11292013.fid	2P-ERK2	5	D2O
0P-ERK2_D2O_AMPPNPtitr2_HMQC_5c_11302013.fid	2P-ERK2	5	D2O
0P-ERK2_D2O_AMPPNPtitr3_HMQC_5c_12012013.fid	2P-ERK2	5	D2O
0P-ERK2_D2O_AMPPNPtitr4_HMQC_5c_12022013.fid	2P-ERK2	5	D2O
0P-ERK2_D2O_AMPPNPtitr5_HMQC_5c_12032013.fid	2P-ERK2	5	D2O

0P-ERK2_D2O_AMPPNPtitr6_HMQC_5c_12032013.fid	2P-ERK2	5	D2O
AMP-PNP to 1H_2P-ERK2[d]			
2PERK2_smp401_D2O_HMQC_25c_11232014_coldprobe_4h.fid	1H_2P-ERK2	25	D2O
2PERK2_smp401_D2O_HMQC_AMPPNP_titr1_25c_11232014_coldprobe_4h.fid	1H_2P-ERK2	25	D2O
2PERK2_smp401_D2O_HMQC_AMPPNP_titr2_25c_11232014_coldprobe_4h.fid	1H_2P-ERK2	25	D2O
2PERK2_smp401_D2O_HMQC_AMPPNP_titr3_25c_11242014_coldprobe_4h.fid	1H_2P-ERK2	25	D2O
2PERK2_smp401_D2O_HMQC_AMPPNP_titr4_25c_11242014_coldprobe_4h.fid	1H_2P-ERK2	25	D2O
2PERK2_smp401_D2O_HMQC_AMPPNP_titr5_25c_11242014_coldprobe_4h.fid	1H_2P-ERK2	25	D2O
2PERK2_smp401_D2O_HMQC_AMPPNP_titr6_25c_11242014_coldprobe_4h.fid	1H_2P-ERK2	25	D2O
AMP-PNP to 1H_0P-ERK2[e]			
0PERK2_smp405_H2O_HMQC_25c_12012014_coldprobe_4h.fid	1H_2P-ERK2	25	D2O
0PERK2_smp405_H2O_HMQC_AMPPNP_titr1_25c_12022014_coldprobe_4h.fid	1H_2P-ERK2	25	D2O
0PERK2_smp405_H2O_HMQC_AMPPNP_titr2_25c_12022014_coldprobe_4h.fid	1H_2P-ERK2	25	D2O
0PERK2_smp405_H2O_HMQC_AMPPNP_titr3_25c_12022014_coldprobe_4h.fid	1H_2P-ERK2	25	D2O
0PERK2_smp405_H2O_HMQC_AMPPNP_titr4_25c_12022014_coldprobe_4h.fid	1H_2P-ERK2	25	D2O
0PERK2_smp405_H2O_HMQC_AMPPNP_titr5_25c_12022014_coldprobe_4h.fid	1H_2P-ERK2	25	D2O
0PERK2_smp405_H2O_HMQC_AMPPNP_titr6_25c_12022014_coldprobe_4h.fid	1H_2P-ERK2	25	D2O
0PERK2_smp405_H2O_HMQC_AMPPNP_titr7_25c_12022014_coldprobe_4h.fid	1H_2P-ERK2	25	D2O

[a]These experiments were conducted on the 800 MHz NMR spectrometer with pulse sequence "hmqc_c13_800_methyl_bufsat", np (number of complex points in t_2) = 2048, ni (number of complex points in t_1) = 144, sw (sweep width in t_2, Hz) = 12019.2, sw1 (sweep width in t_1, Hz) = 5000, nt (number of scans per FID) = 40 (25 °C) or nt = 80 (5 °C) and d1=1.5 s. Data directories in /yao/data/ERK2_2013/2P_ERK2_800/.
[b]Solvent is 95% -99% D2O (labeled as D2O).
[c]These experiments were conducted on the 800 MHz NMR spectrometer with pulse sequence "hmqc_c13_800_methyl_bufsat", np = 2048, ni = 144, sw = 12019.2, sw1= 5000, nt = 40 (25 °C) or nt = 80 (5 °C) and d1=1.5 s. Data directories in /yao/data/ERK2_2013/0P_ERK2_800/.
[d]These experiments were conducted on the 800 MHz NMR spectrometer with pulse sequence "hmqc_c13_800_methyl_bufsat", np = 2048, ni = 144, sw = 12019.2, sw1= 5000, nt = 32 and d1=1.5 s. Data directories in /yao/data/ERK2_2014/2PERK2_800/. This sample was prepared in a protonated background and named "1H_2P-ERK2".
[e]These experiments were conducted on the 800 MHz NMR spectrometer with pulse sequence "hmqc_c13_800_methyl_bufsat", np = 2048, ni = 144, sw = 12019.2, sw1= 5000, nt = 32 and d1=1.5 s. Data directories in /yao/data/ERK2_2014/0PERK2_800/. This sample was prepared in a protonated background and named "1H_0P-ERK2".

4.2.3. Binding of ADP to 2P-ERK2

A 46 mM adenosine 5'-diphosphate (ADP, Sigma Aldrich) stock solution was prepared in the same buffer as the ERK2 sample (NMR buffer in D_2O), and the pD was adjusted to 7.0 (pH = 7.4). U-[^{2}H, ^{15}N, ^{12}C], ^{13}C-methyl-ILV labeled 2P-ERK2 (80 μM, in 90% D_2O) was prepared using the same procedure as described in Chapter 2. ADP was titrated into 80 μM 2P-ERK2 to yield final ADP concentrations of 20 μM, 40 μM, 80 μM, 160 μM, 400 μM and 1 mM, with $[ADP]_t$:$[2P\text{-}ERK2]_t$ ratios of 0.25, 0.5, 1, 2, 5, 12.5, respectively. At each titration point, 2D (^{13}C, ^{1}H) TROSY HMQC spectra were collected at 25 °C and at 10 °C. A 1D ^{31}P experiment was also performed for the ERK2 complexes with $[ADP]_t$ of 160 μM, 400 μM and 1 mM, as described below. To test the effects of phosphate on the 2P-ERK2:ADP complex, 1.0 mM NaPi (pH 7.0) and 0.8 mM fresh ADP were added to the 2P-ERK2 pre-saturated with partially hydrolyzed ADP, and 2D (^{13}C, ^{1}H) TROSY HMQC spectra were collected at 25 °C and at 10 °C on the 600 MHz spectrometer. This 2D (^{13}C, ^{1}H) TROSY HMQC experiment was later repeated on the 800 MHz spectrometer, after adding fresh ADP (2.7 mM) to reach $[ADP]_t$ (non-hydrolyzed + hydrolyzed) = 4.5 mM and 1.0 mM NaPi.

Table 4.3. 2D (^{13}C,^{1}H) TROSY HMQC Experiment Filenames, Parameters and Conditions for ADP Titration with 2P-ERK2[a]

Filename	Sample	Temp (°C)	Solvent[b]
2P_ERK2_13CILV_D2O_HMQC_10C_5hr_600_03022014.fid	2P-ERK2	10	D2O
2P_ERK2_13CILV_D2O_HMQC_25C_4hr_600_03022014.fid	2P-ERK2	25	D2O
2P_ERK2_13CILV_D2O_ADP_titr1_HMQC_10C_600_03022014.fid	2P-ERK2	10	D2O
2P_ERK2_13CILV_D2O_ADP_titr1_HMQC_25C_600_03032014.fid	2P-ERK2	25	D2O
2P_ERK2_13CILV_D2O_ADP_titr2_HMQC_10C_600_03032014.fid	2P-ERK2	10	D2O
2P_ERK2_13CILV_D2O_ADP_titr2_HMQC_25C_600_03032014.fid	2P-ERK2	25	D2O
2P_ERK2_13CILV_D2O_ADP_titr3_HMQC_10C_600_03042014.fid	2P-ERK2	10	D2O
2P_ERK2_13CILV_D2O_ADP_titr3_HMQC_25C_600_03042014.fid	2P-ERK2	25	D2O
2P_ERK2_13CILV_D2O_ADP_titr4_HMQC_10C_600_03052014.fid	2P-ERK2	10	D2O
2P_ERK2_13CILV_D2O_ADP_titr4_HMQC_25C_600_03042014.fid	2P-ERK2	25	D2O
2P_ERK2_13CILV_D2O_ADP_titr5_HMQC_10C_600_03062014.fid	2P-ERK2	10	D2O
2P_ERK2_13CILV_D2O_ADP_titr5_HMQC_25C_600_03062014.fid	2P-ERK2	25	D2O
2P_ERK2_13CILV_D2O_ADP_titr6_HMQC_10C_600_03062014.fid	2P-ERK2	10	D2O
2P_ERK2_13CILV_D2O_ADP_titr6_HMQC_25C_600_03062014.fid	2P-ERK2	25	D2O

[a]These experiments were conducted on the 600 MHz NMR spectrometer with pulse sequence "hmqc_c13_800_methyl_bufsat", np (number of complex points in t_2) = 4096, ni (number of complex points in t_1) = 144, sw (sweep width in t_2, Hz) = 11990, sw1 (sweep width in t_1, Hz) = 4000, nt (number of scans per FID) = 32 (25 °C) or nt = 40 (5 °C) and d1=1.5 s. Data directories in /yao/data/ERK2_2014/2PERK2_600/.
[b]Solvent is either 95% - 99% D2O (labeled as D2O) or 5% D2O (labeled as H2O).

4.2.4. Binding of AMP-PCP and sub-D to 2P-ERK2

U- [^{2}H, ^{15}N, ^{12}C], ^{13}C-methyl-ILV labeled 2P-ERK2 (90 μM, in 90% D_2O) was prepared using the same procedure as described in Chapter 2. 36 mM β,γ-methyleneadenosine 5'-triphosphate (AMP-PCP, Sigma-Aldrich) stock was prepared in NMR buffer (D_2O), and used for titrations with 2P-ERK2. AMP-PCP was titrated into 2P-ERK2 to final concentrations of 135 μM, 270 μM, 720 μM and 1800 μM, corresponding to $[\text{AMP-PCP}]_t$:$[\text{2P-ERK2}]_t$ ratios of 1.5, 3, 8, and 20, respectively. This was shortly followed by a rough titration of the peptide substrate, sub-D (H-FQR KTL QRR NLK GLN LNL X-X-X TGP LSP GPF-NH2, X=AOO=8-amino-3,6-dioxaocatanoyl, Anaspec), into the 2P-ERK2:AMP-PCP complex. A 6.9 mM stock of sub-D was prepared in NMR buffer and the pH of the peptide solution was adjusted to 7.6 using a thin pH electrode. A rough titration of sub-D into the 2P-ERK2:AMP-PCP complex was performed at final sub-D concentrations of 36 μM, 90 μM, and 180 μM, corresponding to $[\text{sub-D}]_t$:$[\text{2P-ERK2}]_t$ ratios of 0.4, 1, and 2, respectively. Each titration point was followed by collecting 2-hour 2D (^{13}C, ^{1}H) methyl-HMQC spectra at 25 °C and 5 °C, respectively.

Table 4.4. 2D (^{13}C,^{1}H) TROSY HMQC Experiment Filenames, Parameters and Conditions in AMP-PNP and sub-D Titrations with 2P-ERK2

Filename	Sample	Temp (°C)	Solvent[a]
AMP-PCP to 2P-ERK2[b]			
2PERK2_smp122409_D2O_AMPPCP_titr1_HMQC_25c_10062014_coldprobe_2h.fid	2P-ERK2	25	D2O
2PERK2_smp122409_D2O_AMPPCP_titr1_HMQC_5c_10062014_coldprobe_2h.fid	2P-ERK2	5	D2O
2PERK2_smp122409_D2O_AMPPCP_titr1_HMQC_5c_10062014_coldprobe_4h.fid	2P-ERK2	5	D2O
2PERK2_smp122409_D2O_AMPPCP_titr2_HMQC_25c_10062014_coldprobe_2h.fid	2P-ERK2	25	D2O
2PERK2_smp122409_D2O_AMPPCP_titr2_HMQC_5c_10062014_coldprobe_2h.fid	2P-ERK2	5	D2O
2PERK2_smp122409_D2O_AMPPCP_titr3_HMQC_25c_10072014_coldprobe_2h.fid	2P-ERK2	25	D2O
2PERK2_smp122409_D2O_AMPPCP_titr3_HMQC_5c_10062014_coldprobe_2h.fid	2P-ERK2	5	D2O
2PERK2_smp122409_D2O_AMPPCP_titr4_HMQC_25c_10072014_coldprobe_2h.fid	2P-ERK2	25	D2O
2PERK2_smp122409_D2O_AMPPCP_titr4_HMQC_5c_10072014_coldprobe_2h.fid	2P-ERK2	5	D2O
2PERK2_smp122409_D2O_AMPPCP_titr4_HMQC_5c_10072014_coldprobe_4h.fid	2P-ERK2	5	D2O
sub-D to 2P-ERK2:AMP-PCP			
2PERK2_smp122409_D2O_AMPPCP_titr4_subDtitr1new_HMQC_25c_10082014_coldprobe_2h.fid	2P-ERK2	25	D2O
2PERK2_smp122409_D2O_AMPPCP_titr4_subDtitr1new_HMQC_5c_10082014_coldprobe_2h.fid	2P-ERK2	5	D2O
2PERK2_smp122409_D2O_AMPPCP_titr4_subDtitr2_HMQC_25c_10082014_coldprobe_2h.fid	2P-ERK2	25	D2O
2PERK2_smp122409_D2O_AMPPCP_titr4_subDtitr2_HMQC_5c_10082014_coldprobe_2h.fid	2P-ERK2	5	D2O
2PERK2_smp122409_D2O_AMPPCP_titr4_subDtitr3_HMQC_25c_10082014_coldprobe_2h.fid	2P-ERK2	25	D2O
2PERK2_smp122409_D2O_AMPPCP_titr4_subDtitr3_HMQC_5c_10082014_coldprobe_2h.fid	2P-ERK2	5	D2O

[a]Solvent is either 95% - 99% D2O (labeled as D2O) or 5% D2O (labeled as H2O).
[b]These experiments were conducted on the 800 MHz NMR spectrometer with pulse sequence "hmqc_c13_800_methyl_bufsat", np (number of complex points in t_2) = 2048, ni (number of complex points in t_1) = 144, sw (sweep width in t_2, Hz) = 12019.2, sw1 (sweep width in t_1, Hz) = 5000, nt (number of scans per FID) = 16 (2 h) or nt = 32 (4 h) and d1=1.5 s. Data directories in /yao/data/ERK2_2014/2PERK2_800/.

4.2.5. Binding of AMP-CP to 2P-ERK2

U- [^{2}H, ^{15}N, ^{12}C], ^{13}C-methyl-ILV labeled 2P-ERK2 (85 μM, in 90% D_2O) was prepared using the same procedure as described in Chapter 2. A 58 mM stock of adenosine 5'-(α,β-methylene)diphosphate (AMP-CP, Sigma-Aldrich) was prepared in NMR buffer (D_2O) and stored at -20 °C. The AMP-CP stock has lower solubility and crystallizes out of solution at low temperature, therefore it had to be re-dissolved by heating in a 37-40 °C water bath before usage. A titration experiment of AMPCP with 2P-ERK2 was performed. AMP-PCP was titrated into 2P-ERK2 to final ligand concentrations of 43 μM, 85 μM, 170 μM, 340 μM, 680 μM, 1400 μM, 2000 μM and 2700 μM, corresponding to $[\text{AMP-CP}]_t$:$[\text{2P-ERK2}]_t$ ratios of 0.5, 1, 2, 4, 8, 16, 24 and 32, respectively. Each titration was followed by a 1hour 2D (^{13}C, ^{1}H) methyl-HMQC spectra collected at 25 °C. In addition, two 4-hour 2D (^{13}C, ^{1}H) methyl-HMQC spectra of 2P-ERK2 were collected at 5 °C prior to the first titration and after the last titration point to better visualize any population change of slow-exchanging peaks.

Table 4.5. 2D (^{13}C,^{1}H) TROSY HMQC Experiment Filenames, Parameters and Conditions in AMP-CP Titration to 2P-ERK2[a]

Filename	Sample	Temp (°C)	Solvent[b]
2PERK2_smp902_D2O_HMQC_25c_11252014_coldprobe_1h.fid	2P-ERK2	25	D2O
2PERK2_smp902_D2O_HMQC_5c_11252014_coldprobe_2h.fid	2P-ERK2	5	D2O
2PERK2_smp902_D2O_AMPCP_titr1_HMQC_25c_11252014_coldprobe_1h.fid	2P-ERK2	25	D2O
2PERK2_smp902_D2O_AMPCP_titr2_HMQC_25c_11252014_coldprobe_1h.fid	2P-ERK2	25	D2O
2PERK2_smp902_D2O_AMPCP_titr3_HMQC_25c_11252014_coldprobe_1h.fid	2P-ERK2	25	D2O
2PERK2_smp902_D2O_AMPCP_titr4_HMQC_25c_11252014_coldprobe_1h.fid	2P-ERK2	25	D2O
2PERK2_smp902_D2O_AMPCP_titr5_HMQC_25c_11252014_coldprobe_1h.fid	2P-ERK2	25	D2O
2PERK2_smp902_D2O_AMPCP_titr6_HMQC_25c_11252014_coldprobe_1h.fid	2P-ERK2	25	D2O
2PERK2_smp902_D2O_AMPCP_titr7_HMQC_25c_11252014_coldprobe_1h.fid	2P-ERK2	25	D2O
2PERK2_smp902_D2O_AMPCP_titr8_HMQC_25c_11252014_coldprobe_1h.fid	2P-ERK2	25	D2O
2PERK2_smp902_D2O_AMPCP_titr8_HMQC_5c_11252014_coldprobe_4h.fid	2P-ERK2	5	D2O

[a]These experiments were conducted on the 800 MHz NMR spectrometer with pulse sequence "hmqc_c13_800_methyl_bufsat", np (number of complex points in t_2) = 2048, ni (number of complex points in t_1) = 144, sw (sweep width in t_2, Hz) = 12019.2, sw1 (sweep width in t_1, Hz) = 5000, nt (number of scans per FID) = 16 (25 °C, 2 h) or nt = 32 (5 °C, 4 h) and d1=1.5 s. Data directories in /yao/data/ERK2_2014/2PERK2_800/.
[b]Solvent is either 95% - 99% D2O (labeled as D2O) or 5% D2O (labeled as H2O).

4.2.6. Enzyme-Coupled Assay for Detecting Hydrolysis

To test the effect of ERK2 inhibitor on ADP hydrolysis, 100 μL solutions of 1.2 mM free ADP in NMR buffer (H_2O), 1.2 mM ADP + 0.2 mM 2P-ERK2, and 1.2 mM ADP+0.2 mM 2P-ERK2+0.25 mM SCH772984 were incubated at room temperature for various of time periods, up to a week. At each time point, 8 μL of each sample was removed from the tube and immediately frozen at -70 °C freezer until the assay was performed.

To test the effect of phosphatase inhibitor on ADP hydrolysis, 35 μL solutions of 1.2 mM free ADP in NMR buffer (H_2O), 1.2 mM ADP + 0.2 mM 2P-ERK2, and 1.2 mM ADP+0.2 mM 2P-ERK2+3X Halt™ protease and phosphatase inhibitor cocktail (Thermo Fisher Scientific) were incubated at room temperature for various time periods, up to a week. 8 μL of each sample was removed from the tube and immediately frozen at -70 °C freezer until the assay was performed.

An enzyme-coupled assay (conceived by Dr. Johannes Rudolph) was performed for convenient detection of ADP hydrolysis. An enzyme mix composed of 25 mM Tris-HCl (pH 7.4), 100 mM NaCl, 10 mM $MgCl_2$, 1 mM phosphoenolpyruvate (PEP), 0.25 mM nicotinamide adenine dinucleotide (NADH), excessive pyruvate kinase (cat. P1506, Sigma-Aldrich) and excessive lactate dehydrogenase (cat. L2500, Sigma-Aldrich) was freshly prepared each time before performing the assay, as described in Table 4.6 and Table 4.7. A series of standard ADP solutions (0.02, 0.04, 0.06, 0.08, and 0.1 mM) was each prepared to 100 μL, using the 1 mM ADP stock and the enzyme mix. The samples to be tested for their ADP hydrolysis levels were diluted (usually 12 times) with the enzyme mix to [ADP] = 0.1 mM (assuming no hydrolysis) and a final volume of 100 μL. Each reaction was incubated for at least 10 min before transferring to a quartz micro-cuvette with 1 cm pathlength and 100 μL chamber volume, and the absorbance at 340 nm was measured using a Varian absorption spectrometer. The absorbance of the standard ADP series was measured in a way from low values (high [ADP]) to high

values (low [ADP]). All samples were measured within 20 min. The cuvette was washed using distilled H_2O (diH_2O) between the measurements of different samples.

Table 4.6. Preparation of 50 mL Tris/Mg Buffer

Volume	Component
1.25 mL	1 M Tris-HCl, pH 7.4
1 mL	5 M NaCl
125 μL	4 M $MgCl_2$
Fill diH_2O to 50 mL	

Table 4.7. Preparation of 1.5 mL Enzyme Mix

Volume	Component
1436 μL	Tris/Mg buffer
60 μL	25 mM PEP[a]
6 μL	62 mM NADH[b]
1 μL	Pyruvate Kinase
1 μL	Lactate Dehydrogenase

[a]PEP was frozen stocks at -20 °C freezer of the Copley Lab, provided by Dr. Johannes Rudolph.
[b]NADH was made fresh each time from powder (e.g. 4.4 mg can be weighed and dissolved in 100 μL H_2O) to avoid oxidation.

4.2.7. Binding of Vertex-11e to ERK2

Methyl-^{1}H,^{13}C-Ile, Leu and Val-labeled 0P- and 2P-ERK2 were prepared as previously described[16] in a buffer containing 50 mM Tris pH 7.4, 150 mM NaCl, 5 mM $MgSO_4$, 0.1 mM EDTA, 5 mM dithiothreitol, 99% D_2O, and 2.5% (v/v) glycerol. Vertex-11e was prepared in a 2.5 mM stock solution in d6-DMSO, due to its limited solubility in D_2O. Vertex-11e (d6-DMSO) was then added to isotopically labeled 2P-ERK2 (40 μM) or 0P-ERK2 (30 μM), to form complexes with ~50% binding stoichiometry ([Vertex-11e]:[protein]=0.5:1) and ~100% binding stoichiometry ([Vertex-11e]:[protein]=1.2:1). The d6-DMSO in the final protein sample was ~1% (v/v).

2D (^{13}C, ^{1}H) HMQC spectra of 0P-ERK2 and 2P-ERK2 were collected on Varian VNMRS 800 MHz (for 0P-ERK2) or 900 MHz (for 2P-ERK2) NMR spectrometers (Table 4.8). Data were collected at 25 °C (8 h for 0P-ERK2; 11 h for 2P-ERK2) and at 5 °C (12h for 0P-ERK2; 18 h for 2P-ERK2). Each spectrum was acquired with 144 (800 MHz) or 160 complex points (900 MHz) in the t_1 (^{13}C)

dimension, corresponding to 28.8 ms at 800 MHz and 29.1 ms at 900 MHz, and 1024 complex points in the acquisition period. WURST40 ^{13}C decoupling was applied during the 85 ms acquisition period and a 1.5 s delay period was used between each scan. The spectra were processed using the software package NMRPipe[25]. Time-domain data in the ^{1}H dimension were apodized by a cosine-squared window function and zero-filled prior to Fourier transformation. The indirect dimension (^{13}C) was apodized by a cosine window function and zero-filled prior to Fourier transformation. Spectra visualization and analysis was performed using CCPNMR Analysis software[26]. Chemical shift perturbations upon Vertex-11e binding were calculated by overlaying the 2D (^{13}C, ^{1}H) NMR spectra of Vertex-11e-bound and free forms of ERK2. In crowded regions of the spectra, the methyl peaks corresponding to the ligand-bound enzyme were assigned as the new peaks that appeared closest to the methyl peaks corresponding to the free enzyme. In this way, the chemical shift perturbation values represent minimum estimates. The combined ^{13}C and ^{1}H chemical shift perturbation (in ppm) upon Vertex-11e binding to 0P- or 2P-ERK2 was calculated using Equation 4.1.

Table 4.8. 2D (^{13}C,^{1}H) TROSY HMQC Experiment Filenames, Parameters and Conditions for Inhibitor Binding to ERK2

Filename	Sample	Temp (°C)	Solvent[a]
Vertex-11e to 2P-ERK2[b]			
2P-ERK2_smp042014_D2O_900_13C_hqmc_5c_04212014_18hrs.fid	2P-ERK2	5	D2O
2P-ERK2_smp042014_D2O_900_13C_hqmc_25c_04222014_11hrs.fid	2P-ERK2	25	D2O
2P-ERK2_smp042014_D2O_11e_titr1_900_13C_hqmc_25c_04242014_11hrs.fid	2P-ERK2	25	D2O
2P-ERK2_smp042014_D2O_11e_titr1_900_13C_hqmc_5c_04242014_18hrs.fid	2P-ERK2	5	D2O
2P-ERK2_smp042014_D2O_11e_titr2_900_13C_hqmc_10c_04272014_18hrs.fid	2P-ERK2	10	D2O
2P-ERK2_smp042014_D2O_11e_titr2_900_13C_hqmc_25c_04262014_11hrs.fid	2P-ERK2	25	D2O
2P-ERK2_smp042014_D2O_11e_titr2_900_13C_hqmc_5c_04252014_18hrs.fid	2P-ERK2	5	D2O
Vertex-11e to 0P-ERK2[c]			
0P-ERK2_D2O_HMQC_25c_05072014.fid	0P-ERK2	25	D2O
0P-ERK2_D2O_HMQC_5c_05072014.fid	0P-ERK2	5	D2O
0P-ERK2_D2O_11e_titr1_HMQC_25c_05072014.fid	0P-ERK2	25	D2O
0P-ERK2_D2O_11e_titr1_HMQC_5c_05072014.fid	0P-ERK2	5	D2O
0P-ERK2_D2O_11e_titr2_HMQC_25c_05072014.fid	0P-ERK2	25	D2O
0P-ERK2_D2O_11e_titr2_HMQC_5c_05072014.fid	0P-ERK2	5	D2O
SCH772984 to 0P-ERK2[d]			
2PERK2_smp122409_D2O_SCH_titr0_HMQC_25c_10142014_coldprobe_4h.fid	2P-ERK2	25	D2O
2PERK2_smp122409_D2O_SCH_titr0_HMQC_5c_10142014_coldprobe_8h.fid	2P-ERK2	5	D2O
2PERK2_smp122409_D2O_SCH_titr1_HMQC_25c_10152014_coldprobe_3h.fid	2P-ERK2	25	D2O
2PERK2_smp122409_D2O_SCH_titr1_HMQC_5c_10152014_coldprobe_6h.fid	2P-ERK2	5	D2O
2PERK2_smp122409_D2O_SCH_titr2_HMQC_25c_10152014_coldprobe_4h.fid	2P-ERK2	25	D2O

2PERK2_smp122409_D2O_SCH_titr2_HMQC_5c_10152014_coldprobe_8h.fid	2P-ERK2	5	D2O
SCH772984 to 0P-ERK2[e]			
0P-ERK2_H2O_HMQC_25c_09042014_coldprobe_8h.fid	0P-ERK2	25	H2O
0P-ERK2_H2O_SCH_1to0p5_HMQC_25c_09042014_coldprobe_8h.fid	0P-ERK2	25	H2O
0P-ERK2_H2O_SCH_1to1p2_HMQC_25c_09052014_coldprobe_8h.fid	0P-ERK2	25	H2O
GDC-0994 to 2P-ERK2[f]			
2P-ERK2_smp903_D2O_900_13C_hqmc_25c_030215_coldprobe_LS_2h20min.fid	2P-ERK2	25	D2O
2P-ERK2_smp903_D2O_900_13C_hqmc_5c_030215_coldprobe_LS_4h40min.fid	2P-ERK2	5	D2O
2P-ERK2_smp903_D2O_900_13C_hqmc_25c_GDCtitr1_030315_coldprobe_LS_2h.fid	2P-ERK2	25	D2O
2P-ERK2_smp903_D2O_900_13C_hqmc_5c_GDCtitr1_030315_coldprobe_LS_4h40min.fid	2P-ERK2	5	D2O
2P-ERK2_smp903_D2O_900_13C_hqmc_25c_GDCtitr2_030315_coldprobe_LS_2h.fid	2P-ERK2	25	D2O
2P-ERK2_smp903_D2O_900_13C_hqmc_5c_GDCtitr2_030315_coldprobe_LS_4h.fid	2P-ERK2	5	D2O

[a]Solvent is either 95% - 99% D2O (labeled as D2O) or 5% D2O (labeled as H2O).
[b]These experiments were conducted on the 900 MHz NMR spectrometer with pulse sequence "hmqc_c13_800_methyl_bufsat", np (number of complex points in t_2) = 2048, ni (number of complex points in t_1) = 144, sw (sweep width in t_2, Hz) = 12019.2, sw1 (sweep width in t_1, Hz) = 5500, nt (number of scans per FID) = 80 (25 °C, 11 h) or 128 (5 °C, 18 h) and d1=1.5 s. Data directories in /yao/data/ERK2_2014/2PERK2_900/.
[c]These experiments were conducted on the 800 MHz NMR spectrometer with pulse sequence "hmqc_c13_800_methyl_bufsat", np = 2048, ni = 144, sw = 12019.2, sw1 = 5000, nt = 64 (25 °C, 4 h) or 96 (5 °C, 8 h) and d1=1.5 s. Data directories in /yao/data/ERK2_2014/0PERK2_800/.
[d]These experiments were conducted on the 800 MHz NMR spectrometer with pulse sequence "hmqc_c13_800_methyl_bufsat", np = 2048, ni = 144, sw = 12019.2, sw1 = 5000, nt = 32 (25 °C, 4 h) or 64 (5 °C, 8 h) and d1=1.5 s. Data directories in /yao/data/ERK2_2014/2PERK2_800/.
[e]These experiments were conducted on the 800 MHz NMR spectrometer with pulse sequence "hmqc_c13_800_methyl_bufsat", np = 2048, ni = 144, sw = 12019.2, sw1 = 5000, nt = 64 and d1=1.5 s. Data directories in /yao/data/ERK2_2014/0PERK2_800/.
[f]These experiments were conducted on the 900 MHz NMR spectrometer with pulse sequence "hmqc_c13_800_methyl_bufsat", np = 2048, ni = 144, sw = 12019.2, sw1 = 5000, nt = 16 (25 °C, 2 h) or 32 (5 °C, 4 h) and d1=1.5 s. Data directories in /yao/data/ERK2_2015/2PERK2_900/.

4.2.8. Binding of SCH772984 to ERK2

ERK2 inhibitor SCH772984 (Cedarlanee Laboratories) was dissolved in DMSO to a concentration of 100 mM, before diluting into 5 mM stock using d6-DMSO. After collecting 2D (^{13}C, ^{1}H) HMQC spectra of a 0.03 mM methyl-^{1}H,^{13}C-Ile, Leu and Val-labeled 0P-ERK2 at 25°C (8 h) and a 2P-ERK2 sample at 25°C (4 h) and 5°C (8 h) for referencing, SCH772984 was titrated into the 2P-ERK2 sample to form complexes with ~50% binding stoichiometry ([SCH772984]:[protein]=0.5:1) and ~100% binding stoichiometry ([SCH772984]:[protein]=1.3:1). After each titration point, 2D (^{13}C, ^{1}H) HMQC spectra were collected at 25°C (3-4 h) and 5°C (6-8 h) for the 2P-ERK2: SCH772984 complex, and (8 h) for the 0P-ERK2: SCH772984 complex at 25°C on Varian VNMRS 800 MHz spectrometer (Table 4.8). The DMSO in the final protein sample was ~1%.

4.2.9. Binding of GDC-0994 to 2P-ERK2

The ERK2 inhibitor, GDC-0994 (MW 439.85, 5 mg, purity > 99%, Selleckchem.com), was dissolved in DMSO to a concentration of 100 mM, before further diluting into a 5 mM stock using d6-DMSO. After collecting a 2D (^{13}C, ^{1}H) HMQC spectra of a 0.042 mM methyl-^{1}H,^{13}C-Ile, Leu and Val-labeled 2P-ERK2 sample as reference, GDC-0994 was then titrated into this 2P-ERK2 sample to form complexes with ~50% binding stoichiometry ([GDC-0994]:[protein]=0.5:1) and ~100% binding stoichiometry ([GDC-0994]:[protein]=1.3:1). After each titration point, 2D (^{13}C, ^{1}H) HMQC spectra were collected at 25°C (2 h) and 5°C (4 h) on Varian VNMRS 900 MHz for the 2P-ERK2:GDC-0994 complex (Table 4.8). The DMSO in the final protein sample was ~1% (v/v).

4.2.10. 1D ^{31}P NMR spectra

1D ^{31}P NMR spectra were collected on a 500 MHz INOVA spectrometer equipped with a broadband probe that detects the ^{31}P nucleus, or a 400 MHz Bruker Avance-III spectrometer. On the 500 MHz INOVA spectrometer, two pulse sequences were used to collect such a 1D ^{31}P NMR spectrum, including "s2pul" (mostly used) and "PHOSPHORUS". In the ^{31}P dimension, a pulse width (pw) of ~18 μs (90 degree) was applied at transmitter power (tpwr) of 54 db, before acquisition time of 400 ms. Proton decoupler was off in this experiment. The transmitter offset was set to 10 ppm, with a spectral width of 86 ppm (sw = 17204.3 Hz, sfrq = 202). Prior to taking the spectrum of the experimental sample, 50 mM triphenylphosphate (TPP) in $CDCl_3$ was used to measure the signal-to-noise of ^{31}P NMR spectra, which was around 140. A typical ^{31}P NMR spectra of a sample containing 0.5 mM AMP-PNP or ADP used 16384 scans with 1 s delay (d1 = 1) between each scan, requiring a total experiment time of 6 h. It is worth noting that because the T_1 relaxation time for AMP-PNP is around 1 s, a delay time of 5 s or longer is recommended to achieve equilibrium of magnetization, although resulting in a much longer experimental time. Experiments with more scans were performed for samples with lower ^{31}P concentrations.

Table 4.9. 1D ^{31}P NMR Experiment Filenames, Parameters and Conditions[a]

Filename	Sample	np	sw	nt	d1
p31_phosphorus_AMP_PNP_D2O_25C_10252013_13hr.fid	AMP-PNP	16384	17204	32768	1
p31_phosphorus_2PERK2_D2O_25C_10252013_13hr.fid	2P-ERK2	8192	8609	32768	1
p31_phosphorus_2PERK2_D2O_25C_10282013_19hr.fid	2P-ERK2	16384	17204	48000	1
p31_phosphorus_AMP_PNP_D2O_25C_01102014_6hr.fid	AMP-PNP	16384	17219	16384	1
p31_phosphorus_0PERK2_D2O_AMPPNP_25C_01112014_6hr.fid	0P-ERK2+AMP-PNP	16384	17219	16384	1
p31_phosphorus_2PERK2_D2O_AMPPNP_25C_01112014_6hr.fid	2P-ERK2+AMP-PNP	16384	17219	16384	1
p31_phosphorus_AMP_PNP_D2O_25C_01122014_6hr.fid	AMP-PNP	16384	17219	16384	1
p31_phosphorus_AMP_PNP_D2O_25C_01132014_6hr.fid	AMP-PNP	16384	17219	16384	1
p31_phosphorus_AMP_PNP_D2O_25C_01222014_6hr.fid	AMP-PNP	16384	17219	16384	1
p31_phosphorus_2PERK2_D2O_ADPtitr4_25C_03052014_6hr.fid	2P-ERK2+ADP	16384	17219	16384	1
p31_phosphorus_2PERK2_D2O_ADPtitr5_25C_03062014_6hr.fid	2P-ERK2+ADP	16384	17219	16384	1
p31_phosphorus_2PERK2_D2O_ADPtitr6_25C_03072014_6hr.fid	2P-ERK2+ADP	16384	17219	16384	1
p31_phosphorus_2PERK2_D2O_ADPtitr6_25C_03242014_6hr.fid	2P-ERK2+ADP	16384	17219	16384	1
p31_phosphorus_2PERK2_D2O_ADPtitr6_25C_04062014_6hr.fid	2P-ERK2+ADP	16384	17219	16384	1
p31_phosphorus_ADP_D2O_Sigma_25C_03062014_5hr.fid	ADP	16384	17219	4000	4
p31_phosphorus_ADP_D2O_Sigma_25C_03072014_5hr.fid	ADP	16384	17219	4000	4

[a]These experiments were conducted on the 500 MHz NMR spectrometer at 25 °C with pulse sequence "s2pul". The solvents for these samples are 95% − 99% D2O. np − number of complex points, sw − sweep width (Hz), nt − number of scans per FID, d1 − interscan delay (s). Data directories in /yao/data/31P_expts/.

4.3. Results

4.3.1. Peptide Binding to 0P- and 2P-ERK2

The methyl assignments allowed a more detailed interpretation of ligand binding to active and inactive ERK2. For example, 2D (^{13}C, ^{1}H) HMQC spectra were used to study chemical shift changes and to determine the dissociation constant (K_d) for binding the Elk1D peptide to 0P-ERK2 or 2P-ERK2 as illustrated in Figure 4.2. The Elk1D peptide is derived from an ERK2 substrate, transcription factor Elk1, and binds to a DEJL-site in ERK2.[163] The chemical shift changes for many methyl resonances upon titration of the peptide show that peptide binding to ERK is in fast exchange on the NMR chemical shift timescale, meaning that the observed chemical shift is a population weighted average of the chemical shifts of the free and bound states. Chemical shift perturbations of the ^{13}C and ^{1}H resonances ($CSP_{C,H}$) for ILV methyls were then globally fit to a binding isotherm yielding a single K_d for binding as well as the magnitude of the chemical shift differences between the free and bound states of ERK2 (Figure 4.2B, Table 4.10). The K_d values obtained for Elk1D binding to 0P- and 2P-

ERK2 were 10 ± 1 and 30 ± 3 μM, respectively. Thus, active ERK2 has a 3-fold lower binding affinity for this peptide than inactive ERK2. Significant chemical shift perturbations ($CSP_{C,H} > 0.03$ ppm) were observed for 9 methyl resonances (both methyls of L110, both methyls of L113, a single methyl of L119, both methyls of L155, a single methyl of L306, and a single methyl of L311) in both 0P- and 2P-ERK2. These residues are close to the DEJL binding interface, which includes the sheet β7, the helices αD and αE and extends to the CD site (see Figure 4.3). Smaller chemical shift perturbations (0.01 to 0.03 ppm) were observed for residues more distant from the binding interface, such as I82 and I124. These residues showed similar magnitudes and direction of chemical shift perturbation in both 0P- and 2P-ERK2, indicating similar conformational changes between inactive and active ERK2 upon Elk1D binding. The location of these residues on the structure is consistent with X-ray structures of 0P-ERK2 in complex with another peptide that binds to the DEJL binding site and with a previous NMR study showing changes in chemical shifts of backbone amides upon Elk1D binding.[59, 164]

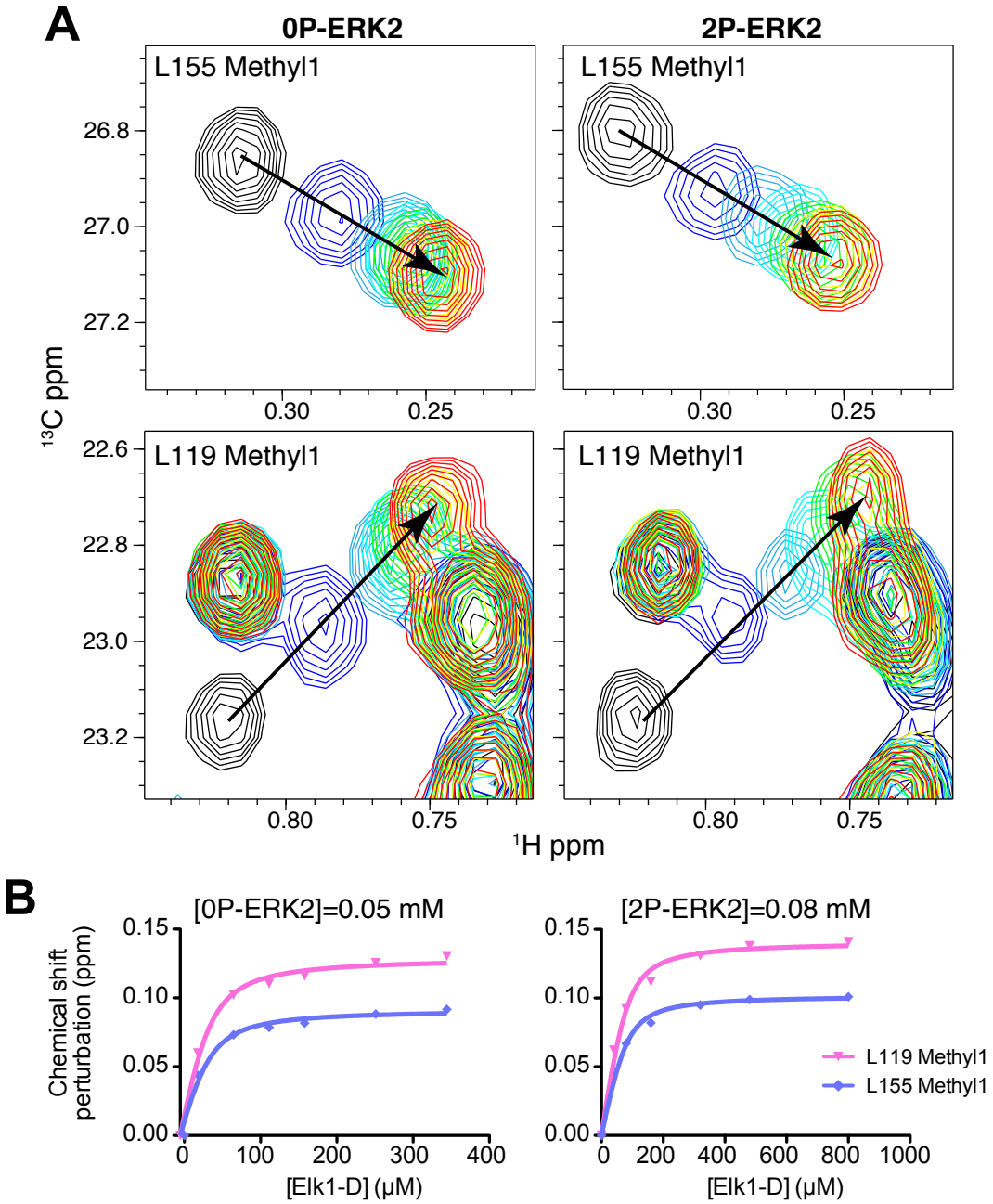

Figure 4.2. Binding of the peptide Elk1D to inactive and active ERK2.
(A) Titration of Elk1D into 0P- or 2P-ERK2 as monitored by chemical shift changes of methyl resonances for L155 and L119 in the 2D HMQC spectra. The arrows show the change in the position of the methyl resonance upon titration with Elk1D, where the free ERK2 is in black and the saturated peak ([0P-ERK2]:[Elk1D]=1:7, [2P-ERK2]:[Elk1D]=1:10) is in red. The $CSP_{C,H}$ values for these methyl resonances are similar in 0P and 2P-ERK2 (Table 4.10). (B) The $CSP_{C,H}$ values for L155 and L119 are plotted against the concentration of Elk1D, where the solid lines are the global fits to a single-site binding curve.

Table 4.10. The chemical shift differences between the free and bound states of ERK2 obtained from global fittings of 0P/2P-ERK2 and Elk1D titration curves.[a]

	0P-ERK2 (free)		0P-ERK2		2P-ERK2	
	C^{methyl} (ppm)	H^{methyl} (ppm)	$\lvert\Delta\delta(^{13}C)\rvert$ (ppm)	$\lvert\Delta\delta(^{1}H)\rvert$ (ppm)	$\lvert\Delta\delta(^{13}C)\rvert$ (ppm)	$\lvert\Delta\delta(^{1}H)\rvert$ (ppm)
L110 Methyl1	23.93	0.70	0.03	0.05	0.05	0.05
L110 Methyl2	26.80	0.67	0.06	0.03	0.09	0.04
L113 Methyl1[b]	26.60	0.82	1.01	0.02	0.90	0.01
L113 Methyl2	24.55	0.82	0.26	0.02	0.27	0.02
L119 Methyl1	23.11	0.82	0.43	0.07	0.49	0.08
L155 Methyl1	26.82	0.31	0.24	0.07	0.29	0.08
L155 Methyl2	25.01	0.17	0.22	0.07	0.18	0.07
L306 Methyl1	27.14	0.70	0.12	0.01	0.13	0.01
L311 Methyl2	26.49	1.08	0.11	0.02	0.10	0.02

[a]The global fitting of 0P-ERK2 titration yielded K_d of 10 μM (± 1 μM). The global fitting of 2P-ERK2 titration yielded K_d of 30 μM (± 3 μM).
The chemical shift differences between the free and bound states of ERK2 of individual methyls usually have $\lvert\Delta\Delta\delta(^{13}C)\rvert$ (Standard error of $\lvert\Delta\delta(^{13}C)\rvert$) of 0.01 ppm and $\lvert\Delta\delta(^{1}H)\rvert$ of 0.001 ppm.
[b]One methyl of L113 undergoes line broadening at the earliest titration point (e.g. [Elk1D]=23 μM in the 0P-ERK2 titration), thus it was not included in the global fitting of fast exchanging methyls using chemical shift perturbation. The CSPs reported for this methyl were from the subtraction of chemical shift of the free ERK2 from chemical shift at the last Elk1D titration point.

Table 4.11. Binding and Kinetic Data for Ligand Interactions with 0P- and 2P-ERK2

	0P-ERK2			2P-ERK2		
	K_d (μM)	k_{on} ($\mu M^{-1}s^{-1}$)	k_{off} (s^{-1})	K_d (μM)	k_{on} ($\mu M^{-1}s^{-1}$)	k_{off} (s^{-1})
Elk1D	10 ± 1	> 3[a] (30[b])	> 30[a] (300[b])	30 ± 3	> 1[a]	> 30[a]
AMP-PNP	200-500	< 0.08[c]	< 80[c]	200-500	< 0.08[c]	< 80[c]
AMP-PCP	300 ± 30[d]	> 0.06[d]	> 18[d]	380 ± 30	> 0.04[e]	>15[e]
sub-D	–	–	–	sub-μM[f]	–	–
ADP	–	–	–	60 ± 10	> 2[g]	> 18[g]
AMP-CP	–	–	–	500 ± 40	>0.08[h]	> 40[h]

[a]Values were obtained using the relationship $k_{ex} = k_{on}[\text{Elk1D}]_{free} + k_{off} > 60$ Hz (e.g. L155), and $K_d = k_{off}/k_{on}$, with $[\text{Elk1D}]_{free}$ of 5 μM and 14 μM for 0P- and 2P-ERK2, respectively. $[\text{Elk1D}]_{free}$ is estimated using $[\text{Elk1D}]_{total}$ at the 1st titration point, $[\text{ERK2}]_{total}$ and K_d.
[b]The k_{on} and k_{off} values were obtained from fits of the line shapes of the L113 methyl peak for titration of Elk1D into 0P-ERK2, where the spectra were simulated using LineShapeKin[165] with $|\Delta\omega|$ of 200 Hz (see Figure 4.4).
[c]Values were obtained using the relationship $k_{ex} = k_{on}[\text{AMP-PNP}]_{free} + k_{off} < 80$ Hz (e.g. slow exchange for L26), using $[\text{AMP-PNP}]_{free}$ of 1 mM for both 0P- and 2P-ERK2. $[\text{AMP-PNP}]_{free}$ is estimated using $[\text{AMP-PNP}]_{total}$ at the last titration point, $[\text{ERK2}]_{total}$ and K_d.
[d]This K_d value is measured with 0P-ERK2 I124A mutant. I124 is far from the ATP binding site and is not expected to cause severe perturbation to the affinity. Information on k_{on} and k_{off} were obtained using the relationship $k_{ex} = k_{on}[\text{AMP-PCP}]_{free} + k_{off} > 36$ Hz (e.g. fast exchange for I82), with $[\text{AMP-PCP}]_{free}$ of 59 μM for 0P-ERK2. This leads to $k_{off} > 18$ Hz or $k_{on} > 0.3\ \mu M^{-1}s^{-1}$. Considering $K_d = k_{off}/k_{on} = 300\ \mu M$, $k_{on} > 0.06\ \mu M^{-1}s^{-1}$ and $k_{off} > 18$ Hz.
[e]Values were obtained using the relationship $k_{ex} = k_{on}[\text{AMP-PCP}]_{free} + k_{off} > 30$ Hz (e.g. fast exchange for L161), with $[\text{AMP-PCP}]_{free}$ of 114 μM for 2P-ERK2. This leads to $k_{off} > 15$ Hz or $k_{on} > 0.13\ \mu M^{-1}s^{-1}$. Considering $K_d = k_{off}/k_{on} = 380\ \mu M$, $k_{on} > 0.04\ \mu M^{-1}s^{-1}$ and $k_{off} > 15$ Hz.
[f]No K_d value is reported because the titration has too few points to yield any accurate K_d value (it yielded K_d value of 2 ± 2 μM).
[g]Values were obtained using the relationship $k_{ex} = k_{on}[\text{ADP}]_{free} + k_{off} > 35$ Hz (e.g. fast exchange for L161), with $[\text{ADP}]_{free}$ of 9 μM for 2P-ERK2. This leads to $k_{off} > 18$ Hz or $k_{on} > 2\ \mu M^{-1}s^{-1}$. Considering $K_d = k_{off}/k_{on} = 60\ \mu M$, $k_{on} > 0.3\ \mu M^{-1}s^{-1}$ and $k_{off} > 18$ Hz.
[h]Values were obtained using the relationship $k_{ex} = k_{on}[\text{AMP-CP}]_{free} + k_{off} > 80$ Hz (e.g. fast exchange for L26), using $[\text{AMP-CP}]_{free}$ of 37 μM for 2P-ERK2. This leads to $k_{off} > 40$ Hz or $k_{on} > 1\ \mu M^{-1}s^{-1}$. Considering $K_d = k_{off}/k_{on} = 500\ \mu M$, $k_{on} > 0.08\ \mu M^{-1}s^{-1}$ and $k_{off} > 40$ Hz.

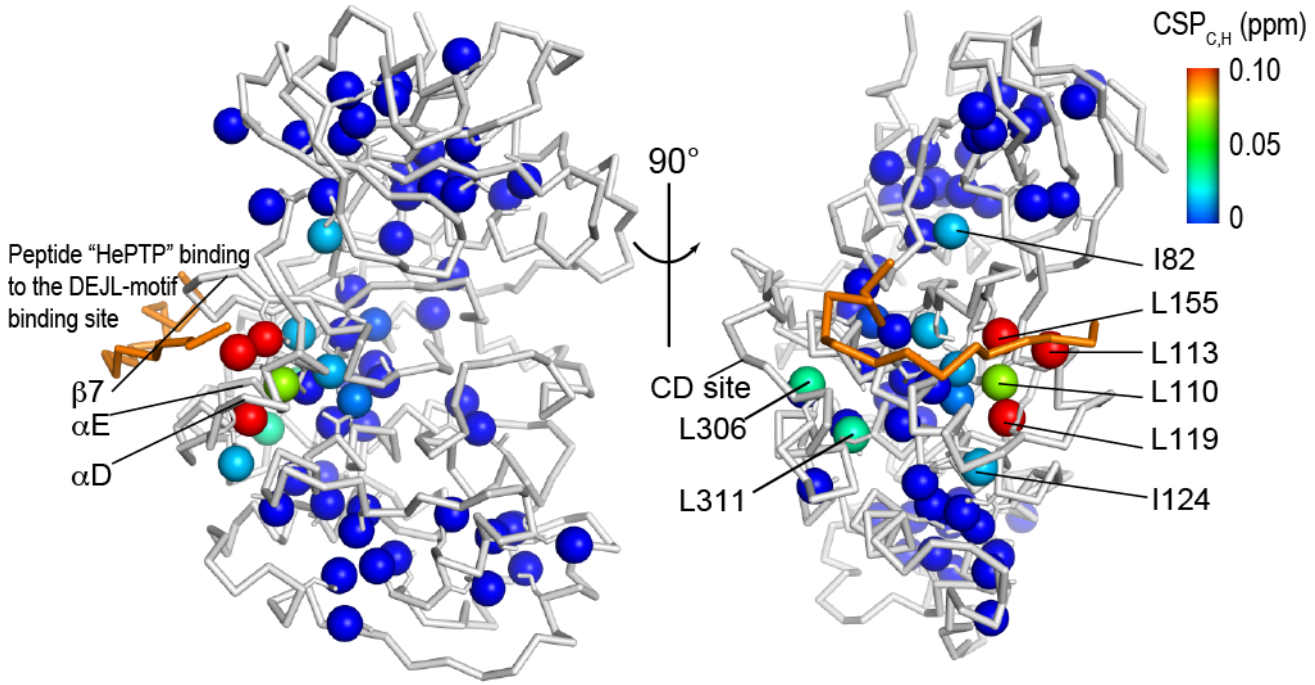

Figure 4.3. Chemical shift perturbation upon binding the Elk1D peptide to inactive and active ERK2. The $CSP_{C,H}$ values for 2P-ERK2 derived from the binding curves are mapped onto the X-ray structure of 0P-ERK2, shown in a complex with a DEJL-motif peptide (colored in gold) derived from hematopoietic tyrosine phosphatase (HePTP, PDB 2GPH). The color scale for the $CSP_{C,H}$ values is on the right, with blue indicating no measurable perturbation and red the largest perturbation.

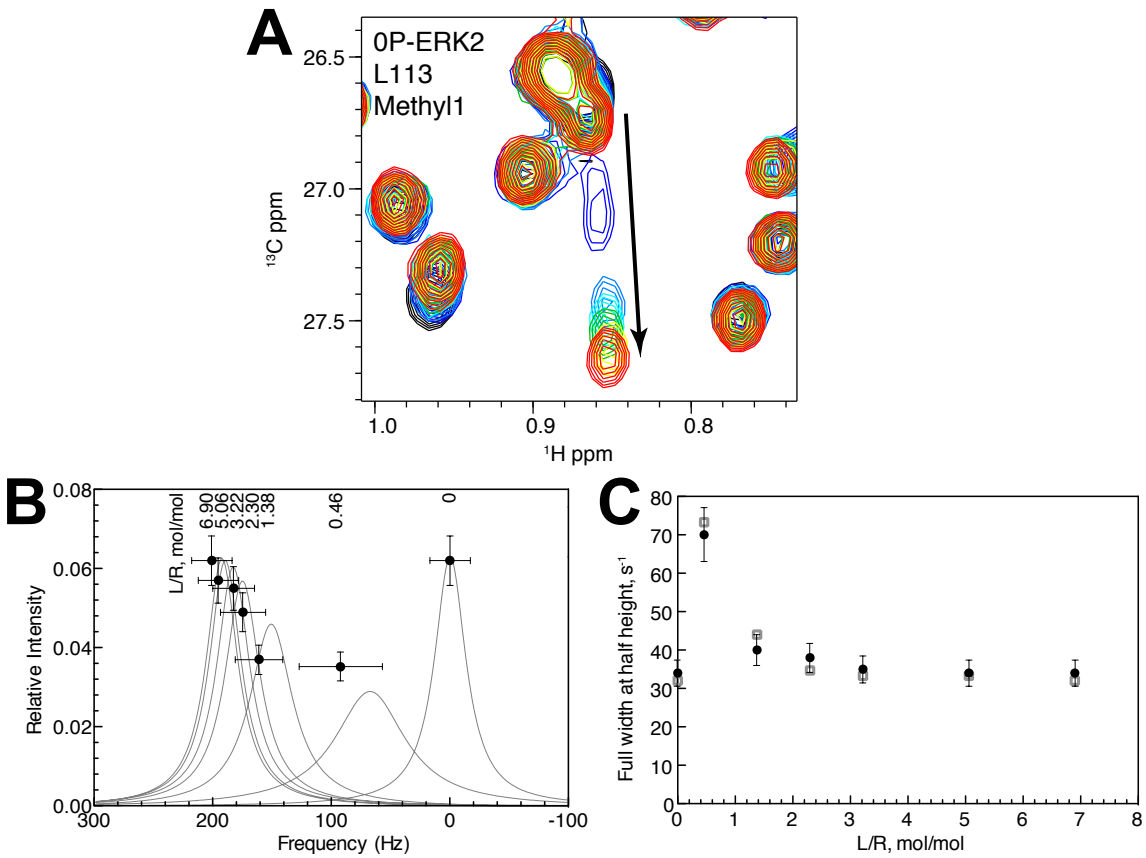

Figure 4.4. Line shape analysis of the HMQC spectra yields kinetic information for Elk1D binding to ERK2. (A) Chemical shift changes for one of the L113 methyls in the HMQC spectra of 0P-ERK2 upon titration with Elk1D. The arrow shows the chemical shift changes with increasing [Elk1D], where the free ERK2 is in black and the saturated peak ([0P-ERK2]:[Elk1D]=1:7) is in red. This methyl resonance is overlapped in free ERK2. (B) Comparison of the simulated and experimental data for titration of 0P-ERK2 with Elk1D. The intensities and ^{13}C chemical shifts of L113 in 0P-ERK2 from the HMQC spectra are shown as filled circles as a function of L/R ($[\text{Elk1D}]_{total}/[\text{0P-ERK2}]_{total}$). Simulated spectra for different L/R ratios are shown in grey. The simulations were performed using LineShapeKin Simulation[165] with $k_{off} = 300\ s^{-1}$, $k_{on} = 30\ \mu M^{-1}\ s^{-1}$, and $|\Delta\omega| = 200$ Hz. The intensity of the saturated peak was used to normalize the experimental and simulated spectra. The intensity of L113 in the free state could not be directly measured due to resonance overlap so the intensity of the saturated peak was used. The intensity of the L113 resonance at L/R = 0.46 could be over-estimated because it is close to other methyls. The errors in chemical shifts were estimated at 50% of the line width and errors in peak intensities were estimated at ± 10%. (C) Experimental (filled circles) and simulated (open squares) line widths of L113 methyl in 0P-ERK2 as a function of L/R ($[\text{Elk1D}]_{total}/[\text{0P-ERK2}]_{total}$). The ^{13}C line width for L113 in the free state could not be directly measured due to resonance overlap, so the line width of saturated peak was used. Experimental line widths were plotted with estimated errors of ± 10%.

4.3.2. AMP-PNP Binding to 0P- and 2P-ERK2

The effects of nucleotide binding to inactive and active ERK2 were studied by monitoring the ILV methyl region of the HMQC spectra of ERK2 as function of the concentration of the ATP analog AMP-PNP. In contrast to the fast exchange observed in Elk1D peptide binding, multiple methyl resonances in 0P- and 2P-ERK2 showed slow or intermediate exchange between free and bound states upon addition of nucleotide, depending on their chemical shift differences between the free and bound states. As seen in Figure 4.5, the volumes for one of the methyl resonances for L26 in both 0P- and 2P-ERK2 decreased with no change in chemical shift upon addition of AMP-PNP and a new resonance was observed at later points of AMP-PNP titration. In 2P-ERK2, the magnitude of the chemical shift difference ($|\Delta\omega|_{1H}$, in Hz) of L26 methyl between free and bound forms is ≈ 80 Hz and is primarily in the ^{1}H dimension. The slow exchange means that k_{ex} is less than 80 Hz, where $k_{ex} = k_{on}[\text{AMP-PNP}]_{free} + k_{off}$. Methyl resonances that showed smaller $|\Delta\omega|$ broadened and shifted upon addition of AMP-PNP, consistent with intermediate to fast exchange between the free and bound forms of 0P/2P-ERK2. It was not possible to accurately determine the K_d values for AMP-PNP binding to ERK2 because being slow or intermediate exchange lowers the signal-to-noise of the methyl peaks, preventing accurate measurement of the peak volumes and therefore populations. Furthermore, the standard equations for extracting kinetic data from 1D line shapes do not apply in 2D spectra unless there is no ^{1}H or ^{13}C chemical shift difference for the two states. Given these limitations, it was still possible to estimate a range of K_d values of 200-500 μM for AMP-PNP binding to 0P- or 2P-ERK2.

The chemical shift perturbations for assigned methyls upon binding of AMP-PNP to 0P- and 2P-ERK2 were mapped onto the X-ray structure of the 0P-ERK2:AMP-PNP complex as illustrated in Figure 4.6. The binding of AMP-PNP induced perturbations throughout the N-terminal lobe and upper C-terminal lobe for both 0P- and 2P-ERK2. The methyls in proximity to the ATP binding site either

showed the largest chemical shift perturbations (e.g. I29, L105, and L155), or were not observed (e.g. V37 and L154) even upon saturation with AMP-PNP (Figure 4.8). The latter methyls were likely not observed due to exchange broadening between multiple conformations in the bound state. Overall, the methyls that were perturbed upon AMP-PNP binding were quite similar between 0P- and 2P-ERK2, with small differences in the magnitudes of perturbations for individual methyls. The comparison of 2D (^{13}C, ^{1}H) HMQC experiments performed on 0P-ERK2 and 2P-ERK2 in the presence and absence of saturating AMP-PNP showed small effect on the populations of T⇌R conformations in either form of kinase, indicating that the major state in 2P-ERK2 (R state) is not further stabilized by nucleotide binding (Figure 4.8, Figure 4.9 and Table 4.12).

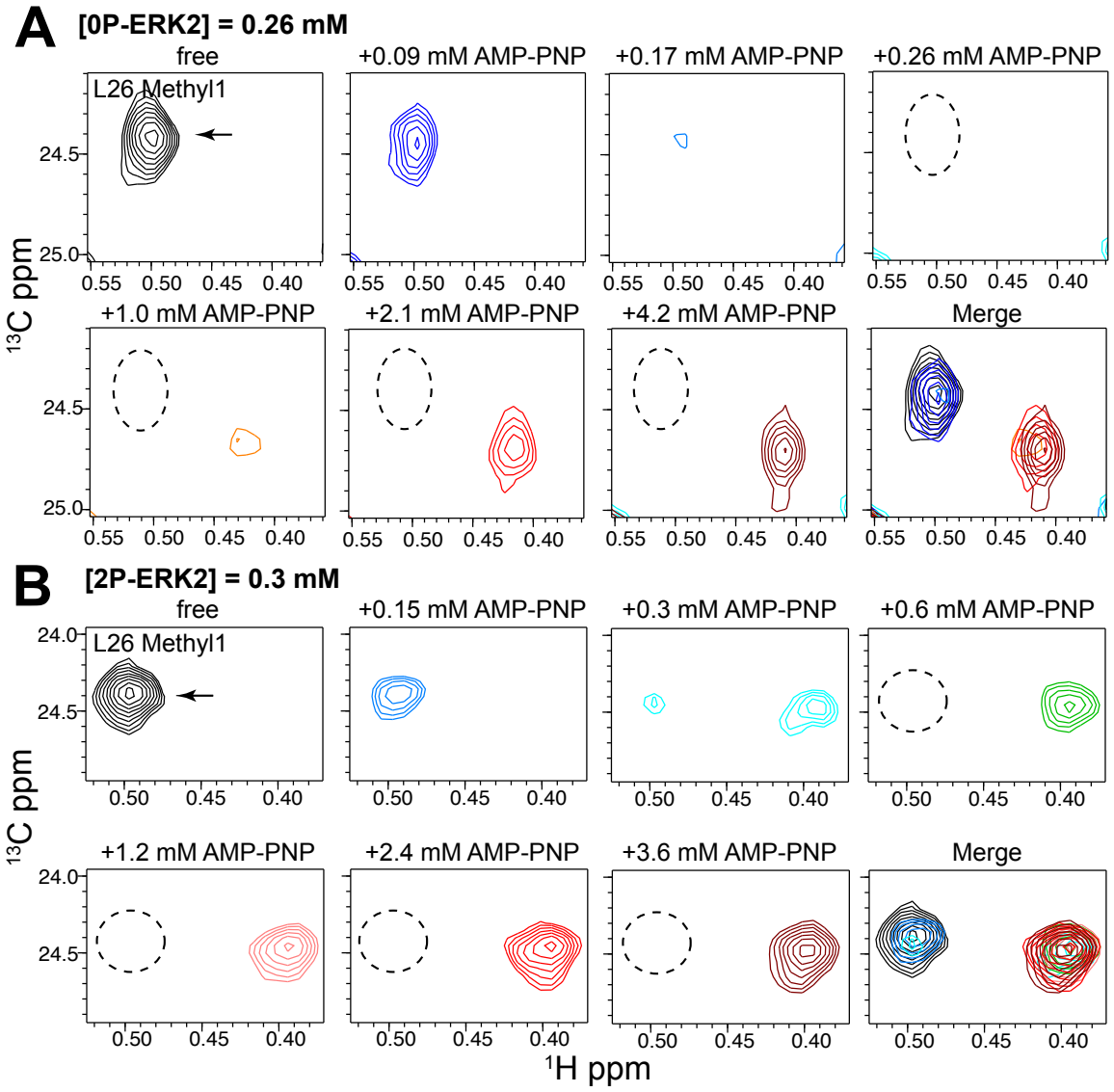

Figure 4.5. Methyl of L26 showed slow exchange during binding of AMP-PNP to inactive and active ERK2. A portion of the Leu/Val region of the 2D HMQC spectra of 0P- and 2P-ERK2 upon titration with AMP-PNP. These spectra show that one of the methyl resonances of L26 is in slow exchange on the NMR chemical shift timescale between free and bound forms for both 0P- and 2P-ERK2. The arrows point to the peak in the free form of ERK2 and the dashed lines outline the position of the free peak.

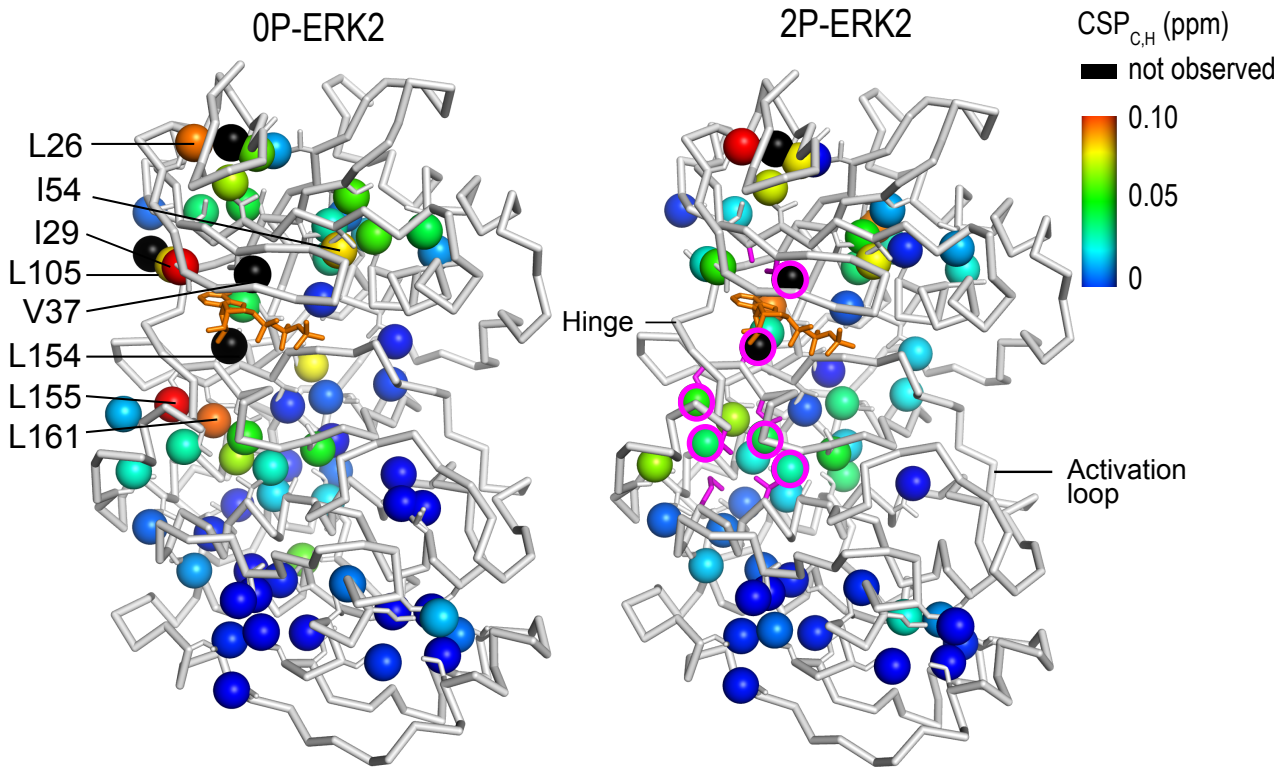

Figure 4.6. Chemical shift perturbation of binding of AMP-PNP to inactive and active ERK2.
The $CSP_{C,H}$ for methyls between the free and AMP-PNP-bound form is mapped onto an X-ray structure of 0P-ERK2 complexed with ATP (PDB 4GT3). The color scale for the $CSP_{C,H}$ values is on the right, with blue indicating no measurable perturbation, red indicating the largest perturbations and magenta indicating that these peaks were not observed in the spectra with saturated AMP-PNP, possibly due to chemical exchange broadening in the bound state. The ligand ATP is highlighted with orange sticks. The side chains of the eight "catalytic spine" residues were shown in magenta sticks. Six out of the eight were I/L/V residues, with their methyls highlighted with magenta circles.

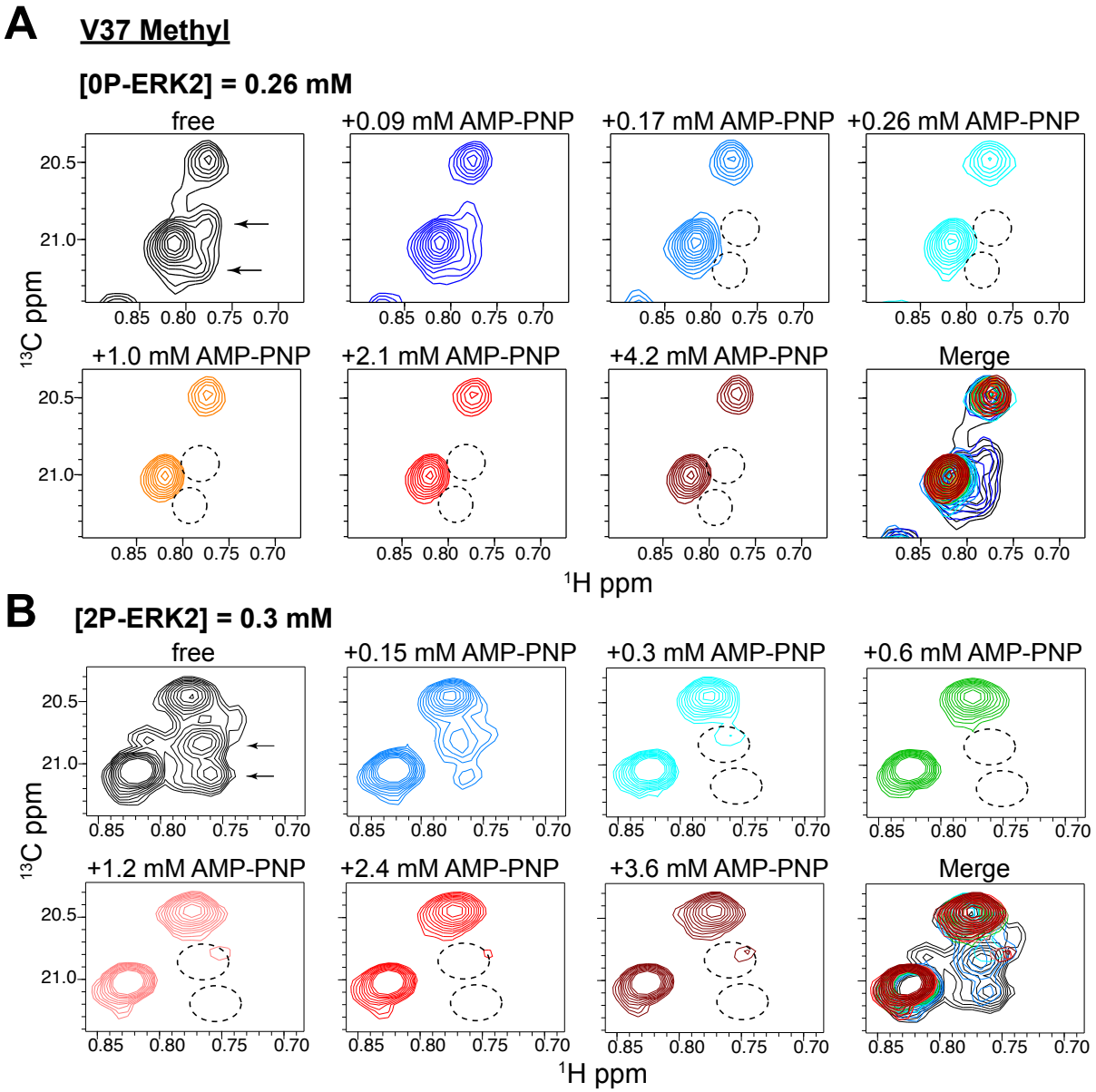

Figure 4.7. Methyl dynamics for binding of AMP-PNP to ERK2.
The V37 methyl region of the HMQC spectra of 0P- and 2P-ERK2 are plotted as a function of [AMP-PNP]. The methyl resonances for V37 were not observed in most of the spectra of the (A) 0P-ERK2: AMP-PNP or (B) 2P-ERK2:AMP-PNP complexes, even at the highest concentration of AMP-PNP. The arrows point to the positions of the methyls in the free form of ERK2 and the dashed ellipses show this position in other spectra. These data indicate that the two methyl resonances of V37 are broadened due to conformational exchange in the AMP-PNP complex for both 0P- and 2P-ERK2.

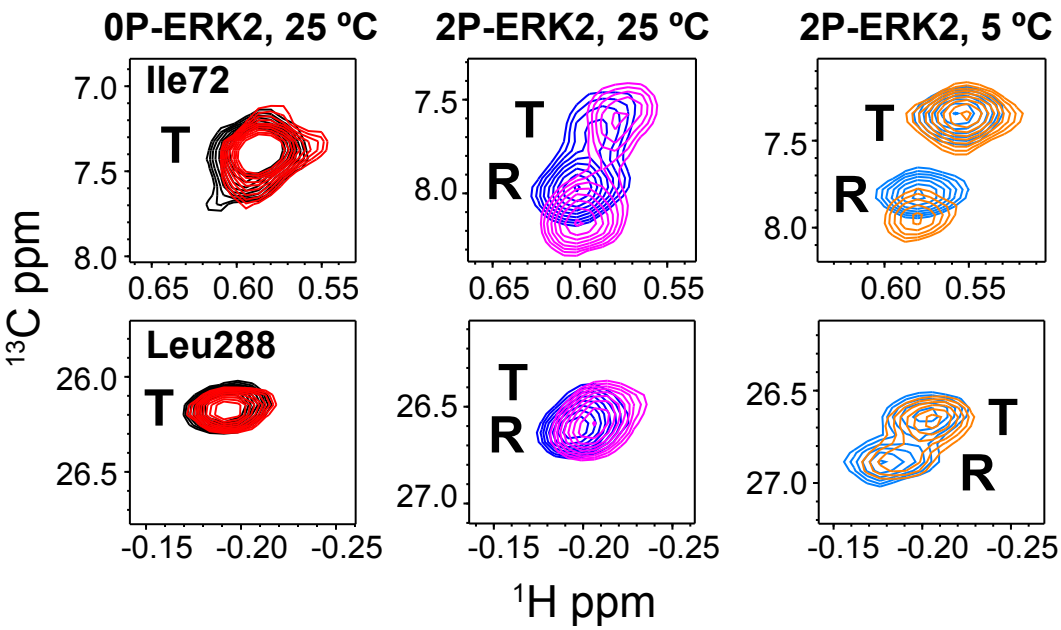

Figure 4.8. Nucleotide binding does not increase the R population in 0P- and 2P-ERK2.
Left: 2D (^{13}C, ^{1}H) HMQC peaks of 0P-ERK2 at 25°C with and without 1 mM AMP-PNP colored in red and black, respectively. Middle: 2P-ERK2 at 25°C with and without AMP-PNP, colored in magenta and blue, respectively. Right: 2P-ERK2 at 5°C, with and without AMP-PNP, colored in orange and skyblue, respectively.

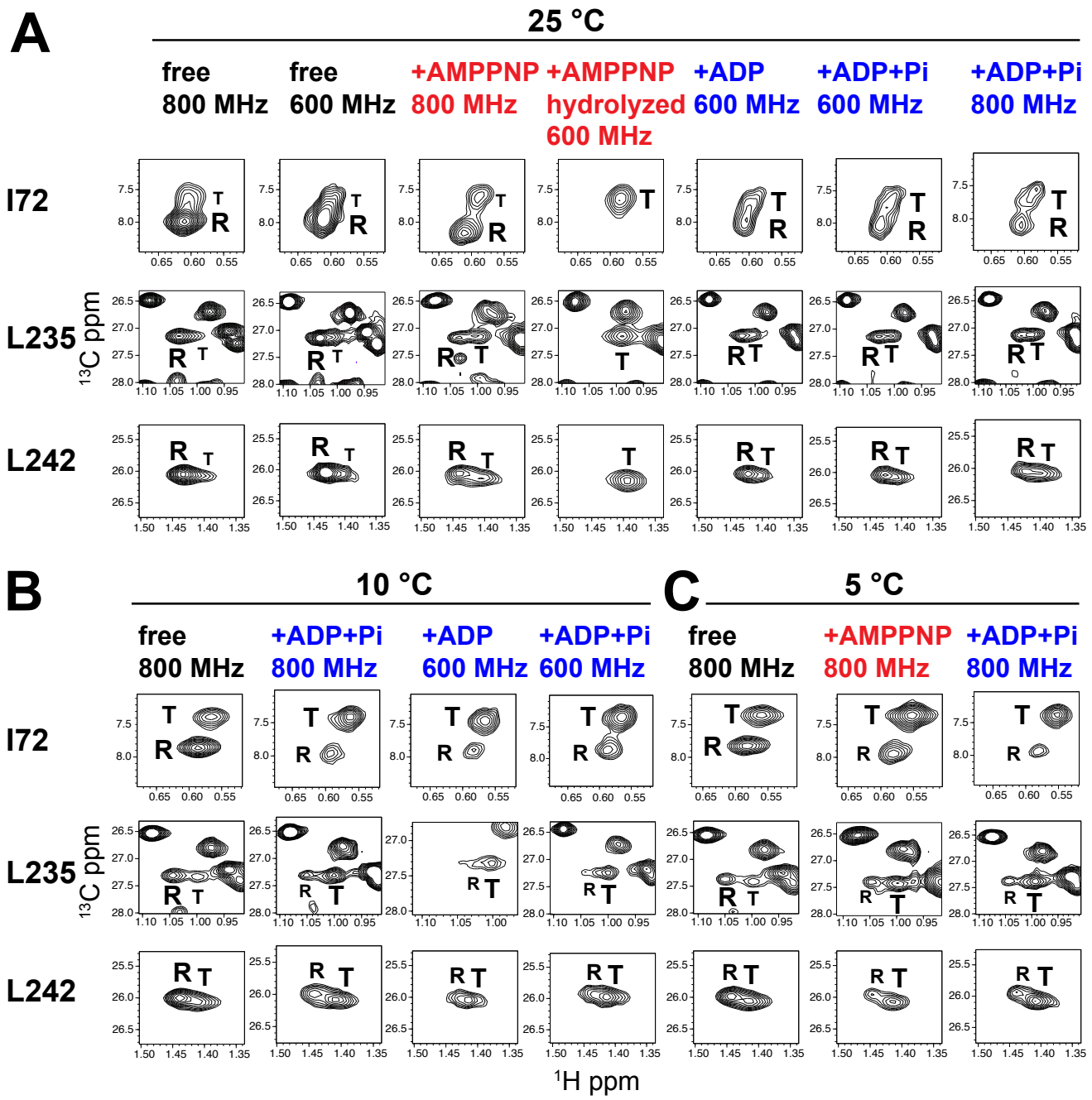

Figure 4.9. The slow-exchanging peaks in 2P-ERK2 upon binding AMP-PNP or ADP.
2D (^{13}C, ^{1}H) HMQC spectra showing slow-exchanging methyls of 2P-ERK2 complexes collected at (A) 25°C; (B) 10°C; and (C) 5°C. A shift to the T conformation was compared to AMP-PNP- or ADP-bound 2P-ERK2 comparing with free 2P-ERK2.

Table 4.12. Peak Volume Estimations of I72 methyl for Ligand Interactions with 0P- and 2P-ERK2

	0P-ERK2				2P-ERK2			
	25 °C		5 °C		25 °C		5 °C	
	T	R	T	R	T	R	T	R
No inhibitor	100	0	100	0	20	80	46[a]	54[a]
AMP-PNP	–	–	–	–	35[b]	65[b]	67[c]	33[c]
ADP	–	–	–	–	–	–	68[d]	32[d]
AMP-CP							64[e]	36[e]
Vertex-11e	100	0	100	0	0	100	0	100
SCH772984	100	0	100	0	100	0	100	0
GDC-0994	–	–	–	–	20	80	53	47

[a]Estimated from Figure 4.9C (the 1st column, I72).
[b]Estimated from Figure 4.9A (the 3rd column, I72).
[c]Estimated from Figure 4.9C (the 2nd column, I72).
[d]Estimated from Figure 4.9C (the 3rd column, I72).
[e]Estimated from Figure 4.24 (the 3rd column, I72).

4.3.3. ADP Binding to 2P-ERK2

To understand the R⇌T conformational dynamics in the binary product-bound complex of 2P-ERK2, ADP was titrated into 2P-ERK2 to form a 2P-ERK2:ADP complex. The methyls in 2P-ERK2 showed either fast exchange (e.g. L161) or slow-intermediate exchange (e.g. L26) during the titration of ADP, dependent on the chemical shift difference between the free and bound forms (Figure 4.10). Chemical shift perturbations of the ^{13}C and ^{1}H resonances ($CSP_{C,H}$) for ILV methyls were then globally fit to a binding isotherm yielding a single K_d for binding as well as the magnitude of the chemical shift differences between the free and bound states of ERK2 (Figure 4.11). The K_d value obtained for ADP to 2P-ERK2 was 60 ± 10 μM (Figure 4.11). Similar to AMP-PNP, ADP showed clear chemical shift perturbations for methyls that are indicative of occupancy at the ATP-binding pocket. Small perturbation on the R⇌T conformational equilibrium with slight increase on the population of the T state comparing with free 2P-ERK2 was observed in the binary product-bound complex of 2P-ERK2 (2P-ERK2:ADP complex) (Figure 4.9). In contrast, the spectra were not perturbed by the addition of sodium phosphate (NaPi) to the 2P-ERK2:ADP complex, indicating that phosphate by itself doesn't bind to 2P-ERK2 (Figure 4.9).

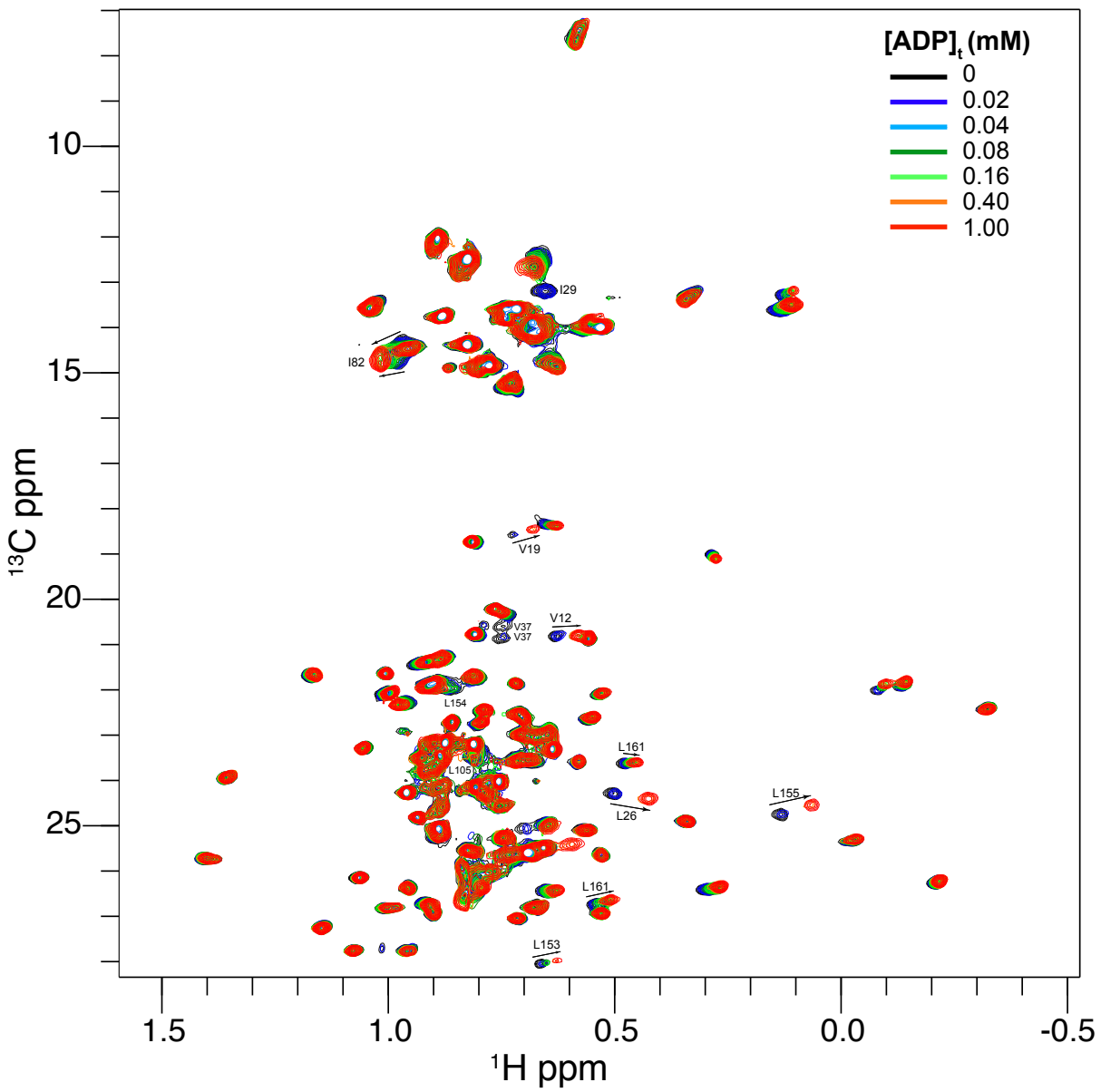

Figure 4.10. Spectral perturbations upon ADP binding to 2P-ERK2.
2D (^{13}C, ^{1}H) HMQC spectra of 2P-ERK2 at different total ADP concentrations ($[ADP]_t$) were overlaid. Clear chemical shift perturbations of methyls were highlighted with arrows, labeled with residue type and number.

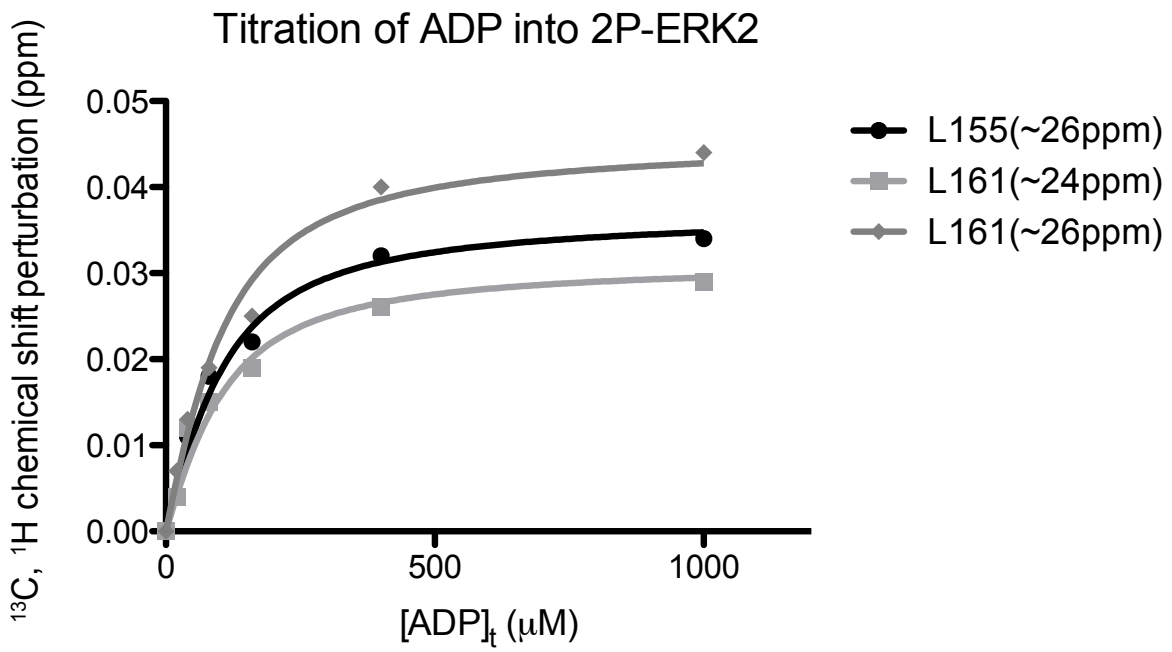

Figure 4.11. Methyl ^{13}C and ^{1}H chemical shift perturbations during ADP titration into 2P-ERK2.
The carbon and proton combined methyl chemical shift perturbations of methyls undergoing fast exchange during the binding (L155, L161) were plotted over different total concentrations of ADP ($[ADP]_t$). The curves reflect a global fitting of these titration points into the same binding event with a shared K_d value.

4.3.4. AMP-PNP and ADP Hydrolysis Occur upon Incubating with ERK2

The 2D (^{13}C, ^{1}H) HMQC spectra on 2P-ERK2 in the presence of AMP-PNP underwent observable changes, one week after the last spectra in the AMP-PNP titration experiment were collected. For example, several methyls that underwent slow-exchange between R⇌T conformations in the 2P-ERK2:AMP-PNP complex showed only the T conformation when a spectrum of the same sample was collected one week later ("AMP-PNP hydrolyzed", Figure 4.9A). To investigate if this change in the spectra was due to dephosphorylation of 2P-ERK2 to 0P-ERK2, the mass-to-charge (m/z) ratio of the activation loop peptide harboring the activating phosphorylation sites was examined by mass spectrometry (Figure 4.12). The analysis of this peptide showed that the 2P-ERK2 has 98% dual-phosphorylation (2P), demonstrating that 2P-ERK2 in the sample was not dephosphorylated. A parallel mass spec analysis was performed for 0P-ERK2, which only m/z of the unphosphorylated activation loop peptide was observed, consistent with 100% unphosphorylated ERK2 (Figure 4.13).

To investigate if the change in NMR spectrum was a result of AMP-PNP hydrolysis, 1D ^{31}P spectra of the same 2P-ERK2 sample containing 1.0-1.15 mM AMP-PNP was collected on a 500 MHz spectrometer, and was compared to a sample of 1.0 mM AMP-PNP newly prepared within 12 h before data collection. The comparison showed clear differences between the samples of AMP-PNP + 2P-ERK2 and the free AMP-PNP. The former showed a 1D ^{31}P spectrum indicating a 50%-70% hydrolyzed AMP-PNP (Figure 4.14A), where 6 resonances are observed, corresponding to the remaining intact AMP-PNP (αP, βP, and γP), phosphates (Pi) and ATP hydrolyzed product (α'P and β'P). In contrast, the latter showed spectra that is characteristic of an intact AMP-PNP, where only resonances for αP, βP, and γP were observed (Figure 4.14E).[166, 167] Thus, AMP-PNP after incubation with 2P-ERK2 for several weeks showed evidence of severe hydrolysis. Similarly, the sample of AMP-PNP incubated with 0P-ERK2 from the parallel titration experiment also showed severe

hydrolysis (Figure 4.14B). In contrast to the AMP-PNP incubated with 0P- or 2P-ERK2, free AMP-PNP incubated at room temperature for 2 weeks (Figure 4.14C-D) showed no significant hydrolysis, indicating that the fast hydrolysis of AMP-PNP is due to the presence of the 0P- or 2P-ERK2 sample.

I then asked if ADP was hydrolyzed during the ADP titration experiment into 2P-ERK2. A control ^{31}P spectra of a newly made (within 12 h) sample of 1.8 mM ADP showed peaks which were characteristic of intact ADP, where only resonances for αP and βP were observed (Figure 4.15A).[168] 1D ^{31}P spectra of the 2P-ERK2 sample was collected ~15 h after each new addition of new ADP and collection of 2D (^{13}C, ^{1}H) HMQC spectra for each titration point. The 1D ^{31}P spectra of the ADP+2P-ERK2 sample were collected at ADP concentrations ($[ADP]_t$) of 0.16, 0.4, and 1.0 mM, which were high enough to provide visible signal in a 6 h ^{31}P experiment (Figure 4.15B-D). Surprisingly, each 1D ^{31}P spectra of the ADP+2P-ERK2 samples all showed new peaks corresponding to AMP and phosphate (Pi), consistent with significant (~70%) hydrolysis of ADP within 15 h after ADP addition. In contrast, the 1D ^{31}P spectra of free ADP remained the same after incubation at room temperature for one week (Figure 4.15E). This difference demonstrates that the 2P-ERK2 sample also induced hydrolysis of ADP.

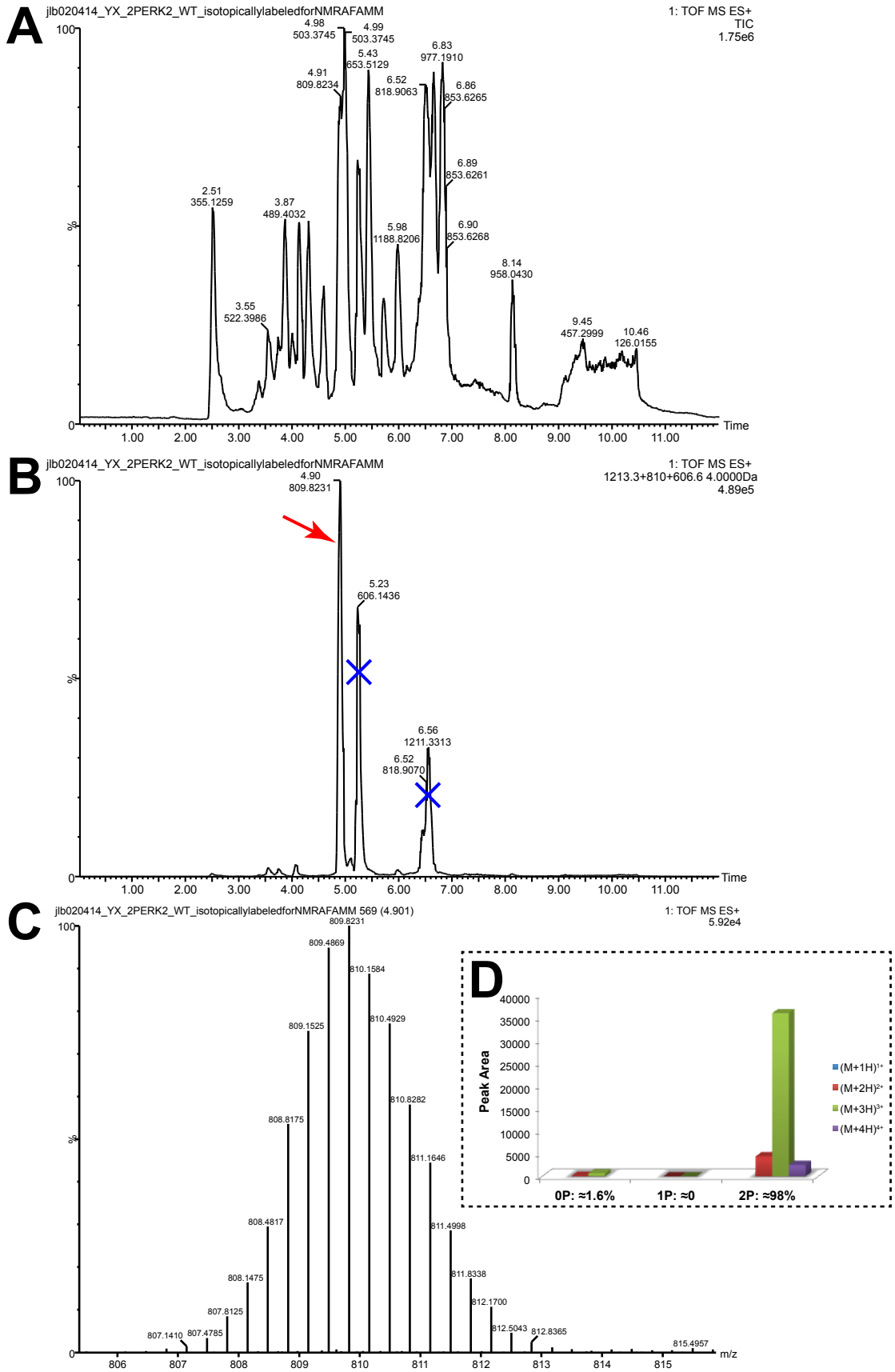
A
jlb020414_YX_2PERK2_WT_isotopicallylabeledforNMRAFAMM
1: TOF MS ES+
TIC
1.75e6
4.98
503.3745
4.99
503.3745
5.43
653.5129
4.91
809.8234
6.83
977.1910
6.52
818.9063
6.86
853.6265
6.89
853.6261
2.51
355.1259
3.87
489.4032
5.98
1188.8206
6.90
853.6268
8.14
958.0430
3.55
522.3986
9.45
457.2999
10.46
126.0155
Time
B
jlb020414_YX_2PERK2_WT_isotopicallylabeledforNMRAFAMM
1: TOF MS ES+
1213.3+810+606.6 4.0000Da
4.89e5
4.90
809.8231
5.23
606.1436
6.56
1211.3313
6.52
818.9070
Time
C
jlb020414_YX_2PERK2_WT_isotopicallylabeledforNMRAFAMM 569 (4.901)
1: TOF MS ES+
5.92e4
809.8231
809.4869
810.1584
809.1525
810.4929
810.8282
808.8175
811.1646
808.4817
811.4998
808.1475
811.8338
807.8125
812.1700
807.1410
807.4785
812.5043
812.8365
815.4957
m/z
D
Peak Area
(M+1H)1+
(M+2H)2+
(M+3H)3+
(M+4H)4+
0P: ≈1.6%
1P: ≈0
2P: ≈98%

Figure 4.12. Time-of-flight mass spectrometry confirmed dual phosphorylation on the activation loop of 2P-ERK2.
(A) The total ion current (TIC) chromatogram from an LC-MS analysis showing the retention times (in minutes) of all the detected peptide ions from a trypsin-digested sample of isotopically labeled 2P-ERK2. (B) The extracted-ion chromatogram (XIC) showing the mass-to-charge ratios (m/z) for the peptide of interest. Here, m/z values of 1213.3 for $(M+2H)^{2+}$, 809.8 $(M+3H)^{3+}$, and 606.6 $(M+4H)^{4+}$ with a m/z window of 4 Da for each were searched to identify the activation loop peptide VADPDHDHTGFpTEpYVATR among all the 2P-ERK2 peptides. The peak that corresponds to the activation loop peptide is labeled with a red arrow. The other peaks result from other trypsin-generated ERK2 peptide ions, and those were labeled with blue crosses. Note that this m/z window used for the search is wider than a search of an unlabeled protein, considering the isotope labeling on 2P-ERK2 yields a wider isotope distribution and therefore a wider mass range. (C) $(M+3H)^{3+}$ isotope distribution for 2P-VADPDHDHTGFTEYVATR centered at 809.8. (D) The m/z expected for 0P, 1P and 2P-forms of this peptide is searched. The sum of peak areas of different charge states was compared between these forms. These spectra were generated by Dr. Jeremy Balsbaugh.

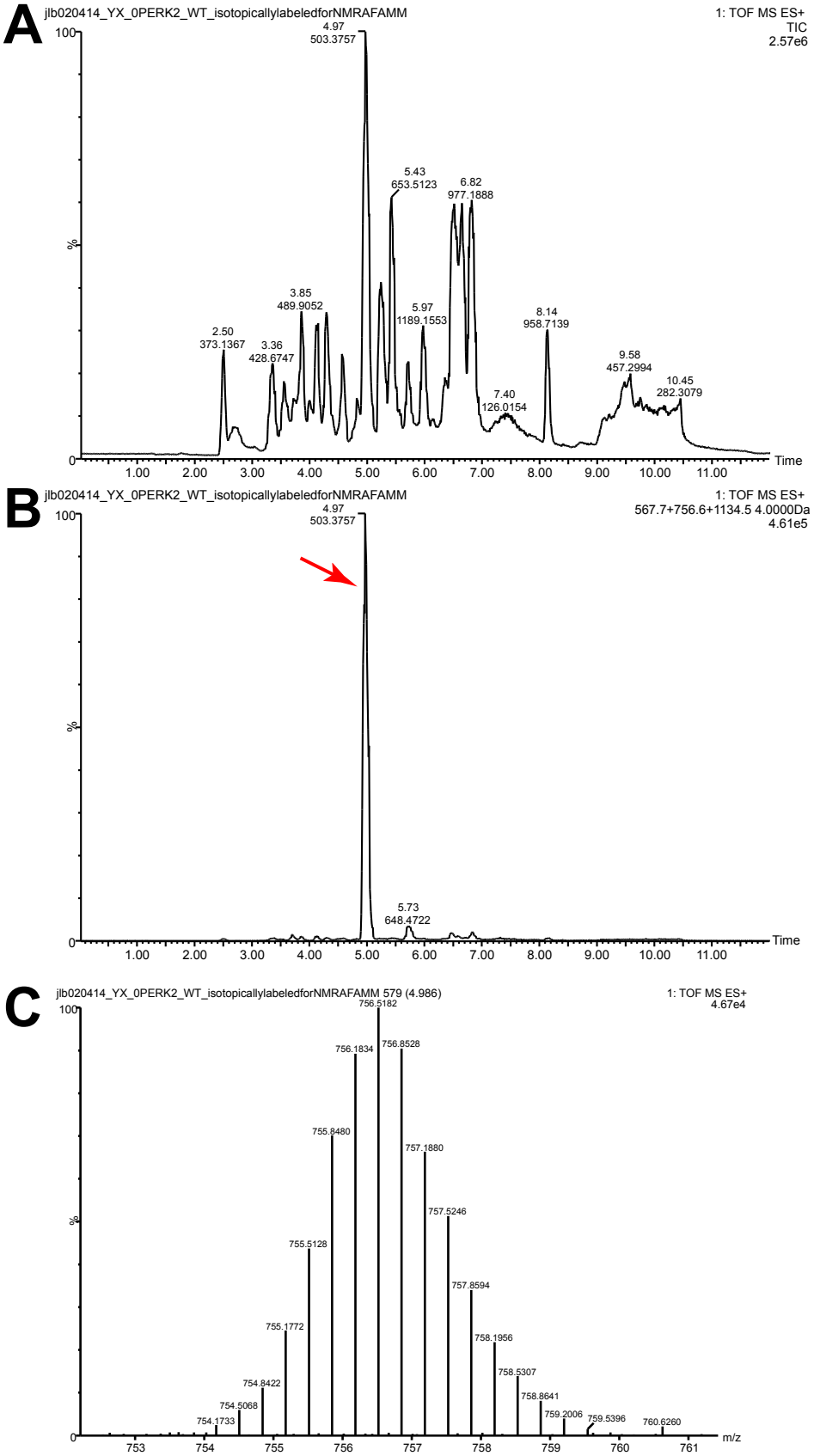
A
jlb020414_YX_0PERK2_WT_isotopicallylabeledforNMRAFAMM
1: TOF MS ES+
TIC
2.57e6
4.97
503.3757
5.43
653.5123
6.82
977.1888
3.85
489.9052
5.97
1189.1553
8.14
958.7139
2.50
373.1367
3.36
428.6747
9.58
457.2994
10.45
282.3079
7.40
126.0154
Time
B
jlb020414_YX_0PERK2_WT_isotopicallylabeledforNMRAFAMM
1: TOF MS ES+
567.7+756.6+1134.5 4.0000Da
4.61e5
4.97
503.3757
5.73
648.4722
Time
C
jlb020414_YX_0PERK2_WT_isotopicallylabeledforNMRAFAMM 579 (4.986)
1: TOF MS ES+
4.67e4
756.5182
756.1834
756.8528
755.8480
757.1880
757.5246
755.5128
757.8594
755.1772
758.1956
758.5307
754.8422
754.5068
758.8641
754.1733
759.2006
759.5396
760.6260
m/z

Figure 4.13. Time-of-flight mass spectrometry showed only unphosphrylated activation loop peptide of 0P-ERK2.
(A) The total ion current (TIC) chromatogram from an LC-MS analysis showing the retention times (in minutes) of all the detected peptide ions from a trypsin-digested sample of isotopically labeled 0P-ERK2. (B) The extracted-ion chromatogram (XIC) showing the mass-to-charge ratios (m/z) for the peptide of interest. Here, m/z values of 1134.5 for $(M+2H)^{2+}$, 756.6 $(M+3H)^{3+}$, and 567.6 $(M+4H)^{4+}$ with a m/z window of 4 Da for each were searched to identify the activation loop peptide VADPDHDHTGFTEYVATR among all the 0P-ERK2 peptides. The peak that corresponds to the activation loop peptide is labeled with a red arrow. Note that this m/z window used for the search is wider than a search of an unlabeled protein, considering the isotope labeling on 0P-ERK2 yields a wider isotope distribution and therefore a wider mass range. (C) $(M+3H)^{3+}$ isotope distribution for 0P-VADPDHDHTGFTEYVATR centered at 756.5. These spectra were generated by Dr. Jeremy Balsbaugh.

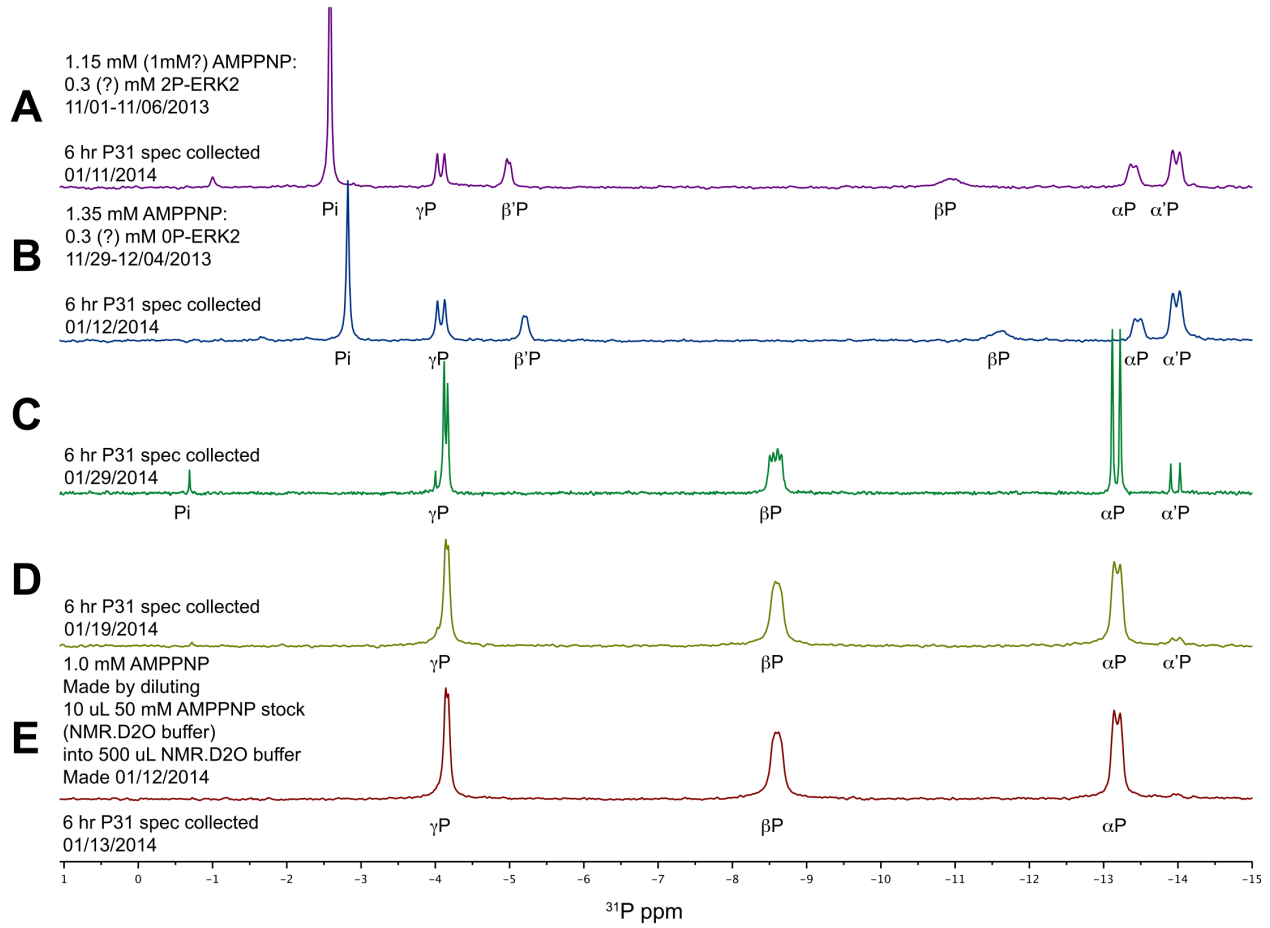

Figure 4.14. AMP-PNP hydrolysis after incubating with ERK2 observed from 1D ^{31}P spectra.
(A) 1D ^{31}P spectra (500 MHz) of 2P-ERK2:AMP-PNP complex collected 2 months after the titration experiment of 1.15 mM AMP-PNP and 0.1-0.3 mM 2P-ERK2 revealed severe AMP-PNP hydrolysis. The question marks indicate that there could be large error on those concentrations. The phosphate peak is labeled as Pi. The peaks from AMP-PNP are labeled αP, βP, and γP. The peaks from AMP-PNP hydrolyzed product are labeled α'P and β'P. (B) 1D ^{31}P spectra (500 MHz) of 0P-ERK2:AMP-PNP complex collected 2 months after the titration experiment of 1.35 mM AMP-PNP and 0.1-0.3 mM 0P-ERK2 revealed severe AMP-PNP hydrolysis. The question marks indicate that there could be large error on those concentrations. (C) 1D ^{31}P spectra (400 MHz) of 1.0 mM AMP-PNP sample collected after 15 days of room temperature incubation. The spectra collected on the 400 MHz have sharper peaks than on the 500 MHz mainly because of reduced chemical shift anisotropy effect at lower field strength. The chemical shifts of Pi, βP and αP are different from these species in (A) and (B), maybe because of different solution pHs. (D) 1D ^{31}P spectra (500 MHz) of 1.0 mM AMP-PNP sample collected after 7 days of room temperature incubation. (E) 1D ^{31}P spectra (500 MHz) of 1.0 mM AMP-PNP sample collected immediately (within 12 h after from preparation).

I next investigated whether the hydrolysis of ADP was due to ATPase activity of 2P-ERK2 or else to contaminants in the 2P-ERK2 sample (e.g. with phosphatase activity), using an enzyme-coupled assay. This assay is able to monitor ADP hydrolysis using a coupled reaction with phosphoenolpyruvate (PEP), pyruvate kinase, nicotinamide adenine dinucleotide (NADH) and lactate dehydrogenase. Pyruvate kinase catalyzes the conversion of ADP into ATP, accompanied by the dephosphorylation of PEP to pyruvate, which is then reduced to lactic acid in the presence of NADH by lactate dehydrogenase (Figure 4.16). Depletion of the NADH concentration can be monitored at 340 nm, using a molar extinction coefficient of 6220 $M^{-1}cm^{-1}$. Thus, low level of ADP hydrolysis yields a high ADP concentration and high consumption of NADH, with low absorbance at 340 nm; whereas severe ADP hydrolysis yields a low ADP concentration and low consumption of NADH with higher absorbance at 340 nm. This assay was tested using 0-0.1 mM ADP to validate its feasibility, before applying it to the ADP+ERK2 samples (Figure 4.17). ADP was incubated with 0.2 mM 2P-ERK2 (in NMR buffer) at room temperature for various periods of time in the presence or absence of the ERK2 inhibitor SCH772984 (0.25 mM), or with NMR buffer. The relative absorbance at 340 nm measured for ADP+ERK2 samples at each time point was unaffected by the presence of SCH772984, indicating completion of hydrolysis after 2-day incubation with or without inhibitor (Figure 4.18A). This suggested that the ATP binding site of 2P-ERK2, which 2P-ERK2 uses for its ATPase activity, was not responsible for the hydrolysis of ADP. Thus, it was more likely that the ADP hydrolysis was due to contaminants in the 2P-ERK2 sample. It is then showed that ADP hydrolysis could be diminished by addition of a 3x Halt phosphatase inhibitor cocktail for at least one week (Figure 4.18B). This provides a method of overcoming artificial hydrolysis in future experiments examining nucleotide binding to 2P-ERK2.

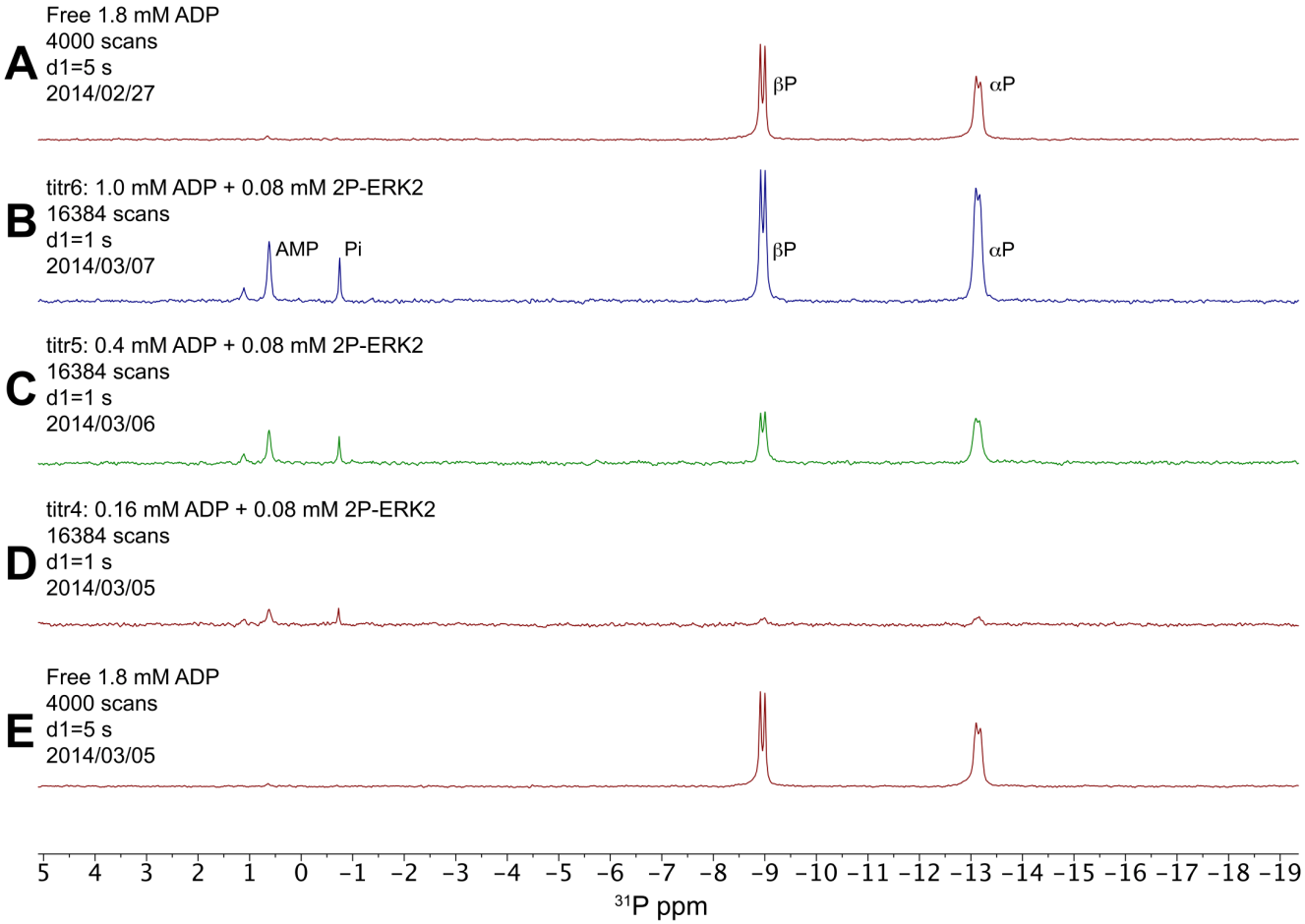

Figure 4.15. ADP hydrolysis after incubating with 2P-ERK2 observed from 1D ^{31}P spectra.
(A) 1D ^{31}P spectra of free 1.8 mM ADP collected on the same day after preparation. The peaks from ADP are assigned to αP and βP. (B) 1D ^{31}P spectra of the 2P-ERK2:ADP complex was collected 14 h after ADP titration point 6, where a 0.6 mM fresh ADP was added to the previous mixture of 0.08 mM 2P-ERK2 + 0.4 mM ADP to yield a mixture of 0.08 mM 2P-ERK2 + 1 mM ADP. Two new peaks showed up, and were assigned to AMP and phosphate (Pi). (C) 1D ^{31}P spectra of the 2P-ERK2:ADP complex was collected 14 h after ADP titration point 5, where a 0.24 mM fresh ADP was added to the previous mixture of 0.08 mM 2P-ERK2 + 0.16 mM ADP to yield a mixture of 0.08 mM 2P-ERK2 + 0.4 mM ADP. (D) 1D ^{31}P spectra of 2P-ERK2:ADP complex was collected 14 h after ADP titration point 4, where a 0.08 mM fresh ADP was added to the previous mixture of 0.08 mM 2P-ERK2 + 0.08 mM ADP to yield a mixture of 0.08 mM 2P-ERK2 + 0.16 mM ADP. ADP titration point 4 was performed 2 days after the initial ADP titration. (E) 1D ^{31}P spectra of free 1.8 mM ADP collected after one week of incubation room at temperature.

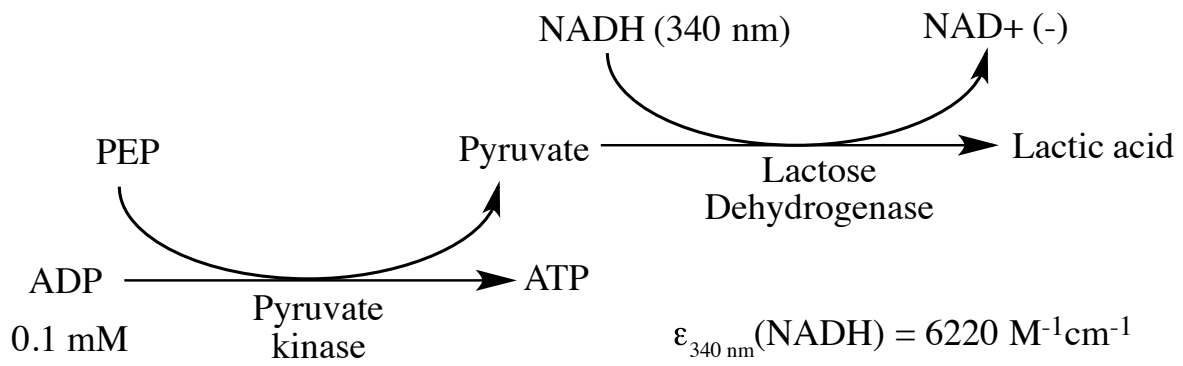

Figure 4.16. Detection of ADP hydrolysis using an enzyme-coupled assay.
The amount of NADH is evaluated at the end-point of this enzyme-coupled assay. ADP is the limiting reagent in the system. Higher amount of ADP (due to low hydrolysis) will consume more NADH, thus result in a low absorbance at 340 nm, whereas a lower amount of ADP (due to severe hydrolysis) will result in a high absorbance at 340 nm.

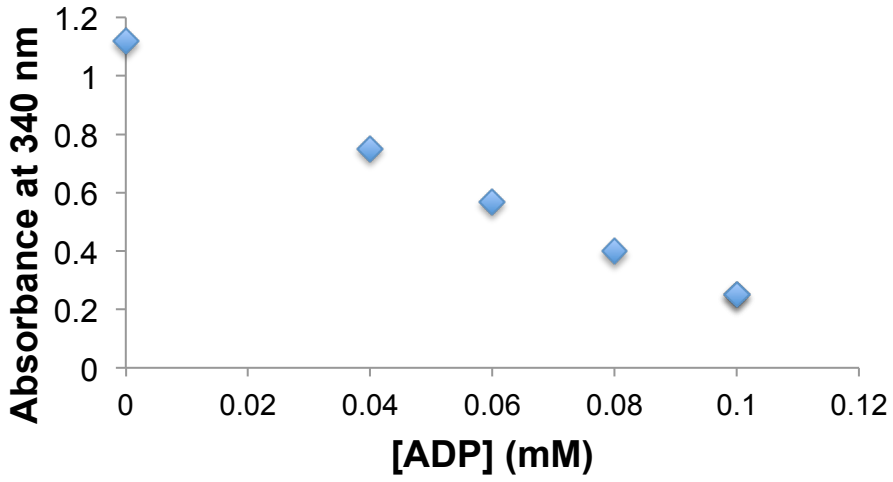

Figure 4.17. A typical calibration curve for the enzyme-coupled assay with different concentrations of ADP.
The absorbance at 340 nm at each ADP concentration was measured on a Varian absorption spectrometer.

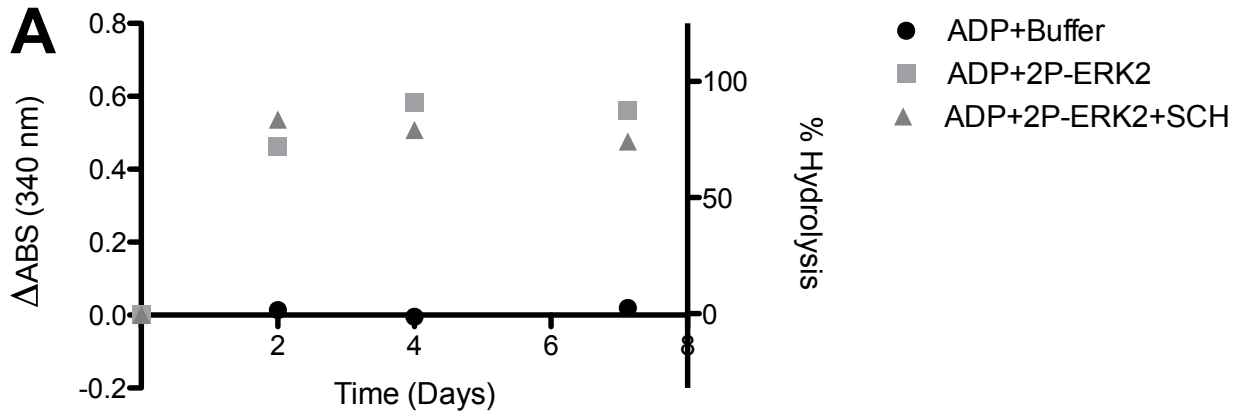

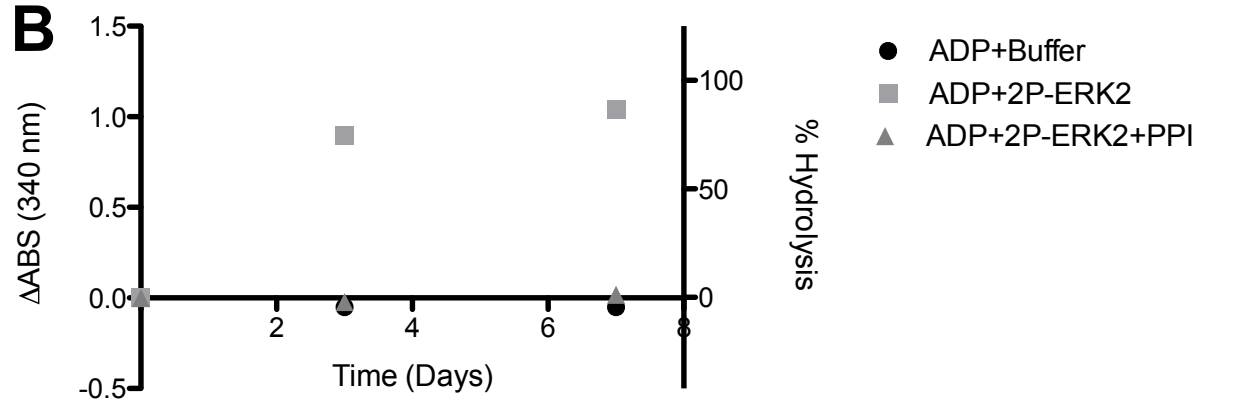

Figure 4.18. ADP hydrolysis was blocked by Halt™ Protease/Phosphatase inhibitor (PPI) cocktail, but not 2P-ERK2 inhibitor.
(A) Absorbances at 340 nm for the ADP/ERK2 sample and the ADP/ERK2/SCH772984 sample increased over time, whereas the absorbance for the ADP/buffer sample was stable over time. [SCH772984]=0.25 mM, [2P-ERK2]=0.2 mM. Absorbance at 340 nm of each sample at day 0 is used as a reference point, and the changes in absorbance (ΔABS) of each sample are plotted over time. A concentration of ADP of 0.1±0.02 mM was used for each time point. As early as day 2, a change in absorbance of ~0.5 is observed for ADP in the presence of ERK2 (with or without ERK2 inhibitor). Using the Beer-Lambert law of $\Delta ABS = \varepsilon \times \Delta c \times l$, the concentration change of NADH as well as ADP is ~ 0.08 mM, yielding ~80% hydrolysis. (B) Absorbance at 340 nm is similar for the ADP/buffer sample and the ADP/ERK2/PPI sample, whereas the absorbance for the ADP/ERK2 sample increases over time. 3x Halt™ protease and phosphatase inhibitors were used to incubate with 2P-ERK2. Absorbance at 340 nm of each sample at day 0 is used as a reference point, and the changes in absorbance (ΔABS) of each sample are plotted over time. Similar to (A), ~80% ADP hydrolysis was observed for the ADP in the presence of ERK2 as early as day 2. The level of ADP hydrolysis of that sample increased to ~90% at day 7. In constrast, the ΔABS for ADP+2P-ERK2+PPI is almost 0 after 7 days, indicating no clear change in ADP concentration.

4.3.5. AMP-PCP and Substrate Peptide sub-D Binding to 2P-ERK2

To examine if the R⇌T conformational dynamics in the ternary complex of 2P-ERK2 are significantly perturbed by the binding of ATP and peptide substrate, the non-hydrolysable ATP analogue AMP-PCP was first titrated into 2P-ERK2 to form a binary enzyme:nucleotide complex. This is followed by titration of the sub-D peptide substrate to form a ternary enzyme:nucleotide:substrate complex. As decribed earlier, the binding of AMP-PNP showed slow exchange for multiple methyls during the titration, including L26 and L155 (Figure 4.5). Here, the binding of AMP-PCP showed intermediate exchange for these methyls (Figure 4.19), and showed fast exchange for other methyls with smaller chemical shift differences between the free and bound states (Figure 4.19), indicative of faster k_{on} and/or k_{off} values, or smaller $\Delta\omega$ than AMP-PNP. Chemical shift perturbations of the ^{13}C and ^{1}H resonances ($CSP_{C,H}$) for ILV methyls were then globally fit to a binding isotherm yielding a single K_d for binding as well as the magnitude of the chemical shift differences between the free and bound states of ERK2 (Figure 4.20). This binding interaction between AMP-PCP and 2P-ERK2 exhibited a dissociation constant (K_d) of 380 ± 30 μM, comparable with AMP-PNP. Similar to AMP-PNP and ADP, AMP-PCP showed clear chemical shift perturbations for methyls that were indicative of occupancy at the ATP-binding pocket. After partial saturation with AMP-PCP, where ERK2 was 81% AMP-PCP-bound ($[AMP\text{-}PCP]_t$:$[ERK2]_t$ = 20:1), sub-D was titrated into 2P-ERK2. Intermediate to fast exchange was observed during the titration of sub-D into 2P-ERK2 (Figure 4.19). The binding of sub-D showed perturbations at a similar set of methyls as the binding of Elk1D peptide, indicating occupancy at the DEJL-site. No significant conformational perturbation on the R⇌T conformational equilibrium was observed between the ternary complex of 2P-ERK2 and free 2P-ERK2 at 25 °C (Figure 4.21). However, at 5 °C the methyls that showed clear slow exchange by two split peaks in free

2P-ERK2 failed to yield split peaks in the AMP-PCP-bound binary or ternary complex of 2P-ERK2, indicating altered conformational dynamics at lower temperature.

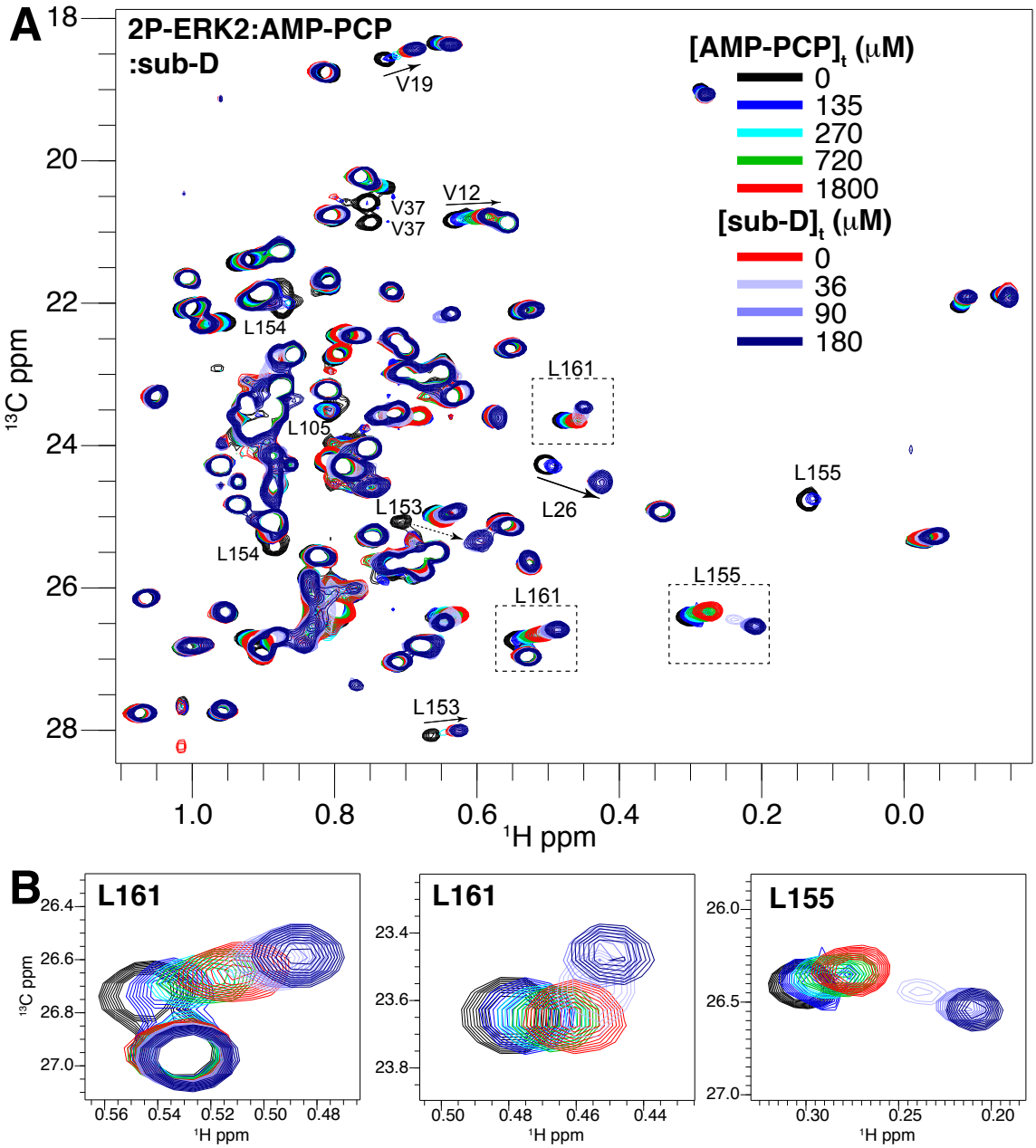

Figure 4.19. Spectral perturbation of 2P-ERK2 upon the binding of AMP-PCP, followed by the binding of the peptide substrate sub-D.
(A) 2D (^{13}C, ^{1}H) HMQC spectra of 2P-ERK2 (90 μM) at 25 °C at different total AMP-PCP concentrations ($[\text{AMP-PCP}]_t$) and total sub-D concentrations ($[\text{sub-D}]_t$)were overlaid. Clear chemical shift perturbations of methyls were highlighted with arrows, labeled with residue type and number. 2P-ERK2 is colored in black, 2P-ERK2 in complex with AMP-PCP is colored in red, and 2P-ERK2:AMP-PCP:sub-D complex is colored in navy. (B) Representative peaks that showed chemical shift perturbations upon both AMP-PCP and sub-D binding.

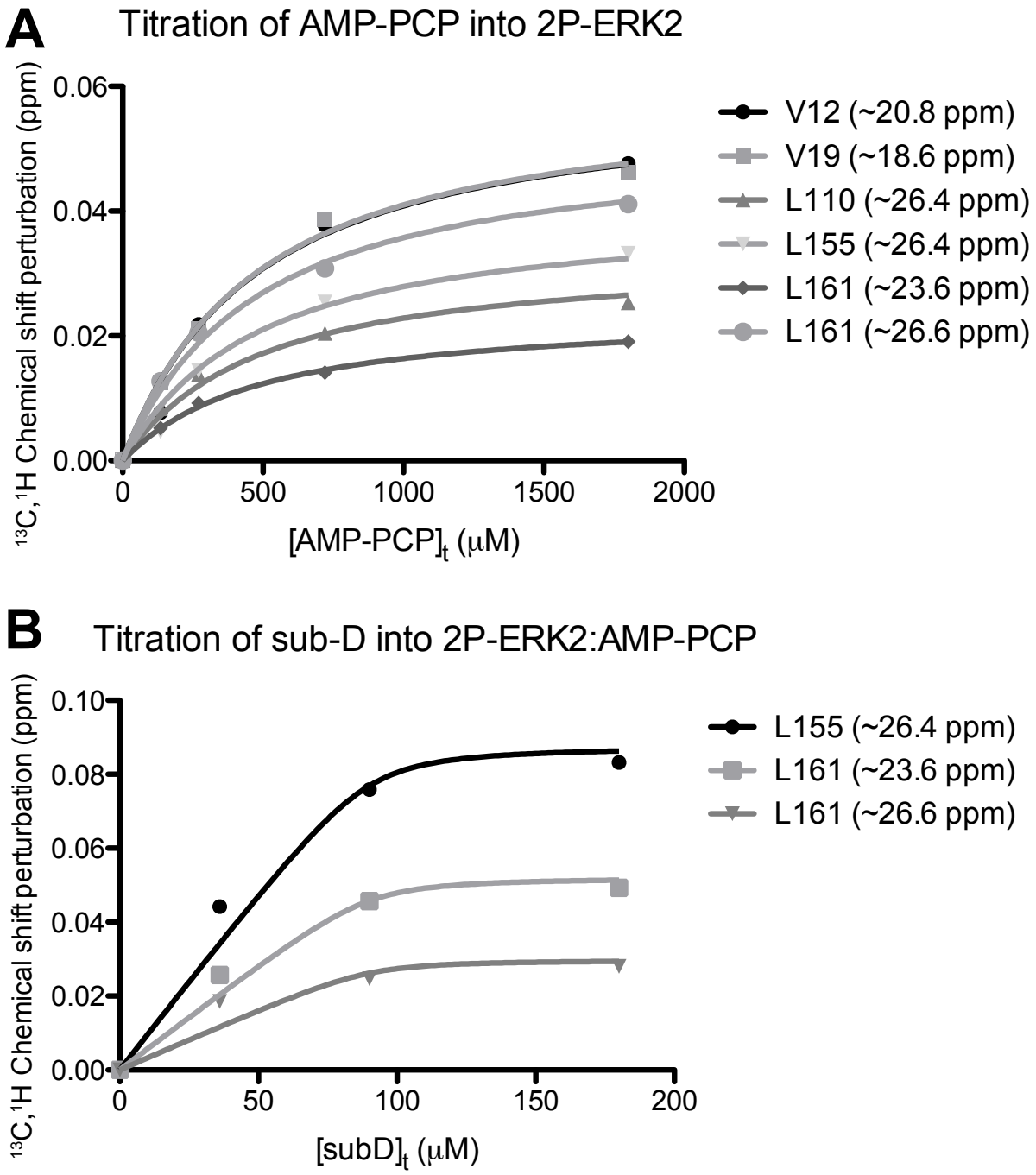

Figure 4.20. Methyl chemical shift perturbations during AMP-PCP and sub-D titration into 2P-ERK2. (A) AMP-PCP was titrated into 2P-ERK2. The carbon and proton combined methyl chemical shift perturbations at 25 °C of methyls undergoing fast exchange during the binding were plotted over different total concentrations of AMP-PCP ($[AMP\text{-}PCP]_t$). The curves reflect a global fitting of these titration points into the same binding event with a shared K_d value. (B) The peptide substrate sub-D was titrated into 2P-ERK2:AMP-PCP complex. The carbon and proton combined methyl chemical shift perturbations at 25 °C of methyls undergoing fast exchange during the binding were plotted over different total concentrations of sub-D ($[sub\text{-}D]_t$). Each curve reflects a global fitting of these titration points into the same binding event with a shared K_d value.

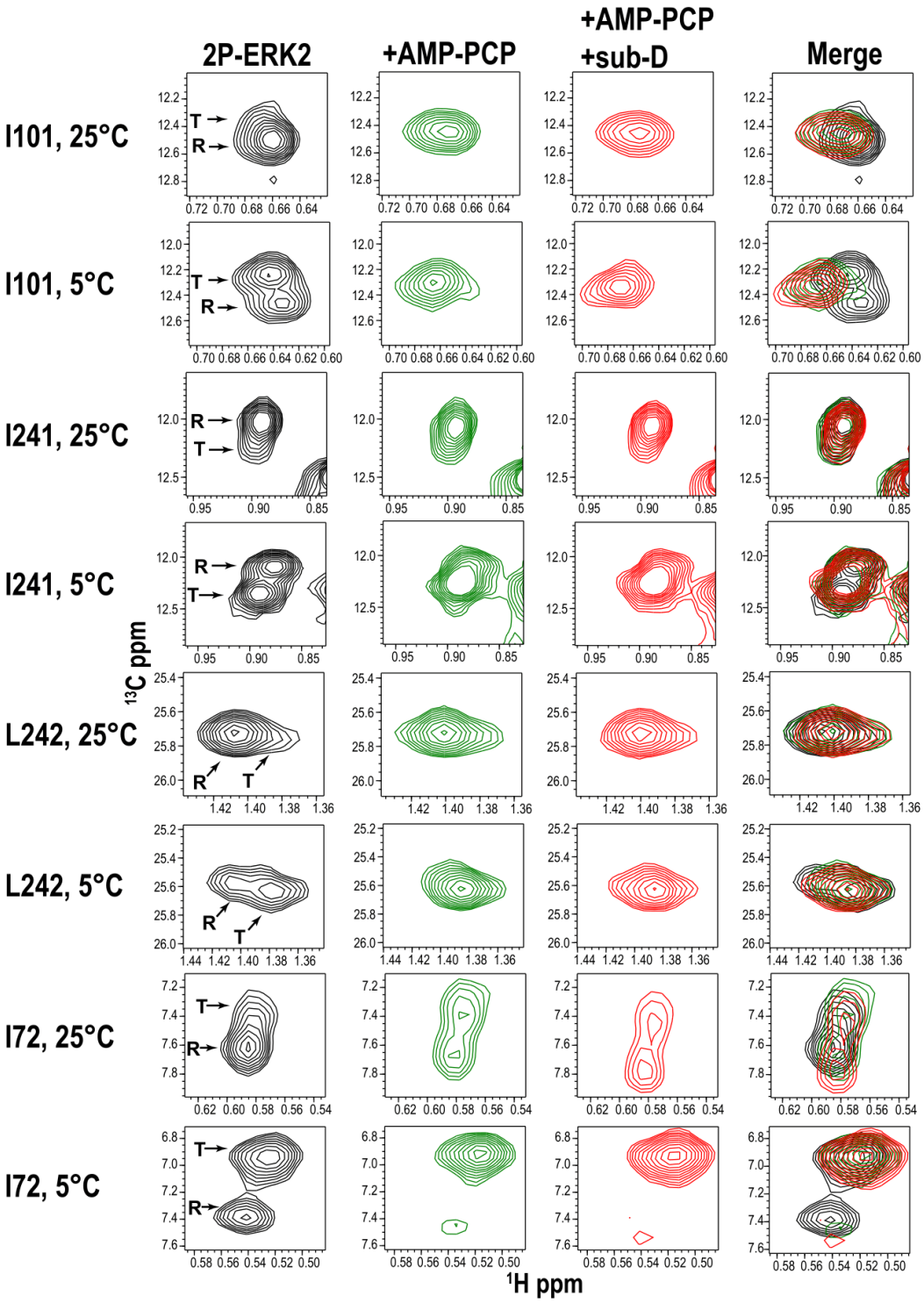

Figure 4.21. Regions in 2D (^{13}C, ^{1}H) HMQC spectra showing slow-exchanging methyls of 2P-ERK2 complexes collected at 25°C and 5°C.
The binding of AMP-PCP didn't show significant perturbation to the R⇌T conformational equilibrium in 2P-ERK2 at 25°C. However, no clear slow-exchange for most of these methyls was observed in both binary (AMP-PCP bound) and the ternary (AMP-PCP and sub-D bound) 2P-ERK2.

4.3.6. AMP-CP Binding to 0P- and 2P-ERK2

To examine if the R⇌T conformational dynamics in the binary product-bound complex of 2P-ERK2 are significantly perturbed by the binding of ADP, the non-hydrolysable ADP analogue AMP-CP was titrated into 2P-ERK2. The binding of AMP-CP showed fast exchange during titration (Figure 4.22), which is indicative of fast kinetics. Chemical shift perturbations of the ^{13}C and ^{1}H resonances ($CSP_{C,H}$) for ILV methyls were then globally fit to a binding isotherm yielding a single K_d for binding as well as the magnitude of the chemical shift differences between the free and bound states of ERK2 (Figure 4.23). The K_d value obtained for AMP-CP binding to 2P-ERK2 was 500 ± 40 μM, 8-fold weaker than the K_d value between ADP and 2P-ERK2 (Figure 4.23). Similar to AMP-PNP and ADP, AMP-CP showed clear chemical shift perturbations for methyls that are indicative of occupancy at the ATP-binding pocket. Similar to ADP, the binding of AMP-CP to 2P-ERK2 showed a small shift on the R⇌T conformational equilibrium with increased T state at 5 °C, comparing with free 2P-ERK2 (Figure 4.24, Table 4.12).

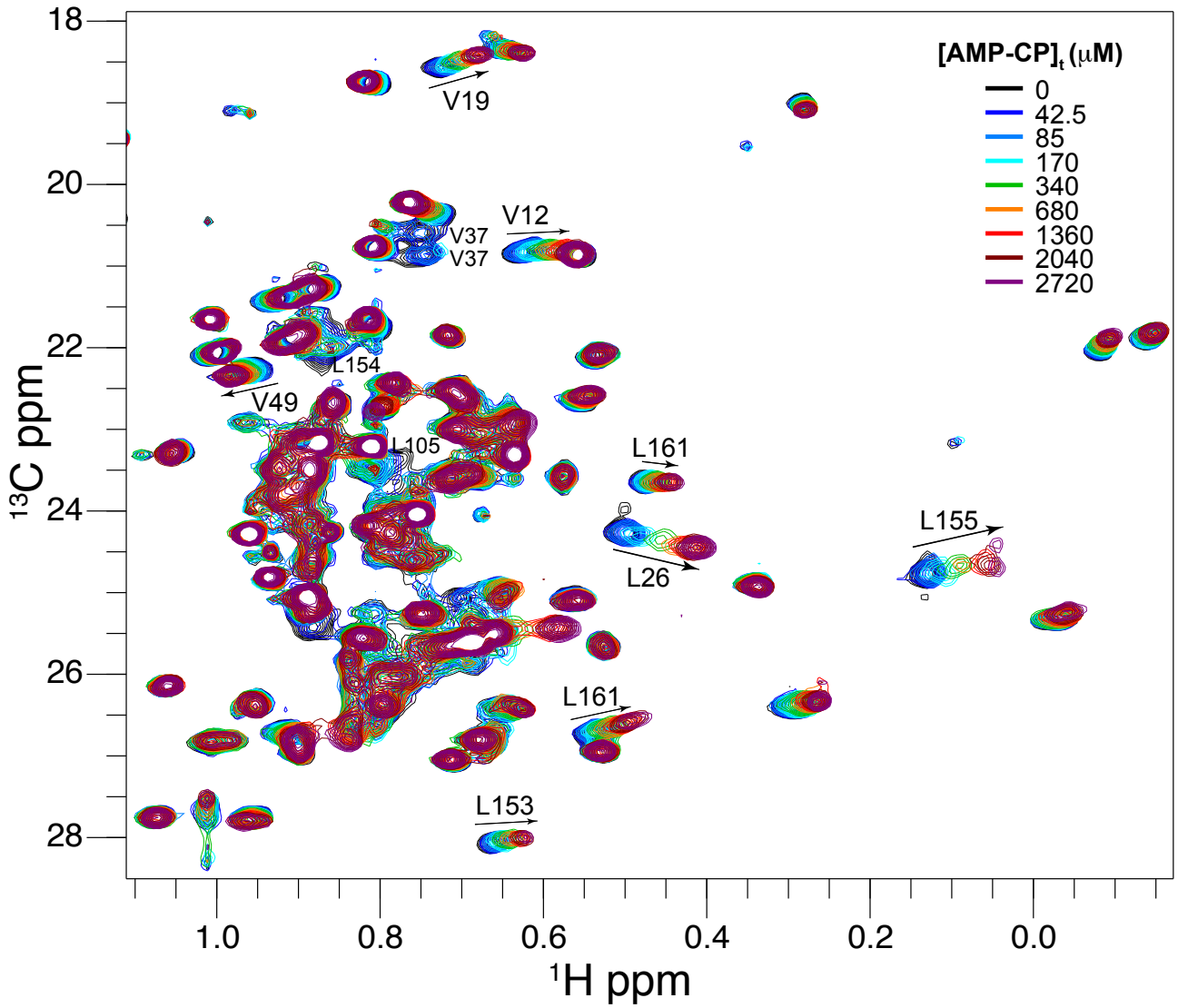

Figure 4.22. Spectral changes of 2P-ERK2 upon the binding of AMP-CP.
2D (^{13}C, ^{1}H) HMQC spectra of 2P-ERK2 (85 μM) at different total AMP-CP concentrations ([AMP-CP]$_t$) are overlaid. Clear chemical shift perturbations of methyls are highlighted with arrows, labeled with residue type and number.

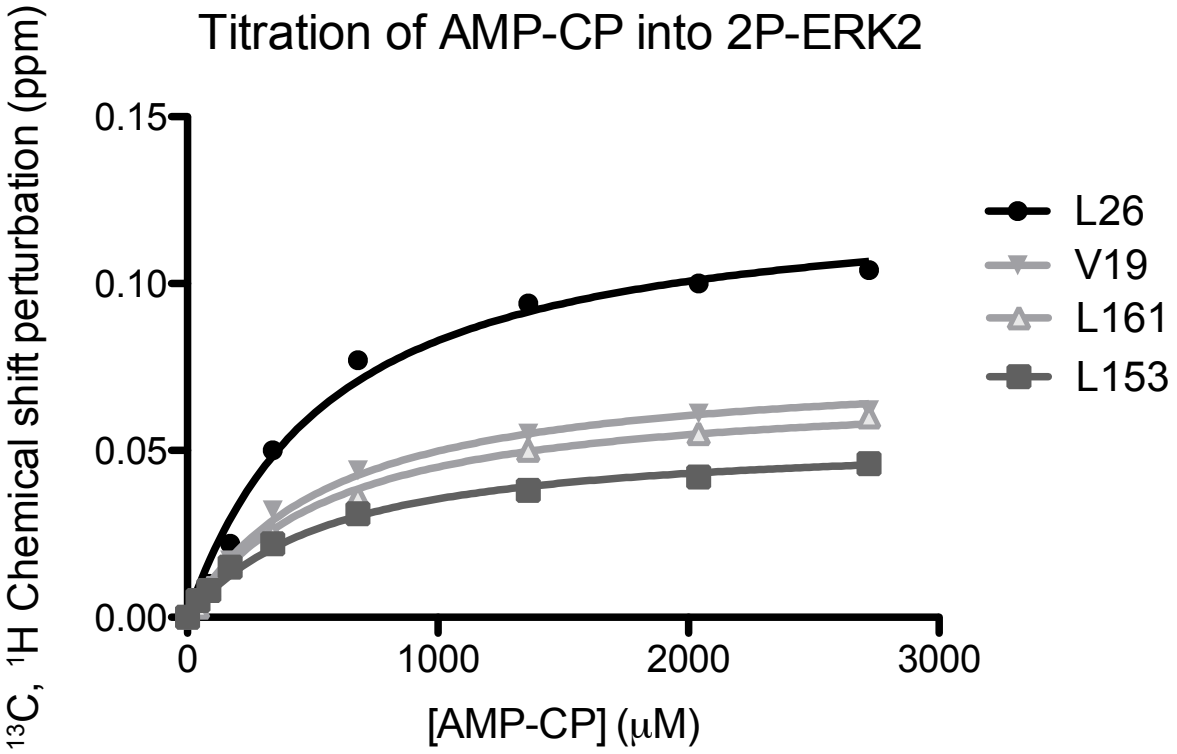

Figure 4.23. Methyl chemical shift perturbations upon AMP-CP titration into 2P-ERK2.
The carbon and proton combined methyl chemical shift perturbations of representative methyls (L26, V19, L161, L153) were plotted as data points over different total concentrations of AMP-CP. The curves are the global fits of these titration points into one binding event with a single K_d value.

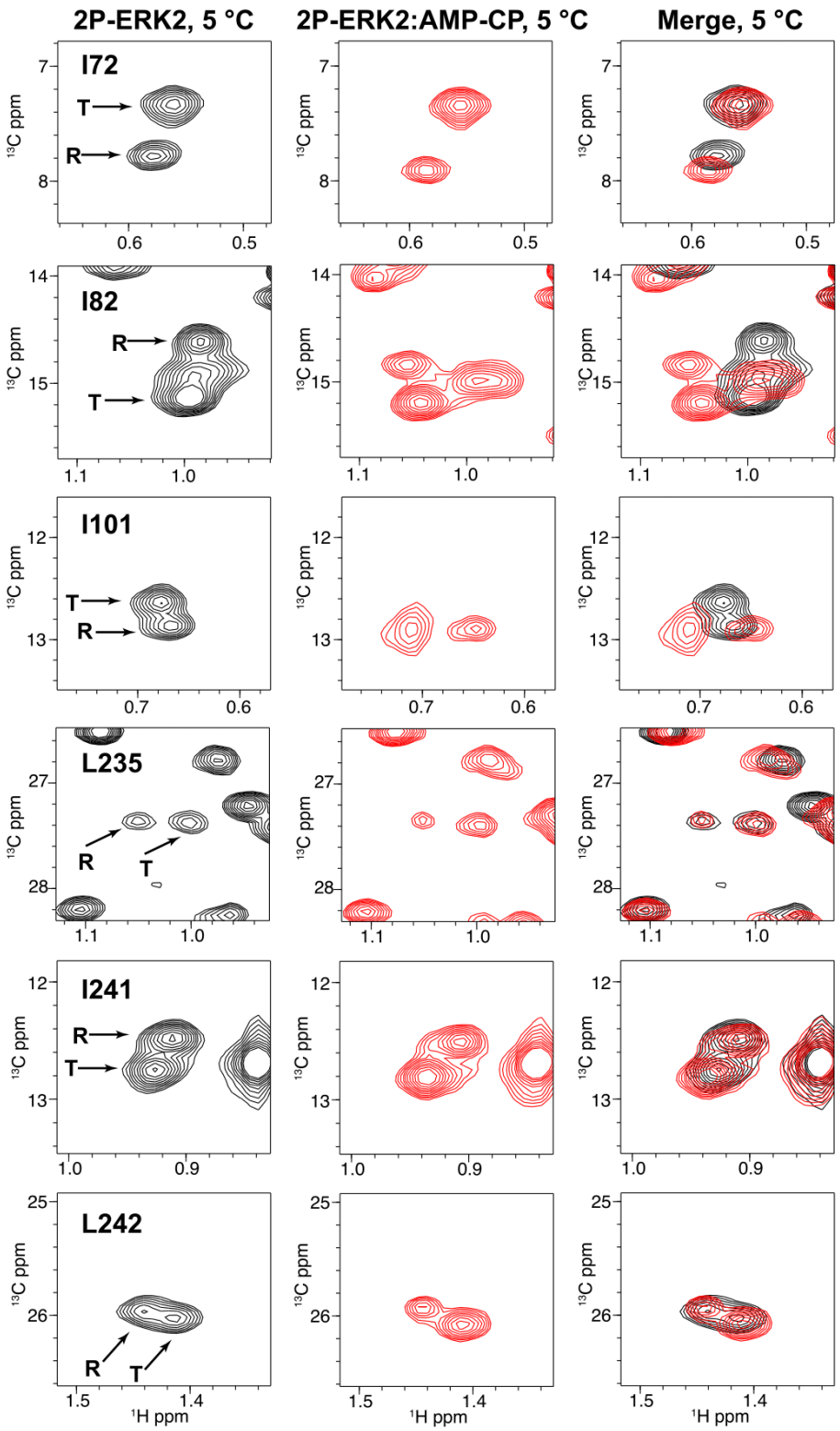

Figure 4.24. The R⇌T equilibrium of slow exchanging methyls in 2P-ERK2 in complex with AMP-CP. A small shift of the equilibrium to the T state was observed for these methyls in the AMP-CP-bound complex of 2P-ERK2 (red).

4.3.7. Inhibitor Vertex-11e Binding to 0P- and 2P-ERK2

To investigate the basis for the differential binding affinities of Vertex-11e to 0P-ERK2 *vs* 2P-ERK2, we examined the effect of Vertex-11e binding by NMR. 2D (^{13}C, ^{1}H) HMQC spectra were collected by titrating Vertex-11e into Ile, Leu, and Val-methyl (^{13}C, ^{1}H) labeled 0P- and 2P-ERK2 and monitoring the chemical shift changes of 70 labeled residues.[16] Slow exchange was observed during the titration, consistent with slow kinetics of Vertex-11e binding to 0P- and 2P-ERK2 (Figure 4.25). The titration ended when peaks reflecting unbound ERK2 were undetectable (Figure 4.26). The chemical shift perturbations upon binding Vertex-11e occurred at similar residues in 0P-ERK2 and 2P-ERK2 (Figure 4.27). As summarized in Figure 4.28, significant chemical shift perturbations were observed throughout the N-terminal lobe as well as the upper C-terminal lobe facing the active site, consistent with Vertex-11e occupancy in the ATP binding pocket. However, differences were observable between 0P- and 2P-ERK2 with respect to the magnitude of chemical shift perturbations. The largest differences occurred at residues L67, L73, I82, I87, I101, L105 and I138, which were significantly perturbed in 0P-ERK2 but not 2P-ERK2, and residues I29, I70, I81, I84, L113 L154 and I209, which were significantly perturbed in 2P-ERK2 but not 0P-ERK2 (Figure 4.27, with residue locations in Figure 4.28). This reveals different modes of Vertex-11e binding to the inactive *vs* active forms of ERK2.

Our previous characterization of ERK2 by methyl-(^{13}C, ^{1}H) multiple-quantum Carr-Purcell-Meiboom-Gill (CPMG) NMR relaxation dispersion experiments[79] showed that 0P-ERK2 adopts one major conformer (which we will refer to as the “T” conformer, 100%), while 2P-ERK2 undergoes equilibrium exchange between two different conformers (“T” and “R” conformers, in the proportions 20%:80% at 25 °C, and 45%:55% at 5 °C). Key residues were found where the chemical shift changes between the two states (in Hz) were larger than the observed chemical exchange rate constant (i.e.,

$\Delta\omega >> k_{ex}$), therefore appearing as two peaks in the HMQC spectra of 2P-ERK2. By comparing the results of the CPMG to HMQC spectra, the relative intensities for each pair of peaks at these key residues were verified to directly report the relative populations of the T and R conformers.

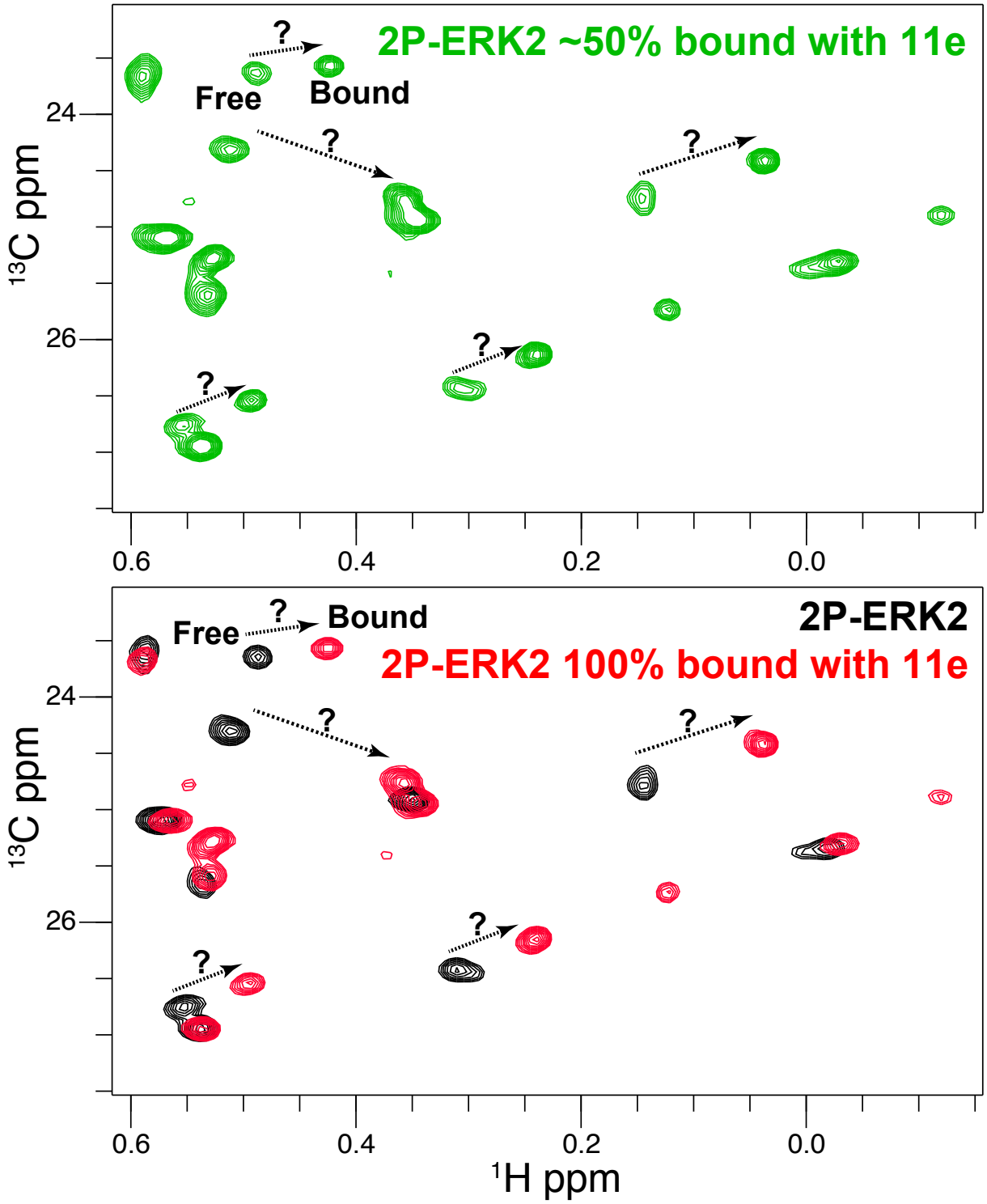

Figure 4.25. Slow exchange was observed when Vertex-11e was titrated into 2P-ERK2.
Part of 2D (^{13}C, ^{1}H) HMQC spectra was plotted, overlaying the free 2P-ERK2 (black), 2P-ERK2 ~50% bound with Vertex-11e ([2P-ERK2]$_t$:[Vertex-11e]$_t$=1:0.5, green), and 2P-ERK2 ~100% bound with Vertex-11e ([2P-ERK2]$_t$:[Vertex-11e]$_t$=1:1.3, red). Dashed arrows with question marks show the tentative shifts between the free and the bound forms of methyl peaks.

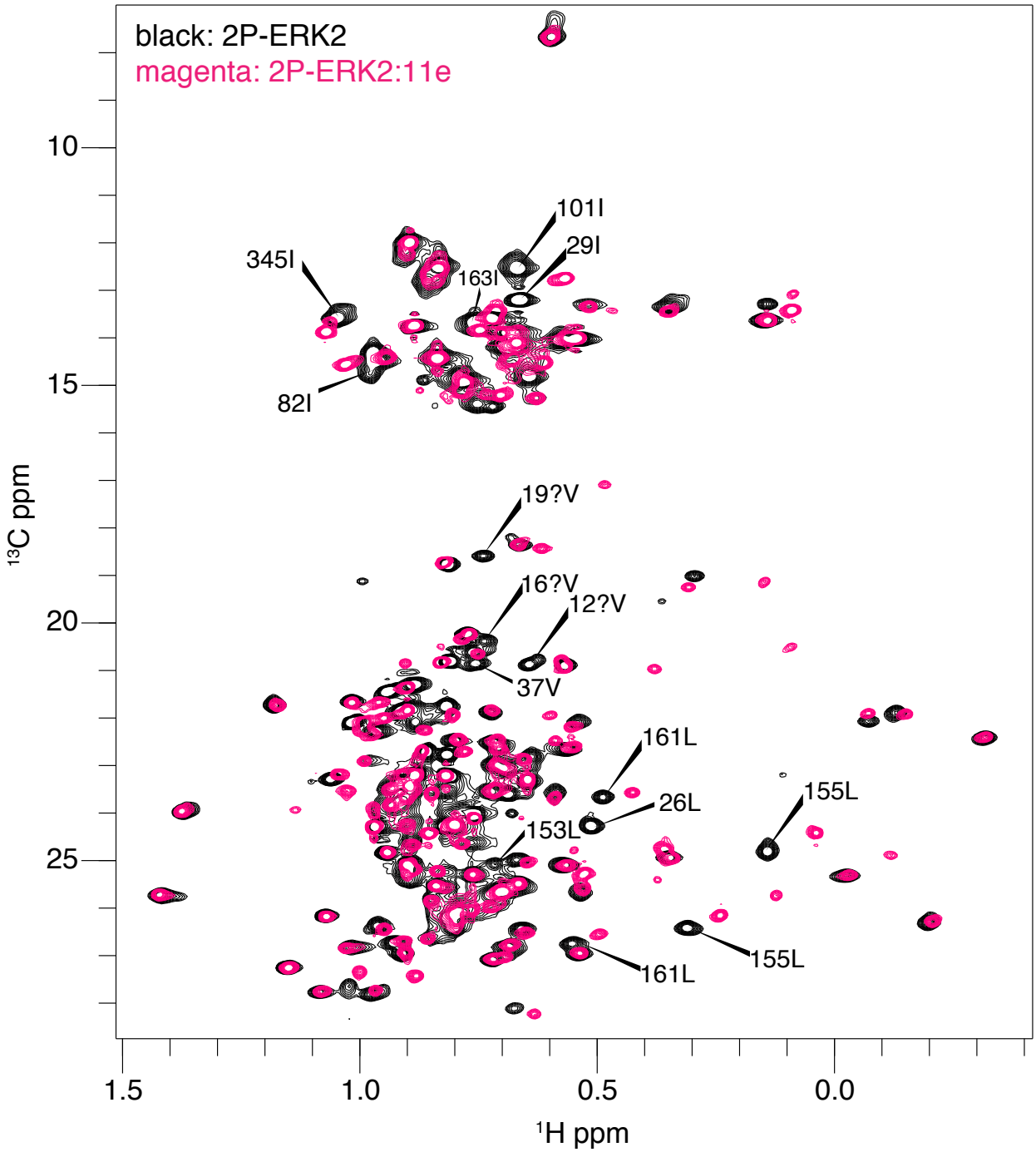

Figure 4.26. Methyl chemical shift perturbations upon Vertex-11e binding to 0P-ERK2.
The Ile, Leu and Val regions of the 2D (^{13}C, ^{1}H) HMQC spectra are shown for 2P-ERK2 (black) and 2P-ERK2:Vertex-11e complex (magenta). Peaks with clear chemical shift perturbations are labeled with residue type and numbers. Labels with question marks are the tentative assignments.

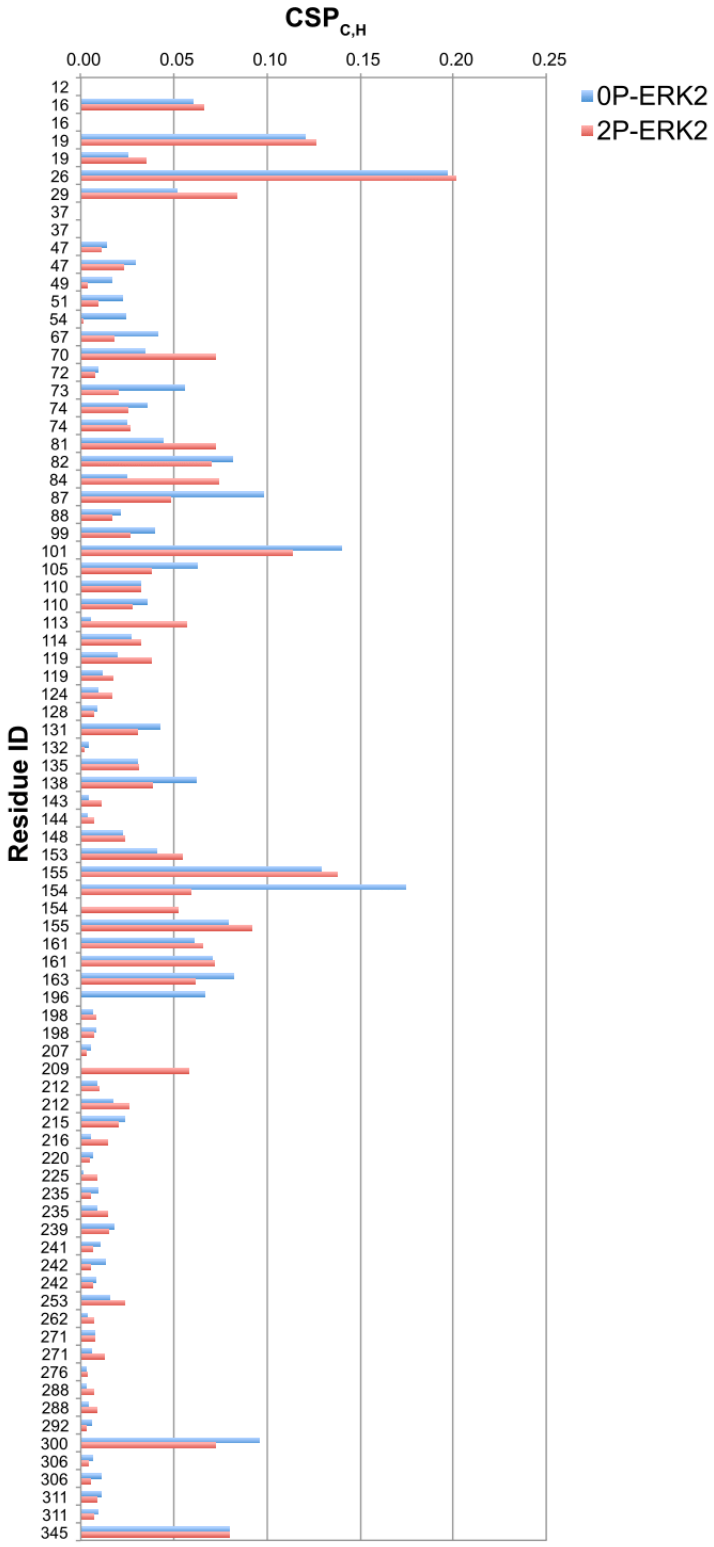

Figure 4.27. Chemical shift perturbations upon binding Vertex-11e to ERK2.
Combined ^{13}C and ^{1}H chemical shift perturbations (in ppm) for assigned ILV methyls upon Vertex-11e binding to 0P-ERK2 (blue) and 2P-ERK2 (red), measured as described in Materials and Methods.

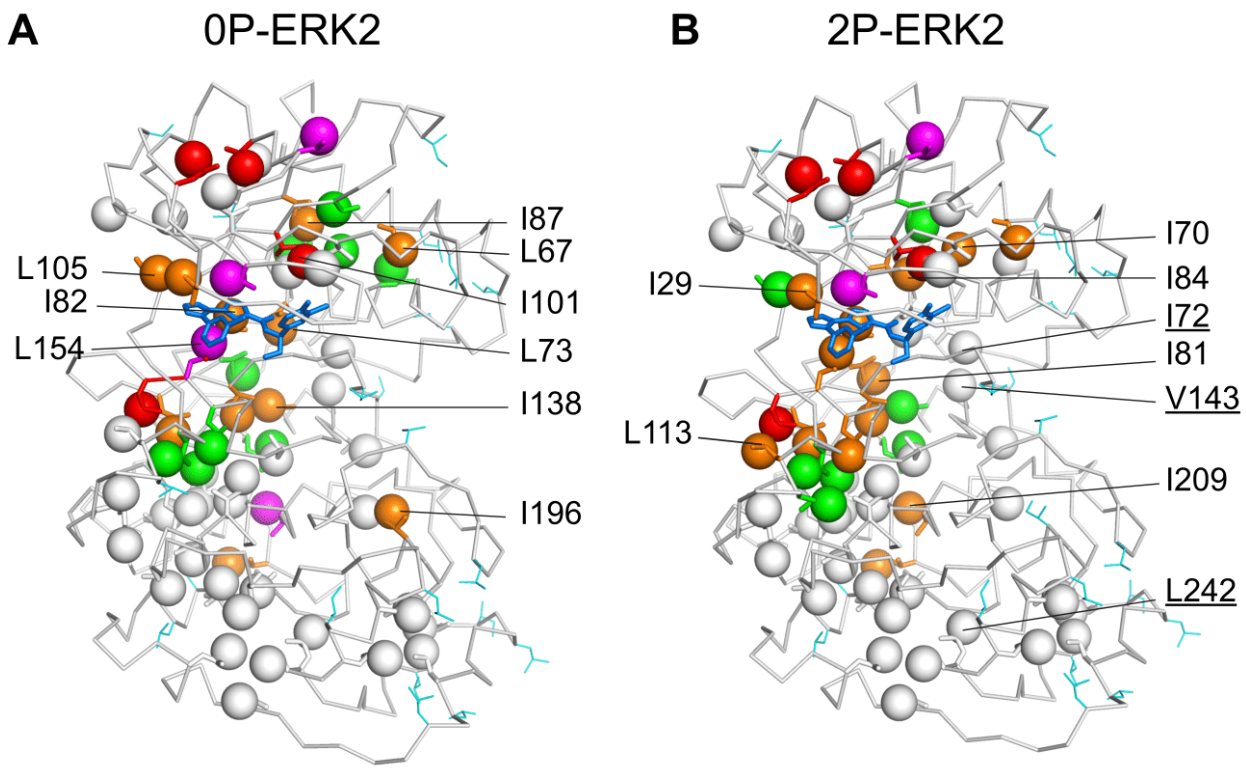

Figure 4.28. Chemical shift perturbations following binding of Vertex-11e to ERK2.
(A and B) Ile, Leu, and Val methyls showing ^{13}C and ^{1}H combined chemical shift perturbations induced by binding of Vertex-11e to (A) 0P-ERK2 and (B) 2P-ERK2. The methyls for individual residues are mapped onto a co-crystal structure of 0P-ERK2 and Vertex-9a (blue), an analogue of Vertex-11e (PDB entry 2OJJ12). Spheres show Ile, Leu, and Val methyls assigned in the 0P-ERK2 and 2P-ERK2 apoenzymes.[79] Side chains are shown as sticks when the methyl assignment is absent or ambiguous. Colors indicate chemical shift perturbations induced by Vertex-11e binding: <0.03 ppm (white), 0.03−0.05 ppm (green), 0.05−0.1 ppm (orange), and >0.1 ppm (red). Magenta indicates residues with peaks missing in the Vertex-11e:ERK2 complexes, most likely due to changes in methyl dynamics. Labeled residues showed significant differences in chemical shift perturbation upon Vertex-11e binding between ERK2 forms, increasing in 0P-ERK2 (A) or 2P-ERK2 (B) (see Figure 4.27). In panel B, methyls underlined indicate the positions of I72, V143, and L242, which show no chemical shift perturbation upon binding of Vertex-11e but report the populations of T and R conformers (see Figure 4.29).

Examination of these key residues showed that different conformations were formed in the complexes of Vertex-11e with inactive *vs* active kinase (Figure 4.29). Whereas binding of Vertex-11e to 0P-ERK2 formed the T conformer seen in 0P-ERK2-apoenzyme, binding to 2P-ERK2 formed the R-conformer. Thus, Vertex-11e adopts different conformations in ERK2 depending on the kinase activity state, providing a structural basis to explain the differential affinities of Vertex-11e for 0P-ERK2 and 2P-ERK2. Importantly, inhibitor binding to 2P-ERK2 resulted in a substantial shift in equilibrium between T and R conformers. In its apo-enzyme form, 2P-ERK2 interconverts between T and R, whose equilibrium ratios are 20:80 at 25 °C, and 50:50 at 5 °C. Upon ligand binding, the equilibrium shifted completely to the R conformer, at both temperatures. This reveals properties of conformational selection in the active kinase, and the capability of inhibitor binding to regulate the thermodynamics of conformational exchange.

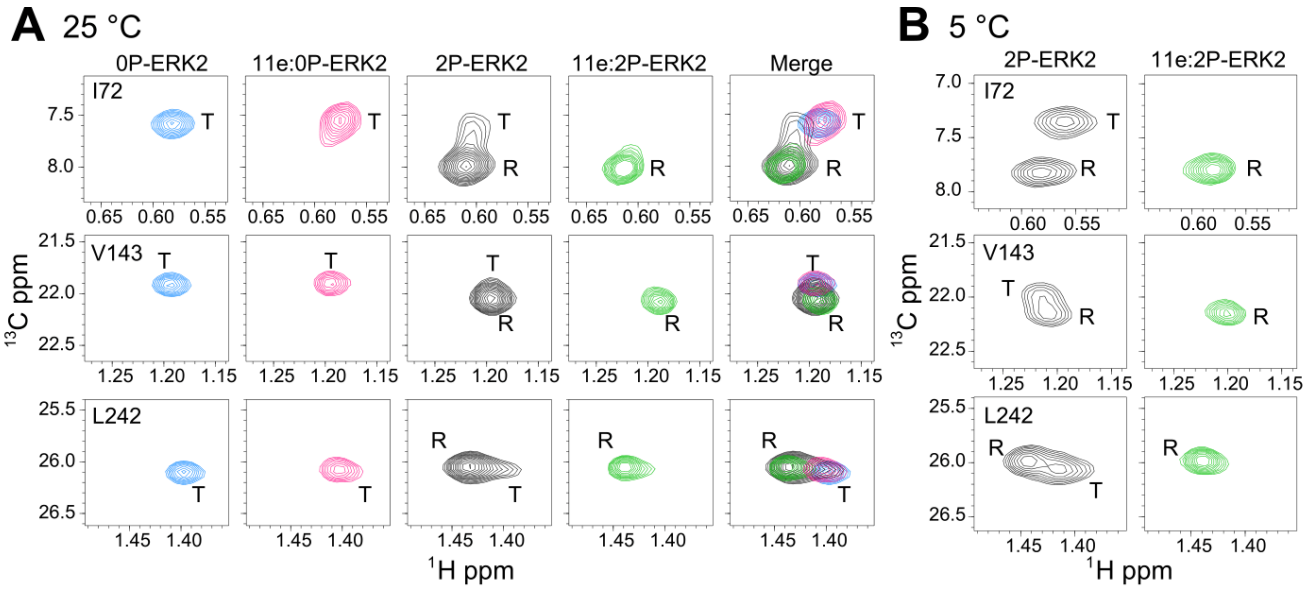

Figure 4.29. Vertex-11e stabilizes the R conformer in 2P-ERK2.
(A) 2D (^{13}C, ^{1}H) HMQC spectra collected at 25 °C, showing methyl peaks of key residues I72, V143, and L242, which report T and R conformers.[79] Their locations in the structure are shown in Figure 4.28. The spectra show that the Vertex-11e:0P-ERK2 complex (pink) adopts the T conformer, observed in the 0P-ERK2 apoenzyme (blue). In contrast, the Vertex-11e:2P-ERK2 complex stabilizes the R conformer (green), shifting the equilibrium between T and R conformers observed in the 2P-ERK2 apoenzyme (black). (B) The same methyl peaks as in panel A, but for spectra collected at 5 °C, showing the more pronounced shift in equilibrium toward the R conformer in the Vertex-11e:2P-ERK2 complex (green), compared to the 2P-ERK2 apoenzyme (black).

4.3.8. Inhibitor SCH772984 Binding to 0P- and 2P-ERK2

The effect of binding SCH772984, another inhibitor of ERK2, to 0P- and 2P-ERK2 was monitored using 2D (^{13}C, ^{1}H) HMQC spectra. Similar to the binding of Vertex-11e, slow exchange was also observed when SCH772984 was titrated into ERK2, consistent with slow kinetics of SCH772984 binding to 0P/2P-ERK2 (Figure 4.30). The titration was stopped when peaks reflecting unbound ERK2 were undetectable. The chemical shift perturbations upon binding SCH772984 occurred at similar residues in 0P-ERK2 and 2P-ERK2 (Figure 4.31, Figure 4.32). Significant chemical shift perturbations were observed on the entire N-terminal lobe and upper C-terminal lobe of ERK2 (Figure 4.33), consistent with the occupancy of SCH772984 in the ATP binding pocket. In addition to these significant chemical shift perturbations, methyls that undergo slow exchange between R⇌T conformational equilibrium in free 2P-ERK2 showed only chemical shifts that are similar to the T conformation (named T' conformation to specify T in the inhibitor-bound form, Figure 4.32, Figure 4.34). To understand how differently Vertex-11e and SCH772984 bind to 2P-ERK2, 2D spectra of the 2P-ERK2:Vertex-11e complex, the 2P-ERK2:SCH772984 complex, and free 2P-ERK2 were overlaid (Figure 4.35). For example, methyls of L155 and L161 shifted to similar chemical shifts, whereas I29 and I101 shifted to very different chemical shifts upon the binding of these two inhibitors. It is likely that these methyls, which deviated in their chemical shifts in the Vertex-11e or SCH772984-bound forms of 2P-ERK2, may reflect the different binding modes formed with these two inhibitors.

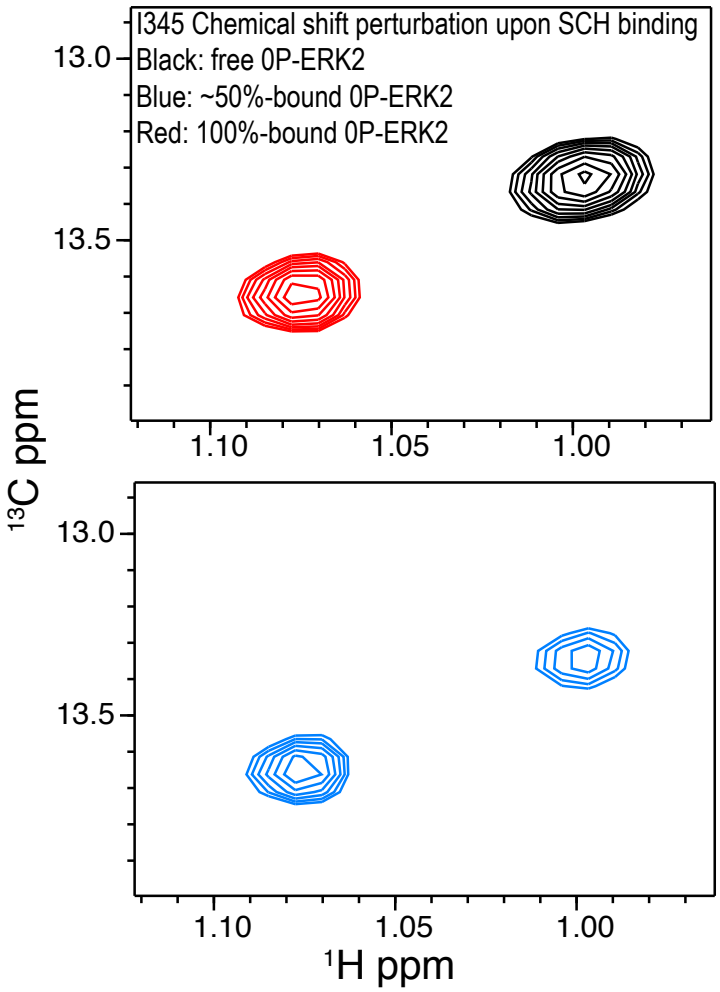

Figure 4.30. Slow exchange was observed during the titration of SCH772984 into 0P-ERK2, using the peak of I345 as an example.
The peak of I345 in free 0P-ERK2 was shown in black (upper panel), and in ~100% SCH772984-bound 0P-ERK2 was shown in red (upper panel). Two peaks of comparable intensities were observed at the chemical shifts of the free-form peak and the bound-form peak, when 0P-ERK2 is ~50% bound with SCH772984.

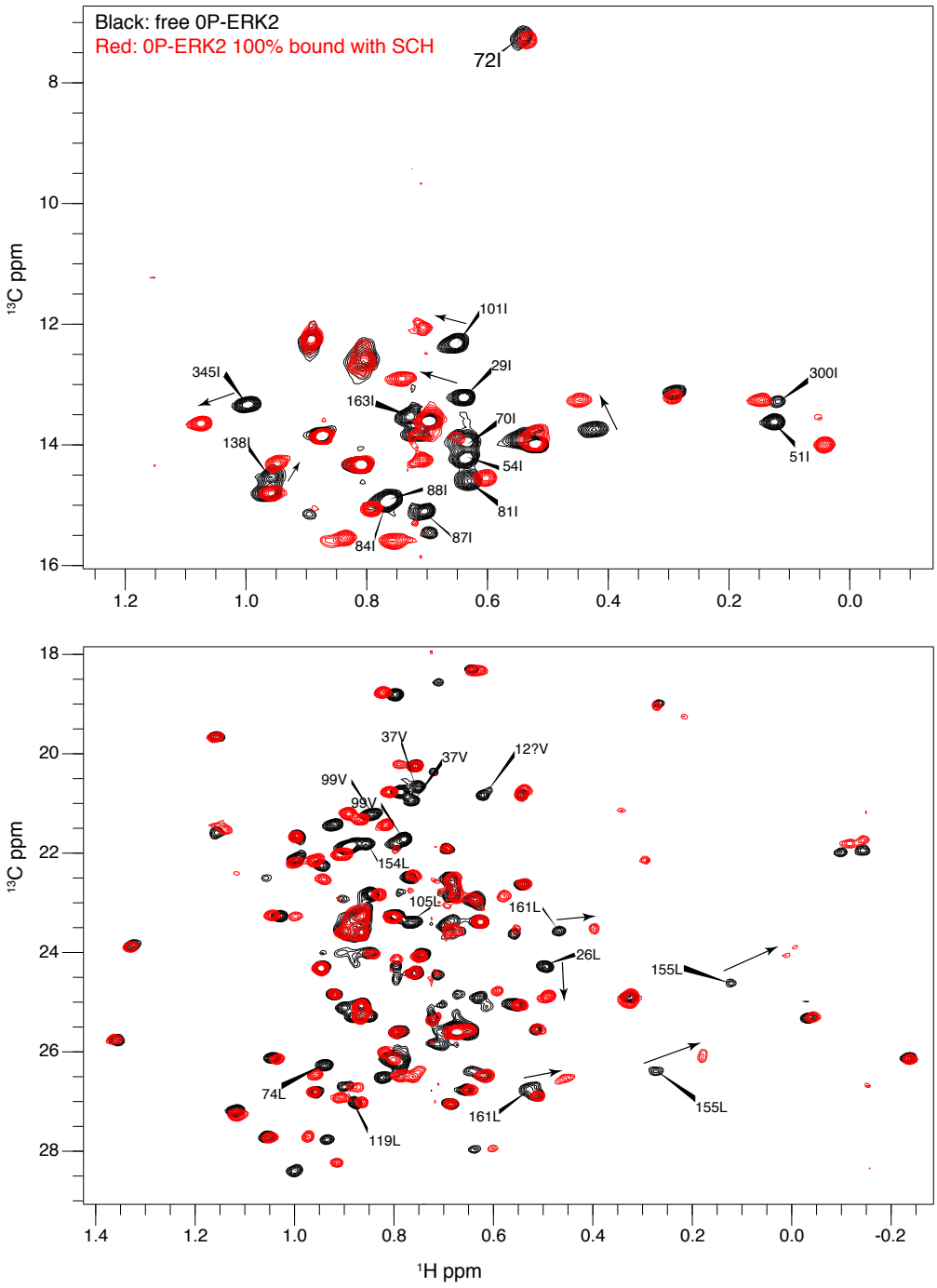

Figure 4.31. Methyl chemical shift perturbations upon SCH772984 binding to 0P-ERK2.
The Ile (upper panel) and Leu/Val (bottom panel) regions of the 2D (^{13}C, ^{1}H) HMQC spectra were shown for 0P-ERK2 (black) and 0P-ERK2:SCH772984 complex (red). Peaks with clear chemical shift perturbations were labeled with residue type and numbers. Arrows point from the peak of the free protein to the potential bound-form peak.

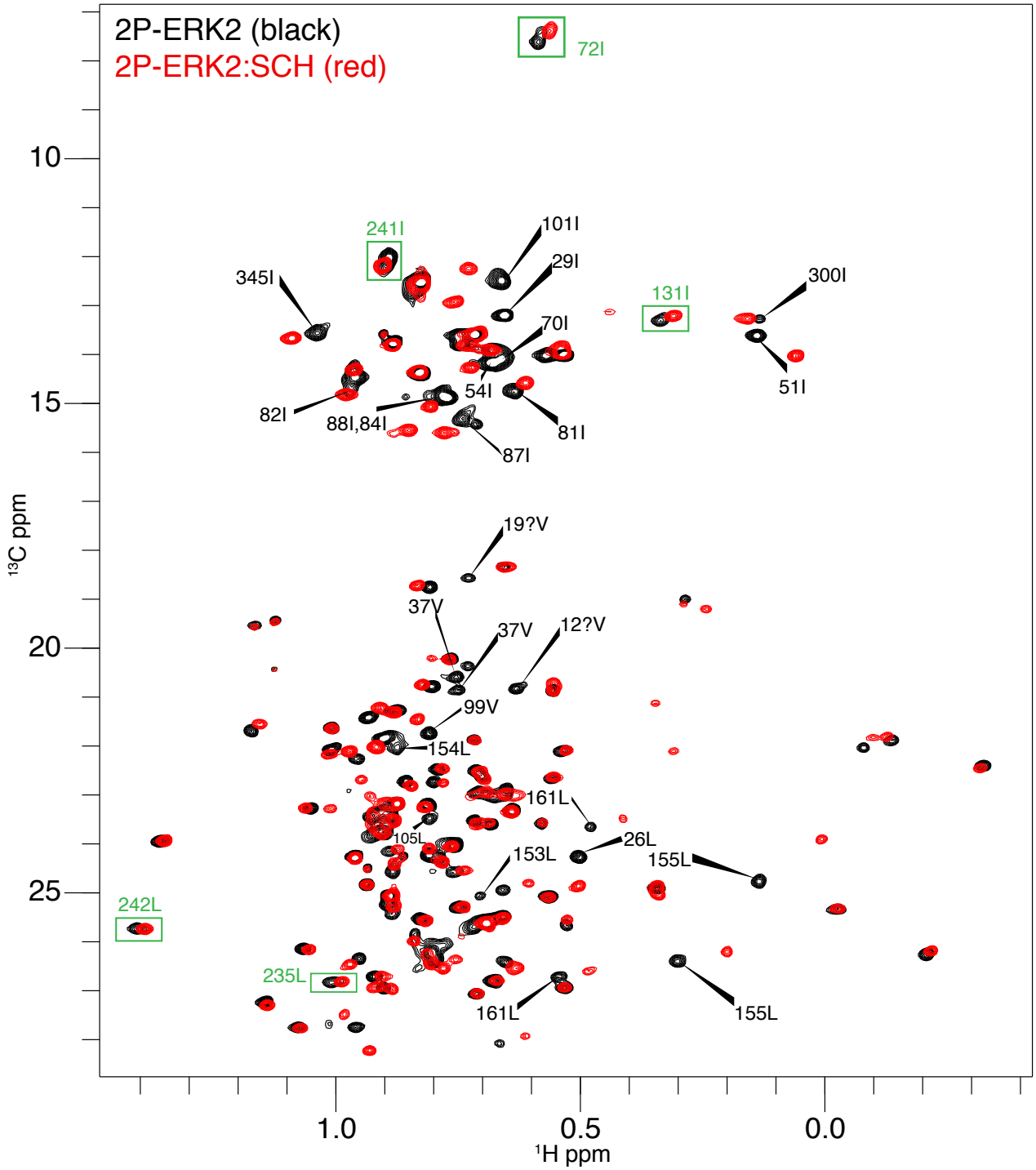

Figure 4.32. Methyl chemical shift perturbations upon SCH772984 binding to 2P-ERK2.
The Ile, Leu and Val regions of the 2D (^{13}C, ^{1}H) HMQC spectra are shown for 2P-ERK2 (black) and 2P-ERK2:SCH772984 complex (red). Peaks with clear chemical shift perturbations are labeled with residue type and numbers. Methyls that showed T conformation in the 2P-ERK2:SCH772984 complex spectra are labeled with green squares.

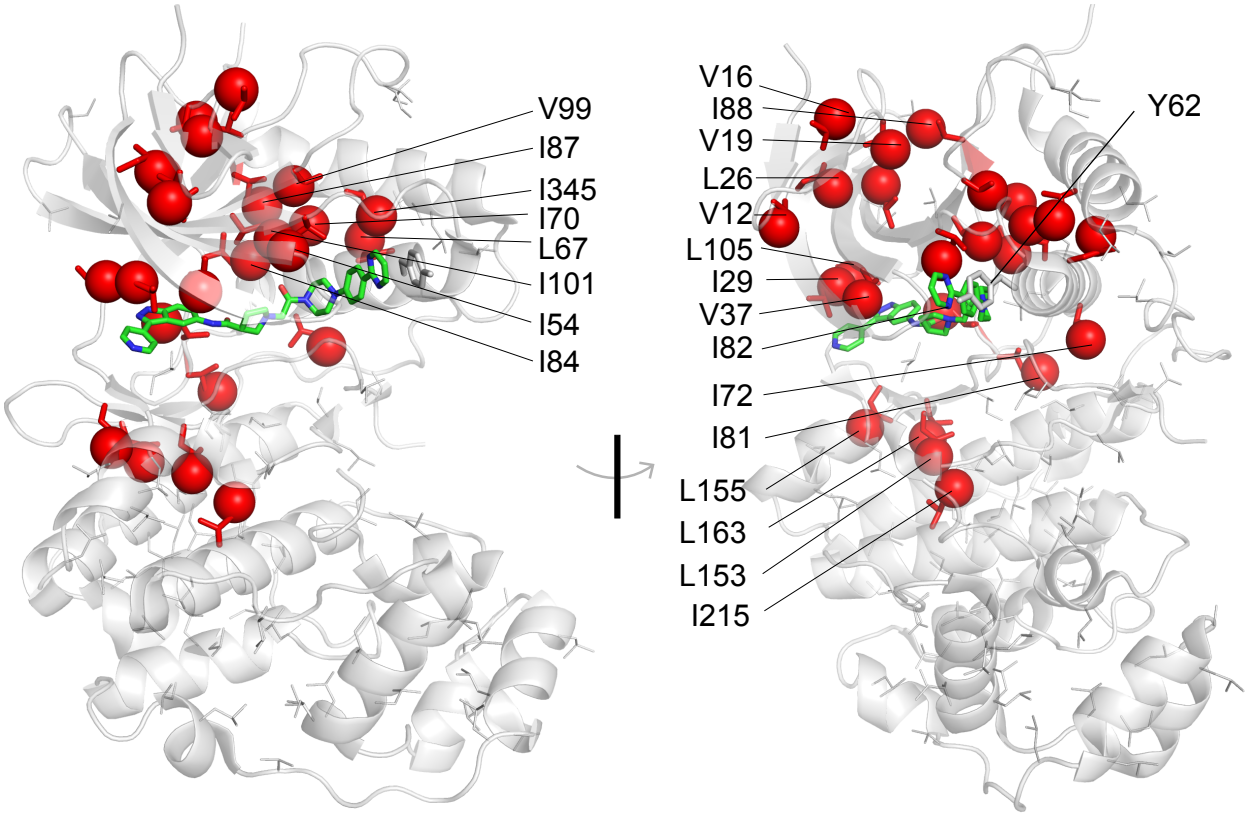

Figure 4.33. Chemical shift perturbations on 2P-ERK2 induced by the binding of SCH772984. Methyls of 2P-ERK2 that showed significant chemical shift perturbations ($CSH_{C,H}$ > 0.05 ppm, red spheres) upon SCH772984 binding are mapped onto crystal structure of 0P-ERK2:SCH772984 complex (PDB 4qta, grey cartoon). SCH772984 is shown in sticks, and colored based on atom types (green-carbon, blue-amide, red-oxygen). The side chains of these residues are labeled with red sticks. The side chain of Y62, which shows aromatic stacking interaction with part of SCH772984, is presented in grey sticks.

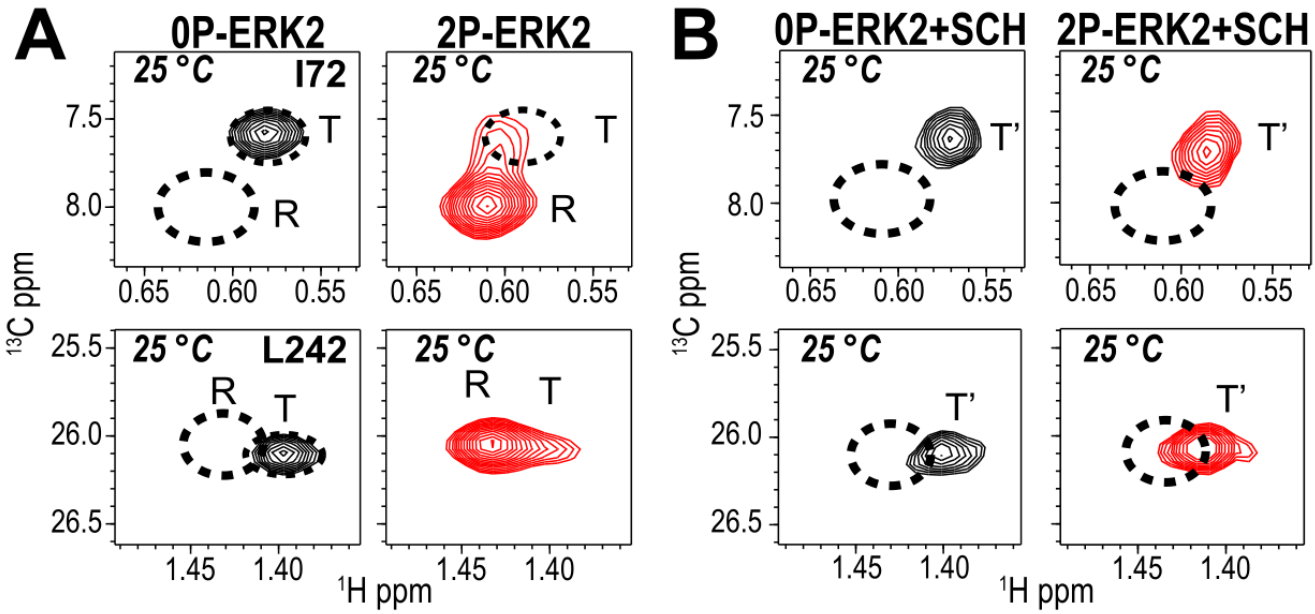

Figure 4.34. SCH772984 stabilizes the T' (T in the inhibitor-bound form) conformation of 2P-ERK2. (A) 2D (^{13}C, ^{1}H) HMQC spectra showing I72 and L242 methyl peaks in 0P-ERK2 and 2P-ERK2 at 25 °C. The chemical shifts that correspond to R or T conformations were shown in ellipses. (B) 2D (^{13}C, ^{1}H) HMQC spectra showing I72 and L242 methyl peaks in 0P-ERK2 and 2P-ERK2 that were ~100% bound to SCH772984 at 25 °C. The chemical shifts that correspond to R or T conformations were shown in ellipses. Both I72 and L242 methyl showed chemical shifts consistent with T' conformation, whereas no peak was observed on the chemical shift of the R' conformation (ellipses).

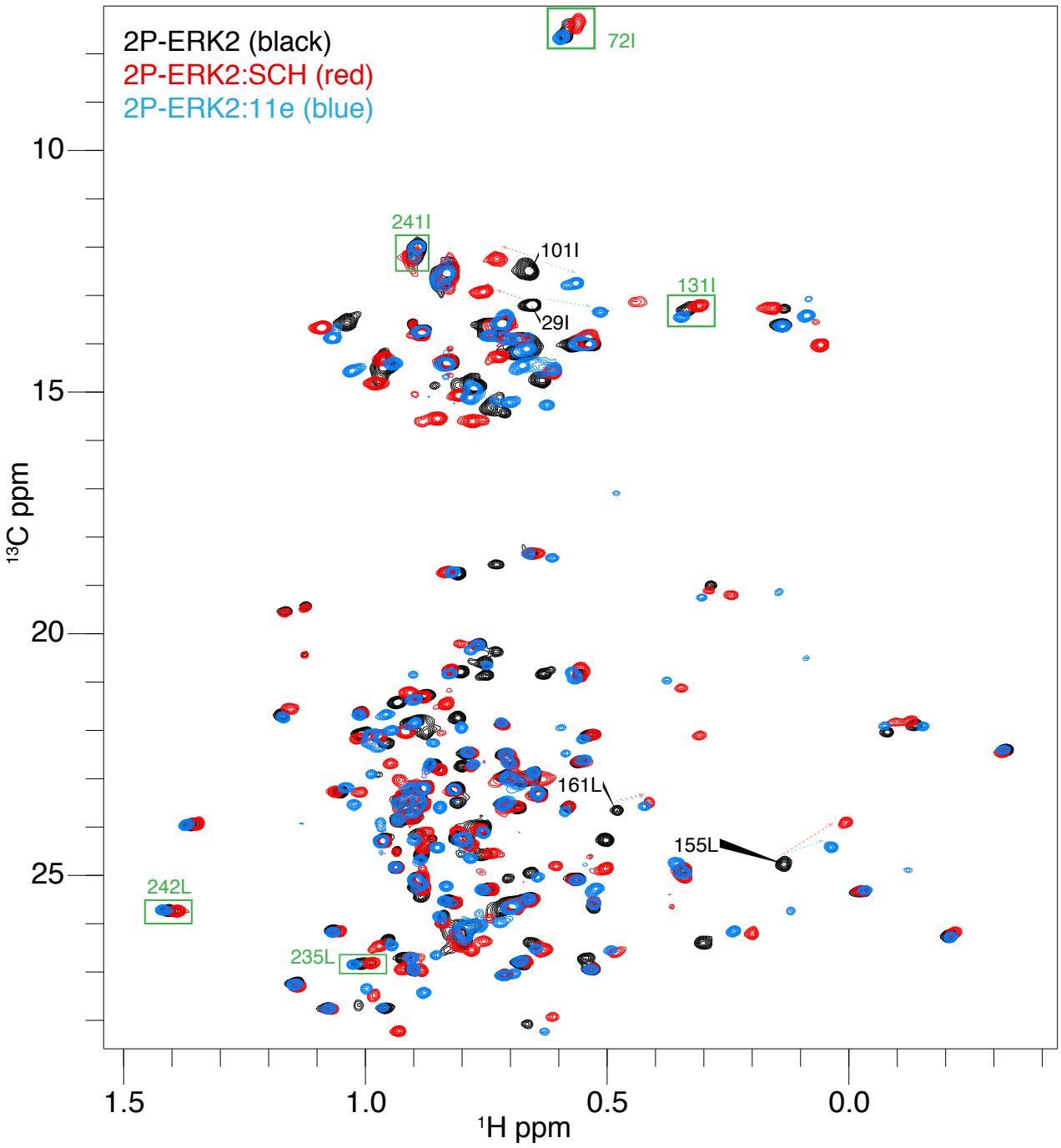

Figure 4.35. Comparison of spectral changes upon Vertex-11e and SCH772984 binding.
The Ile, Leu and Val regions of the 2D (^{13}C, ^{1}H) HMQC spectra were shown for 2P-ERK2 (black), 2P-ERK2:Vertex-11e (blue) and 2P-ERK2:SCH772984 complex (red). The dashed arrows labeled the potential chemical shifts of several methyls in their Vertex-11e or SCH772984 bound forms. Chemical shifts of some methyls (e.g. I29 and I101) are very different between the two inhibitor-bound forms, whereas chemical shifts of other methyls (e.g. L161 and L155) are similar between the two inhibitor-bound forms. Methyls that are showed R⇌T conformational stabilization were labeled with green squares.

4.3.9. Inhibitor GDC-0994 Binding to 2P-ERK2

Because both Vertex-11e and SCH772984 shifted the T⇌R conformational equilibrium on 2P-ERK2, I've wondered if the effects were a result of their tight binding affinities. Thus I tested if GDC-0994, another tight inhibitor of 2P-ERK2 that binds to the ATP-binding pocket, could stabilize 2P-ERK2 into the R or T conformation using 2D (^{13}C, ^{1}H) HMQC experiments. Similar to the other two inhibitors, slow exchange was observed during the binding of GDC-0994 to 2P-ERK2 (Figure 4.36), consistent with slow kinetics of GDC-0994 binding to 0P/2P-ERK2. The titration was stopped when peaks reflecting unbound ERK2 were undetectable. The chemical shift perturbations of methyls on 2P-ERK2 induced by the binding of GDC-0994 are mapped onto the structure of ERK2 (Figure 4.38). Upon the binding of GDC-0994, the majority of chemical shift perturbations were mostly observed in the N-terminal lobe, with only a few methyls perturbed in the upper C-terminal lobe, consistent with GDC-0994 occupancy in the ATP binding pocket. Fewer methyls showed chemical shift perturbations larger than 0.05 ppm upon binding GDC-0994 when compared to SCH772984, and most of these perturbations occurred closer to the hinge region of ERK2 instead of the region where SCH772984 forms an aromatic stacking interaction with Y62 (Figure 4.33). Unlike SCH772984, the binding of GDC-0994 did not shift the T⇌R conformational equilibrium in 2P-ERK2, as seen in I72 and L242 (Figure 4.39), indicating that the conformational stabilization effect observed with Vertex-11e and SCH772984 is not always correlated with their high binding affinities.

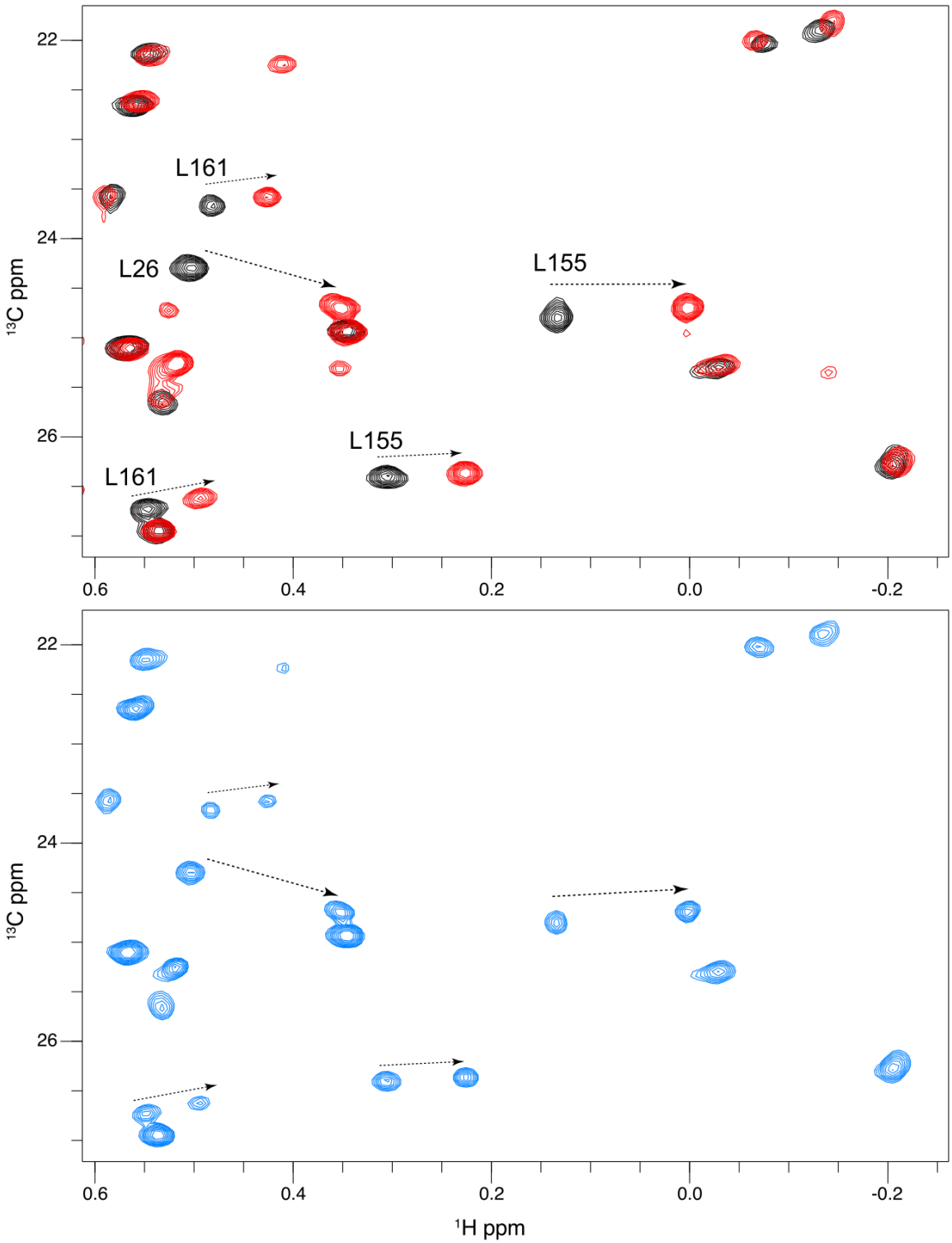

Figure 4.36. Slow exchange was observed during the binding of GDC-0994 to 2P-ERK2.
In the upper panel, part of 2D (^{13}C, ^{1}H) HMQC spectra of free 2P-ERK2 (black) is overlaid with 2P-ERK2:GDC-0994 complex of ~100% binding stoichiometry (red). The lower panel shows the same region of 2D (^{13}C, ^{1}H) HMQC spectra of 2P-ERK2:GDC-0994 complex of 50% binding stoichiometry (blue). The dashed arrows labeled the potential chemical shifts of several methyls in their GDC-0994 bound forms.

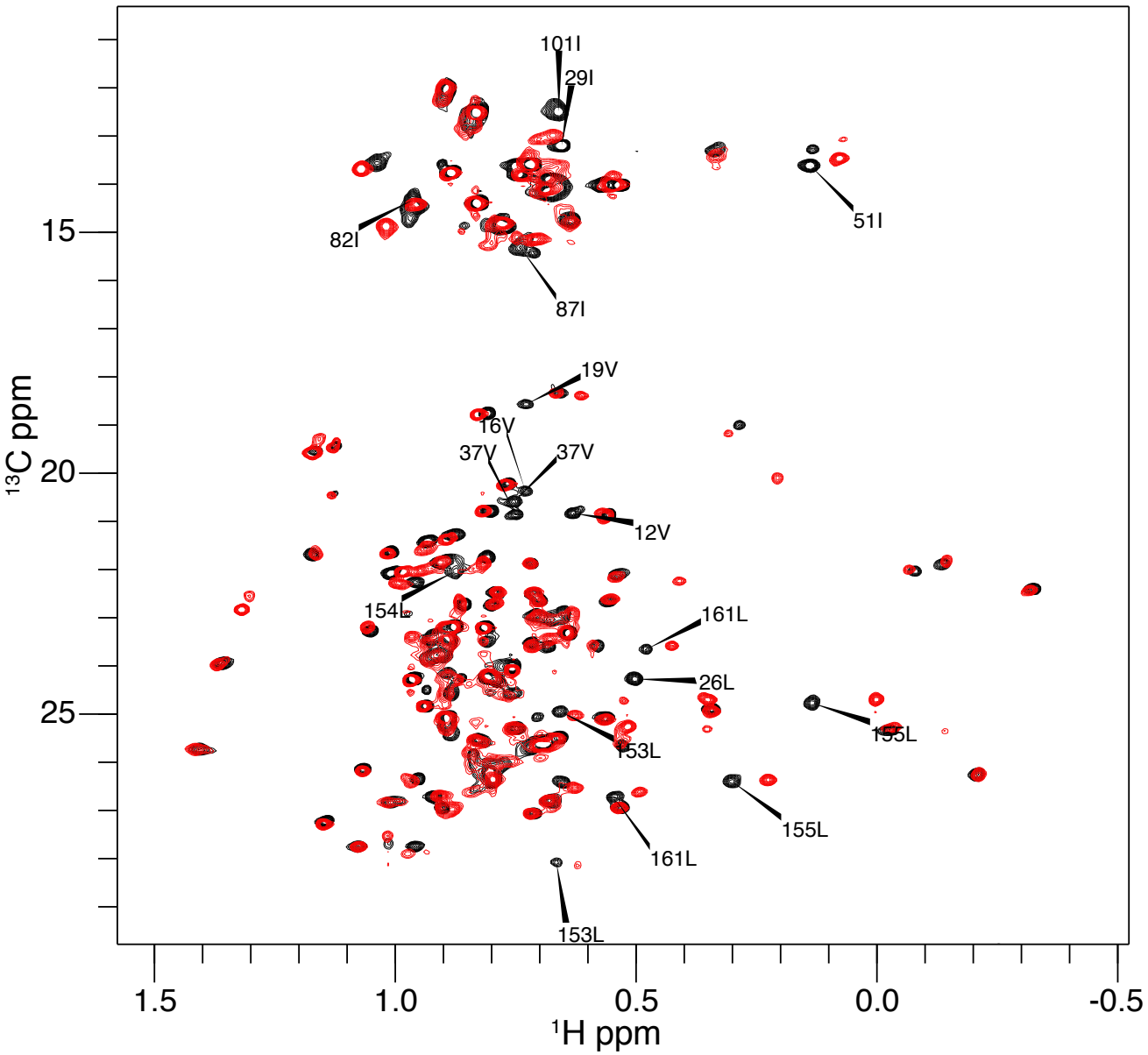

Figure 4.37. Methyl chemical shift perturbations upon GDC-0994 binding to 2P-ERK2.
The Ile, Leu and Val regions of the 2D (^{13}C, ^{1}H) HMQC spectra are shown for 2P-ERK2 (black) and 2P-ERK2:GDC-0994 complex (red). Peaks with clear chemical shift perturbations are labeled with residue type and numbers.

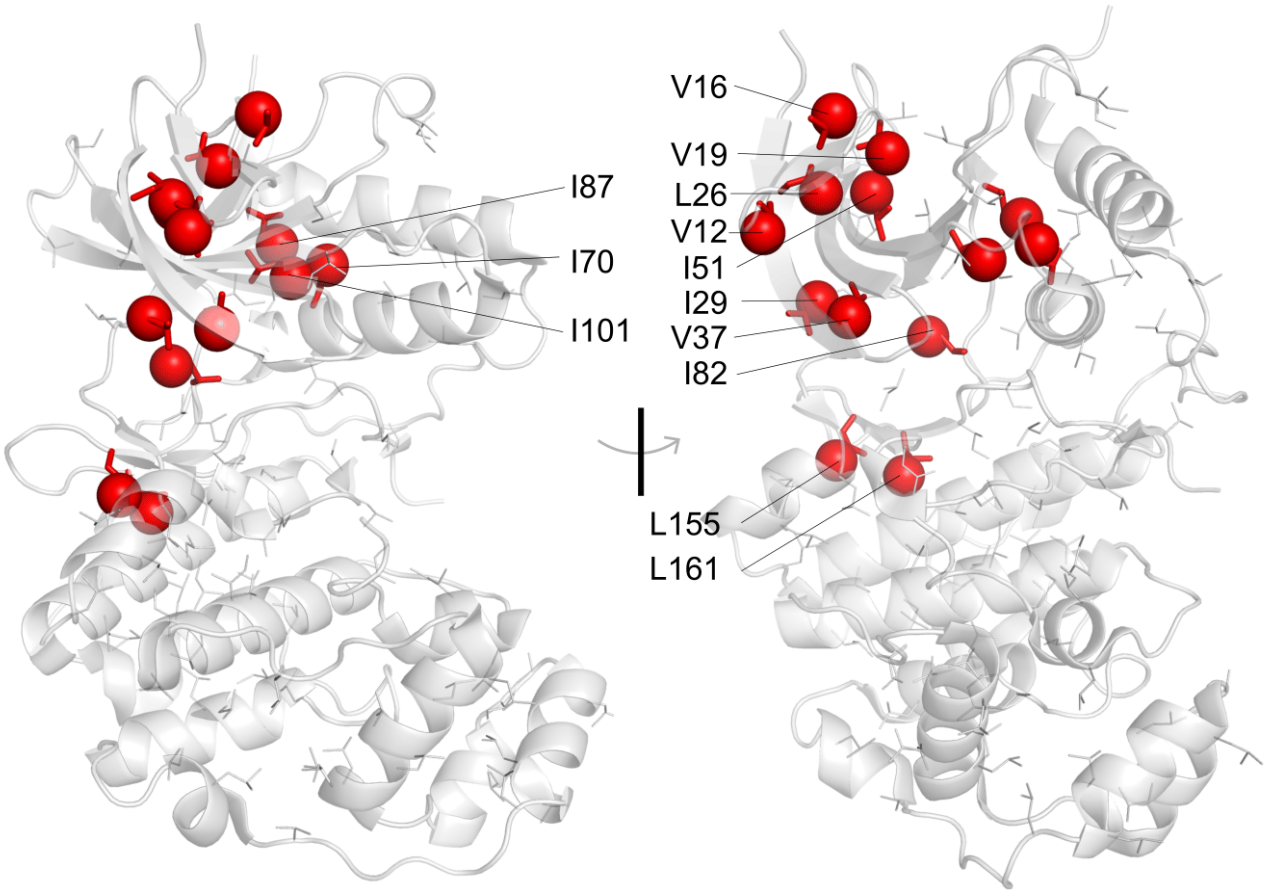

Figure 4.38. Chemical shift perturbations on 2P-ERK2 induced by the binding of GDC-0994.
Methyls of 2P-ERK2 that showed significant chemical shift perturbations ($CSH_{C,H}$ > 0.05 ppm, red spheres) upon GDC-0994 binding were mapped onto crystal structure of 0P-ERK2:SCH772984 complex (PDB 4qta, grey cartoon). The side chains of these residues are labeled with red sticks.

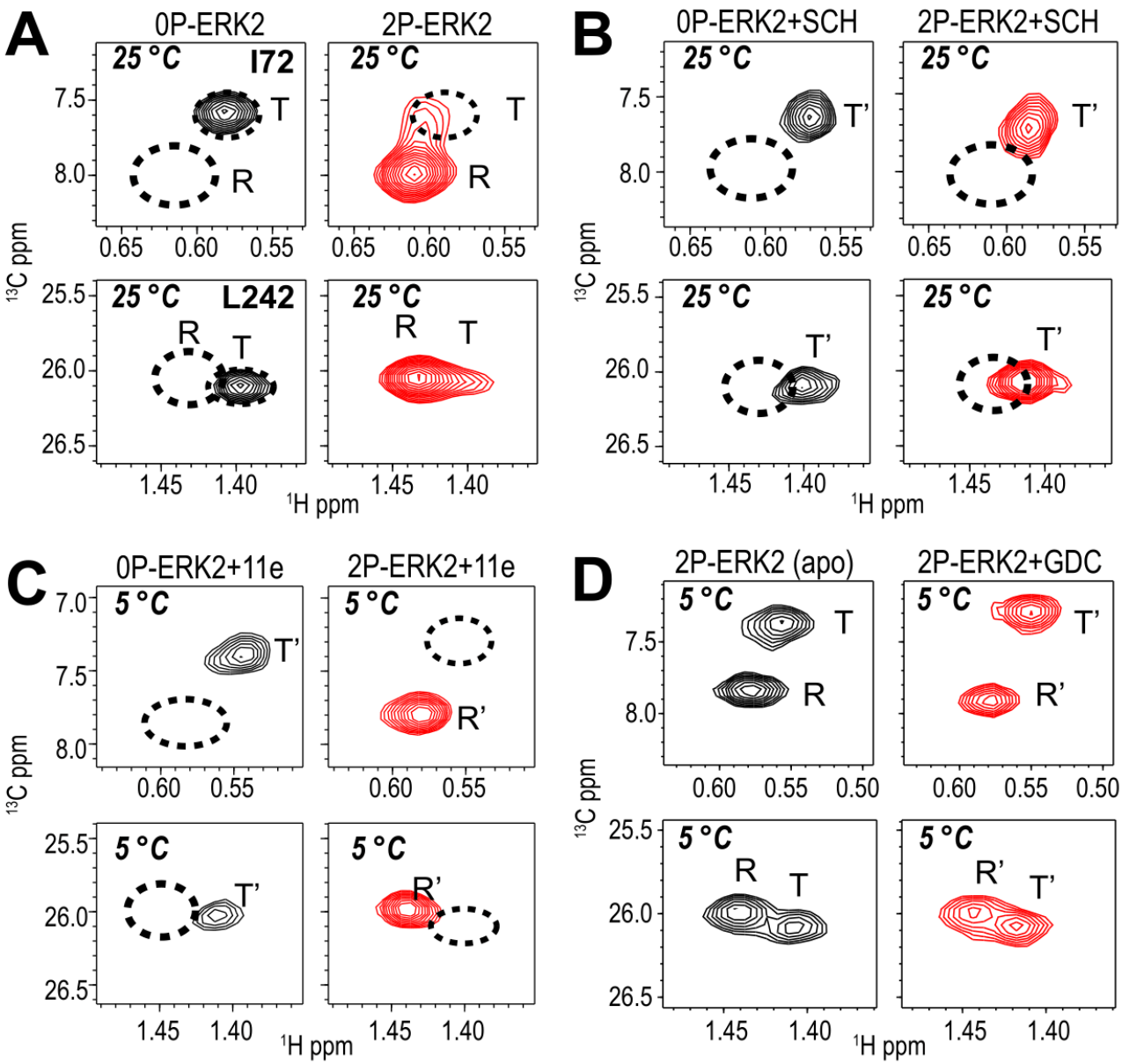

Figure 4.39. Different conformational stabilization effects of 2P-ERK2 by different inhibitors. (A) 2D (^{13}C, ^{1}H) HMQC spectra showing methyls of I72 and L242 that adopt the T conformation in 0P-ERK2, and a R⇌T conformational equilibrium in 2P-ERK2 at 25 °C. (B) 2D (^{13}C, ^{1}H) HMQC spectra showing methyls of I72 and L242 that adopt T' (inhibitor-bound form of T) conformation in both SCH772984-bound complexes of 0P- and 2P-ERK2 at 25 °C. (C) 2D (^{13}C, ^{1}H) HMQC spectra showing methyls of I72 and L242 that adopt T' (bound form of T) conformation in Vertex-11e-bound complex of 0P-ERK2, but R' (bound form of R) conformation in Vertex-11e-bound complex of 2P-ERK2 at 5 °C. (D) 2D (^{13}C, ^{1}H) HMQC spectra showing methyls of I72 and L242 that adopt a R⇌T conformational equilibrium in 2P-ERK2 at 5 °C. The equilibrium is not significantly affected by the binding of GDC-0994.

4.4. Discussion

The function of protein kinases, such as ERK2, is accomplished by binding with various ligands. Our study reveals two significant insights into the behavior of ligand binding to ERK2. First, we present a detailed analysis of the binding of physiological-relevant ligands to ERK2, including docking peptides from substrate proteins and nucleotides in the presence and/or absence of peptide substrates. These titration experiments provided estimates of K_d, and under optimal conditions provided insights on the association and dissociation rate constants (Table 4.11). The binary and ternary complexes of 2P-ERK2 showed no significant perturbation on the R⇌T interconversion but a small shift to enhance the T conformation when compared to free 2P-ERK2. Second, we demonstrate that the tight inhibitors of 2P-ERK2 (Vertex-11e, SCH772984, and GDC-0994) display differences in allosteric properties when bound to 2P-ERK2. According to the chemical shift of the slow-exchanging peaks, all three inhibitors formed a state similar to the T state upon binding to 0P-ERK2. In contrast, the binding of Vertex-11e to 2P-ERK2 strongly shifted the equilibrium between T and R states from 50% R to 100% R state at 5 °C, whereas the binding of SCH772984 to 2P-ERK2 dramatically shifted the equilibrium from 20% T to 100% T state at 25 °C. Unlike Vertex-11e and SCH772984, the binding of GDC-0994 showed no significant effect on the T⇌R equilibrium. Thus, the active form of the ERK2 kinase can be inhibited through multiple mechanisms that provide conformational selection.

4.4.1. Using Methyl Groups to Probe Elk1D Binding to ERK2

Once methyl groups have been assigned in a protein they provide multiple valuable probes of structure, function, and mechanism of action. The DEJL-motif binding site is one of the major docking sites that ERK2 uses to bind its activating kinase, substrates and scaffold proteins.[27, 45] The large set of methyl assignments obtained in this study was used to measure the binding affinity of the DEJL-motif peptide, Elk1D, to 0P- and 2P-ERK2 and also to set a lower limit on rate constants for binding. There

was a 3-fold difference in the K_d for Elk1D binding to the inactive *vs* active forms of ERK2 (Table 4.10). The K_d for Elk1D binding to 0P-ERK2 (10 μM) was similar to the previously measured K_d of 5 μM for the full-length Elk1 protein to a mutant of 0P-ERK2 with disrupted DEF-site that was competent to bind only at the DEJL-site.[145] The DEJL-docking interaction has been previously studied,[34, 59] but there are currently no kinetic data for binding to this site. The NMR titration of Elk1D into 0P- or 2P-ERK2 showed some peaks in fast exchange (Figure 4.2), which provides limits on the association and dissociation rate constants of the binding. For a chemical shift difference between free and bound forms, $|\Delta\omega|$, of 60 Hz and (e.g. L155) and a $[\text{Elk1D}]_{total}$ of 23 μM in the titration of 0P-ERK2 (Figure 4.2), the exchange rate constant for the binding, k_{ex} (where $k_{ex} = k_{on}[\text{Elk1D}]_{free} + k_{off}$) is larger than 60 Hz, yielding $k_{on} > 6\ \mu M^{-1}s^{-1}$ or $k_{off} > 30\ s^{-1}$. Taking account into that $K_d = 10\ \mu M$, this yields that $k_{on} > 3\ \mu M^{-1}s^{-1}$ and $k_{off} > 30\ s^{-1}$ (Table 4.11). However, most methyls showed chemical shift changes in both dimensions, increasing the complexity of kinetic analysis. One methyl resonance of L113 (Figure 4.4) showed exchange broadening at $[\text{Elk1D}]_{total} = 23\ \mu M$ in the titration of 0P-ERK2, indicating fast-intermediate exchange. This resonance in 0P-ERK2 showed $|\Delta\omega(^{13}C)|$ of 200 Hz and very small $|\Delta\omega(^{1}H)|$ (Figure 4.4), making it possible to simulate the observed exchange broadening with k_{on} of 30 $\mu M^{-1}s^{-1}$ and k_{off} of 300 s^{-1} (Figure 4.4). All the methyls that showed significant chemical shift changes upon binding of the Elk1D peptide in both active and inactive ERK2 were in proximity to the known DEJL-motif binding site,[163] indicating no perturbation of the rest of the molecule (Figure 4.3 and Table 4.10). This is consistent with local perturbations in p38α, observed in a previous solution study of the peptide/protein HePTP binding to its DEJL-motif.[169]

The Elk1 protein can bind to both the DEJL- and DEF-docking sites in 2P-ERK2,[144] but it only binds the DEJL-site in 0P-ERK2, because the DEF-site is sterically blocked by the activation loop.[34] One question is whether Elk1 shows a preference for binding to one, and not both, of these sites.

Previous studies of an Elk1F peptide that binds to the DEF-site in 2P-ERK2 yielded K_d = 8 μM, k_{on} = 56 $\mu M^{-1}s^{-1}$ and k_{off} = 450 s^{-1}.[170] These results are comparable to those obtained here for the DEJL-site binding peptide Elk1D (Table 4.11). This suggests that these two motifs of Elk1 bind with no kinetic or thermodynamic preference to the different docking sites in 2P-ERK2.

4.4.2. Using Methyl Groups to Probe AMP-PNP Binding to ERK2

Our measurements of AMP-PNP binding also provided insight into the enzymology of ERK2. Multiple methyl resonances in 0P- or 2P-ERK2 were in slow exchange on the chemical shift time scale in the NMR titration with AMP-PNP (Figure 4.5). As noted above, this made it difficult to obtain precise K_d values for AMP-PNP binding but they were in the range of 200 - 500 μM for both 0P- and 2P-ERK2 (Table 4.11), which is consistent with values previously determined by isothermal titration calorimetry.[81, 171] The similarity in K_d between 0P- and 2P-ERK2 is quite different from the situation for MAP kinase p38α, which showed >30 fold increase in the binding affinity of ATP upon phosphorylation (>15 mM for 0P-p38α and 430 μM for 2P-p38α).[172] The observed slow exchange for the methyl resonance of L26 during the titration of AMP-PNP into 2P-ERK2, which has a $|\Delta\omega(^1H)| \approx$ 80 Hz, yielded upper limits of $k_{on} < 0.08\ \mu M^{-1}s^{-1}$ and $k_{off} < 80\ s^{-1}$ (see Figure 4.5, Table 4.11). These limits are consistent with a previous study that measured $k_{on,ATP} = 0.015\ \mu M^{-1}s^{-1}$ and $k_{off,\ ATP} = 0.5\ s^{-1}$ for formation of the ternary MBP-bound complex of Tyr-185 phosphorylated (pY) ERK2.[155]

The methyls of L26 show the expected behavior for resonances in slow exchange during NMR titration of AMP-PNP (Figure 4.5). However, some other methyls that showed chemical shift perturbations in the titration with AMP-PNP for either 0P- or 2P-ERK2 were not observed in the HMQC spectrum upon saturation of the ligand. For example, titration with AMP-PNP reduces the intensities of the methyl resonances of V37 for the free form of ERK2 in the HMQC spectra but the

resonances of the bound form are not observed (Figure 4.7). This indicates that these methyl resonances are undergoing intermediate exchange between conformers in the AMP-PNP-bound form.

Finally, our results provide information about the structural perturbations on ERK2 induced by binding different ligands. In contrast to the primarily local perturbations induced by Elk1D, the binding of AMP-PNP to both 0P- and 2P-ERK2 showed chemical shift perturbations for methyls throughout the N-terminal and the upper C-terminal lobes (Figure 4.6). Similarly, 2P-p38α also showed methyl chemical shift perturbations distant from the ATP binding site upon the binding of an ATP analog.[172] These results suggest that nucleotide binding to kinases causes long-range conformational perturbations in both the N- and C-terminal lobes. This may arise from the assembly of the so-called "catalytic spine", which is a spatially conserved hydrophobic motif identified from crystal structures of active kinases that is formed by residues in both the N- and C-terminal lobes, and is completed by the adenine ring of ATP.[28] All of the ILV residues of the proposed catalytic spine showed clear methyl chemical shift perturbations upon AMP-PNP binding (Figure 4.6), which may result from the transition to the assembled form of the catalytic spine. Such long-range conformational perturbations upon binding ATP may arise from a common mechanism that kinases use to achieve a catalytically productive conformation.

4.4.3. Conformational Dynamics in the Binary and Ternary Complexes of 2P-ERK2

The activation of a protein kinase has usually been described with a model of a conformational switch from domain opening (inactive form) to closure ("active" form). Using this model, the T⇌R conformational equilibrium in free 2P-ERK2 suggests that the T conformation corresponds to the open or inactive form, whereas the R conformation corresponds to the closed or "active" form. Since the R conformation is only 80% populated in free 2P-ERK2, such a model would strongly suggest that free 2P-ERK2 is still not fully active, and may yield even higher populated (e.g. 100%) R conformation in a catalytically relevant form by binding with ATP and substrate. Here, the 2D TROSY-HMQC spectra show that the T⇌R conformational equilibrium was largely unperturbed and showed small enhancement of the T conformation in the substrate (analogue)-bound complexes of 2P-ERK2, including the AMP-PNP-bound binary complex, the AMP-PCP-bound binary complex and the AMP-PCP/sub-D-ternary complex of 2P-ERK2 at 25 °C. This is a strong indication that the active, 2P-ERK2 is still interconverting between T and R conformations when it's performing catalysis. Instead, it still interconverts between the T and R conformations. Thus, the T and R conformations may not simply correspond to the open/"inactive" and closed/"active" forms of ERK2.

The T⇌R conformational equilibrium was also largely unperturbed in the AMP-PNP-bound binary complex of 2P-ERK2 at lower temperature (5 °C). Interestingly, the slow exchanging peaks in 2P-ERK2 don't show clear sign of two slow exchanging peaks in the AMP-PCP-bound binary complex or the AMP-PCP/sub-D-ternary complex of 2P-ERK2 at 5 °C (Figure 4.21), indicating altered conformational dynamics from 2P-ERK2 in complex with AMP-PNP. This could be due to a highly biased population, smaller chemical shift difference between the two states, or higher exchange rate constants in this complex when compared to free 2P-ERK2. This suggests that AMP-PCP induces a conformational perturbation to 2P-ERK2 at lower temperature that is not observed in the complex with

AMP-PNP. Although AMP-PNP and AMP-PCP have comparable affinities for 2P-ERK2, it is not clear if AMP-PCP is a reliable ATP or AMP-PNP analogue.

A small shift favoring the T conformation was also observed in several product (analogue) -bound complexes of 2P-ERK2, including the ADP- or AMP-CP-bound binary complex (Figure 4.9 and Figure 4.24). It is worth noting that AMP-CP has an 8-fold weaker affinity for 2P-ERK2 relative to ADP, thus raising a caveat whether AMP-CP is a reliable ADP analogue. This result suggests that the small perturbation on T⇌R conformational equilibrium might accompany the catalytic step, the R conformation is then restored upon ADP dissociation to form the apoenzyme, preparing to form the next Michaelis complex. In this way, motions in 2P-ERK2 may enable ligand-induced conformational changes needed for turnover of enzyme intermediates.

4.4.4. Conformational Selection by Inhibitor Binding to ERK2

Our study provides new insight into the behavior of ATP-binding site inhibitors towards ERK2. Chapter 3 already showed that upon phosphorylation, constraints to dynamics are released in ERK2, to allow equilibrium exchange between T and R conformers. In other words, phosphorylation enabled conformational exchange in 2P-ERK2 not seen in 0P-ERK2. Here, I demonstrate that one of these inhibitors, Vertex-11e, which binds with differential affinities to the 0P- and 2P-ERK2, adopts the T conformation when binding with 0P-ERK2 and the R conformation when binding with 2P-ERK2. Conformational selectivity has been described in Type-II inhibitors of other protein kinases, and here for the first time on ERK2. Type-II inhibitors bind to the protein kinase by trapping nonproductive active site conformers. Such inhibitor is thought to yield higher selectivity than the ATP-competitive inhibitors, since the ATP binding site is conserved among many protein kinases. Most Type II inhibitors described to date stabilize a kinase inactive conformation, involving a “DFG-out” conformer, which disrupts Mg^{2+}-ATP binding by distorting the structure of the conserved DFG motif.

For example, the binding of the Abl kinase inhibitor imatinib to Abl kinase leads to the activation loop re-arrangement and the opening of an allosteric pocket. The allosteric pocket is occupied by part of imatinib and a DFG-out conformation is adopted. However, in ERK2 the DFG-out conformation has only been achieved by incorporating multiple mutations, combined with binding of a Type-II p38 MAP kinase inhibitor.[173] In its wild-type form, ERK2 shows no indication that the DFG-out conformation is adopted. The crystal structures of 0P-ERK2 bound to Vertex-11e and SCH772984 both clearly show a DFG-in conformation.[174] Thus, it is unlikely that the T and R conformers differ by a DFG-flip. Thus, Vertex-11e is different from classic Type-II kinase inhibitors in that Vertex-11e stabilizes different conformations in 0P- and 2P-ERK2 despite binding both tightly with the DFG-in conformation. Given that all co-crystal structures so far have been determined using 0P-ERK2, future X-ray structures of inhibitors in complex with 2P-ERK2 are needed to determine the structural differences between ligand-bound T and R conformers. Thus, the behavior of Vertex-11e resembles that of Type-II kinase inhibitors, which binds to the protein kinase by trapping nonproductive active site conformers.

Importantly, Vertex-11e differs from classic Type II inhibitors by showing higher selectivity for the R conformer, which is the major conformation in 2P-ERK2. The behavior of Vertex-11e predicts that it would preferentially bind 2P-ERK2 in cells. This might be advantageous under conditions where tissue levels of inhibitor are limiting, given that the cellular abundance of ERK1/2 typically reaches micromolar concentrations. Preferential binding to the active form (2P) of the kinase would minimize competition for inhibitor by the larger pool of 0P-ERK2. We propose that the T⇌R conformational equilibrium in ERK2 provides a new property to examine in structure-activity studies, which may inform the mechanism of inhibitor binding and cellular potency.

We also showed that SCH772984, another potent inhibitor of 2P-ERK2, formed T' (T conformation in the inhibitor-bound form) conformation in both 0P-ERK2 and 2P-ERK2. It indicates that the conformational shift to the R conformation observed in 2P-ERK2:Vertex-11e complex is not conserved among different tight inhibitors. Instead, the conformation selection is more likely a feature that is highly dependent on the idiosyncratic features of these inhibitors. The co-crystal structure of 0P-ERK2 and SCH772984 showed that SCH772984 access a novel-binding pocket in proximity to the Glycine-rich loop and the helix αC, and is characterized by a π-stacking interaction between its aromatic group and the aromatic side chain of Tyr62 on the helix αC, leading to re-arrangement of the Glycine-rich loop.[174] In contrast, the π-stacking interaction in the co-crystal structure of 0P-ERK2 and Vertex-11e was formed by the aromatic side chains of Tyr34 from the Glycine-rich loop and Tyr62. Thus, it is likely that the aromatic group on SCH772984 occupies this new pocket and interacts with Tyr62 by competing off the side chain of Tyr34.

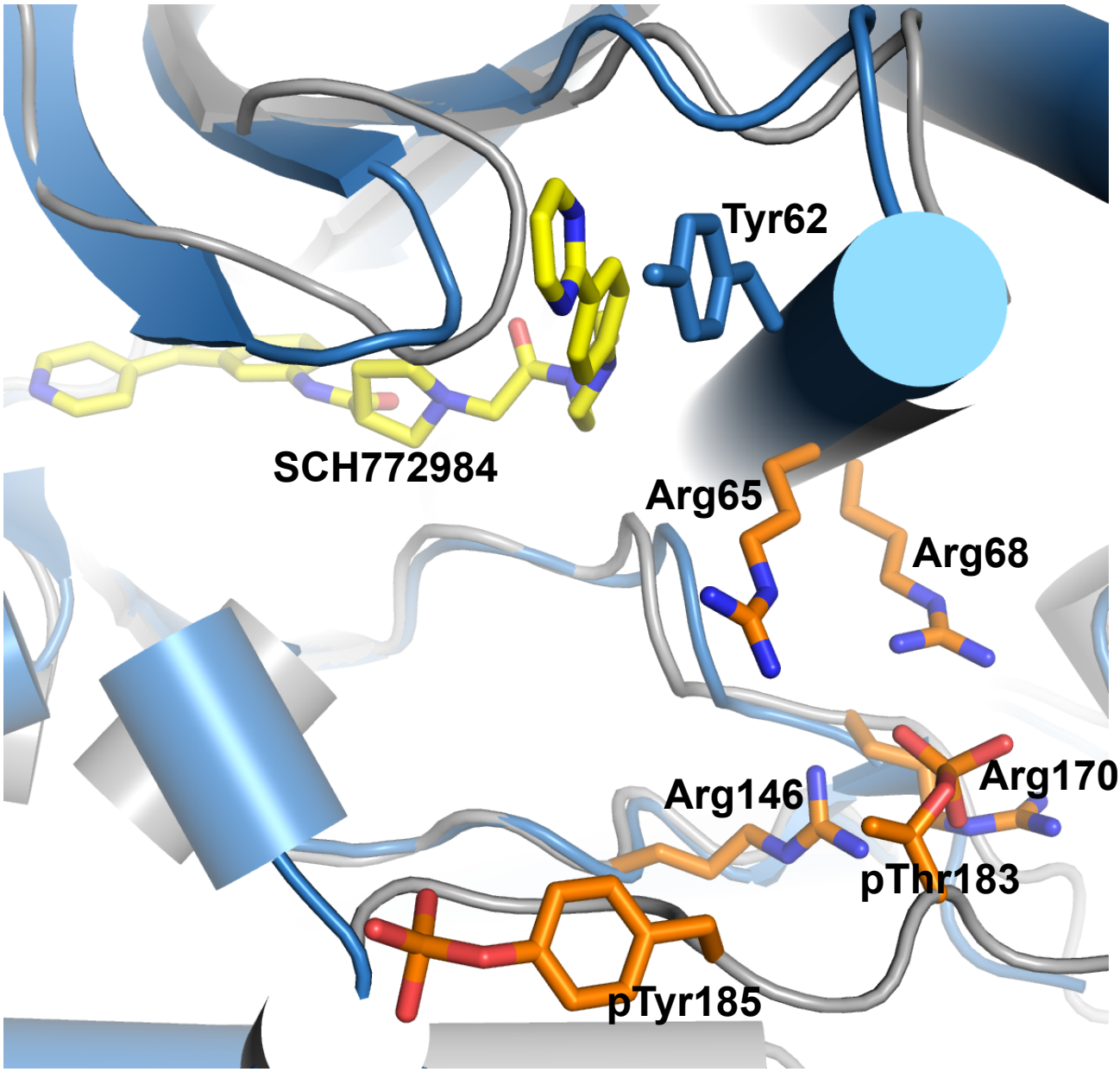

Figure 4.40. Co-crystal structure of SCH772984 and 0P-ERK2 show that the inhibitor SCH772984 accesses a novel-binding pocket out of the ATP binding site.
The backbone of 0P-ERK2 is shown with cartoon. SCH772984, side chains of Tyr62, Arg65, Arg68, Arg146, Arg170 and the phosphorylation sites pThr183 and pTyr185 are shown with sticks. π-stacking interaction is formed between SCH772984 and the aromatic side chain of Tyr62.

This structural difference in the co-crystal structures of 0P-ERK2 with different inhibitors may provide insights on the T⇌R conformational exchange. The crystal structure of 2P-ERK2 showed the formation of inter-domain ion pairs between the side chains of Arg65 and Arg68 on the helix αC and the phosphate of Thr183, whereas such an interaction was absent in 0P-ERK2 due to the lack of

phosphate. Thus, it is reasonable to suspect that the R state, which is the major population in 2P-ERK2, is associated with a conformation that is characteristic of intact inter-domain Arg-pThr ion pairs, whereas the T state is characteristic of disrupted inter-domain ion pairs. Since Tyr62 is also on the helix αC, in proximity to the arginines that form inter-domain ion pairs, the disruption of the Tyr62-Tyr34 π-stacking interaction by SCH772984 is likely to perturb the inter-domain ion pairs. Such perturbation in SCH772984-bound 2P-ERK2 may be the cause of shifting the T⇌R conformational equilibrium into the T state.

Conformational selection or stabilization induced by the binding of tight inhibitors has been observed in multiple other kinases. For example, the binding of BIRB796, a p38α inhibitor with K_d of 0.1 nM, suppressed the conformational dynamics on the Phe amide of the DFG motif of active p38α and stabilized its DFG-out conformation.[175] Another example is the catalytic domain of the protein kinase A, which showed suppressed micro- to millisecond dynamics upon the binding of a potent peptide inhibitor PKI_{5-24} (K_i = 2 nM[176]).[128] Although the conformational selection is usually reported on tight-binding ligands of protein kinases, it was unclear if the tight affinity of binding is causal for conformational selectivity. Here we show that in contrast to the clear conformational selectivity of Vertex-11e and SCH772984, another potent inhibitor of ERK2, GDC-0994, does not perturb the T⇌R conformational dynamics upon binding to 2P-ERK2 (Figure 4.36). This indicates that conformational selectivity is not a result of tight binding, but is the result of the unique structures of individual inhibitors.

Finally, it is asked to what degree does T⇌R conformational exchange account for the property of slow dissociation in these conformation selective inhibitors of ERK2. Conformational selection has been associated with long residence times and inhibitor potency. For example, slow off-rates have been reported for p38, MET, IGF1R and VEGFR inhibitors, and ascribed to their selective binding to the

DFG-out conformation.[177-181] Slow dissociation and higher cell retention of ponatinib has also been used to explain its higher potency towards BCR-ABL in primary acute myeloid leukemia cells.[182] Thus, conformational selection in kinase inhibitors may prove to be a valuable means of conferring slow tight binding, leading to higher potency and cellular efficacy.[183] It is also suspected that the slow association or dissociation of Vertex-11e and SCH772984 might be explained by the interconversion between T- and R-conformers. The most commonly observed mechanism for slow tight binding is a two-step model where the enzyme and inhibitor associate rapidly followed by a slow conformational change to a tight-binding complex ($E + I \rightleftharpoons EI \rightleftharpoons EI^*$).[184] Although previous CPMG studies of 2P-ERK2 measured rate constants for T⇌R conformational exchange of 240 s^{-1} and 60 s^{-1} in the forward and reverse directions, respectively; there is currently no information on the kinetics of T⇌R conformational exchange in the inhibitor-bound 2P-ERK2 complex. Thus, it remains unknown if the slow dissociation of Vertex-11e is correlated with the T⇌R conformational exchange. Further studies are needed to understand the structural basis of slow inhibition, and examine the linkage between allostery and kinetics in ERK2.

4.5. Summary

In this chapter, the effects of binding to 0P- or 2P-ERK2 induced by various ligands of ERK2 are reported using 2D methyl-TROSY-HMQC experiments, including tight inhibitors and physiological-relevant ligands such as nucleotides or substrate peptides. Binding affinities and chemical shift perturbations are reported for these binding events. Under optimal cases, ranges of the association and dissociation rate constants of the binding could be derived. In contrast to phosphorylation, which induced a conformational shift from the T state in 0P-ERK2 to a dominant R state in 2P-ERK2, the binding of ATP analogues in absence or presence of peptide substrate didn't further enhance the population of the R state. In contrast, the T⇌R conformational dynamics showed

small shift to the T conformation upon the binding of nucleotides (analogues) to 2P-ERK2. The binding of ADP to 2P-ERK2 induced slight shift to the T conformation. This result suggests that the nucleotide-bound binary complex of 2P-ERK2 is not in 100% R conformation; thus, it is likely that the R state does not simply represent the "active" form of the kinase. Instead, small perturbations of the T⇌R conformational dynamics accompany the catalytic cycle of ERK2. In contrast, several tight inhibitors of ERK2 dramatically perturbed the T⇌R conformational dynamics in 2P-ERK2. Vertex-11e strongly shifted the equilibrium completely to the R conformation, whereas SCH772984 strongly shifted the equilibrium completely to a conformation that is similar to T. The capability of inhibitors to stabilize different conformations may be associated with perturbations of the inter-domain ion pairs of 2P-ERK2.

Chapter 5. Conclusion and Future Directions

The goal of this thesis was to understand the regulatory mechanism for the MAP kinase, ERK2, involving changes in conformational dynamics upon activation and ligand binding measured using solution NMR techniques. Chapter 2 reported ~60% of Ile, Leu and Val (ILV) methyl assignments for ILV ^{13}C methyl-protonated, U-[^{2}H,^{15}N]-labeled 0P- and 2P-ERK2, providing sufficient methyl probes for understanding the structure, function and dynamics of ERK2 in later chapters. These assignments were obtained using a structure-based assignment strategy, comparing distance information obtained from 3D methyl-methyl nuclear Overhauser effect (NOE) spectroscopy with the X-ray structure. If higher percentage of the methyl assignment is needed, Paramagnetic Relaxation Enhancement (PRE)[104] and/or mutagenesis[57] of surface methyls could be used to complement the NOE constraints. This strategy can be applied to other large protein systems where the backbone assignment procedure often breaks down due to rapid relaxation and spectral overlap, resulting in few backbone assignments. This strategy is expected to be widely used for large protein systems since it can be easily adapted on proteins with alternative methyl labeling, such as on other residues (e.g. Thr[54], Ala[185], and Met[55, 98]) or stereospecific labeling of Leu/Val methyls[72, 186, 187].

Chapter 3 reported altered μs-ms methyl conformational dynamics upon the activation of ERK2 using CPMG relaxation experiments and 2D line shape analysis. The inactive ERK2 showed only localized methyl dynamics, consistent with one major conformation. In contrast, the active ERK2 showed methyl dynamics that were consistent with two conformations which undergo exchange with forward and reverse rate constants of 240 s^{-1} and 60 s^{-1} at 25 °C. Line shape analysis revealed that the major conformation (80% at 25 °C) of the active ERK2 is a new state that was not sampled by the inactive ERK2, whereas the minor conformation (20% at 25 °C) of active ERK2 is similar to the dominant conformation of inactive ERK2. An ERK2 mutant that was designed to increase its hinge

flexibility by mutating hinge residues $M^{106}E^{107}$ to GG also showed methyl dynamics that were consistent with exchange between two conformations. Thus, the major conformation in active ERK2 allows sampling of a new "relaxed" (R) state whereas the minor conformation is restrained in a "tense" (T) state. This provides a model in which 2P-ERK2 interconverts between two conformations T and R, with $k_{TR} = 240\ s^{-1}$ and $k_{RT} = 60\ s^{-1}$ at 25 °C.

Chapter 4 extended the study to the regulation of ERK2 upon ligand binding, including catalytically relevant nucleotides, nucleotide analogues and substrates, as well as small molecule inhibitors. The binary or ternary complexes of ERK2 bound to nucleotides and/or substrates did not shift the enzyme conformation to 100% R; instead, they showed either no significant perturbation of the T ⇌ R equilibrium with only small perturbations on the T ⇌ R equilibrium towards the T conformer. In contrast, the binding of certain high-affinity ATP-binding site inhibitors induced dramatic changes to the T ⇌ R equilibrium of 2P-ERK2. Specifically, Vertex-11e stabilized the R conformation to 100%, whereas SCH772984 stabilized the T conformation to 100%. The stabilization of distinct conformational states by different inhibitors revealed that ERK2 is a kinase available for conformational selection, an unusual attribute for kinases that has potential importance for therapeutic drug design.

One of the questions to be explored in the future is the conformational significance of the T ⇌ R equilibrium in 2P-ERK2. Two simple hypotheses can be proposed to understand this:

One possibility is that the R conformation corresponds to an active form of ERK2 given that it is major in 2P-ERK2, whereas the T conformation corresponds to an inactive form. For example, one might envision an open to closed model of protein kinase, where the open conformation (T) corresponds to the inactive form and the closed conformation (R) corresponds to the active form. In such a case, k_{RT} would represent the rate constant for shifting the kinase from a closed conformation to

an open conformation. Coincidentally, the measured k_{RT} = 60 s^{-1} was comparable to the rate constant for product dissociation reported previously for 2P-ERK2 (56 s^{-1}).[149, 188] Further studies are needed to determine if this correlation also holds up when k_{RT} is measured for the product-bound 2P-ERK2 ternary complex. Dalby and co-workers reported that the product dissociation of 2P-ERK2 during the catalysis of Ets1 is mainly rate-limited by the dissociation of ADP.[147] For this purpose, the conformational dynamics of ADP-bound 2P-ERK2 is of particular interest.

The alternative possibility is that the ability of 2P-ERK2 to undergo μs-ms conformational dynamics, instead of the population of the R conformation, is critical for catalysis. Under this assumption, the kinetics of T ⇌ R equilibrium in the catalytically relevant complexes of ERK2 could reflect transitions from one enzyme intermediate state to the next. Such coupling between catalysis and conformational dynamics is similar to that reported for catalytically relevant complexes of dihydrofolate reductase (DHFR) by Wright and co-workers, based on the matching between rate constants for conformational dynamics of DHFR and rate constants for steps in catalytic turnover.[39] However, we note that the substrate/co-factor dissociation constants (k_{off}) for DHFR are typically slower than the μs-ms time scale,[189, 190] whereas the substrate dissociation constants for ERK2 fall into the millisecond timescale, as estimated in Chapter 4. This could lead to difficulty in deciphering whether the conformational dynamics in the ternary complex of ERK2 is contributed by ligand binding or by the T ⇌ R equilibrium.

The structure of the R conformation as well as the structural difference between R and T conformations remains to be determined. Given that the population of the R state decreases with lower temperature, it is possible that at the cryogenic temperatures where X-ray data are collected, the major conformations seen in published apo-2P-ERK2 structures reflect the T state. X-ray studies are ongoing to try and trap 2P-ERK2 in its R conformation. The inhibitor-induced conformational selection on 2P-

ERK2 suggests a strategy for this, involving X-ray structural determination of 2P-ERK2:inhibitor complexes representing R or T conformations. Because the NMR studies showed that the 2P-ERK2:Vertex-11e complex stabilized the R conformation to 100% at temperatures as low as 5 °C, this complex could potentially yield a structure of the R state. Similarly, the conformational equilibrium shifted from 20% T to 100% T conformation in SCH772984-bound 2P-ERK2, providing a means of determining a structure of 2P-ERK2 in the T state. The structural differences between R and T conformations will provide new insights towards understanding the regulation of ERK2. Knapp and co-workers have suggested that SCH772984 binds 0P-ERK2 by occupying a novel, allosteric pocket between Gly-rich loop and the helix αC.[174] This pocket is in proximity to two arginines (Arg65, Arg68), which form inter-domain salt bridges with the phosphate on Thr183 of 2P-ERK2.[33] If SCH772984 binds to 2P-ERK2 in a similar way, then it is possible that the stabilization of the T conformation in the 2P-ERK2:SCH772984 complex results from perturbation or even breakage of the inter-domain Arg-pThr salt bridges, as discussed in Chapter 4. This would test the hypothesis that the T conformation corresponds to a state with a broken inter-domain salt bridge, whereas the R state is characteristic of intact inter-domain salt bridge. This hypothesis could be tested in the future, by examining Arg65/68 mutants of 2P-ERK2 to see if a 100% T conformation is observed when the inter-domain salt bridge cannot form.

The physiological outcome of conformational stabilization effects on 2P-ERK2 by different inhibitors is worth further investigation, in order to know – is it better for an inhibitor to stabilize the R state or the T state in ERK2? Future studies are anticipated using cell-based assays to assess the extent to which conformational selection contributes to inhibitor potency in cells, measured by cell killing and inhibition of targets of the MAP kinase pathway. One difficulty of such study would be to separate the effects of different binding kinetics of the inhibitors from differential conformational stabilization.

Understanding the correlation between drug potency and conformational stabilization effect of ERK2 inhibitors will lead to new insights for inhibitor design.

Bibliography

(1) Zhang, W., and Liu, H. T. (2002) MAPK signal pathways in the regulation of cell proliferation in mammalian cells, *Cell research 12*, 9-18.

(2) Dhillon, A. S., Hagan, S., Rath, O., and Kolch, W. (2007) MAP kinase signalling pathways in cancer, *Oncogene 26*, 3279-3290.

(3) Fabian, J. R., Daar, I. O., and Morrison, D. K. (1993) Critical tyrosine residues regulate the enzymatic and biological activity of Raf-1 kinase, *Mol. Cell. Biol. 13*, 7170-7179.

(4) Marais, R., Light, Y., Paterson, H. F., and Marshall, C. J. (1995) Ras recruits Raf-1 to the plasma membrane for activation by tyrosine phosphorylation, *EMBO J. 14*, 3136-3145.

(5) Rushworth, L. K., Hindley, A. D., O'Neill, E., and Kolch, W. (2006) Regulation and role of Raf-1/B-Raf heterodimerization, *Mol. Cell. Biol. 26*, 2262-2272.

(6) Lavoie, H., and Therrien, M. (2015) Regulation of RAF protein kinases in ERK signalling, *Nat. Rev. Mol. Cell Biol. 16*, 281-298.

(7) Claperon, A., and Therrien, M. (2007) KSR and CNK: two scaffolds regulating RAS-mediated RAF activation, *Oncogene 26*, 3143-3158.

(8) Eishingdrelo, H., and Kongsamut, S. (2013) Minireview: Targeting GPCR Activated ERK Pathways for Drug Discovery, *Curr Chem Genom Transl Med 7*, 9-15.

(9) Crespo, P., Xu, N., Simonds, W. F., and Gutkind, J. S. (1994) Ras-dependent activation of MAP kinase pathway mediated by G-protein beta gamma subunits, *Nature 369*, 418-420.

(10) van Biesen, T., Hawes, B. E., Raymond, J. R., Luttrell, L. M., Koch, W. J., and Lefkowitz, R. J. (1996) G(o)-protein alpha-subunits activate mitogen-activated protein kinase via a novel protein kinase C-dependent mechanism, *J. Biol. Chem. 271*, 1266-1269.

(11) Muslin, A. J. (2008) MAPK signalling in cardiovascular health and disease: molecular mechanisms and therapeutic targets, *Clin. Sci. 115*, 203-218.

(12) Zhu, X. W., Lee, H. G., Raina, A. K., Perry, G., and Smith, M. A. (2002) The role of mitogen-activated protein kinase pathways in Alzheimer's disease, *Neurosignals 11*, 270-281.

(13) Ascierto, P. A., Kirkwood, J. M., Grob, J. J., Simeone, E., Grimaldi, A. M., Maio, M., Palmieri, G., Testori, A., Marincola, F. M., and Mozzillo, N. (2012) The role of BRAF V600 mutation in melanoma, *J. Transl. Med. 10*, 85.

(14) Chapman, P. B., Hauschild, A., Robert, C., Haanen, J. B., Ascierto, P., Larkin, J., Dummer, R., Garbe, C., Testori, A., Maio, M., Hogg, D., Lorigan, P., Lebbe, C., Jouary, T., Schadendorf, D., Ribas, A., O'Day, S. J., Sosman, J. A., Kirkwood, J. M., Eggermont, A. M., Dreno, B., Nolop, K., Li, J., Nelson, B., Hou, J., Lee, R. J., Flaherty, K. T., McArthur, G. A., and Group, B.-S.

(2011) Improved survival with vemurafenib in melanoma with BRAF V600E mutation, *N. Engl. J. Med. 364*, 2507-2516.

(15) Hauschild, A., Grob, J. J., Demidov, L. V., Jouary, T., Gutzmer, R., Millward, M., Rutkowski, P., Blank, C. U., Miller, W. H., Jr., Kaempgen, E., Martin-Algarra, S., Karaszewska, B., Mauch, C., Chiarion-Sileni, V., Martin, A. M., Swann, S., Haney, P., Mirakhur, B., Guckert, M. E., Goodman, V., and Chapman, P. B. (2012) Dabrafenib in BRAF-mutated metastatic melanoma: a multicentre, open-label, phase 3 randomised controlled trial, *Lancet 380*, 358-365.

(16) Robert, C., Karaszewska, B., Schachter, J., Rutkowski, P., Mackiewicz, A., Stroiakovski, D., Lichinitser, M., Dummer, R., Grange, F., Mortier, L., Chiarion-Sileni, V., Drucis, K., Krajsova, I., Hauschild, A., Lorigan, P., Wolter, P., Long, G. V., Flaherty, K., Nathan, P., Ribas, A., Martin, A. M., Sun, P., Crist, W., Legos, J., Rubin, S. D., Little, S. M., and Schadendorf, D. (2015) Improved Overall Survival in Melanoma with Combined Dabrafenib and Trametinib, *N. Engl. J. Med. 372*, 30-39.

(17) Morris, E. J., Jha, S., Restaino, C. R., Dayananth, P., Zhu, H., Cooper, A., Carr, D., Deng, Y., Jin, W., Black, S., Long, B., Liu, J., Dinunzio, E., Windsor, W., Zhang, R., Zhao, S., Angagaw, M. H., Pinheiro, E. M., Desai, J., Xiao, L., Shipps, G., Hruza, A., Wang, J., Kelly, J., Paliwal, S., Gao, X., Babu, B. S., Zhu, L., Daublain, P., Zhang, L., Lutterbach, B. A., Pelletier, M. R., Philippar, U., Siliphaivanh, P., Witter, D., Kirschmeier, P., Bishop, W. R., Hicklin, D., Gilliland, D. G., Jayaraman, L., Zawel, L., Fawell, S., and Samatar, A. A. (2013) Discovery of a novel ERK inhibitor with activity in models of acquired resistance to BRAF and MEK inhibitors, *Cancer Discov. 3*, 742-750.

(18) Hatzivassiliou, G., Liu, B., O'Brien, C., Spoerke, J. M., Hoeflich, K. P., Haverty, P. M., Soriano, R., Forrest, W. F., Heldens, S., Chen, H., Toy, K., Ha, C., Zhou, W., Song, K., Friedman, L. S., Amler, L. C., Hampton, G. M., Moffat, J., Belvin, M., and Lackner, M. R. (2012) ERK inhibition overcomes acquired resistance to MEK inhibitors, *Mol. Cancer Ther. 11*, 1143-1154.

(19) Knighton, D. R., Zheng, J. H., Ten Eyck, L. F., Ashford, V. A., Xuong, N. H., Taylor, S. S., and Sowadski, J. M. (1991) Crystal structure of the catalytic subunit of cyclic adenosine monophosphate-dependent protein kinase, *Science 253*, 407-414.

(20) Taylor, S. S., and Kornev, A. P. (2011) Protein kinases: evolution of dynamic regulatory proteins, *Trends Biochem. Sci 36*, 65-77.

(21) Johnson, D. A., Akamine, P., Radzio-Andzelm, E., Madhusudan, M., and Taylor, S. S. (2001) Dynamics of cAMP-dependent protein kinase, *Chem. Rev. 101*, 2243-2270.

(22) Adams, J. A. (2001) Kinetic and catalytic mechanisms of protein kinases, *Chem. Rev. 101*, 2271-2290.

(23) Zheng, J., Trafny, E. A., Knighton, D. R., Xuong, N. H., Taylor, S. S., Ten Eyck, L. F., and Sowadski, J. M. (1993) 2.2 A refined crystal structure of the catalytic subunit of cAMP-dependent protein kinase complexed with MnATP and a peptide inhibitor, *Acta Crystallogr. D Biol. Crystallogr. 49*, 362-365.

(24) Huse, M., and Kuriyan, J. (2002) The conformational plasticity of protein kinases, *Cell 109*, 275-282.

(25) Nolen, B., Taylor, S., and Ghosh, G. (2004) Regulation of protein kinases; controlling activity through activation segment conformation, *Mol. Cell 15*, 661-675.

(26) Endicott, J. A., Noble, M. E., and Johnson, L. N. (2012) The structural basis for control of eukaryotic protein kinases, *Annu. Rev. Biochem 81*, 587-613.

(27) Palmieri, L., and Rastelli, G. (2013) alpha C helix displacement as a general approach for allosteric modulation of protein kinases, *Drug Discov. Today 18*, 407-414.

(28) Kornev, A. P., Haste, N. M., Taylor, S. S., and Eyck, L. F. (2006) Surface comparison of active and inactive protein kinases identifies a conserved activation mechanism, *Proc. Natl. Acad. Sci. U. S. A. 103*, 17783-17788.

(29) Steichen, J. M., Kuchinskas, M., Keshwani, M. M., Yang, J., Adams, J. A., and Taylor, S. S. (2012) Structural basis for the regulation of protein kinase A by activation loop phosphorylation, *J. Biol. Chem. 287*, 14672-14680.

(30) Payne, D. M., Rossomando, A. J., Martino, P., Erickson, A. K., Her, J. H., Shabanowitz, J., Hunt, D. F., Weber, M. J., and Sturgill, T. W. (1991) Identification of the regulatory phosphorylation sites in pp42/mitogen-activated protein kinase (MAP kinase), *EMBO J. 10*, 885-892.

(31) Prowse, C. N., and Lew, J. (2001) Mechanism of activation of ERK2 by dual phosphorylation, *J. Biol. Chem. 276*, 99-103.

(32) Zhang, F., Strand, A., Robbins, D., Cobb, M. H., and Goldsmith, E. J. (1994) Atomic structure of the MAP kinase ERK2 at 2.3 A resolution, *Nature 367*, 704-711.

(33) Canagarajah, B. J., Khokhlatchev, A., Cobb, M. H., and Goldsmith, E. J. (1997) Activation mechanism of the MAP kinase ERK2 by dual phosphorylation, *Cell 90*, 859-869.

(34) Lee, T., Hoofnagle, A. N., Kabuyama, Y., Stroud, J., Min, X., Goldsmith, E. J., Chen, L., Resing, K. A., and Ahn, N. G. (2004) Docking motif interactions in MAP kinases revealed by hydrogen exchange mass spectrometry, *Mol. Cell 14*, 43-55.

(35) Palmer, A. G., 3rd. (2004) NMR characterization of the dynamics of biomacromolecules, *Chem. Rev. 104*, 3623-3640.

(36) Zhou, J., and Adams, J. A. (1997) Participation of ADP dissociation in the rate-determining step in cAMP-dependent protein kinase, *Biochemistry 36*, 15733-15738.

(37) Mittermaier, A. K., and Kay, L. E. (2009) Observing biological dynamics at atomic resolution using NMR, *Trends Biochem. Sci 34*, 601-611.

(38) Korzhnev, D. M., Kloiber, K., Kanelis, V., Tugarinov, V., and Kay, L. E. (2004) Probing slow dynamics in high molecular weight proteins by methyl-TROSY NMR spectroscopy: application to a 723-residue enzyme, *J. Am. Chem. Soc. 126*, 3964-3973.

(39) Boehr, D. D., McElheny, D., Dyson, H. J., and Wright, P. E. (2006) The dynamic energy landscape of dihydrofolate reductase catalysis, *Science 313*, 1638-1642.

(40) Wiesner, S., Wybenga-Groot, L. E., Warner, N., Lin, H., Pawson, T., Forman-Kay, J. D., and Sicheri, F. (2006) A change in conformational dynamics underlies the activation of Eph receptor tyrosine kinases, *EMBO J. 25*, 4686-4696.

(41) Venters, R. A., Thompson, R., and Cavanagh, J. (2002) Current approaches for the study of large proteins by NMR, *J. Mol. Struct. 602*, 275-292.

(42) Wider, G., and Wuthrich, K. (1999) NMR spectroscopy of large molecules and multimolecular assemblies in solution, *Curr. Opin. Struct. Biol. 9*, 594-601.

(43) Pervushin, K., Riek, R., Wider, G., and Wuthrich, K. (1997) Attenuated T-2 relaxation by mutual cancellation of dipole-dipole coupling and chemical shift anisotropy indicates an avenue to NMR structures of very large biological macromolecules in solution, *Proc. Natl. Acad. Sci. U. S. A. 94*, 12366-12371.

(44) Grzesiek, S., Anglister, J., Ren, H., and Bax, A. (1993) C-13 Line Narrowing by H-2 Decoupling in H-2/C-13/N-15-Enriched Proteins - Application to Triple-Resonance 4d J-Connectivity of Sequential Amides, *J. Am. Chem. Soc. 115*, 4369-4370.

(45) Ruschak, A. M., and Kay, L. E. (2010) Methyl groups as probes of supra-molecular structure, dynamics and function, *J. Biomol. NMR 46*, 75-87.

(46) Fernandez, C., and Wider, G. (2003) TROSY in NMR studies of the structure and function of large biological macromolecules, *Curr. Opin. Struct. Biol. 13*, 570-580.

(47) Yamazaki, T., Lee, W., Arrowsmith, C. H., Muhandiram, D. R., and Kay, L. E. (1994) A Suite of Triple-Resonance Nmr Experiments for the Backbone Assignment of N-15, C-13, H-2 Labeled Proteins with High-Sensitivity, *J. Am. Chem. Soc. 116*, 11655-11666.

(48) Grzesiek, S., Anglister, J., Ren, H., and Bax, A. (1993) C-13 Line Narrowing by H-2 Decoupling in H-2/C-13/N-15-Enriched Proteins - Application to Triple-Resonance 4d J-Connectivity of Sequential Amides, *Journal of the American Chemical Society 115*, 4369-4370.

(49) Gardner, K. H., and Kay, L. E. (1997) Production and incorporation of N-15, C-13, H-2 (H-1-delta 1 methyl) isoleucine into proteins for multidimensional NMR studies, *J. Am. Chem. Soc. 119*, 7599-7600.

(50) Goto, N. K., Gardner, K. H., Mueller, G. A., Willis, R. C., and Kay, L. E. (1999) A robust and cost-effective method for the production of Val, Leu, Ile (delta 1) methyl-protonated N-15-, C-13-, H-2-labeled proteins, *J. Biomol. NMR 13*, 369-374.

(51) Rosen, M. K., Gardner, K. H., Willis, R. C., Parris, W. E., Pawson, T., and Kay, L. E. (1996) Selective methyl group protonation of perdeuterated proteins, *J. Mol. Biol. 263*, 627-636.

(52) Kay, L. E., Bull, T. E., Nicholson, L. K., Griesinger, C., Schwalbe, H., Bax, A., and Torchia, D. A. (1992) The Measurement of Heteronuclear Transverse Relaxation-Times in Ax3 Spin Systems Via Polarization-Transfer Techniques, *J. Magn. Reson. 100*, 538-558.

(53) Sprangers, R., Velyvis, A., and Kay, L. E. (2007) Solution NMR of supramolecular complexes: providing new insights into function, *Nat. Methods 4*, 697-703.

(54) Sinha, K., Jen-Jacobson, L., and Rule, G. S. (2011) Specific labeling of threonine methyl groups for NMR studies of protein-nucleic acid complexes, *Biochemistry 50*, 10189-10191.

(55) Fischer, M., Kloiber, K., Hausler, J., Ledolter, K., Konrat, R., and Schmid, W. (2007) Synthesis of a 13C-methyl-group-labeled methionine precursor as a useful tool for simplifying protein structural analysis by NMR spectroscopy, *ChemBioChem 8*, 610-612.

(56) Tugarinov, V., and Kay, L. E. (2003) Ile, Leu, and Val methyl assignments of the 723-residue malate synthase G using a new labeling strategy and novel NMR methods, *J. Am. Chem. Soc. 125*, 13868-13878.

(57) Amero, C., Asuncion Dura, M., Noirclerc-Savoye, M., Perollier, A., Gallet, B., Plevin, M. J., Vernet, T., Franzetti, B., and Boisbouvier, J. (2011) A systematic mutagenesis-driven strategy for site-resolved NMR studies of supramolecular assemblies, *J. Biomol. NMR 50*, 229-236.

(58) Sprangers, R., and Kay, L. E. (2007) Quantitative dynamics and binding studies of the 20S proteasome by NMR, *Nature 445*, 618-622.

(59) Piserchio, A., Warthaka, M., Devkota, A. K., Kaoud, T. S., Lee, S., Abramczyk, O., Ren, P., Dalby, K. N., and Ghose, R. (2011) Solution NMR insights into docking interactions involving inactive ERK2, *Biochemistry 50*, 3660-3672.

(60) Ruschak, A. M., and Kay, L. E. (2010) Methyl groups as probes of supra-molecular structure, dynamics and function, *J. Biomol. NMR 46*, 75-87.

(61) Ollerenshaw, J. E., Tugarinov, V., and Kay, L. E. (2003) Methyl TROSY: explanation and experimental verification, *Magn. Reson. Chem. 41*, 843-852.

(62) Plevin, M. J., and Boisbouvier, J. (2012) Isotope-Labelling of Methyl Groups for NMR Studies of Large Proteins, In *Recent Developments in Biomolecular Nmr* (Clore, M., and Potts, J., Eds.), pp 1-24, Royal Society of Chemistry, London.

(63) Tzeng, S. R., and Kalodimos, C. G. (2011) Protein dynamics and allostery: an NMR view, *Curr. Opin. Struct. Biol. 21*, 62-67.

(64) Rosenzweig, R., and Kay, L. E. (2014) Bringing dynamic molecular machines into focus by methyl-TROSY NMR, *Annu. Rev. Biochem 83*, 291-315.

(65) Ruschak, A. M., and Kay, L. E. (2012) Proteasome allostery as a population shift between interchanging conformers, *Proc. Natl. Acad. Sci. U. S. A. 109*, E3454-3462.

(66) Englander, S. W., and Wand, A. J. (1987) Main-chain-directed strategy for the assignment of 1H NMR spectra of proteins, *Biochemistry 26*, 5953-5958.

(67) Bartels, C., Billeter, M., Guntert, P., and Wuthrich, K. (1996) Automated sequence-specific NMR assignment of homologous proteins using the program GARANT, *J. Biomol. NMR 7*, 207-213.

(68) Apaydin, M. S., Conitzer, V., and Donald, B. R. (2008) Structure-based protein NMR assignments using native structural ensembles, *J. Biomol. NMR 40*, 263-276.

(69) Xu, Y., Liu, M., Simpson, P. J., Isaacson, R., Cota, E., Marchant, J., Yang, D., Zhang, X., Freemont, P., and Matthews, S. (2009) Automated assignment in selectively methyl-labeled proteins, *J. Am. Chem. Soc. 131*, 9480-9481.

(70) Sahakyan, A. B., Vranken, W. F., Cavalli, A., and Vendruscolo, M. (2011) Structure-based prediction of methyl chemical shifts in proteins, *J. Biomol. NMR 50*, 331-346.

(71) Chao, F. A., Shi, L., Masterson, L. R., and Veglia, G. (2012) FLAMEnGO: a fuzzy logic approach for methyl group assignment using NOESY and paramagnetic relaxation enhancement data, *J. Magn. Reson. 214*, 103-110.

(72) Mas, G., Crublet, E., Hamelin, O., Gans, P., and Boisbouvier, J. (2013) Specific labeling and assignment strategies of valine methyl groups for NMR studies of high molecular weight proteins, *J. Biomol. NMR 57*, 251-262.

(73) Xu, Y., and Matthews, S. (2013) MAP-XSII: an improved program for the automatic assignment of methyl resonances in large proteins, *J. Biomol. NMR 55*, 179-187.

(74) Chao, F. A., Kim, J., Xia, Y., Milligan, M., Rowe, N., and Veglia, G. (2014) FLAMEnGO 2.0: an enhanced fuzzy logic algorithm for structure-based assignment of methyl group resonances, *J. Magn. Reson. 245*, 17-23.

(75) Tugarinov, V., Venditti, V., and Marius Clore, G. (2014) A NMR experiment for simultaneous correlations of valine and leucine/isoleucine methyls with carbonyl chemical shifts in proteins, *J. Biomol. NMR 58*, 1-8.

(76) Hu, W., Namanja, A. T., Wong, S., and Chen, Y. (2012) Selective editing of Val and Leu methyl groups in high molecular weight protein NMR, *J. Biomol. NMR 53*, 113-124.

(77) Zhang, W., and Liu, H. T. (2002) MAPK signal pathways in the regulation of cell proliferation in mammalian cells, *Cell Res. 12*, 9-18.

(78) Rose, B. A., Force, T., and Wang, Y. (2010) Mitogen-activated protein kinase signaling in the heart: angels versus demons in a heart-breaking tale, *Physiol. Rev. 90*, 1507-1546.

(79) Xiao, Y., Lee, T., Latham, M. P., Warner, L. R., Tanimoto, A., Pardi, A., and Ahn, N. G. (2014) Phosphorylation releases constraints to domain motion in ERK2, *Proc. Natl. Acad. Sci. U. S. A. 111*, 2506-2511.

(80) Francis, D. M., Rozycki, B., Tortajada, A., Hummer, G., Peti, W., and Page, R. (2011) Resting and active states of the ERK2:HePTP complex, *J. Am. Chem. Soc. 133*, 17138-17141.

(81) Lee, T., Hoofnagle, A. N., Resing, K. A., and Ahn, N. G. (2005) Hydrogen exchange solvent protection by an ATP analogue reveals conformational changes in ERK2 upon activation, *J. Mol. Biol. 353*, 600-612.

(82) Shapiro, P. S., Vaisberg, E., Hunt, A. J., Tolwinski, N. S., Whalen, A. M., McIntosh, J. R., and Ahn, N. G. (1998) Activation of the MKK/ERK pathway during somatic cell mitosis: direct interactions of active ERK with kinetochores and regulation of the mitotic 3F3/2 phosphoantigen, *J. Cell Biol. 142*, 1533-1545.

(83) Vranken, W. F., Boucher, W., Stevens, T. J., Fogh, R. H., Pajon, A., Llinas, M., Ulrich, E. L., Markley, J. L., Ionides, J., and Laue, E. D. (2005) The CCPN data model for NMR spectroscopy: development of a software pipeline, *Proteins 59*, 687-696.

(84) Zwahlen, C., Gardner, K. H., Sarma, S. P., Horita, D. A., Byrd, R. A., and Kay, L. E. (1998) An NMR experiment for measuring methyl-methyl NOEs in C-13-labeled proteins with high resolution, *J. Am. Chem. Soc. 120*, 7617-7625.

(85) Shaka, A. J., Lee, C. J., and Pines, A. (1988) Iterative Schemes for Bilinear Operators - Application to Spin Decoupling, *J. Magn. Reson. 77*, 274-293.

(86) Zhu, G. A., and Bax, A. (1992) 2-Dimensional Linear Prediction for Signals Truncated in Both Dimensions, *J. Magn. Reson. 98*, 192-199.

(87) Fesik, S. W., and Zuiderweg, E. R. P. (1988) Heteronuclear 3-Dimensional Nmr-Spectroscopy - a Strategy for the Simplification of Homonuclear Two-Dimensional Nmr-Spectra, *J. Magn. Reson. 78*, 588-593.

(88) Delaglio, F., Grzesiek, S., Vuister, G. W., Zhu, G., Pfeifer, J., and Bax, A. (1995) NMRPipe: a multidimensional spectral processing system based on UNIX pipes, *J. Biomol. NMR 6*, 277-293.

(89) Fraczkiewicz, R., and Braun, W. (1998) Exact and efficient analytical calculation of the accessible surface areas and their gradients for macromolecules, *J. Comput. Chem. 19*, 319-333.

(90) King, J. L., and Jukes, T. H. (1969) Non-Darwinian evolution, *Science 164*, 788-798.

(91) Ulrich, E. L., Akutsu, H., Doreleijers, J. F., Harano, Y., Ioannidis, Y. E., Lin, J., Livny, M., Mading, S., Maziuk, D., Miller, Z., Nakatani, E., Schulte, C. F., Tolmie, D. E., Kent Wenger, R., Yao, H., and Markley, J. L. (2008) BioMagResBank, *Nucleic Acids Res. 36*, D402-408.

(92) Motlagh, H. N., Wrabl, J. O., Li, J., and Hilser, V. J. (2014) The ensemble nature of allostery, *Nature 508*, 331-339.

(93) Baldwin, A. J., and Kay, L. E. (2009) NMR spectroscopy brings invisible protein states into focus, *Nat. Chem. Biol. 5*, 808-814.

(94) Tong, M., and Seeliger, M. A. (2015) Targeting conformational plasticity of protein kinases, *ACS Chem. Biol. 10*, 190-200.

(95) Sinha, K., Jen-Jacobson, L., and Rule, G. S. (2013) Divide and conquer is always best: sensitivity of methyl correlation experiments, *J. Biomol. NMR 56*, 331-335.

(96) Kainosho, M., Torizawa, T., Iwashita, Y., Terauchi, T., Mei Ono, A., and Guntert, P. (2006) Optimal isotope labelling for NMR protein structure determinations, *Nature 440*, 52-57.

(97) Neri, D., Szyperski, T., Otting, G., Senn, H., and Wuthrich, K. (1989) Stereospecific nuclear magnetic resonance assignments of the methyl groups of valine and leucine in the DNA-binding domain of the 434 repressor by biosynthetically directed fractional 13C labeling, *Biochemistry 28*, 7510-7516.

(98) Gelis, I., Bonvin, A. M., Keramisanou, D., Koukaki, M., Gouridis, G., Karamanou, S., Economou, A., and Kalodimos, C. G. (2007) Structural basis for signal-sequence recognition by the translocase motor SecA as determined by NMR, *Cell 131*, 756-769.

(99) Velyvis, A., Schachman, H. K., and Kay, L. E. (2009) Assignment of Ile, Leu, and Val methyl correlations in supra-molecular systems: an application to aspartate transcarbamoylase, *J. Am. Chem. Soc. 131*, 16534-16543.

(100) Stratmann, D., Guittet, E., and van Heijenoort, C. (2010) Robust structure-based resonance assignment for functional protein studies by NMR, *J. Biomol. NMR 46*, 157-173.

(101) Stratmann, D., van Heijenoort, C., and Guittet, E. (2009) NOEnet-Use of NOE networks for NMR resonance assignment of proteins with known 3D structure, *Bioinformatics 25*, 474-481.

(102) Crippen, G. M., Rousaki, A., Revington, M., Zhang, Y., and Zuiderweg, E. R. (2010) SAGA: rapid automatic mainchain NMR assignment for large proteins, *J. Biomol. NMR 46*, 281-298.

(103) MacRaild, C. A., and Norton, R. S. (2014) RASP: rapid and robust backbone chemical shift assignments from protein structure, *J. Biomol. NMR 58*, 155-163.

(104) Venditti, V., Fawzi, N. L., and Clore, G. M. (2011) Automated sequence- and stereo-specific assignment of methyl-labeled proteins by paramagnetic relaxation and methyl-methyl nuclear Overhauser enhancement spectroscopy, *J. Biomol. NMR 51*, 319-328.

(105) Jones, B. E., Rajagopal, P., and Klevit, R. E. (1997) Phosphorylation on histidine is accompanied by localized structural changes in the phosphocarrier protein, HPr from Bacillus subtilis, *Protein Sci. 6*, 2107-2119.

(106) Roskoski, R., Jr. (2012) ERK1/2 MAP kinases: structure, function, and regulation, *Pharmacol. Res. 66*, 105-143.

(107) Pearson, G., Robinson, F., Beers Gibson, T., Xu, B. E., Karandikar, M., Berman, K., and Cobb, M. H. (2001) Mitogen-activated protein (MAP) kinase pathways: regulation and physiological functions, *Endocr. Rev. 22*, 153-183.

(108) Hoofnagle, A. N., Stoner, J. W., Lee, T., Eaton, S. S., and Ahn, N. G. (2004) Phosphorylation-dependent changes in structure and dynamics in ERK2 detected by SDSL and EPR, *Biophys. J. 86*, 395-403.

(109) Hoofnagle, A. N., Resing, K. A., Goldsmith, E. J., and Ahn, N. G. (2001) Changes in protein conformational mobility upon activation of extracellular regulated protein kinase-2 as detected by hydrogen exchange, *Proc. Natl. Acad. Sci. U. S. A. 98*, 956-961.

(110) Smock, R. G., and Gierasch, L. M. (2009) Sending signals dynamically, *Science 324*, 198-203.

(111) Nagar, B., Hantschel, O., Young, M. A., Scheffzek, K., Veach, D., Bornmann, W., Clarkson, B., Superti-Furga, G., and Kuriyan, J. (2003) Structural basis for the autoinhibition of c-Abl tyrosine kinase, *Cell 112*, 859-871.

(112) Bhabha, G., Lee, J., Ekiert, D. C., Gam, J., Wilson, I. A., Dyson, H. J., Benkovic, S. J., and Wright, P. E. (2011) A dynamic knockout reveals that conformational fluctuations influence the chemical step of enzyme catalysis, *Science 332*, 234-238.

(113) Eisenmesser, E. Z., Millet, O., Labeikovsky, W., Korzhnev, D. M., Wolf-Watz, M., Bosco, D. A., Skalicky, J. J., Kay, L. E., and Kern, D. (2005) Intrinsic dynamics of an enzyme underlies catalysis, *Nature 438*, 117-121.

(114) Fraser, J. S., Clarkson, M. W., Degnan, S. C., Erion, R., Kern, D., and Alber, T. (2009) Hidden alternative structures of proline isomerase essential for catalysis, *Nature 462*, 669-673.

(115) Korzhnev, D. M., Kloiber, K., and Kay, L. E. (2004) Multiple-quantum relaxation dispersion NMR spectroscopy probing millisecond time-scale dynamics in proteins: theory and application, *J. Am. Chem. Soc. 126*, 7320-7329.

(116) Kupce, E., and Freeman, R. (1995) Adiabatic Pulses for Wide-Band Inversion and Broad-Band Decoupling, *J. Magn. Reson., Ser A 115*, 273-276.

(117) Skrynnikov, N. R., Mulder, F. A., Hon, B., Dahlquist, F. W., and Kay, L. E. (2001) Probing slow time scale dynamics at methyl-containing side chains in proteins by relaxation dispersion NMR measurements: application to methionine residues in a cavity mutant of T4 lysozyme, *J. Am. Chem. Soc. 123*, 4556-4566.

(118) Korzhnev, D. M., Salvatella, X., Vendruscolo, M., Di Nardo, A. A., Davidson, A. R., Dobson, C. M., and Kay, L. E. (2004) Low-populated folding intermediates of Fyn SH3 characterized by relaxation dispersion NMR, *Nature 430*, 586-590.

(119) Vallurupalli, P., Hansen, D. F., Stollar, E., Meirovitch, E., and Kay, L. E. (2007) Measurement of bond vector orientations in invisible excited states of proteins, *Proc. Natl. Acad. Sci. U. S. A. 104*, 18473-18477.

(120) Korzhnev, D. M., Mittermaier, A. K., and Kay, L. E. (2005) Cross-correlated spin relaxation effects in methyl 1H CPMG-based relaxation dispersion experiments: complications and a simple solution, *J. Biomol. NMR 31*, 337-342.

(121) Helgstrand, M., Hard, T., and Allard, P. (2000) Simulations of NMR pulse sequences during equilibrium and non-equilibrium chemical exchange, *J. Biomol. NMR 18*, 49-63.

(122) Loria, J. P., Rance, M., and Palmer, A. G., 3rd. (1999) A TROSY CPMG sequence for characterizing chemical exchange in large proteins, *J. Biomol. NMR 15*, 151-155.

(123) Chang, R. (2005) *Physical chemistry for the biosciences*, University Science, Sansalito, Calif.

(124) Khokhlatchev, A. V., Canagarajah, B., Wilsbacher, J., Robinson, M., Atkinson, M., Goldsmith, E., and Cobb, M. H. (1998) Phosphorylation of the MAP kinase ERK2 promotes its homodimerization and nuclear translocation, *Cell 93*, 605-615.

(125) Sinha, N., Kumar, S., and Nussinov, R. (2001) Interdomain interactions in hinge-bending transitions, *Structure 9*, 1165-1181.

(126) Robbins, D. J., Zhen, E., Owaki, H., Vanderbilt, C. A., Ebert, D., Geppert, T. D., and Cobb, M. H. (1993) Regulation and properties of extracellular signal-regulated protein kinases 1 and 2 in vitro, *J. Biol. Chem. 268*, 5097-5106.

(127) Akamine, P., Madhusudan, Wu, J., Xuong, N. H., Ten Eyck, L. F., and Taylor, S. S. (2003) Dynamic features of cAMP-dependent protein kinase revealed by apoenzyme crystal structure, *J. Mol. Biol. 327*, 159-171.

(128) Masterson, L. R., Shi, L., Metcalfe, E., Gao, J., Taylor, S. S., and Veglia, G. (2011) Dynamically committed, uncommitted, and quenched states encoded in protein kinase A revealed by NMR spectroscopy, *Proc. Natl. Acad. Sci. U. S. A. 108*, 6969-6974.

(129) Masterson, L. R., Cheng, C., Yu, T., Tonelli, M., Kornev, A., Taylor, S. S., and Veglia, G. (2010) Dynamics connect substrate recognition to catalysis in protein kinase A, *Nat. Chem. Biol. 6*, 821-828.

(130) Boehr, D. D., McElheny, D., Dyson, H. J., and Wright, P. E. (2010) Millisecond timescale fluctuations in dihydrofolate reductase are exquisitely sensitive to the bound ligands, *Proc. Natl. Acad. Sci. U. S. A. 107*, 1373-1378.

(131) Gardino, A. K., Villali, J., Kivenson, A., Lei, M., Liu, C. F., Steindel, P., Eisenmesser, E. Z., Labeikovsky, W., Wolf-Watz, M., Clarkson, M. W., and Kern, D. (2009) Transient non-native hydrogen bonds promote activation of a signaling protein, *Cell 139*, 1109-1118.

(132) Chen, H., Ma, J., Li, W., Eliseenkova, A. V., Xu, C., Neubert, T. A., Miller, W. T., and Mohammadi, M. (2007) A molecular brake in the kinase hinge region regulates the activity of receptor tyrosine kinases, *Mol. Cell 27*, 717-730.

(133) Deindl, S., Kadlecek, T. A., Brdicka, T., Cao, X., Weiss, A., and Kuriyan, J. (2007) Structural basis for the inhibition of tyrosine kinase activity of ZAP-70, *Cell 129*, 735-746.

(134) Shan, Y., Eastwood, M. P., Zhang, X., Kim, E. T., Arkhipov, A., Dror, R. O., Jumper, J., Kuriyan, J., and Shaw, D. E. (2012) Oncogenic mutations counteract intrinsic disorder in the EGFR kinase and promote receptor dimerization, *Cell 149*, 860-870.

(135) Shan, Y., Arkhipov, A., Kim, E. T., Pan, A. C., and Shaw, D. E. (2013) Transitions to catalytically inactive conformations in EGFR kinase, *Proc. Natl. Acad. Sci. U. S. A. 110*, 7270-7275.

(136) Treisman, R. (1996) Regulation of transcription by MAP kinase cascades, *Curr. Opin. Cell Biol. 8*, 205-215.

(137) Cohen-Armon, M., Visochek, L., Rozensal, D., Kalal, A., Geistrikh, I., Klein, R., Bendetz-Nezer, S., Yao, Z., and Seger, R. (2007) DNA-independent PARP-1 activation by phosphorylated ERK2 increases Elk1 activity: a link to histone acetylation, *Mol. Cell 25*, 297-308.

(138) Sharrocks, A. D., Yang, S. H., and Galanis, A. (2000) Docking domains and substrate-specificity determination for MAP kinases, *Trends Biochem. Sci 25*, 448-453.

(139) Kallunki, T., Su, B., Tsigelny, I., Sluss, H. K., Derijard, B., Moore, G., Davis, R., and Karin, M. (1994) Jnk2 Contains a Specificity-Determining Region Responsible for Efficient C-Jun Binding and Phosphorylation, *Genes Dev. 8*, 2996-3007.

(140) Yasuda, J., Whitmarsh, A. J., Cavanagh, J., Sharma, M., and Davis, R. J. (1999) The JIP group of mitogen-activated protein kinase scaffold proteins, *Mol. Cell. Biol. 19*, 7245-7254.

(141) Pulido, R., Zuniga, A., and Ullrich, A. (1998) PTP-SL and STEP protein tyrosine phosphatases regulate the activation of the extracellular signal-regulated kinases ERK1 and ERK2 by association through a kinase interaction motif, *EMBO J. 17*, 7337-7350.

(142) Zuniga, A., Torres, J., Ubeda, J., and Pulido, R. (1999) Interaction of mitogen-activated protein kinases with the kinase interaction motif of the tyrosine phosphatase PTP-SL provides substrate specificity and retains ERK2 in the cytoplasm, *J. Biol. Chem. 274*, 21900-21907.

(143) Bardwell, L., and Thorner, J. (1996) A conserved motif at the amino termini of MEKs might mediate high-affinity interaction with the cognate MAPKs, *Trends Biochem. Sci 21*, 373-374.

(144) Akella, R., Moon, T. M., and Goldsmith, E. J. (2008) Unique MAP Kinase binding sites, *Biochim. Biophys. Acta 1784*, 48-55.

(145) Burkhard, K. A., Chen, F., and Shapiro, P. (2011) Quantitative analysis of ERK2 interactions with substrate proteins: roles for kinase docking domains and activity in determining binding affinity, *J. Biol. Chem. 286*, 2477-2485.

(146) Callaway, K. A., Rainey, M. A., Riggs, A. F., Abramczyk, O., and Dalby, K. N. (2006) Properties and regulation of a transiently assembled ERK2.Ets-1 signaling complex, *Biochemistry 45*, 13719-13733.

(147) Callaway, K., Waas, W. F., Rainey, M. A., Ren, P., and Dalby, K. N. (2010) Phosphorylation of the transcription factor Ets-1 by ERK2: rapid dissociation of ADP and phospho-Ets-1, *Biochemistry 49*, 3619-3630.

(148) Mace, P. D., Wallez, Y., Egger, M. F., Dobaczewska, M. K., Robinson, H., Pasquale, E. B., and Riedl, S. J. (2013) Structure of ERK2 bound to PEA-15 reveals a mechanism for rapid release of activated MAPK, *Nat Commun 4*, 1681.

(149) Waas, W. F., Rainey, M. A., Szafranska, A. E., and Dalby, K. N. (2003) Two rate-limiting steps in the kinetic mechanism of the serine/threonine specific protein kinase ERK2: a case of fast phosphorylation followed by fast product release, *Biochemistry 42*, 12273-12286.

(150) Wang, Z., Canagarajah, B. J., Boehm, J. C., Kassisa, S., Cobb, M. H., Young, P. R., Abdel-Meguid, S., Adams, J. L., and Goldsmith, E. J. (1998) Structural basis of inhibitor selectivity in MAP kinases, *Structure 6*, 1117-1128.

(151) Ohori, M., Kinoshita, T., Okubo, M., Sato, K., Yamazaki, A., Arakawa, H., Nishimura, S., Inamura, N., Nakajima, H., Neya, M., Miyake, H., and Fujii, T. (2005) Identification of a selective ERK inhibitor and structural determination of the inhibitor-ERK2 complex, *Biochem. Biophys. Res. Commun. 336*, 357-363.

(152) Aronov, A. M., Baker, C., Bemis, G. W., Cao, J., Chen, G., Ford, P. J., Germann, U. A., Green, J., Hale, M. R., Jacobs, M., Janetka, J. W., Maltais, F., Martinez-Botella, G., Namchuk, M. N., Straub, J., Tang, Q., and Xie, X. (2007) Flipped out: structure-guided design of selective pyrazolylpyrrole ERK inhibitors, *J. Med. Chem. 50*, 1280-1287.

(153) Aronov, A. M., Tang, Q., Martinez-Botella, G., Bemis, G. W., Cao, J., Chen, G., Ewing, N. P., Ford, P. J., Germann, U. A., Green, J., Hale, M. R., Jacobs, M., Janetka, J. W., Maltais, F., Markland, W., Namchuk, M. N., Nanthakumar, S., Poondru, S., Straub, J., ter Haar, E., and Xie, X. (2009) Structure-guided design of potent and selective pyrimidylpyrrole inhibitors of extracellular signal-regulated kinase (ERK) using conformational control, *J. Med. Chem. 52*, 6362-6368.

(154) Robarge, K., Schwarz, J., Blake, J., Burkard, M., Chan, J., Chen, H. F., Chou, K. J., Diaz, D., Gaudino, J., Gould, S., Grina, J., Xin, L. H., Liu, L. C., Martinson, M., Moreno, D. A., Orr, C., Pacheco, P., Qin, A., Rasor, K., Ren, L., Shahidi-Latham, S., Stults, J., Sullivan, F., Wang, W. R., Yin, P., Zhou, A. H., Belvin, M., Merchant, M., and Moffat, J. G. (2014) Discovery of GDC-0994, a potent and selective ERK1/2 inhibitor in early clinical development, *Cancer Res. 74*.

(155) Prowse, C. N., Deal, M. S., and Lew, J. (2001) The complete pathway for catalytic activation of the mitogen-activated protein kinase, ERK2, *J. Biol. Chem. 276*, 40817-40823.

(156) Goetz, E. M., Ghandi, M., Treacy, D. J., Wagle, N., and Garraway, L. A. (2014) ERK mutations confer resistance to mitogen-activated protein kinase pathway inhibitors, *Cancer Res. 74*, 7079-7089.

(157) Zhao, Z., Wu, H., Wang, L., Liu, Y., Knapp, S., Liu, Q., and Gray, N. S. (2014) Exploration of type II binding mode: A privileged approach for kinase inhibitor focused drug discovery?, *ACS Chem. Biol. 9*, 1230-1241.

(158) Lovering, F., McDonald, J., Whitlock, G. A., Glossop, P. A., Phillips, C., Bent, A., Sabnis, Y., Ryan, M., Fitz, L., Lee, J., Chang, J. S., Han, S., Kurumbail, R., and Thorarensen, A. (2012) Identification of type-II inhibitors using kinase structures, *Chem. Biol. Drug Des. 80*, 657-664.

(159) Wood, E. R., Truesdale, A. T., McDonald, O. B., Yuan, D., Hassell, A., Dickerson, S. H., Ellis, B., Pennisi, C., Horne, E., Lackey, K., Alligood, K. J., Rusnak, D. W., Gilmer, T. M., and Shewchuk, L. (2004) A unique structure for epidermal growth factor receptor bound to GW572016 (Lapatinib): relationships among protein conformation, inhibitor off-rate, and receptor activity in tumor cells, *Cancer Res. 64*, 6652-6659.

(160) Fernandes, N., Bailey, D. E., VanVranken, D. L., and Allbritton, N. L. (2007) Use of docking peptides to design modular substrates with high efficiency for mitogen-activated protein kinase extracellular signal-regulated kinase, *ACS Chem. Biol. 2*, 665-673.

(161) Lee, S., Warthaka, M., Yan, C., Kaoud, T. S., Ren, P., and Dalby, K. N. (2011) Examining docking interactions on ERK2 with modular peptide substrates, *Biochemistry 50*, 9500-9510.

(162) Cavanagh, J., Fairbrother, W. J., Palmer, A. G., Rance, M., and Skelton, N. J. (2007) Protein NMR Spectroscopy: Principles and Practice, 2nd Edition, *Protein Nmr Spectroscopy: Principles and Practice, 2nd Edition*, 1-888.

(163) Garai, A., Zeke, A., Gogl, G., Toro, I., Fordos, F., Blankenburg, H., Barkai, T., Varga, J., Alexa, A., Emig, D., Albrecht, M., and Remenyi, A. (2012) Specificity of linear motifs that bind to a common mitogen-activated protein kinase docking groove, *Sci Signal 5*, ra74.

(164) Zhou, T., Sun, L., Humphreys, J., and Goldsmith, E. J. (2006) Docking interactions induce exposure of activation loop in the MAP kinase ERK2, *Structure 14*, 1011-1019.

(165) Kovrigin, E. L. (2012) NMR line shapes and multi-state binding equilibria, *J. Biomol. NMR 53*, 257-270.

(166) Suzuki, Y., Shimizu, T., Morii, H., and Tanokura, M. (1997) Hydrolysis of AMPPNP by the motor domain of ncd, a kinesin-related protein, *FEBS Lett. 409*, 29-32.

(167) Shriver, J. W., and Sykes, B. D. (1981) Phosphorus-31 nuclear magnetic resonance evidence for two conformations of myosin subfragment-1.nucleotide complexes, *Biochemistry 20*, 2004-2012.

(168) Mascaros, P. A., Bazzicalupi, C., Bianchi, A., Giorgi, C., Valero, M. D., Garzon, R. L., Salido, M. L., and Valtancoli, B. (2011) Molecular recognition of ADP over ATP in aqueous solution by a polyammonium receptor containing a pyrimidine residue, *Chem. Commun. (Camb.) 47*, 2814-2816.

(169) Francis, D. M., Rozycki, B., Koveal, D., Hummer, G., Page, R., and Peti, W. (2011) Structural basis of p38alpha regulation by hematopoietic tyrosine phosphatase, *Nat. Chem. Biol. 7*, 916-924.

(170) Piserchio, A., Ramakrishan, V., Wang, H., Kaoud, T. S., Arshava, B., Dutta, K., Dalby, K. N., and Ghose, R. (2015) Structural and Dynamic Features of F-recruitment Site Driven Substrate Phosphorylation by ERK2, *Sci. Rep. 5*, 11127.

(171) Sours, K. M., Xiao, Y., and Ahn, N. G. (2014) Extracellular-regulated kinase 2 is activated by the enhancement of hinge flexibility, *J. Mol. Biol. 426*, 1925-1935.

(172) Tokunaga, Y., Takeuchi, K., Takahashi, H., and Shimada, I. (2014) Allosteric enhancement of MAP kinase p38alpha's activity and substrate selectivity by docking interactions, *Nat. Struct. Mol. Biol. 21*, 704-711.

(173) Hari, S. B., Merritt, E. A., and Maly, D. J. (2013) Sequence determinants of a specific inactive protein kinase conformation, *Chem. Biol. 20*, 806-815.

(174) Chaikuad, A., Tacconi, E. M. C., Zimmer, J., Liang, Y. K., Gray, N. S., Tarsounas, M., and Knapp, S. (2014) A unique inhibitor binding site in ERK1/2 is associated with slow binding kinetics, *Nat. Chem. Biol. 10*, 853-+.

(175) Vogtherr, M., Saxena, K., Hoelder, S., Grimme, S., Betz, M., Schieborr, U., Pescatore, B., Robin, M., Delarbre, L., Langer, T., Wendt, K. U., and Schwalbe, H. (2006) NMR characterization of kinase p38 dynamics in free and ligand-bound forms, *Angew Chem Int Edit 45*, 993-997.

(176) Cheng, H. C., Kemp, B. E., Pearson, R. B., Smith, A. J., Misconi, L., Van Patten, S. M., and Walsh, D. A. (1986) A potent synthetic peptide inhibitor of the cAMP-dependent protein kinase, *J. Biol. Chem. 261*, 989-992.

(177) Iwata, H., Imamura, S., Hori, A., Hixon, M. S., Kimura, H., and Miki, H. (2011) Biochemical characterization of TAK-593, a novel VEGFR/PDGFR inhibitor with a two-step slow binding mechanism, *Biochemistry 50*, 738-751.

(178) Iwata, H., Imamura, S., Hori, A., Hixon, M. S., Kimura, H., and Miki, H. (2011) Biochemical characterization of a novel type-II VEGFR2 kinase inhibitor: comparison of binding to non-phosphorylated and phosphorylated VEGFR2, *Bioorg. Med. Chem. 19*, 5342-5351.

(179) Millan, D. S., Bunnage, M. E., Burrows, J. L., Butcher, K. J., Dodd, P. G., Evans, T. J., Fairman, D. A., Hughes, S. J., Kilty, I. C., Lemaitre, A., Lewthwaite, R. A., Mahnke, A., Mathias, J. P., Philip, J., Smith, R. T., Stefaniak, M. H., Yeadon, M., and Phillips, C. (2011)

Design and synthesis of inhaled p38 inhibitors for the treatment of chronic obstructive pulmonary disease, *J. Med. Chem. 54*, 7797-7814.

(180) Yan, S. B., Peek, V. L., Ajamie, R., Buchanan, S. G., Graff, J. R., Heidler, S. A., Hui, Y. H., Huss, K. L., Konicek, B. W., Manro, J. R., Shih, C., Stewart, J. A., Stewart, T. R., Stout, S. L., Uhlik, M. T., Um, S. L., Wang, Y., Wu, W. J., Yan, L., Yang, W. J., Zhong, B. Y., and Walgren, R. A. (2013) LY2801653 is an orally bioavailable multi-kinase inhibitor with potent activity against MET, MST1R, and other oncoproteins, and displays anti-tumor activities in mouse xenograft models, *Invest. New Drugs 31*, 833-844.

(181) Lesuisse, D., Mauger, J., Nemecek, C., Maignan, S., Boiziau, J., Harlow, G., Hittinger, A., Ruf, S., Strobel, H., Nair, A., Ritter, K., Malleron, J. L., Dagallier, A., El-Ahmad, Y., Guilloteau, J. P., Guizani, H., Bouchard, H., and Venot, C. (2011) Discovery of the first non-ATP competitive IGF-1R kinase inhibitors: advantages in comparison with competitive inhibitors, *Bioorg. Med. Chem. Lett. 21*, 2224-2228.

(182) Lovering, F., McDonald, J., Whitlock, G. A., Glossop, P. A., Phillips, C., Bent, A., Sabnis, Y., Ryan, M., Fitz, L., Lee, J., Chang, J. S., Han, S., Kurumbail, R., and Thorarensen, A. (2012) Identification of Type-II Inhibitors Using Kinase Structures, *Chemical biology & drug design 80*, 657-664.

(183) Hu, Y., Furtmann, N., and Bajorath, J. (2015) Current compound coverage of the kinome, *J. Med. Chem. 58*, 30-40.

(184) Schloss, J. V. (1988) Significance of Slow-Binding Enzyme-Inhibition and Its Relationship to Reaction-Intermediate Analogs, *Acc. Chem. Res. 21*, 348-353.

(185) Isaacson, R. L., Simpson, P. J., Liu, M., Cota, E., Zhang, X., Freemont, P., and Matthews, S. (2007) A new labeling method for methyl transverse relaxation-optimized spectroscopy NMR spectra of alanine residues, *J. Am. Chem. Soc. 129*, 15428-15429.

(186) Gans, P., Hamelin, O., Sounier, R., Ayala, I., Dura, M. A., Amero, C. D., Noirclerc-Savoye, M., Franzetti, B., Plevin, M. J., and Boisbouvier, J. (2010) Stereospecific isotopic labeling of methyl groups for NMR spectroscopic studies of high-molecular-weight proteins, *Angew. Chem. Int. Ed. Engl. 49*, 1958-1962.

(187) Miyanoiri, Y., Takeda, M., Okuma, K., Ono, A. M., Terauchi, T., and Kainosho, M. (2013) Differential isotope-labeling for Leu and Val residues in a protein by E. coli cellular expression using stereo-specifically methyl labeled amino acids, *J. Biomol. NMR 57*, 237-249.

(188) Prowse, C. N., Hagopian, J. C., Cobb, M. H., Ahn, N. G., and Lew, J. (2000) Catalytic reaction pathway for the mitogen-activated protein kinase ERK2, *Biochemistry 39*, 6258-6266.

(189) Lee, J., Yennawar, N. H., Gam, J., and Benkovic, S. J. (2010) Kinetic and structural characterization of dihydrofolate reductase from Streptococcus pneumoniae, *Biochemistry 49*, 195-206.

(190) Rajagopalan, P. T., Zhang, Z., McCourt, L., Dwyer, M., Benkovic, S. J., and Hammes, G. G. (2002) Interaction of dihydrofolate reductase with methotrexate: ensemble and single-molecule kinetics, *Proc. Natl. Acad. Sci. U. S. A. 99*, 13481-13486.

Appendix 1. Limited Backbone Assignments of ERK2

A1.1. Introduction

Solution insights of the MAP kinase, extracellular regulated kinase-2 (ERK2), using NMR is essential for understanding its regulation and dynamics. However, its relatively large size (42 kDa) results in fast relaxation of the NMR signal, and thus it is difficult to obtain backbone assignments through the standard triple resonance experiments. Partial (~50%) backbone assignments for ERK2 were published by Ghose and co-workers in 2011.[59] However, the differences in solvent conditions may result in inaccuracies, if their assignments were to be directly transferred to ours. Here, I report auxiliary experiments that I and my predecessors performed in order to achieve a limited number of independent backbone assignments in ERK2. These validate and/or expand the existing backbone assignments made by Ghose et al.[59]

A1.2. Materials and Methods

A1.2.1.2D ^{15}N-TROSY-HSQC Experiments for ERK2 and Mutants

A series of 2D ^{15}N-TROSY-HSQC experiments were collected on the 800 MHz spectrometer on ILV methyl-protonated, U-[^{2}H,^{15}N] 0P-ERK2, its mutants and 2P-ERK2 in 95% H_2O, which were the identical protein preparations described in Chapter 2. These ^{15}N-HSQC experiments used a "gNhsqc.c" pulse sequence to correlate the ^{15}N amide with the attached proton (NH) of residue i, using J coupling constant between amide and proton of 93 Hz. A TROSY option was applied for this experiment. The ^{1}H carrier was placed at H_2O (4.7 ppm) and the ^{15}N carrier was placed at 120 ppm. The spectra contained 2048 and 64 complex points over sweep widths of 11261.3 and 2950.1 Hz in the ^{1}H and ^{15}N dimensions. For the samples with concentrations of 0.3-0.4 mM, a total of 16 transients were usually acquired with a delay time (d1) of 1.4 s, leading to 1 h of acquisition time. The flag f1180 was set to 'y' so that t_1 starts at half dwell-time, and later during spectral processing resulted a (-90,

180) phasing in t_1 (^{15}N) dimension. Table A1.2 lists representative filenames and experimental parameters.

Table A1.1. 2D ^{15}N-TROSY-HSQC Experiment Filenames, Parameters and Conditions.

Filename[a]	Sample	np	ni	sw	sw1	nt	d1
0pERK2_smp032910_25C_hNhsqc_012411.fid[b]	0P-ERK2	2048	112	12019.2	2950.1	16	2
0P_ERK2_smp101611_25C_gNhsqc_101611.fid[c]	0P-ERK2	2048	64	11261.3	2950.1	16	1.3
0pERK2_H2O_03302011.fid[d]	0P-ERK2	2048	112	12019.2	2950.1	16	2
2pERK2_smp021910_25C_hNhsqc_012411.fid[b]	2P-ERK2	2048	112	12019.2	2950.1	16	2
0P-ERK2_I101A_gNhsqc_022311.fid[e]	I101A	2048	160	12019.2	2950.1	16	2
0P-ERK2_L105A_15NgNhsqc_022211.fid[e]	L105A	2048	160	12019.2	2950.1	16	2
gNhsqctrosy_0P-ERK2_L110A_ILV_021811.fid[e]	L110A	2048	112	12019.2	2950.1	16	2
gNhsqc_ERK2L113A_060710.fid[e]	L113A	2048	112	12019.2	2950.1	32	2
0P-ERK2-I124A_gNhsqc_ILV_021711.fid[e]	I124A	2048	112	12019.2	2950.1	16	2
gNhsqc_13cILV_ERK2I196A_060410.fid[e]	I196A	2048	112	12019.2	2950.1	32	2
gNhsqc_ERK2_L238A_060510.fid[e]	I238A	2048	112	12019.2	2950.1	32	2

[a] All these experiments were performed on the 800 MHz spectrometer at 25 °C.
[b] Data directories in /yao/data/ERK2_2011/.
[c] Data directories in /yao/data/ERK2_2011/0P-ERK2_smp101611_H2O/.
[d] Data directories in /yao/data/ERK2_2011/0pERK2_100D2O_033111/.
[e] Data directories in /yao/data/0p_ERK2_mutants/. Then go to the data directory for each mutant.

A1.2.2.3D-HNCA Experiment

A 3D-HNCA experiment was collected at 25 °C using the 800 MHz spectrometer on an ILV methyl-protonated, U-[^2H,^{15}N,^{13}C]-labeled 0P-ERK2 sample in NMR buffer in H_2O as described in Chapter 2. The HNCA experiment utilized a pulse sequence "ghn_ca.c" to correlate Cα of residue i with N(i), NH(i) and N(i+1), NH(i+1). A TROSY option was applied for this experiment. The ^1H carrier was placed at H_2O (4.7 ppm). The ^{13}C carrier was placed on 56 ppm, and the ^{15}N carrier was placed on 120 ppm. The spectra contained 2048, 48 and 40 complex points over sweep widths of 11261.3, 6028.3 and 2950.1 Hz in the ^1H, ^{13}C and ^{15}N dimensions. A total of 16 transients were acquired with a delay time (d1) of 1.7 s, leading to 64 hours of acquisition time. The flag f1180 was set to 'n' so that t_1 starts at zero dwell-time, and later during spectral processing resulted a (0, 0) phasing in t_1 (^{13}C) dimension. The flag f2180 was set to 'y' so that t_2 starts at half dwell-time, and later during spectral processing resulted a (-90, 180) phasing in t_2 (^{15}N) dimension. Time-domain data in the ^1H dimension were apodized by a cosine window function and zero-filled prior to Fourier transformation.

The indirect dimensions were also apodized by a cosine window function and zero-filled prior to Fourier transformation. Further visualization and analysis of the spectra was performed using the program CcpNmr Analysis[83]. Table A1.2 lists the filenames and experimental parameters.

A1.2.3. 3D-HNCO Experiment

A 3D-HNCO experiment was collected by Dr. Lisa Warner at 25 °C using the 600 MHz spectrometer on a U-[^{2}H,^{15}N,^{13}C]-labeled 0P-ERK2 sample in NMR buffer in H_2O. The HNCO experiment utilized a pulse sequence "ghn_co.c" to correlate CO of residue i with N(i+1) and NH(i+1). A TROSY option was applied for this experiment. The ^{1}H carrier was placed at H_2O (4.7 ppm). The ^{13}C carrier was placed on 174 ppm, and the ^{15}N carrier was placed on 120 ppm. The spectra contained 2048, 48 and 40 complex points over sweep widths of 11990.4 (sw, sweep width in t_3), 2000 (sw1, sweep width in t_1) and 1944.3 (sw2, sweep width in t_2) Hz in the ^{1}H, ^{13}C and ^{15}N dimensions. A total of 16 transients were acquired with a delay time (d1) of 1.5 s, leading to 64 hours of acquisition time. The flag f1180 was set to 'n' so that t_1 starts at zero dwell-time, and later during spectral processing resulted a (0, 0) phasing in t_1 (^{13}C) dimension. The flag f2180 was set to 'y' so that t_2 starts at half dwell-time, and later during spectral processing resulted a (-90, 180) phasing in t_2 (^{15}N) dimension. Time-domain data in the ^{1}H dimension were apodized by a squared cosine window function and zero-filled prior to Fourier transformation. The indirect dimensions were also apodized by a cosine window function and zero-filled prior to Fourier transformation. Further visualization and analysis of the spectra was performed using the program CcpNmr Analysis[83]. Table A1.2 lists the filenames and experimental parameters.

Table A1.2. Backbone Assignments Relevant Filenames, Parameters and Conditions.

Filename[a]	Type	B_0	sequence	np	ni	ni2
0P_ERK2_smp101611_25C_3D_no2Hdec_ghnca_112111.fid[a]	HNCA	800	ghn_ca.c	2048	48	40
ghnco_f1f2f3_2H15N13C_ERK2_050310.fid[b]	HNCO	600	ghn_co.c	2048	55	39

B_0 – magnetic field strength
np – number of complex points in t_3
ni – number of complex points in t_1

ni2 − number of complex points in t_2
[a] Data directories in /yao/data/ERK2_2011/0P-ERK2_smp101611_H2O/.
[b] Data directories in /yao/data/LISA/2H13C15NERK033010_Lisa_more/600/.

A1.2.4.2D Experiments for Selective Labeled ERK2

A series of 2D ^{15}N-HSQC experiments were collected on the 800 MHz spectrometer on residue-specific ^{15}NH labeled ERK2 samples by Dr. Michael Latham, including Ile, Leu, Phe, Tyr and Ala. He also collected a series of 2D HN(CO) experiments on U-[^{2}H,^{15}N]-labeled, and residue-specific ^{13}CO-labeled ERK2 samples on the 800 MHz spectrometer, including Leu, Val, and Tyr. These experiments were well documented in his Thesis. Here, no new experiments were performed, but these experiments were re-analyzed in a combinatorial manner as described below.

A1.3. Strategy and Results

To make independent and confident backbone assignments, the first step is to identify the residue type of amides on a ^{15}N TROSY-HSQC of ERK2 (Figure A1.1). This identification included three aspects: (1) Gly/Thr were identified from other residues by their unique amide chemical shifts, here a range between 98-105 ppm was used as cutoffs; (2) Gly is distinguished from Thr by their upfield Cα chemical shifts, here residues with Cα chemical shifts between 41-49 ppm were identified as Gly; (3) 2D ^{15}N TROSY-HSQC spectra of selectively ^{1}H, ^{15}N labeled amides of Ile, Leu, Phe, Tyr, and Ala were collected by Dr. Michael Latham. These spectra only show amide cross peaks for the residues that are ^{15}NH labeled. Thus, residue types of these selectively labeled amides are encoded in such spectra. 2D HN(CO) spectra of selectively labeled carbonyls ($^{14}N_{i-1}H$-$^{13}C_{i-1}O$-$^{15}N_iH$) of Leu, Val and Tyr were were collected by Dr. Michael Latham. These spectra only show amide crosspeaks for the residue (i) immediately after the ^{13}CO-labeled residue (i-1). Thus, residue types of the labeled carbonyls can be identified from these 2D HN(CO) spectra.

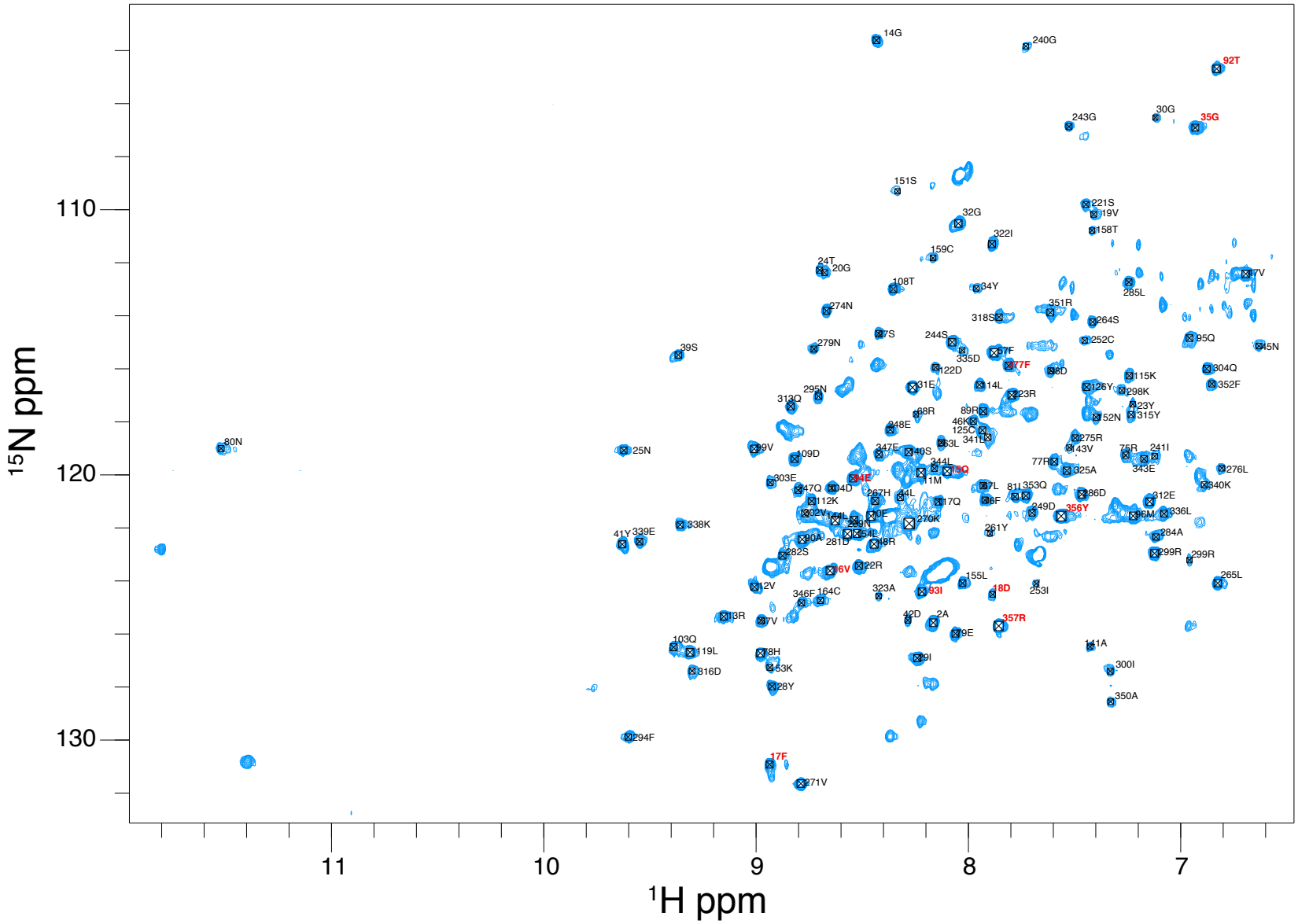

Figure A1.1. A representative 2D ^{15}N-TROSY-HSQC spectrum of 0P-ERK2.
This spectrum was collected using the same sample as for the 3D HNCA experiments. The "pre-assignments" transferred from Ghose's backbone assignments were labeled in black, with residue number and type. The confident assignments that we made were labeled in red.

The second step is to search for sequential amides. This searching process was performed using two methods: (1) By overlapping the ^{15}N TROSY-HSQC spectra of an selectively labeled amide and HN(CO) spectra of selectively labeled carbonyls; an amide peak that is observed in both an amide and an carbonyl labeling spectra reflects specific amino acid combinations. For example, if an amide peak is observed in both ^{15}N TROSY-HSQC spectra of selectively labeled Phe-NH and HN(CO) spectra of selectively labeled Val-CO, it indicates a "VF" combination in the sequence. Because this combination is unique in the sequence of ERK2, it can be confidently assigned to V16CO-F17NH (Figure A1.2). (2) Looking for matching Cα to identify sequential residues from HNCA. This yields high ambiguity because of the severe spectral overlap in the Cα region. Thus, some pre-assignments were included to facilitate this matching process. A total of 139 amide assignments published by Ghose and co-workers (BMRB Entry: 17748) were directly transferred to the nearest amides on our ^{15}N-HSQC spectra to yield "pre-assignments". For each of the transferred amide assignments for residue (i), its Cα, and optimally the Cα of residue (i-1) is identified from HNCA spectra. If the (i-1) Cα of a pre-assigned residue (i) matches the pre-assigned residue (i-1), then the two assignments were connected. The connectivities that included at least 3 residues were plotted in Figure A1.3 and Figure A1.4. All the pre-assignments were recorded in Table A1.3. From the analysis, 57 amides showed residue i or (i-1) residue-type that were consistent with the pre-assignments; and out of these 12 could be confidently assigned (Table A1.3).

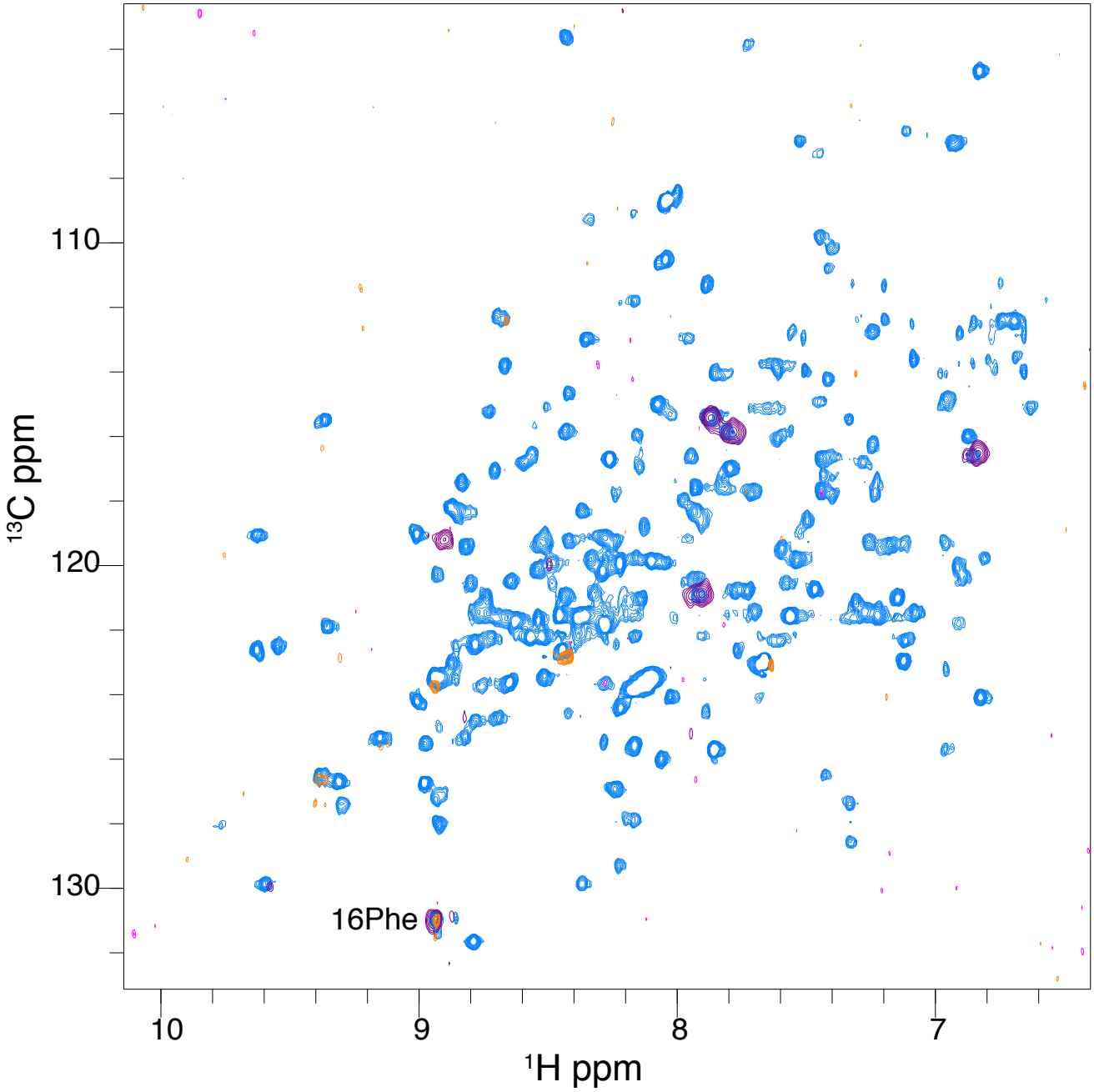

Figure A1.2. The amide assignment of Phe16. The ^{15}N-HSQC spectrum of 0P-ERK2 is shown in blue. The ^{15}N-HSQC spectrum of the Phe-NH selectively labeled ERK2 sample is shown in purple. The HN(CO) spectrum of Val-CO selectively labeled ERK2 sample is shown in orange. The peak where all three spectra showed overlap was assigned to Phe16.

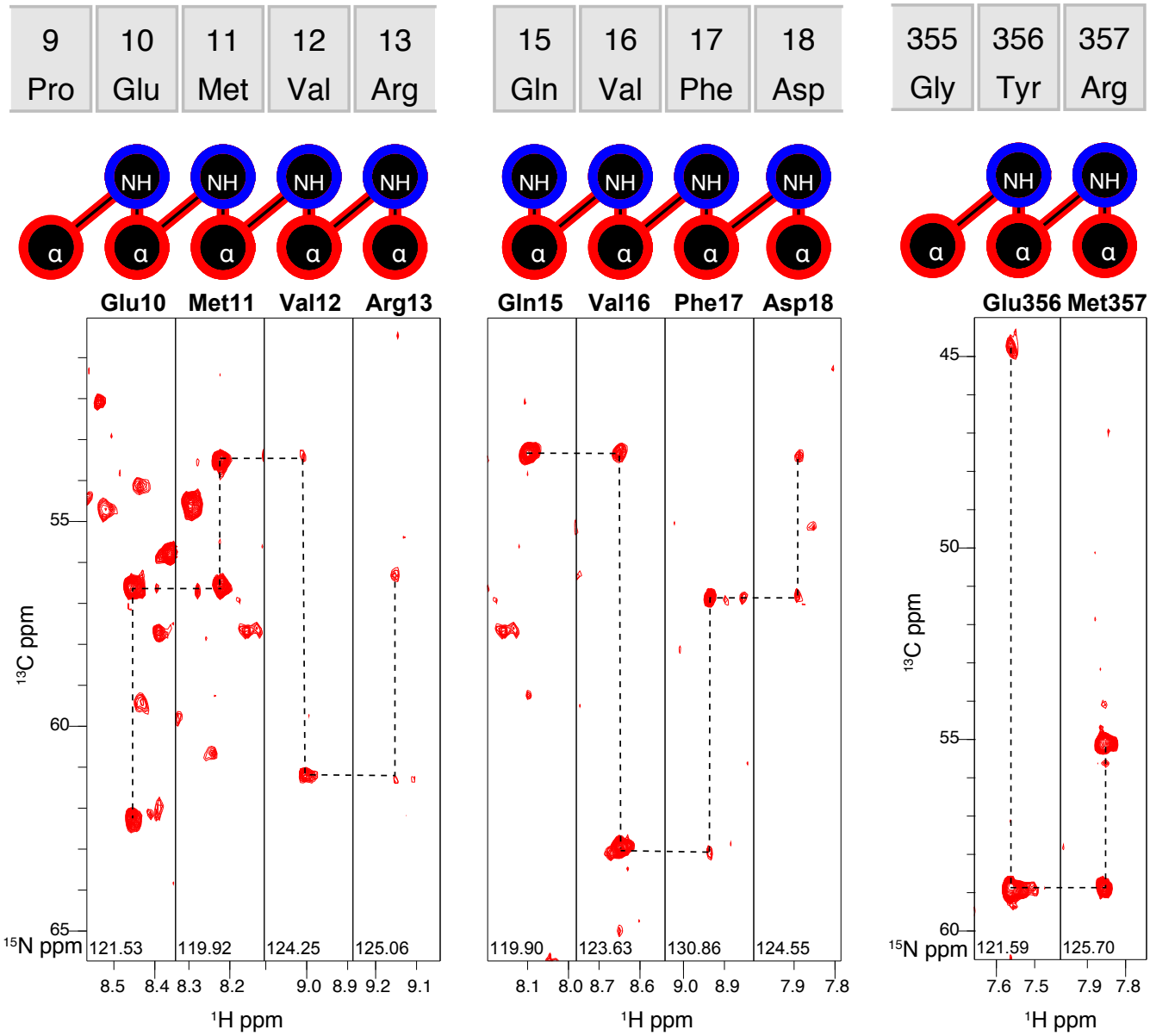

Figure A1.3. HNCA connectivities of residue number 9-13, 15-18 and 355-357.
The resonances for the Cα of residue (i-1) and residue i are observed from the same HNCA strip plot for the amide of residue i. These two Cα resonances are connected with vertical dashes, and the Cα resonances of residue i and of residue i+1 are connected with horizontal dashes.

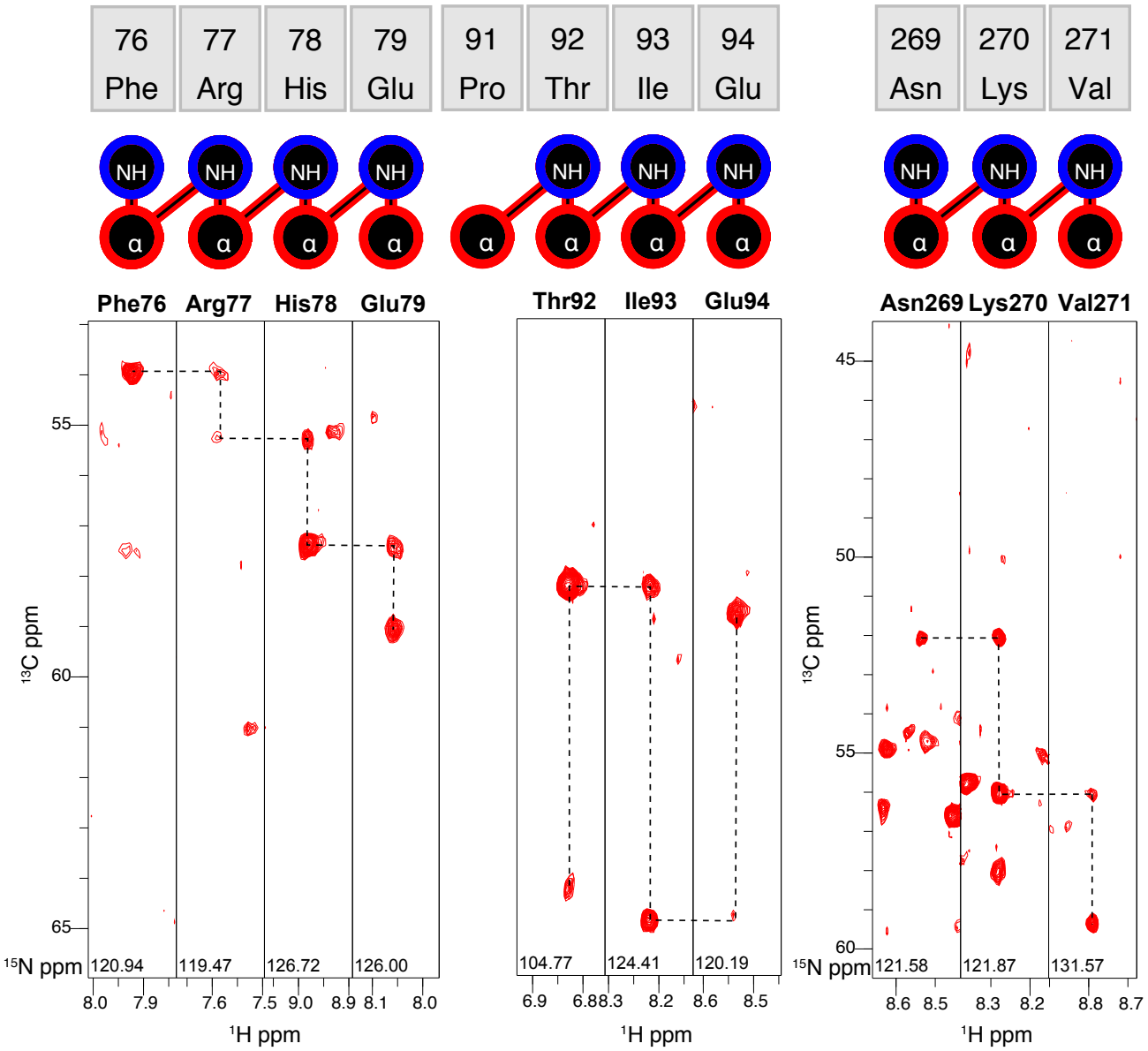

Figure A1.4. HNCA connectivities of residue number 76-79, 91-94 and 269-271.
The resonances for the Cα of residue (i-1) and residue i are observed from the same HNCA strip plot for the amide of residue i. These two Cα resonances are connected with vertical dashes, and the Cα resonances of residue i and of residue i+1 are connected with horizontal dashes.

Table A1.3. Limited backbone assignment for 0P-ERK2.

Res ID	Res Type	Atom Type	Chemical shift	Notes/Clues	Conclusion
2	Ala	N	125.58	AlaNH	Consistent
2	Ala	H	8.17		
2	Ala	CO	175.73		
9	Pro	Ca	62.19		
10	Glu	N	121.55		
10	Glu	H	8.46		
10	Glu	CO	176.72		
10	Glu	Ca	56.65		
11	Met	N	119.91		
11	Met	H	8.22		
11	Met	CO	174.90		
11	Met	Ca	53.50		
12	Val	N	124.22	IleNH (an overlapping peak?), ValNH	Consistent
12	Val	H	9.01		
12	Val	CO	176.16		
12	Val	Ca	61.18		
13	Arg	N	125.34		
13	Arg	H	9.15		
13	Arg	CO	174.88		
13	Arg	Ca	56.31		
14	Gly	N	103.61		
14	Gly	H	8.43		
14	Gly	CO	176.55		
15	**Gln**	**N**	**119.86**	**HNCA 17(confident)-16-15**	**Confident**
15	**Gln**	**H**	**8.10**		
15	**Gln**	**CO**	**173.81**		
15	**Gln**	**Ca**	**53.34**		
16	**Val**	**N**	**123.62**	**HNCA 17(confident)-16, ValNH**	**Confident**
16	**Val**	**H**	**8.65**		
16	**Val**	**CO**	**175.21**		
16	**Val**	**Ca**	**62.98**		
17	**Phe**	**N**	**130.93**	**ValCO(V16), PheNH, unique seq=VF**	**Confident**
17	**Phe**	**H**	**8.94**		
17	**Phe**	**CO**	**175.84**		
17	**Phe**	**Ca**	**56.80**		
18	**Asp**	**N**	**124.51**	**HNCA 18-17(confident)**	**Confident**
18	**Asp**	**H**	**7.89**		
18	**Asp**	**CO**	**174.79**		
18	**Asp**	**Ca**	**53.42**		
19	Val	N	110.17		
19	Val	H	7.41		
19	Val	CO	174.41		

19	Val	Ca	59.68		
20	Gly	N	112.37		
20	Gly	H	8.68		
20	Gly	CO	176.25		
22	Arg	N	123.43		
22	Arg	H	8.52		
22	Arg	CO	177.52		
22	Arg	Ca	60.01		
23	Tyr	N	117.33	TyrNH	Consistent
23	Tyr	H	7.23		
23	Tyr	CO	175.63		
23	Tyr	Ca	55.24		
24	Thr	N	112.28	TyrCO(23Tyr)	Consistent
24	Thr	H	8.70		
24	Thr	CO	175.39		
24	Thr	Ca	59.38		
25	Asn	N	119.08		
25	Asn	H	9.62		
25	Asn	CO	174.09		
25	Asn	Ca	53.79		
26	Leu	Ca	54.71		
27	Ser	N	114.67	LeuCO(26Leu)	Consistent
27	Ser	H	8.42		
27	Ser	CO	178.95		
27	Ser	Ca	56.58		
28	Tyr	N	127.98	TyrNH	Consistent
28	Tyr	H	8.92		
28	Tyr	CO	173.35		
28	Tyr	Ca	60.10		
29	Ile	N	126.91	TyrCO(28Tyr)	Consistent
29	Ile	H	8.24		
29	Ile	CO	175.44		
30	Gly	N	106.52		
30	Gly	H	7.12		
30	Gly	CO	175.44		
30	Gly	Ca	45.42		
31	Glu	N	116.71		
31	Glu	H	8.26		
31	Glu	CO	170.22		
31	Glu	Ca	54.93		
32	Gly	N	110.52		
32	Gly	H	8.05		
32	Gly	CO	175.54		
32	Gly	Ca	54.99		
34	Tyr	N	112.97	TyrNH	Consistent

34	Tyr	H	7.96		
34	Tyr	CO	178.20		
35	**Gly**	**N**	**106.91**	**TyrCO(34Tyr), unique seq=YG**	**Confident**
35	**Gly**	**H**	**6.93**		
35	**Gly**	**CO**	**174.59**		
35	**Gly**	**Ca**	**44.91**		
37	Val	N	125.49	ValNH	Consistent
37	Val	H	8.98		
37	Val	CO	173.74		
37	Val	Ca	60.57		
39	Ser	N	115.48		
39	Ser	H	9.37		
39	Ser	Ca	55.54		
41	Tyr	N	122.62	TyrNH	Consistent
41	Tyr	H	9.63		
41	Tyr	CO	174.39		
41	Tyr	Ca	58.03		
42	Asp	N	125.48	TyrCO(41Tyr), not assigned before	Consistent
42	Asp	H	8.29		
42	Asp	CO	173.74		
42	Asp	Ca	52.03		
44	Leu	N	120.85		
44	Leu	H	8.32		
45	Asn	N	115.14	LeuCO(44Leu)	Consistent
45	Asn	H	6.63		
45	Asn	Ca	59.80		
46	Lys	N	117.98		
46	Lys	H	7.98		
46	Lys	CO	174.18		
46	Lys	Ca	56.37		
47	Val	N	112.42	ValNH	Consistent
47	Val	H	6.69		
47	Val	Ca	58.58		
47	Val	Ca	58.56		
48	Arg	N	122.61	ValCO(47Val)	Consistent
48	Arg	H	8.44		
48	Arg	CO	173.97		
48	Arg	Ca	55.84		
53	Lys	N	127.26		
53	Lys	H	8.93		
53	Lys	CO	174.88		
53	Lys	Ca	55.13		
57	Phe	N	115.40	LeuNH (overlapping peak?), PheNH	Consistent
57	Phe	H	7.88		
57	Phe	CO	177.16		

57	Phe	Ca	61.37		
67	Leu	N	120.41	LeuNH	Consistent
67	Leu	H	7.93		
67	Leu	CO	175.20		
67	Leu	Ca	57.52		
68	Arg	N	117.72		
68	Arg	H	8.25		
68	Arg	CO	177.31		
75	Arg	N	119.26		
75	Arg	H	7.26		
75	Arg	CO	178.83		
75	Arg	Ca	56.03		
76	Phe	N	120.95		
76	Phe	H	7.92		
76	Phe	CO	176.65		
76	Phe	Ca	53.97		
77	Arg	N	119.50		
77	Arg	H	7.60		
77	Arg	CO	175.25		
77	Arg	Ca	55.24		
78	His	N	126.72		
78	His	H	8.98		
78	His	CO	173.36		
78	His	Ca	57.37		
79	Glu	N	125.98		
79	Glu	H	8.06		
79	Glu	CO	175.28		
79	Glu	Ca	59.09		
80	Asn	N	119.01		
80	Asn	H	11.52		
81	Ile	N	120.82	IleNH	Consistent
81	Ile	H	7.78		
81	Ile	CO	173.82		
81	Ile	Ca	60.40		
89	Arg	N	117.60		
89	Arg	H	7.93		
89	Arg	CO	175.40		
89	Arg	Ca	54.31		
90	Ala	N	122.43		
90	Ala	H	8.78		
90	Ala	CO	175.28		
90	Ala	Ca	51.16		
91	Pro	Ca	64.20		
92	**Thr**	**N**	**104.69**	**Amide=T/G, Ca!=G, thus =T, HNCA 93(confident)-92**	**Confident**

92	**Thr**	**H**	**6.83**		
92	**Thr**	**CO**	**177.37**		
92	**Thr**	**Ca**	**58.23**		
93	**Ile**	**N**	**124.40**	**IleNH, unique seq=TI**	**Confident**
93	**Ile**	**H**	**8.22**		
93	**Ile**	**CO**	**174.76**		
93	**Ile**	**Ca**	**64.88**		
94	**Glu**	**N**	**120.13**	**HNCA 94-93**	**Confident**
94	**Glu**	**H**	**8.54**		
94	**Glu**	**CO**	**177.30**		
94	**Glu**	**Ca**	**58.82**		
95	Gln	N	114.84		
95	Gln	H	6.96		
95	Gln	CO	178.46		
95	Gln	Ca	55.23		
96	Met	N	121.55		
96	Met	H	7.22		
96	Met	CO	175.34		
96	Met	Ca	55.82		
98	Asp	N	116.07	HNCA 99-98	Consistent
98	Asp	H	7.61		
98	Asp	CO	174.90		
98	Asp	Ca	51.60		
99	Val	N	119.02	ValNH	Consistent
99	Val	H	9.01		
99	Val	CO	174.59		
99	Val	Ca	60.46		
103	Gln	N	126.50		
103	Gln	H	9.39		
103	Gln	CO	175.40		
103	Gln	Ca	53.28		
104	Asp	N	120.50		
104	Asp	H	8.64		
104	Asp	CO	173.54		
104	Asp	Ca	54.71		
108	Thr	N	112.99		
108	Thr	H	8.35		
108	Thr	CO	176.35		
108	Thr	Ca	58.99		
109	Asp	N	119.40	LeuNH	Consistent
109	Asp	H	8.82		
109	Asp	CO	172.95		
109	Asp	Ca	53.17		
112	Lys	N	120.99	TyrCO(111Tyr)	Consistent
112	Lys	H	8.74		

112	Lys	CO	177.57		
112	Lys	Ca	59.24		
114	Leu	N	116.60	LeuNH	Consistent
114	Leu	H	7.95		
114	Leu	CO	179.36		
114	Leu	Ca	56.00		
115	Lys	N	116.26	LeuCO(114Leu)	Consistent
115	Lys	H	7.24		
115	Lys	CO	179.02		
115	Lys	Ca	56.97		
117	Gln	N	121.01		
117	Gln	H	8.14		
117	Gln	CO	174.23		
117	Gln	Ca	54.77		
118	His	Ca	54.65		
119	Leu	N	126.69	LeuNH	Consistent
119	Leu	H	9.31		
119	Leu	CO	175.42		
119	Leu	Ca	54.10		
122	Asp	N	115.95	LeuNH	Consistent
122	Asp	H	8.15		
122	Asp	CO	176.77		
122	Asp	Ca	56.80		
125	Cys	N	118.32		
125	Cys	H	7.93		
125	Cys	CO	177.08		
125	Cys	Ca	62.58		
126	Tyr	N	116.69	TyrNH	Consistent
126	Tyr	H	7.44		
126	Tyr	CO	175.53		
126	Tyr	Ca	58.68		
140	Ser	N	119.14		
140	Ser	H	8.28		
140	Ser	CO	181.02		
140	Ser	CO	172.36		
141	Ala	N	126.48	AlaNH	Consistent
141	Ala	H	7.43		
141	Ala	CO	175.28		
143	Val	N	118.97		
143	Val	H	7.52		
143	Val	CO	173.06		
143	Val	Ca	61.03		
144	Leu	N	121.72		
144	Leu	H	8.63		
144	Leu	CO	174.63		

144	Leu	Ca	54.92		
151	Ser	N	109.30		
151	Ser	H	8.33		
151	Ser	CO	176.38		
152	Asn	N	117.82		
152	Asn	H	7.40		
152	Asn	CO	173.49		
152	Asn	Ca	52.15		
154	Leu	N	122.21		
154	Leu	H	8.52		
154	Leu	CO	174.91		
154	Leu	Ca	54.70		
155	Leu	N	124.08	LeuNH	Consistent
155	Leu	H	8.03		
155	Leu	CO	173.75		
155	Leu	Ca	53.16		
158	Thr	N	110.78		
158	Thr	H	7.42		
159	Cys	N	111.82		
159	Cys	H	8.17		
159	Cys	CO	174.00		
164	Cys	N	124.73		
164	Cys	H	8.70		
164	Cys	CO	175.51		
164	Cys	Ca	55.24		
221	Ser	N	109.80		
221	Ser	H	7.45		
221	Ser	CO	178.95		
223	Arg	N	116.99		
223	Arg	H	7.80		
223	Arg	CO	173.33		
223	Arg	Ca	53.19		
240	Gly	N	103.84		
240	Gly	H	7.73		
241	Ile	N	119.30		
241	Ile	H	7.12		
243	Gly	N	106.86	LeuCO(242Leu), seq = LG(240,243) or LT(183,293)	Consistent
243	Gly	H	7.53		
243	Gly	CO	178.95		
244	Ser	N	115.00		
244	Ser	H	8.08		
244	Ser	CO	171.99		
244	Ser	Ca	58.28		
247	Gln	N	120.58		

247	Gln	H	8.80		
247	Gln	CO	174.53		
248	Glu	N	118.30		
248	Glu	H	8.37		
248	Glu	CO	178.42		
248	Glu	Ca	58.98		
249	Asp	N	121.43		
249	Asp	H	7.70		
249	Asp	CO	178.93		
252	Cys	N	114.93		
252	Cys	H	7.45		
252	Cys	CO	176.35		
253	Ile	N	124.10	IleNH	Consistent
253	Ile	H	7.68		
253	Ile	CO	174.52		
261	Tyr	N	122.22	TyrNH	Consistent
261	Tyr	H	7.90		
261	Tyr	CO	178.42		
263	Leu	N	118.78	LeuNH	Consistent
263	Leu	H	8.13		
263	Leu	CO	180.15		
263	Leu	Ca	56.67		
264	Ser	N	114.23		
264	Ser	H	7.41		
264	Ser	CO	177.61		
264	Ser	Ca	58.74		
265	Leu	N	124.08	LeuNH	Consistent
265	Leu	H	6.83		
265	Leu	CO	174.06		
265	Leu	Ca	52.84		
266	Pro	Ca	59.39		
267	His	N	120.98		
267	His	H	8.44		
267	His	CO	175.48		
267	His	Ca	54.16		
269	Asn	N	121.71		
269	Asn	H	8.54		
269	Asn	CO	175.72		
269	Asn	Ca	52.09		
270	Lys	N	121.84		
270	Lys	H	8.28		
270	Lys	CO	174.41		
270	Lys	Ca	56.05		
271	Val	N	131.64	ValNH	Consistent
271	Val	H	8.79		

271	Val	CO	176.71		
271	Val	Ca	59.36		
274	Asn	N	113.81		
274	Asn	H	8.67		
274	Asn	CO	178.11		
274	Asn	Ca	54.36		
275	Arg	N	118.61		
275	Arg	H	7.50		
275	Arg	CO	175.90		
275	Arg	Ca	56.58		
276	Leu	N	119.75	LeuNH	Consistent
276	Leu	H	6.81		
276	Leu	CO	177.74		
276	Leu	Ca	56.05		
277	**Phe**	**N**	**115.88**	**LeuCO(276Leu), PheNH, unique seq=LF**	**Confident**
277	**Phe**	**H**	**7.81**		
277	**Phe**	**CO**	**177.05**		
277	**Phe**	**Ca**	**53.61**		
279	Asn	N	115.26		
279	Asn	H	8.73		
279	Asn	CO	177.70		
280	Ala	Ca	51.39		
281	Asp	N	122.23		
281	Asp	H	8.57		
281	Asp	CO	176.67		
281	Asp	Ca	54.46		
282	Ser	N	123.04		
282	Ser	H	8.88		
282	Ser	CO	177.71		
284	Ala	N	122.34	AlaNH	Consistent
284	Ala	H	7.12		
284	Ala	CO	178.80		
284	Ala	Ca	54.57		
285	Leu	N	112.73	LeuNH	Consistent
285	Leu	H	7.24		
285	Leu	CO	179.35		
285	Leu	Ca	56.12		
286	Asp	N	120.73	LeuCO(285Leu)	Consistent
286	Asp	H	7.47		
286	Asp	CO	178.64		
286	Asp	Ca	57.46		
294	Phe	N	129.88		
294	Phe	H	9.60		
294	Phe	CO	174.70		

295	Asn	N	117.04		
295	Asn	H	8.71		
295	Asn	CO	174.57		
298	Lys	N	116.82		
298	Lys	H	7.28		
298	Lys	CO	176.49		
298	Lys	Ca	52.15		
299	Arg	N	123.21		
299	Arg	H	6.96		
299	Arg	CO	175.52		
300	Ile	N	127.40		
300	Ile	H	7.33		
300	Ile	CO	175.81		
302	Val	N	121.45		
302	Val	H	8.77		
302	Val	CO	179.21		
303	Glu	N	120.28		
303	Glu	H	8.93		
303	Glu	CO	175.62		
304	Gln	N	115.99		
304	Gln	H	6.88		
304	Gln	CO	179.11		
304	Gln	Ca	57.51		
311	Leu	Ca	53.39		
312	Glu	N	121.01	LeuCO(311Leu)	Consistent
312	Glu	H	7.15		
312	Glu	CO	177.61		
312	Glu	Ca	58.99		
313	Gln	N	117.42		
313	Gln	H	8.84		
313	Gln	CO	177.39		
313	Gln	Ca	57.08		
315	Tyr	N	117.73	TyrNH	Consistent
315	Tyr	H	7.23		
315	Tyr	CO	174.90		
315	Tyr	Ca	57.37		
316	Asp	N	127.39	TyrCO(315Tyr)	Consistent
316	Asp	H	9.30		
316	Asp	CO	176.51		
318	Ser	N	114.05		
318	Ser	H	7.86		
318	Ser	CO	178.57		
318	Ser	Ca	59.95		
322	Ile	N	111.30	IleNH	Consistent
322	Ile	H	7.89		

322	Ile	CO	176.61		
322	Ile	Ca	59.09		
323	Ala	N	124.57		
323	Ala	H	8.42		
323	Ala	CO	175.64		
325	Ala	N	119.84		
325	Ala	H	7.54		
325	Ala	CO	175.75		
325	Ala	Ca	49.58		
335	Asp	N	115.30		
335	Asp	H	8.03		
335	Asp	CO	176.38		
336	Leu	N	121.46	LeuNH	Consistent
336	Leu	H	7.08		
336	Leu	CO	176.26		
336	Leu	Ca	52.52		
338	Lys	N	121.88		
338	Lys	H	9.36		
338	Lys	CO	178.91		
339	Glu	N	122.52		
339	Glu	H	9.55		
339	Glu	CO	177.99		
340	Lys	N	120.37		
340	Lys	H	6.89		
340	Lys	CO	178.88		
341	Leu	N	118.58		
341	Leu	H	7.91		
341	Leu	CO	178.95		
341	Leu	Ca	57.89		
343	Glu	N	119.40		
343	Glu	H	7.17		
343	Glu	CO	177.95		
343	Glu	Ca	59.39		
344	Leu	N	119.76		
344	Leu	H	8.16		
344	Leu	CO	179.21		
344	Leu	Ca	57.71		
346	Phe	N	124.83		
346	Phe	H	8.79		
346	Phe	CO	178.50		
346	Phe	Ca	62.92		
347	Glu	N	119.23		
347	Glu	H	8.42		
347	Glu	CO	177.32		
347	Glu	Ca	59.14		

350	Ala	N	128.55	AlaNH	Consistent
350	Ala	H	7.33		
350	Ala	CO	175.85		
351	Arg	N	113.88		
351	Arg	H	7.61		
351	Arg	CO	180.35		
352	Phe	N	116.57	PheNH, TyrNH(overlapping peak?)	Consistent
352	Phe	H	6.85		
352	Phe	CO	175.58		
352	Phe	Ca	58.09		
353	Gln	N	120.79		
353	Gln	H	7.73		
353	Gln	CO	176.12		
353	Gln	Ca	53.33		
355	Gly	Ca	44.83		
356	**Tyr**	**N**	**121.55**	**TyrNH, HNCA (i-1) Gly, seq =G202Y203T(no) or G355Y356R**	**Confident**
356	**Tyr**	**H**	**7.56**		
356	**Tyr**	**CO**	**174.27**		
356	**Tyr**	**Ca**	**58.91**		
357	**Arg**	**N**	**125.70**	**TyrCO(356Y), HNCA 356(confident)-357**	**Confident**
357	**Arg**	**H**	**7.86**		
357	**Arg**	**CO**	**175.74**		
357	**Arg**	**Ca**	**55.12**		